UNIVERSITY OF SOUTHAMPTON

FACULTY OF SCIENCE

School of Chemistry

Low Viscosity Nematics: Design of Dopants

by

Sophie Marchant-Lane

Thesis for the degree of Doctor of Philosophy

February 2005

In honour of my Grandparents
Evan and Barbara

UNIVERSITY OF SOUTHAMPTON

ABSTRACT

FACULTY OF SCIENCE

CHEMISTRY

Doctor of Philosophy

LOW VISCOSITY NEMATICS: DESIGN OF DOPANTS

by Sophie Marchant-Lane

The rotational viscosity, γ_1, of a nematic liquid crystal is of special importance because it determines the switching times for display devices. However, the understanding of the molecular factors that control γ_1 is not well-developed. This thesis details an experimental investigation into the relaxation dynamics of a wide range of nematogenic mixtures. The dimeric materials used as dopants in the host nematic mixture, ZLI-4792, have been synthesised and their effect on the host studied.

There are a variety of techniques available for the determination of γ_1 and a direct method in which a sample with a uniformly aligned director is initially inclined at an angle to a magnetic field has been used. Since the diamagnetic anisotropy is positive, the director in this orientation is unstable and it realigns parallel to the field; the relaxation time for this process is directly proportional to the rotational viscosity coefficient. To determine the relaxation time it is necessary to measure the time dependence of the angle between the director and the magnetic field. ESR spectroscopy provides a powerful technique with which to do this. A novel ESR spectroscopy experiment has been devised which allows the determination of the field-induced director relaxation time from a single ESR spectrum.

During the investigation into the dynamics of the doped nematic mixtures an unexpected gelling behaviour was observed for four of the dimeric dopants. These gelled systems were then studied using a range of techniques in order to develop an understanding of this novel behaviour. Crystal structures of the pure dopants show that the molecules pack in a sheet array; this suggests the network, which traps the liquid crystal, has a sheet structure. The form of the ESR spectrum obtained for the gelled systems shows that the magnetic field is unable to align the director, indicating that the director is pinned at the surface of the sheets.

Some Trimeric dopants were also synthesised and their gelling behaviour studied.

Chapter 1

Introduction to Nematic Liquid Crystals

Contents

Chapter 2

Rotational Viscosity Coefficient

Contents

Chapter 3

Electron Spin Resonance Spectroscopy

Contents

Chapter 4

Doped nematic systems

Contents

Chapter 5

Liquid Crystal Gels

Contents

Chapter 6

Experimental

Contents

Chapter 1

Introduction to Nematic Liquid Crystals

Figures

Chapter 2

Rotational Viscosity Coefficient

Tables

Figures

Chapter 3

Electron Spin Resonance Spectroscopy

Figures

Chapter 4

Doped nematic systems

Tables

Figures

Chapter 5

Liquid Crystal Gels

Tables

Figures

Appendix A

ESR Experimental Parameters

Tables

Appendix B

ESR Results for the Doped Systems

Tables

Acknowledgements

During the course of my PhD I have had support from many people, without whom I would not have been able to reach this point.

First and foremost, I would like to thank Professor Geoffrey Luckhurst for his constant support, encouragement, expertise and time over the last three and a half years.

A special thank you goes to my other supervisors, Dr David Dunmur and Dr Martin Grossel, for their guidance and time. David for his help, enthusiastic support and valuable discussions and Martin for making organic chemistry enjoyable.
I would like to express my gratitude to all of my supervisors for giving me the confidence to get this far, for their patience, and for inspiring my interest in the subject.

Massive appreciation goes to Hitachi for sponsoring this research project and supplying me with the necessary materials.

I would like to thank to Azizah Mainal for her hard work on the variable temperature NMR experiments, Professor Sugimura for his work on the dynamic NMR experiments and James Orton for his work on the crystal structures. To the numerous project and summer students who have contributed to the work in this thesis, particularly Nefeli for her hard work on the gelled systems.

I also wish to thank Dr Bakhir Timimi (Tim) for his perseverance in teaching me how to use the ESR spectrometer.

I am always indebted to Professor George Attard who guided me onto this path in the first place.

To the people who have made my time in the lab so enjoyable.

I would like to express my total appreciation to my family for their attempts at being interested in my work and for just being there for me and finally to Tom for his love, understanding and patience over the last six years.

Abbreviations

LCD = Liquid Crystal Display

TN = Twisted Nematic

STN = Super Twisted Nematic

VA = Vertical Alignment

IPS = In-Plane Switching

ESR = Electron Spin Resonance

NMR = Nuclear Magnetic Resonance

DSC = Differential Scanning Calorimetry

5CB = 4-pentyl-4'-cyanobiphenyl

8CB = 4-octyl-4'-cyanobiphenyl

DCM = Dichloromethane

DMF = Dimethylformamide

RT = Room Temperature

PCH5 = 4-(*trans*-4'-pentylcyclohexyl)benzonitrile

Table of Symbols

Symbol	Description
$\hat{n}$	Director
φ	Angle between the molecular long axis and the director
$\overline{P}_2$	Second rank orientational order parameter
$\overline{P}_2^n$	Director orientational order parameter
$\Delta\tilde{\varepsilon}$	Dielectric anisotropy
V_{th}	Threshold voltage
$\Delta\tilde{\chi}$	Diamagnetic susceptibility
θ	Angle between the dipole and the molecular long axis
β	Angle between the director and the magnetic field
ϕ	Twist angle
γ_1	Rotational viscosity
τ	Director relaxation time
$\tilde{A}_{\parallel}$	Parallel hyperfine tensor
$\tilde{A}_{\perp}$	Perpendicular hyperfine tensor
a_{iso}	Isotropic hyperfine splitting
λ	Wavelength of light
$\Delta\tilde{n}$	Birefringence
p	Pitch of helix
d	Thickness of cell
K_1	Splay elastic constant
K_2	Twist elastic constant
K_3	Bend elastic constant
$\Delta\tilde{\nu}$	Quadrupolar splitting

Chapter 1

Introduction to Nematic Liquid Crystals

1.1 Introduction

Liquid crystals were first discovered in the late nineteenth century, but their unique physical properties have only been exploited in the last thirty years for such technological applications as digital watches, calculators, flat screen display devices for computers, mobile telephones and more recently liquid crystal display (LCD) televisions. The market for these display devices has reached many billions of pounds in the last decade. Liquid crystals also have applications for non-display technologies which include temperature sensors and optical switches. They have also been used in the production of two tone paint for cars, see picture below (courtesy of BASF),

and polymer liquid crystals are utilised for high strength fibres, the most common of which is Kevlar.

The discovery of liquid crystals is usually attributed to an Austrian botanist by the name of Friedrich Reinitzer. In 1888 he experimented with a substance closely related to cholesterol and noted that it had two melting points; the first at 145.5°C when it melted from a solid to a cloudy liquid and then at 178.5°C it turned into a clear liquid. He also noted some unusual optical behaviour on cooling, where the sample changed colour. Reinitzer sent his sample to Otto Lehmann who characterised the sample using a polarising microscope and noticed the similarity to some of his own samples. He first referred to them as soft crystals but later used the term crystalline fluids. However, as he became convinced that the opaque phase was a uniform phase of matter exhibiting properties of both solids and liquids and he coined the term liquid crystals.

A liquid crystal is a state of matter that occurs between a solid and a liquid, hence the name. Another term commonly used is 'mesophase', meaning intermediate phase. Liquid crystals are therefore considered the fourth state of matter as they are fluid like a liquid but have some long range order among the molecules which is inherent for a solid.

This Thesis will concentrate on the class of liquid crystals known as thermotropics. As the name indicates their existence depends on temperature. When a thermotropic liquid crystal is heated from its solid or crystalline state it turns into a turbid liquid (the liquid crystalline phase or mesophase), which when observed between crossed polarisers exhibits strong birefringence. If heating continues, eventually another phase transition occurs where the turbid liquid becomes clear, and if visualized between crossed polarisers appears dark because the birefringence has vanished. This transition is known generally as the clearing point or the isotropic transition temperature. Some mesogenic compounds maybe polymorphic, that is they exhibit more than one liquid crystal phase between the solid and isotropic phases. However, this chapter is only going to describe one of the liquid crystal phases; the nematic phase, which is the simplest and most common of all the liquid crystal phases.

1.2 The Nematic Phase

The centres of mass of the molecules constituting a solid all have specific locations within a lattice with their molecular axes pointing in certain directions; hence a solid has long range positional order. When a solid melts into an isotropic liquid this order is completely lost as the molecules (and hence their centres of mass) now have random positions. Liquid crystals differ from isotropic liquids due to the orientational order of the molecules, which destroys the isotropy of the liquid and produces anisotropy (not all the directions in the liquid crystal are equivalent). Solids can be either isotropic or anisotropic depending on the molecules that occupy the specific lattice sites. A solid with cubic symmetry is isotropic whereas solids with all other symmetries are anisotropic. This anisotropy means that the elastic, electric, magnetic or optical properties will give different values dependent on the direction along which they are measured.

For a compound to form a nematic liquid crystal its constituent molecules must have one axis that is different to the other two. The most common type of molecule that forms a liquid crystal phase is a rod-like molecule; in which one molecular axis is much longer than the other two. These compounds are known as calamatic liquid crystals. Liquid crystals can also be formed from disc shaped molecules in which one molecular axis is much shorter than the other two. These compounds are known as discotic liquid crystals.

The important structural feature of all thermotropic liquid crystals is the presence of a rigid moiety which allows the preservation of the elongated or discotic shape essential for alignment. The simplest and most disordered liquid crystal phase is the nematic phase in which the molecules are, on average, aligned with their axes of cylindrical symmetry parallel to one another. A local preferred direction is thus defined and is described by a unit vector known as the director, $\hat{\boldsymbol{n}}$, around which there is rotational symmetry therefore, the phase is said to be uniaxial, which means that there is only one principal axis that governs the properties of the phase. A characteristic of the nematic phase is that the axis of symmetry has no polarity, even if the molecules themselves are polar and as a consequence the sign of the unit vector is of no physical importance as $\hat{\boldsymbol{n}}$ and $-\hat{\boldsymbol{n}}$ are equivalent. The nematic phase is fluid due to the lack of long-range positional order of the centres of mass of the molecules, allowing them to move freely. Figure 1 shows a schematic representation of the molecular organisation in a nematic phase.

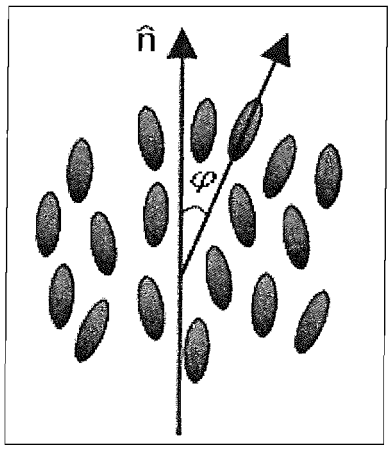

Figure 1: Schematic representation of the nematic phase at a molecular level.

The word nematic comes from the Greek word meaning thread-like because the typical texture observed for a nematic under a polarising microscope consists of many dark lines. These dark lines originate from differences in the director pattern caused by defects in the director field and are known as disclinations, see Figure 2. These disclinations result from optical extinction caused by the crossed polarisers. For this optical extinction to occur the director must be aligned in the direction of either of the two polarisers. These disclinations can meet at points, which give rise to defects known as brush defects, the most common of which is the four brush defect.

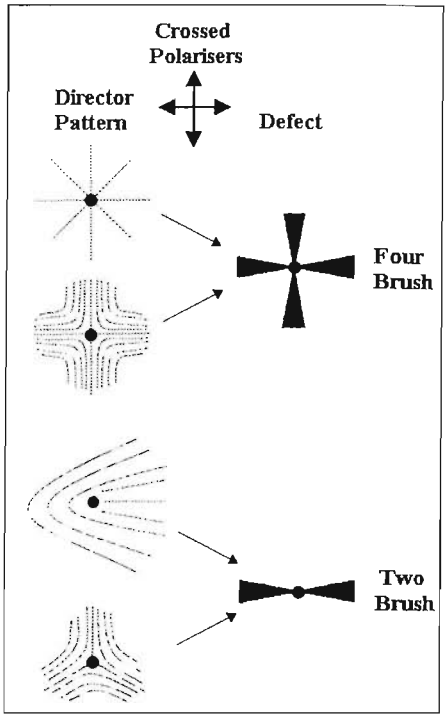

Figure 2: The alignment of the director resulting in brush defects.

A nematic texture observed when the sample is homogeneously aligned is known as the Schlieren texture and a typical example is shown in Figure 3, in which the birefringence changes throughout the sample producing a colour change across the texture. However some of this sample is not fully aligned as the defects indicate.

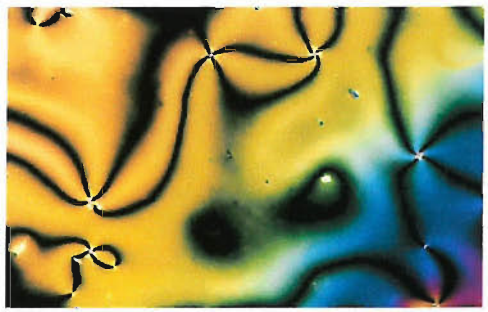

Figure 3: Schlieren texture of a nematic liquid crystal.

The orientational order of the molecular long axes with respect to the director can be defined by the second rank orientational order parameter, $\overline{P}_2$, for molecules with D_{nh} symmetry or higher with n≥3

$$\overline{P}_2 = \frac{\overline{3\cos^2\varphi - 1}}{2}, \qquad (1)$$

where φ is the angle between the director and the molecular symmetry axes (long axes of the molecule). This orientational order parameter is a measure of the molecular

fluctuations and is strongly temperature dependent. As the temperature is increased the molecular fluctuations increase, decreasing the order and hence $\overline{P}_2$. The order parameter takes the value of 0 (for an isotropic liquid) and 1 (for a fully aligned sample). However, usually for a nematic an upper limit of 0.8 is observed at low temperatures ($T/T_N = 0.8$) and a lower limit of ~0.3-0.4 is observed at the nematic-isotropic transition ($T/T_N = 0.98$), see Figure 4.

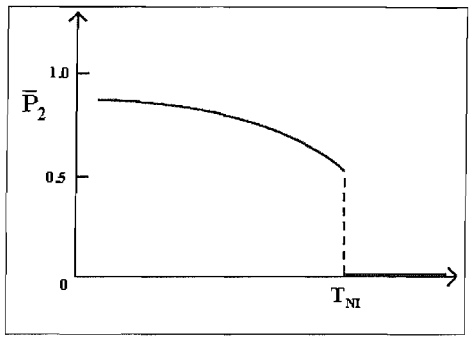

Figure 4: Plot of the order parameter vs. temperature for a nematic liquid crystal.

Additional orientational order parameters can be defined, for example $\overline{P}_4$ which is the average value of the fourth Legendre polynomial,

$$\overline{P}_4 = \frac{1}{8}\left\langle 35\cos^4\varphi - 30\cos^2\varphi + 3\right\rangle, \tag{2}$$

This higher order parameter is more difficult to measure than the second rank orientational order parameter.

1.3 Continuum theory of nematic liquid crystals

The continuum theory was first proposed by Zocher [1] and Oseen [2], however Frank [3] presented the elastic theory in a simpler and more comprehensive way. In order to obtain a nematic sample in which the director is uniformly aligned careful surface treatments and/or the use of external fields are required. The director in a bulk liquid crystal normally varies with position and is therefore not uniform, but on a microscopic level the local distribution of the molecules does not vary, so it is assumed that any orientational or positional order parameters do not vary in the sample. The continuum theory, therefore, only concerns itself with the elastic properties of the sample and assumes all order parameters remain constant and hence the phase remains locally uniaxial. The only point where this assumption breaks down is where there are defects in the director field; however these defects will be ignored in this discussion. In a thin layer sample where the boundary conditions do not produce parallel orientations of the director, a curvature is introduced in which, the director

undergoes a change from one orientation to another. Curvature can also occur if the orientating effect of an external field competes with the conditions set at the boundaries. This curvature is theoretically described by the continuum theory which gives the elastic energy as a function of the curvature. The fundamental equation of the continuum theory for a non-chiral nematic is given by [3]

$$F_{dist} = \frac{1}{2}K_1\left[\nabla \cdot \hat{\boldsymbol{n}}\right]^2 + \frac{1}{2}K_2\left[\hat{\boldsymbol{n}} \cdot \left(\nabla \times \hat{\boldsymbol{n}}\right)\right]^2 + \frac{1}{2}K_3\left|\hat{\boldsymbol{n}} \times \left(\nabla \times \hat{\boldsymbol{n}}\right)\right|^2, \tag{3}$$

where F_{dist} is the distortion free energy per unit volume, K_1, K_2 and K_3 are the elastic constants otherwise known as the Zocher-Oseen-Frank constants. These three constants describe how 'stiff' the nematic liquid crystal is to distortions of the director. Evaluation of the derivatives in each term at a point in a liquid crystal where the director at the origin is along the z-axis gives three examples that highlight the meaning of this expression for the free energy per unit volume. The first derivative of n_z with x, y, z is zero at the origin.

Splay:
$$\left[\nabla \cdot \hat{\boldsymbol{n}}\right]^2 = \left[\left(\frac{\partial n_x}{\partial x}\right)_{y,z} + \left(\frac{\partial n_y}{\partial y}\right)_{x,z}\right]^2, \tag{4}$$

Twist:
$$\left[\hat{\boldsymbol{n}} \cdot \left(\nabla \times \hat{\boldsymbol{n}}\right)\right]^2 = \left[\left(\frac{\partial n_y}{\partial x}\right)_{y,z} - \left(\frac{\partial n_x}{\partial y}\right)_{x,z}\right]^2, \tag{5}$$

Bend:
$$\left|\hat{\boldsymbol{n}} \times \left(\nabla \times \hat{\boldsymbol{n}}\right)\right|^2 = \left(\frac{\partial n_x}{\partial z}\right)^2_{x,y} + \left(\frac{\partial n_y}{\partial z}\right)^2_{x,y}, \tag{6}$$

Figure 5 shows three principal director distortions called splay, twist and bend. Therefore, K_1, K_2 and K_3 are known as the splay, twist and bend distortion constants, respectively. Typical values for these constants are about 10^{-12}N, with K_3 larger than K_1 and K_2.

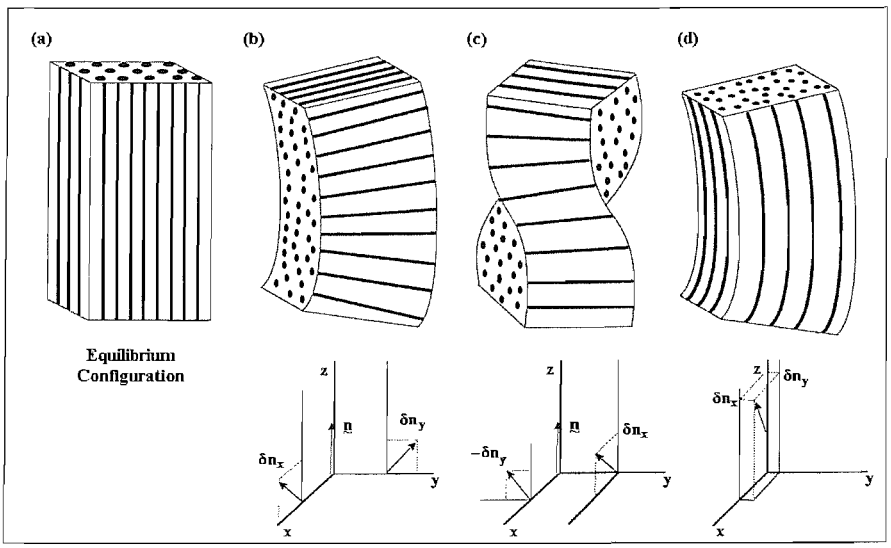

Figure 5: The three principle distortions of the director; (b) splay, (c) twist, and (d) bend.

For a bulk nematic the total elastic energy associated with the distortion must be a minimum in order to obtain equilibrium conditions. In the presence of a magnetic or electric field the total free energy is the sum of the magnetic free energy density [4]

$$F_{mag} = -\frac{1}{2}\mu_0^{-1}\Delta\tilde{\chi}(\boldsymbol{B}\cdot\hat{\boldsymbol{n}})^2, \tag{7}$$

or the electric free energy density

$$F_{diel} = -\frac{1}{2}\varepsilon_0\Delta\tilde{\varepsilon}(\boldsymbol{E}\cdot\hat{\boldsymbol{n}})^2, \tag{8}$$

and the elastic free energy density, (see Equation 3).

Consider the case where there are defects; quite clearly the assumption that the order parameter remains constant is no longer correct. At a point defect the order has been lost and the expression for the distortion free energy now has to include the order parameter. The Landau-de Gennes theory models the defects as isotropic cores and therefore they have included the order parameter in their expression.

1.4 External influences

1.4.1 Surfaces

To obtain a perfectly uniform director within a nematic sample, surface treatments, external fields or a combination of the two is required. Two extreme types of director alignment are possible with the use of surfaces alone; uniform planar (in the past known as homogeneous) and homeotropic. In the uniform planar alignment the director of the liquid crystal phase is orientated parallel to the supporting substrates and to a given direction, see Figure 6(a). A thin film of uniform planar aligned liquid crystal exhibits strong birefringence when viewed between crossed polarisers and if the sample is not perfectly aligned disclinations or defects are observed.

Homeotropic alignment is where the director is aligned perpendicular to the supporting substrate; see Figure 6(b). The polarisation of the light is not changed by a homeotropic sample and therefore complete blackness is observed under a polarising microscope.

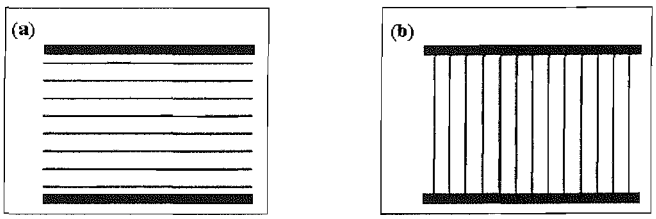

Figure 6: Types of surface alignment; (a) uniform planar and (b) homeotropic.

The homeotropic alignment is achieved by treating the glass substrates (surfaces) with base and then acid to produce a surface covered with silanol groups which, will interact with polar liquid crystals such as 4-pentyl-4'-cyanobiphenyl (5CB). The alignment layer of molecules at the surface will in turn interact with the molecules from the bulk and hence induce normal alignment to the surface. However, this will not work for non-polar liquid crystals, so the glass is treated at high temperatures with long chain alcohols in order to produce an alkylated surface. These long alkyl chains, which are normal to the glass, will then interact with the alkyl chains of the nematogenic molecule to induce perpendicular alignment.

The production of the uniform planar alignment is not quite as easy as it requires the glass substrates to be covered with multifunctional groups such polyimides and then followed by rubbing in order to induce a preferred alignment direction. Obviously any alignment in-between these two extremes can be achieved. Introducing a pre-tilt in the anchoring alignment layer can produce a range of director orientations across the cell, see the twist and bend cell configurations in Figure 7, which have been induced by a field but can just as well be created by surface alignments. The splay geometry is induced by a combination of surface treatments and anti-parallel rubbing of the coated substrates. On the other hand the bend geometry is induced by parallel rubbing of the coated substrates.

1.4.2 Magnetic fields

Interaction of materials with magnetic fields is divided into two categories: Paramagnetic and diamagnetic. Molecules that are paramagnetic have one or more unpaired electrons which will force the sample to move to regions of high field, whereas compounds that are diamagnetic have no unpaired electrons and will be forced to regions of low magnetic field. Liquid crystal molecules as with most organic molecules are generally diamagnetic. When a diamagnetic material is subjected to a uniform magnetic field its energy is changed, this change is given by

$$U = -\chi B^2 / 2\mu_0, \tag{9}$$

where χ is the magnetic susceptibility, B is the magnetic flux density and μ_0 is the permeability of a vacuum. The value of the magnetic susceptibility for diamagnetic species is negative so they become more stable as they move to regions of low field. For liquid crystals however, the situation is more interesting as the magnetic susceptibility can take one of two values, $\tilde{\chi}_{\parallel}$ along the director and $\tilde{\chi}_{\perp}$ perpendicular to the director, due to the anisotropy of the phase. The anisotropic magnetic susceptibility (diamagnetic susceptibility) is given by

$$\Delta\tilde{\chi} = \tilde{\chi}_{\parallel} - \tilde{\chi}_{\perp}, \tag{10}$$

The tilde shows the value in the liquid crystal phase.

The difference in energy between the director being aligned parallel to the magnetic field and perpendicular to it is;

$$\Delta U = -\Delta\tilde{\chi}B^2 / 2\mu_0. \tag{11}$$

Therefore, if $\Delta\tilde{\chi}$ is positive then the energy difference, ΔU, is negative so the director will align parallel to the magnetic field and vice versa. The sign of $\Delta\tilde{\chi}$ is determined by the molecular structure of the constituent molecules. For rod-like mesogens containing several aromatic rings $\Delta\tilde{\chi}$ is positive and those containing only cyclohexyl rings tend to have a negative value. The field needed to align the director fully is very low in comparison with the fields needed to produce comparable macroscopic order in an isotropic liquid. This difference is due to the long range order in the nematic phase and so the value of $\Delta\tilde{\chi}$ obtained is essentially that of the entire sample rather than a single molecule as is the case for an isotropic liquid. The diamagnetic susceptibility of a nematic is temperature dependent due to the fact that the orientational order changes with temperature. The magnetic flux density needed to align a nematic sample fully will increase with increasing temperature.

1.4.3 Electric fields

The response of nematogens to electric fields is of the utmost importance for display applications. Understanding the response of liquid crystals to electric fields is not difficult as it is analogous to what happens in a magnetic field. There are subtle differences, due to the fact that the electric field experienced by the molecule is not necessarily the same as the applied field, but these will be ignored. For a uniaxial mesophase subjected to an electric field, E, the energy change will depend on whether the field is applied parallel or perpendicular to the director. The resultant energy difference is

$$\Delta U = \varepsilon_0 \Delta\tilde{\varepsilon} E^2. \tag{12}$$

where ε_0 is the permittivity of a vacuum and $\Delta\tilde{\varepsilon}$ is the relative anisotropy in the permittivity or dielectric anisotropy of the nematic and is given by

$$\Delta\tilde{\varepsilon} = \tilde{\varepsilon}_{\parallel} - \tilde{\varepsilon}_{\perp}. \tag{13}$$

If the dielectric anisotropy is positive the directors aligns parallel to the electric field, just like the analogous case for the diamagnetic susceptibility. The electric fields needed to align the director are low and are normally only a few volts across a thin cell. The value of

the dielectric anisotropy is dependent on the orientational order of the system as for $\Delta\tilde{\chi}$, and the extent of this dependence is shown in Equation (14), which combines two molecular contributions with the orientational order parameter, $\overline{P}_2$ [5]

$$\Delta\tilde{\varepsilon} = \frac{nhF}{\varepsilon_0}\left[(\alpha_l - \alpha_t) + F\left(\mu^2 / k_B T\right)\left(3\cos^2\theta - 1\right)/2\right]\overline{P}_2, \tag{14}$$

where α_l is the polarizability along the long axis of the molecule and α_t is the polarizability at right angles to this axis. The other terms are given by;

$$h = 3\bar{\varepsilon}/(2\bar{\varepsilon} + 1), \tag{15}$$

with $\bar{\varepsilon}$ being the average permittivity

$$\bar{\varepsilon} = (\varepsilon_{\parallel} + 2\varepsilon_{\perp})/3, \tag{16}$$

and

$$F = (1 - f\bar{\alpha})^{-1}, \tag{17}$$

where $\bar{\alpha}$ is the average polarizability;

$$\bar{\alpha} = (\alpha_l + 2\alpha_t)/3, \tag{18}$$

and

$$f = 2n(\bar{\varepsilon} - 1)/3\varepsilon_0(2\bar{\varepsilon} + 1). \tag{19}$$

The term $(\alpha_l - \alpha_t)$ in Equation (14) is the contribution to $\Delta\tilde{\varepsilon}$ from a non-polar nematic. Whereas the term $\left(\mu^2 / k_B T\right)\left(3\cos^2\theta - 1\right)/2$ is the contribution from the dipole in a polar nematic with a single dipole, μ. Here θ is the angle made between the dipole and the molecular long axis.

1.5 Elastic constants

1.5.1 The Freedericksz transition

The three elastic constants, K_1, K_2 and K_3, as described in Section 1.3 can be measured by three relatively simple experiments devised by Freedericksz. The experiments highlight the large effect of the interaction between the mesogens and surfaces. When the alignment at a boundary opposes the response to an applied field a threshold phenomena called the Freedericksz transition occurs.

For the twist elastic constant a cell with uniform planar alignment is prepared and then a magnetic field is applied perpendicular to the director but in the plane of the sample. For a liquid crystal with a positive diamagnetic susceptibility the director will realign parallel to the magnetic field, therefore undergoing a twist deformation, see Figure 7(a).

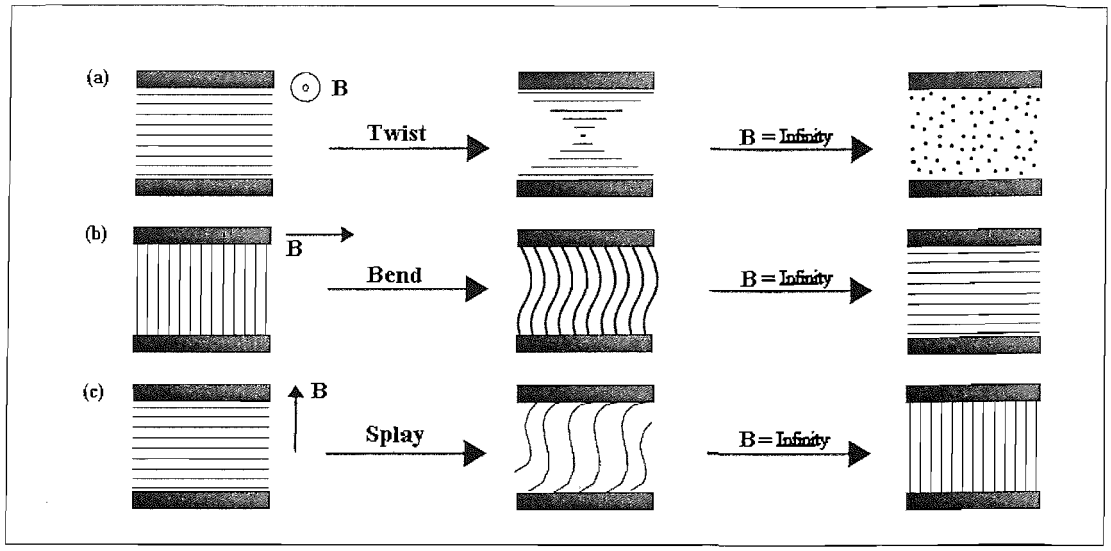

Figure 7: Configuration of the cells before and after the Freedericksz transition for the (a) twist, (b) bend and (c) splay deformations.

Initially the angle, β, between the director and the applied field does not change with the increasing field and the elastic forces are dominant. Then a threshold field, B_{th}, is reached and the angle begins to decrease until eventually the elastic forces are overcome and the magnetic energy is dominant. This is illustrated by the plot in Figure 8 which gives the director orientation, β_m, in the middle of the cell.

As the magnetic field is increased, the director moves from an initial orientation, where $\beta_m = 90^\circ$ to the magnetic field, to its new equilibrium position and limiting value of $\beta_m = 0^\circ$.

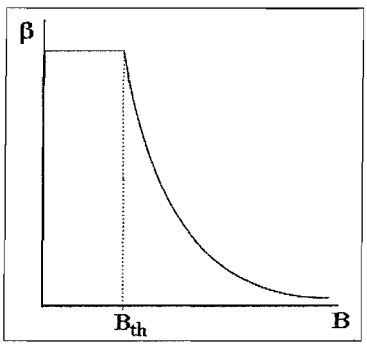

Figure 8: A plot of angle vs. magnetic flux density showing the threshold field of a cell.

At the threshold field the elastic and magnetic energies balance;

$$U_{magnetic} \approx U_{elastic}, \tag{20}$$

therefore

$$\Delta\tilde{\chi}B^2 / 2\mu_0 \approx K_2 / d^2, \tag{21}$$

giving

$$K_2 \approx \Delta\tilde{\chi}B_{th}^2 d^2 / 2\mu_0. \tag{22}$$

This approximate result is similar to the exact result [6]

$$K_i = \Delta\tilde{\chi} B_{th}^2 d^2 / \pi^2 \mu_0. \qquad i=1,2,3 \qquad (23)$$

The experiments for the determination of the splay and bend deformations are similar and only differ in the initial orientation of the director with respect to the surface and the direction of the applied field. The initial and final geometries of the cells are illustrated in Figure 7(b) and (c). The equations for the two elastic constants are found to have the same form as Equation (22). The twist deformation is the easiest to produce and the corresponding elastic constant tends to have lower values, whilst the bend deformation is the hardest and the corresponding elastic constant takes higher values i.e. for the same sample the bend deformation requires a higher magnetic field to realign the director than the field required for the twist deformation. The elastic constants are found to increase as the temperature decreases due to the increase in orientational order of the system upon lowering of the temperature. It was predicted and found that the elastic constants are proportional to the square of the order parameter, $\overline{P}_2$ [7].

1.5.2 Elastic constants and molecular structure

Experimental results have shown that the length and breadth of the molecules dramatically influence the elastic constants. This has been illustrated by Schadt and Muller [8] who found very little change in the values for K_1 and K_3 (and hence the ratio K_3/K_1) for a variety of compounds with similar length to breadth ratios. They varied the core units of the molecules but kept the end groups the same in their comparison. However, if the length to breadth ratio is changed the ratio K_3/K_1 either increases or decreases depending on the type of groups added to increase the length of the molecules. These additions can be split into two categories: Rigid molecules and flexible molecules.

(i) Rigid molecules: Leenhouts *et al* [9] found that by adding relatively rigid groups to increase the length of the molecules increases the ratio K_3/K_1.

(ii) Molecules with flexible groups: It has been shown that the addition of an alkyl or alkoxy chain to an aromatic core of a molecule decreases the ratio K_3/K_1 [10]. This decrease in the ratio is due to the fact that K_1 increases whilst K_3 remains unaltered. However, there are exceptions to this general rule. The ratio K_3/K_1 is important when considering the application of liquid crystals to display devices as this ratio governs the steepness of the voltage-transmission curves, see Section 1.8.3.

1.6 Optical properties

1.6.1 Polarised light

An electromagnetic wave consists of propagating electric and magnetic fields. For the propagation of an electromagnetic wave to occur both the electric and magnetic fields must point in a direction perpendicular to the propagation direction, and in addition, the electric field must always be orthogonal to the magnetic field, see Figure 9.

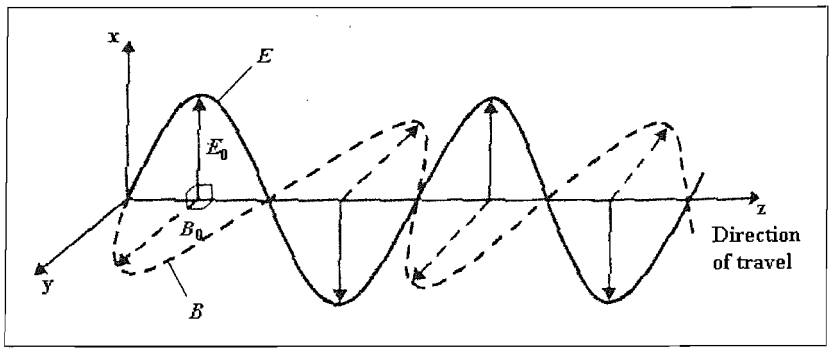

Figure 9: Schematic representation of a plane polarised light wave illustrating that E and B are mutually perpendicular.

Light is an electromagnetic wave with a wavelength of between 0.4 and 0.7 μm and is the only form of electromagnetic wave which is visible to the human eye. The orientation of the electric and magnetic fields in the plane perpendicular to the direction of propagation determines the polarisation of the wave. Only the orientation of the electric field is going to be discussed as the magnetic field always remains perpendicular to the electric field. When the electric field is orientated along the x-axis, as shown in Figure 9, the wave is said to be linearly polarised with the polarisation direction being the x-axis. The polarisation direction, however, can be in any direction in the plane orthogonal to the propagation direction. Figure 10 shows an electromagnetic wave polarised in the xy plane.

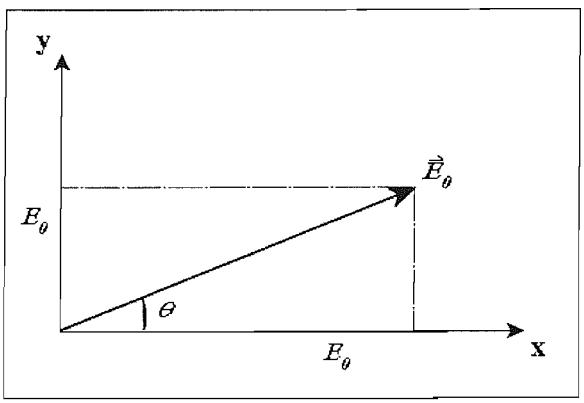

Figure 10: Electromagnetic wave polarised in the xy plane.

The angle, θ, is given by

$$\theta = \tan^{-1}\left(\frac{E_{0y}}{E_{0x}}\right), \tag{24}$$

where E_{0x} and E_{0y} are the electric field amplitudes in the x and y directions, respectively.

The basic electromagnetic wave possesses electric and magnetic fields which oscillate sinusoidally in both space and time. If these oscillations are in phase the light is said to be linearly polarised with the direction of polarisation given by Equation (24). However, two other forms of polarisation are possible; circular and elliptical. Circularly polarised light is produced if the oscillations are out of phase by 90° and $E_{0x} = E_{0y}$ and elliptically polarised light is produced if the oscillations are again out of phase by 90° but now E_{0x} does not equal E_{0y} or if $E_{0x} = E_{0y}$ but the oscillations are out of phase by less than 90° or greater than 90°.

1.6.2 Refractive index, birefringence and optical retardation

When light enters a material, its velocity is reduced and hence its wavelength decreases by a factor known as the refractive index. In most liquid crystals the refractive index is equal to the square root of the high frequency relative permittivity or dielectric constant. A uniaxial liquid crystal has two principal refractive indices, the ordinary, n_o, and the extraordinary, n_e. The ordinary refractive index is associated with a light wave in which the electric vector vibrates perpendicular to the optical axis and the extraordinary index is observed for a linearly polarised light wave in which the electric vector is parallel to the optical axis. In the nematic phase the optical axis is given by the director, $\hat{\boldsymbol{n}}$, with the directions parallel and perpendicular to the director given by

$$n_o = n_\perp, \tag{25}$$

and

$$n_e = n_\parallel. \tag{26}$$

In other words, light polarised parallel to the director propagates according to the index of refraction $n_\parallel$ and light polarised perpendicular to the director propagates according to another index of refraction $n_\perp$. The (linear) birefringence is then given by the difference between these two indices of refraction

$$\Delta\tilde{n} = \tilde{n}_e - \tilde{n}_o = \tilde{n}_\parallel - \tilde{n}_\perp. \tag{27}$$

The birefringence for rod-like molecules is always positive, as the parallel refractive index is larger than the perpendicular refractive index, and varies from values close to zero to

about 0.4. Due to this birefringence light polarised along different directions travels at different velocities. This means that as the light propagates through the sample the two perpendicular components of the electric field which entered the sample in phase gradually grow out of phase. This is known as optical retardation and is very important in liquid crystals. The textures observed in a polarising microscope are caused by birefringence. In a polarising microscope the light travels through a polariser, into the liquid crystal sample and through a second polariser crossed at 90° to the first polariser and finally to the observer's eye. The crossed polarisers extinguish any light which has not undergone a change in its polarisation state and darkness is observed. If the director is parallel to either of the crossed polarisers at any point in the sample then the incident light propagates according to a single index of refraction and no change in polarisation is observed. The light is then unable to pass through the second polariser and blackness is observed. If the director, however, is at some angle to both of the polarisers the propagating light has two components one parallel and perpendicular to the director. These components travel at different velocities according to their corresponding indices of refraction introducing a phase difference between them. The light then emerges elliptically polarised. A proportion of this light is able to pass through the second polariser and the sample appears bright and coloured in that location. The colours are observed with differing intensities because optical retardation is a function of wavelength and so some colours pass through the second polariser with more intensity producing highly coloured samples. The last case in which no optical retardation occurs is when the light propagates along the director. Since the index of refraction for light polarised in all directions perpendicular to the director is the same the liquid crystal appears dark due to no change in polarisation.

1.7 Director dynamics

1.7.1 The torque-balance equation

The discussion so far has only considered the static behaviour of nematic liquid crystals in response to external influences. This section is going to describe the dynamics of the nematic phase when a magnetic field is applied. A nematic liquid crystal flows like a normal organic liquid, however when a sample is aligned, the flow depends on the orientation of the director with respect to the flow direction and velocity gradients due to the anisotropy of the phase. Consider a nematic liquid crystal in a cylindrical sample tube whose axis is placed perpendicular to an applied magnetic field. The director will align parallel with the magnetic field, providing the diamagnetic susceptibility anisotropy is

positive. If the sample is inclined at some angle, β, to the magnetic field, relaxation of the director back to its equilibrium position parallel to the magnetic field will occur, see Figure 11.

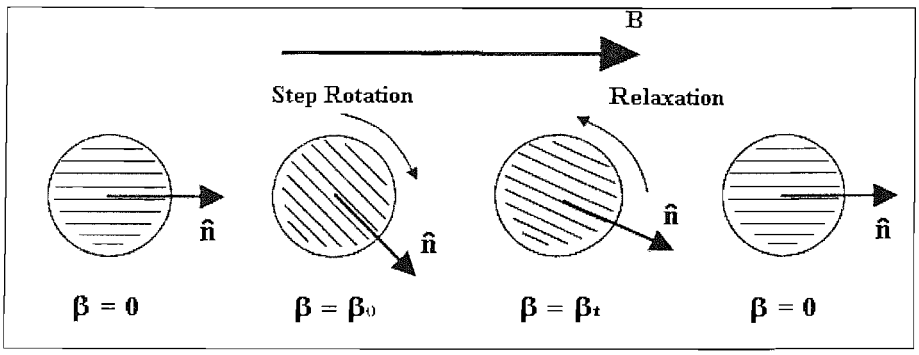

Figure 11: Schematic representation of the director relaxation process after rotation.

This rotational motion of the director is described by the torque-balance equation [11];

$$I\frac{d\Omega}{dt}=\Gamma_{Mag}+\Gamma_{elast}+\Gamma_{visc}, \tag{28}$$

where $I\frac{d\Omega}{dt}$ represents the inertial term; I is the moment of inertia per unit volume and Ω is the local angular velocity of the director and the terms on the right-hand side represents the torque per unit volume due to the magnetic forces, elastic forces and frictional (viscous) forces. At low angular velocity the inertial term is small in comparison with the elastic and viscous torques. In some experiments the bulk sample is assumed to move as a monodomain with no surface forces acting so the elastic torque can be ignored [12]. This then leaves

$$\Gamma_{Mag}+\Gamma_{Visc}=0, \tag{29}$$

therefore providing the director rotates without translational motion of the molecules i.e. no flow, this equation becomes

$$\gamma_1\frac{d\beta}{dt}=-\frac{\Delta\tilde{\chi}}{2\mu_0}B^2\sin 2\beta. \tag{30}$$

Rearrangement gives

$$\frac{d\beta}{\sin 2\beta}=-\frac{\Delta\tilde{\chi}B^2}{2\mu_0\gamma_1}dt, \tag{31}$$

and integration of Equation (30) gives

$$\tan\beta_t=\tan\beta_0\exp(-t/\tau), \tag{32}$$

where β_0 is the starting angle between the director and the applied field and β_t is the angle at time, t. The field-induced relaxation time, τ, is given by

$$\tau = \frac{\gamma_1 \mu_0}{\Delta \tilde{\chi} B^2}. \tag{33}$$

The rotational viscosity, γ_1, can then be calculated providing the relaxation time and diamagnetic susceptibility are known.

To illustrate the time dependence of the director orientation, β_t, has been calculated from Equation (32) for the initial orientations $\beta_0 = 45°$ and $\beta_0 = 89.9°$ and plotted against the scaled time, t^* (= t / τ). The results are shown in Figure 12. $\beta_0 = 90°$ was not used due to the failure of the theory as *tan* 90 = ∞ in Equation (32) and because Γ_{Mag} is zero in Equation (30) the director would not move.

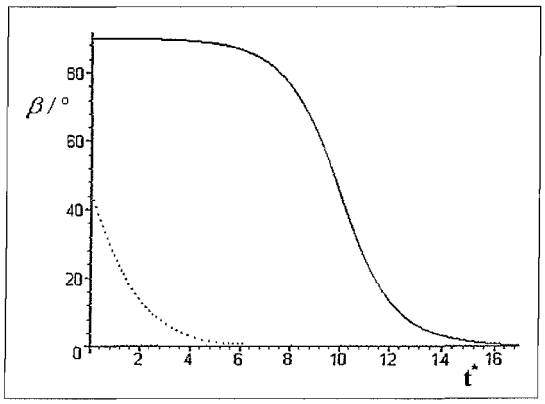

Figure 12: The dependence of the director orientation, β, on the scaled time, t^*, calculated from Equation (26) with $\beta_0 = 45°$ (-------) and $\beta_0 = 89.9°$ (——).

For $\beta_0 = 45°$ the director orientation changes immediately and continuously until it reaches its equilibrium value 0° when the director is aligned parallel to the magnetic field. In contrast the extreme case of $\beta_0 = 89.9°$ is quite different; the director orientation initially changes so slowly that it gives the impression of a lengthy induction period for the alignment process. After which there is a rapid change in the director orientation and then the return of the director to being parallel to the magnetic field, same as for the 45° case. However, in display technology the surface forces play an important role in the switching of the device and so it is no longer possible to ignore the elastic torque in Equation (28) because the director is non-uniform as for the 90° rotation.

1.7.2 Dynamics of the twist Freedericksz transition

Application of a magnetic field across a cell with uniform planar alignment causes the director to undergo a twist deformation. When this magnetic field is removed the director twist is removed and the elastic forces cause the director to align parallel to the substrates. The rate at which this alignment occurs is given by the solution of the torque-balance equation in which the elastic torque producing the alignment is balanced by the viscous forces resisting it. The viscous torque is dependent on the rate of change of the director orientation with the twist angle, ϕ, varying across the cell $\phi(z)$. The viscous torque at a specific point in the cell is given by

$$\Gamma_{visc} = \gamma_1 \frac{d\phi(z)}{dt}, \tag{34}$$

and the elastic torque by

$$\Gamma_{elast} = K_2 \frac{d^2\phi(z)}{dz^2}, \tag{35}$$

the torque-balance equation is then

$$\gamma_1 \frac{d\phi(z)}{dt} = K_2 \frac{d^2\phi(z)}{dz^2}. \tag{36}$$

It is assumed that $\phi(z)$ varies sinusoidally across the cell so that

$$\phi(z) = \phi_m \cos(\pi z / d), \tag{37}$$

where ϕ_m is the maximum twist angle and occurs in the middle of the cell. For infinite anchoring the twist angle at the surface is zero so that when $z = \pm d/2$, $\phi(z)$ is zero. The differential of $\phi(z)$ allows the determination of the elastic torque

$$\frac{d\phi(z)}{dz} = -\frac{\pi}{d}\phi_m \sin(\pi z / d), \tag{38}$$

and

$$\frac{d^2\phi(z)}{dz^2} = -\left(\frac{\pi}{d}\right)^2 \phi_m \cos(\pi z / d), \tag{39}$$

substitution for $\phi(z)$ from Equation (37) gives

$$\frac{d^2\phi(z)}{dz^2} = -\left(\frac{\pi}{d}\right)^2 \phi(z). \tag{40}$$

The torque-balance equation can now be written as

$$\gamma_1 \frac{d\phi(z)}{dt} = -K_2\left(\frac{\pi}{d}\right)^2 \phi(z), \tag{41}$$

rearrangement gives

$$\frac{d\phi(z)}{\phi(z)} = -\frac{K_2}{\gamma_1}\left(\frac{\pi}{d}\right)^2 dt, \tag{42}$$

and integration gives

$$\left[\ln\phi(z)\right]_{\phi_0(z)}^{\phi_t(z)} = -\frac{K_2\pi^2}{\gamma_1 d^2}\left[t\right]_0^t, \tag{43}$$

the solution is then

$$\phi_t(z) = \phi_0(z)exp\left(-t/\tau\right), \tag{44}$$

where the turn-off relaxation time, τ_{off}, is

$$\tau_{off} = \frac{\gamma_1 d^2}{\pi^2 K_2}. \tag{45}$$

For the turn-on situation where the magnetic field is applied across the cell the magnetic torque opposes the elastic torque and needs to be included in the torque-balance equation. The magnetic torque is given by

$$\Gamma_{mag} = -\frac{\Delta\tilde{\chi}}{2\mu_0}B^2 \sin 2\beta, \tag{46}$$

where β is the angle between the magnetic field and the director. This can be substituted by ϕ as

$$\beta = \frac{\pi}{2} - \phi, \tag{47}$$

so

$$\sin 2\beta = \sin(\pi - 2\phi) = \sin\pi\cos 2\phi - \cos\pi \sin 2\phi = \sin 2\phi, \tag{48}$$

the magnetic torque is now given by

$$\Gamma_{mag} = -\frac{\Delta\tilde{\chi}}{2\mu_0}B^2 \sin 2\phi. \tag{49}$$

For values of the magnetic field close to the Freedericksz threshold voltage of the cell i.e. small values of ϕ it is assumed that

$$\sin 2\phi \cong 2\phi, \tag{50}$$

so the torque-balance equation is then

$$\gamma_1 \frac{\partial\phi(z)}{\partial t} = \left(\frac{K_2\pi^2}{d^2} - \frac{\Delta\tilde{\chi}B^2}{\mu_0}\right)\phi(z). \tag{51}$$

Integration and re-arrangement gives the same result as Equation (44) but with the relaxation time for the turn-on process, τ_{on}, given by

$$\tau_{on} = \gamma_1 \left(\frac{\mu_0}{\Delta\tilde{\chi} B^2} - \frac{d^2}{\pi^2 K_2} \right). \quad (52)$$

1.8 Liquid crystal display devices

1.8.1 Introduction to displays

There is much commercial interest in liquid crystal display devices due to the fact that they are thin, lightweight, portable and have low power consumption. They were first used for simple digital watches and pocket calculators but now are utilized for personal computers and televisions. The prerequisite for commercial liquid crystals to be used in LCDs is a broad nematic range of -40°C to 100°C in order to guarantee the operating temperature range of the displays. One physical property exploited for display devices is the birefringence of liquid crystals. However, all devices rely on the application of an electric field to control them, therefore electrical properties such as the dielectric anisotropy play a fundamental role. The switching time of LCDs is another vital property for displays as it determines how rapidly the director orientation can be changed on application or removal of an external field. The switching times are largely governed by the rotational viscosity, γ_1. The exact device behaviour depends on the nature and configuration of the cell used. The basic construction of most devices is the same; the liquid crystal is contained within a cell formed of two glass plates, which are separated by a thin plastic spacer, typically several μm thick, and sealed with a thermoplastic resin, see Figure 13.

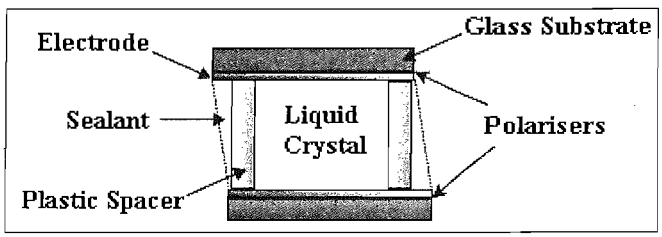

Figure 13: Construction of a typical cell for a display device.

In order to apply an electric field, the glass surface is coated with an alloy of indium and tin oxides. These electrodes are then covered with plastic to stop electrochemical degradation of the liquid crystal. The surfaces are also treated to produce the preferred alignment of the director, dependent on the type of device.

The development of display devices is largely governed by the performance of the mesogenic materials. All display devices use liquid crystal mixtures made up of many components in order to obtain a system which exhibits the ideal physical properties

essential for the particular application. This is because the likelihood of finding a single component liquid crystal which exhibits all the desired physical properties necessary for the display is nearly impossible. Optimisation of liquid crystal mixtures is the focal point in the design of new materials for the improved performance of display applications. This section is going focus on the basic properties of devices and their required physical properties.

1.8.2 Field-induced birefringence display

For this type of display the initial director orientation when the cell is in the off-state is surface induced homeotropic alignment, illustrated in Figure 6(b). The director is optically uniform so the plane of polarised light passing through the cell is not rotated and hence the display appears dark. Providing the liquid crystal has a negative dielectric anisotropy, $\Delta\tilde{\varepsilon}$, the director will deform on application of an electric field (which is applied parallel to the optical axis) across the cell [13]. The director will tend to align orthogonal to the field and so undergoes a bend deformation, Figure 7(b) illustrates this change in director orientation. This deformation destroys the optical uniformity within the plane of the cell introducing birefringence and so some, if not all, of the elliptically polarised light passes through the crossed polariser and the display appears bright. This is because the index of refraction for light polarised parallel to the director is different from the index of refraction for light polarised perpendicular to the director i.e. a phase difference is introduced caused by the difference in their velocities as they move through the liquid crystal. The amount of optical retardation is wavelength dependent (as $\Delta\tilde{n}$ varies with wavelength) producing a coloured display, which is undesirable as the colour is uncontrollable, with some colours passing through the second polariser with more intensity than other colours. For the electric field to overcome the elastic forces and to produce this change in optical transmission, a threshold voltage must be exceeded which is dependent on the bend elastic constant, K_3, and the dielectric anisotropy according to

$$V_{th} \sim (K_3 / \Delta\tilde{\varepsilon})^{1/2}, \tag{53}$$

It is desirable to have a low potential for display purposes and in this case this can be achieved by reducing the bend elastic constant or by increasing the dielectric anisotropy. The amount of optical retardation is governed by the magnitude of the voltage applied to the display and so intensities in between the brightest and darkest states can be achieved.

1.8.3 Twisted nematic (TN) display

Many displays are based on a cell with a twisted structure in which the director forms a one quarter helix across the cell. This twist in the director originates from surfaces with uniform planar alignment which has had one of the surfaces rotated by 90°; see Figure 14(a).

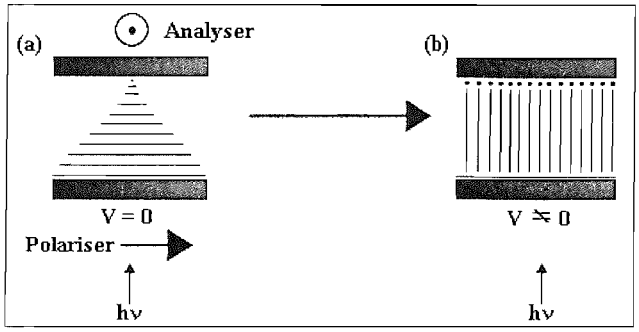

Figure 14: Alignment of the director in a twisted nematic device (a) before and (b) after the application of an electric field above the threshold.

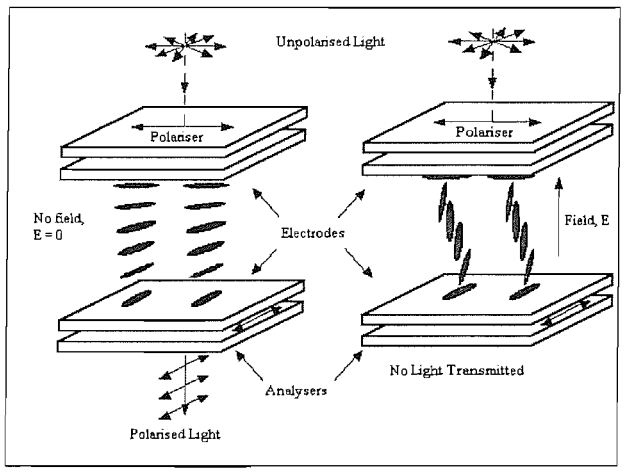

Figure 15: Detailed representation of the TN cell.

The plane of polarised light is rotated by the twisted director through 90° so the cell appears transparent. The light emerges elliptically polarised unless the Mauguin condition is satisfied and then the light emerges linearly polarised. The Mauguin condition for the 90° TN nematic cell is

$$\Delta\tilde{n}d >> \frac{\lambda}{2}, \tag{54}$$

where d is the total layer thickness and λ is the wavelength of light. In practice this inequality is only partially fulfilled resulting in a reduction of the display's brightness and slight colouration of the display. Providing the dielectric anisotropy of the liquid crystal is positive, the quarter helix of the director is unwound and aligned parallel to the field on

application of an electric field, the director at each surface however is not reorientated and remains at the initial positions perpendicular to the field due to infinite anchoring. The optical axes are now uniform within the plane of the cell and so the plane of polarised light is no longer rotated; the cell is black, see Figure 14(b). Again for the electric field to become dominant over the elastic forces and realign the director, a threshold voltage has to be overcome. However, in this case the threshold voltage is dependent on all three elastic constants, as all three elastic deformations are involved. This threshold voltage for a TN display is given by, [14]

$$V_{th} = \pi \left[\frac{\left(K_1 + (K_3 - 2K_2)/4\right)}{\varepsilon_0 \Delta\tilde{\varepsilon}} \right]^{1/2}, \tag{55}$$

Despite the fact that the threshold voltage is well-defined, the amount of transmitted light varies gradually as the helix is deformed. The transmission as a function of voltage is shown in Figure 16.

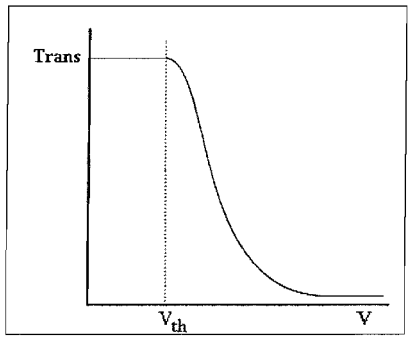

Figure 16: Variation of transmittance with voltage for a TN cell.

In order to obtain good contrast between the on and the off-states it is necessary to apply a voltage that is at least twice that of the threshold voltage. For application purposes it would be desirable to have the optical transmission change more sharply with the applied voltage. The steepness of the transmission-voltage curve can be increased by decreasing the ratio K_3/K_1 [15]. The switching times for the TN mode when an electric field is applied, τ_{on}, and when the electric field is removed, τ_{off}, are given by [16]

$$\tau_{on} = \frac{\gamma_1 d^2}{\varepsilon_0 \Delta\tilde{\varepsilon} V^2 - \pi^2 \left\{K_1 + \left(K_3 - 2K_2\right)/4\right\}}, \tag{56}$$

and

$$\tau_{off} = \frac{\gamma_1 d^2}{\pi^2 \left\{K_1 + \left(K_3 - 2K_2\right)/4\right\}}, \tag{57}$$

where V is the applied electric potential. These equations show that the response times for the TN mode depend on all three elastic constants and the rotational viscosity, γ_1.

There are two main types of twisted nematic display; the first is known a passive display device in which no light is generated by the display itself, instead a reflector is placed below the bottom substrate and ambient light passing through the display is reflected back to be rotated once again through 90°. This reflection gives the display a silvery appearance. This display consumes very little power as very little current flows between the ITO electrodes which make it ideal for battery powered devices, however one disadvantage is that this display does not work in poor light conditions. The second type of TN display utilises a backlight. The light now passes only once through the display creating black characters on a bright background. The use of the backlight greatly increases the power consumption but does allow the use of the display in darkness.

The passive TN cell is not good enough to use for computer screens and is mainly used for low resolution displays such as calculators and wrist watches. The next display discussed is similar to the TN cell but with more twist in the director.

1.8.4 Super-twisted nematic (STN) display

In the super-twisted nematic cell the director forms a three-quarter helix from one surface to the other. This alignment is achieved by the same method as the TN cell apart from one surface being rotated through 270° with respect to the other. A 270° rotation has a higher elastic energy than a 90° rotation, so chiral dopants are added to help the surface forces stabilise the structure, sustaining a twist that is greater than 90°. By adjusting the concentration of the chiral dopant, the pitch, p, of the mixture can be matched to produce the three-quarter helix across the cell of thickness, d

$$p \sim 4d/3. \tag{58}$$

The STN cell responds to an electric field in the same way as the TN cell by rotating the director towards the field direction, but the additional twist in the STN cell has a substantial effect on the optical properties of the nematic film and the background appears coloured. This is due to the optical properties of the STN in the off-state not satisfying the Mauguin condition, which for a twist greater than 90° is

$$\Delta\tilde{n}d >> \frac{\phi\lambda}{\pi}, \tag{59}$$

where ϕ is the total twist angle [14].

The transmitted light is therefore not guided and emerges elliptically polarised. The extent to which this occurs is wavelength dependent and so in white light the off-state appears

coloured as well as the on-state. This problem is overcome by placing two STN cells together which have opposite twists, i.e. the second compensating cell has a twist of the opposite sense. Only one of the cells needs to have a voltage applied whilst the second cell removes the residual birefringence of the liquid crystal layer. The cell will now switch between white and black. The main advantage of the STN device is the sharp change in the transmission of light with respect to the applied voltage. Figure 17 shows this variation in transmission.

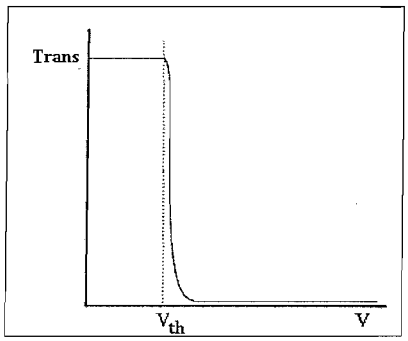

Figure 17: Variation of transmittance with voltage for a STN cell.

The super-twist stores far more elastic energy resulting in this rapid change. As the ratios, K_3/K_1 and $\Delta\tilde{\varepsilon}/\tilde{\varepsilon}_\perp$ decrease, the steepness of the transmission curve increases. In the STN case the twist elastic constant is increased resulting in a decrease of the ratio K_3/K_1.
The STN display is widely used for desktop personal computers (PCs).
In this discussion on displays the surface orientation of the director has been assumed to be fixed in the surface plane enabling a threshold response. However, it has been found that the performance of displays can be greatly improved if a pre-tilt is introduced to the cell by the pinning of the director at certain angles to the surface. Pre-tilts of up to 60° can be used, in other words the director is tilted with respect to the surface by up to 60°. This pre-tilt in the director increases the viewing angle of the displays but detrimentally affects the off-state by introducing some light to the otherwise dark state. This is because light is rotated by the director; this can be compensated for by placing a cell of the opposite tilt before the second polariser.

1.8.5 Vertically aligned (VA) display

The VA mode was first introduced in a monitor display in 1998 [17]. The director in the VA mode is initially perpendicular to the substrates (homeotropic alignment). The required nematic liquid crystals have to possess a negative dielectric anisotropy if they are to be influenced by the applied field applied across the cell. The so-called off-state (i.e. no

electric field applied) appears black due to the lack of elliptical polarisation of the plane of polarised light. On the application of the electric field the director tries to align perpendicular to the applied field, due to the dielectric negativity. The alignment of the director in the on and off states is shown in Figure 18. The switching time from black to white, of the order of milliseconds, has been achieved for the VA mode [18]. The design of the pixels and the electrodes leads to high brightness of the display due to a high aperture ratio, where the aperture ratio is the ratio between the optically active components and the operational components of the cell. This means that good contrast ratios can be achieved because the black state is independent of the wavelength of light and operating temperature, while the on state produces high brightness. The VA mode is one of the most promising LCD technologies for TV applications at present, this is due to its unique combination of good contrast, wide viewing angle and fast switching times.

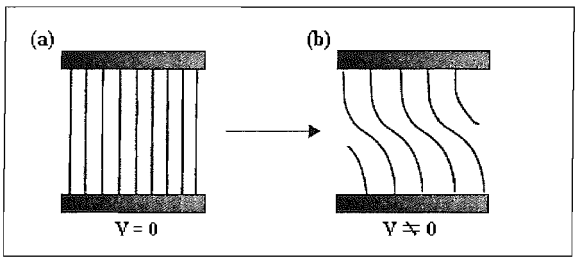

Figure 18: Alignment of the director in a vertically aligned nematic device (a) before and (b) after the application of an electric field.

It is thought that the VA mode along with the IPS (see next section) mode will dominate the large screen TV market in the future due to their low power consumption, despite their need for backlighting, in comparison with other technologies like plasma display panels (PDPs). The materials used in the VA display must be dielectrically negative and have a low rotational viscosity, which is difficult to achieve with highly fluorinated laterally substituted mesogens.

1.8.6 In-plane switching mode (IPS)

The reorientation of the director in an IPS display takes place in a plane parallel to the substrates. The electrodes are therefore constructed on the same side on one of the substrates and are known as interdigitated electrodes. The director is at first parallel to the field direction and parallel to the substrates, but when the field is applied the director moves to be orthogonal with the field. Liquid crystal materials that are dielectrically positive or negative can be used, although materials with a negative dielectric anisotropy

are preferred. This alignment of the director for a dielectrically negative liquid crystal is shown in Figure 19.

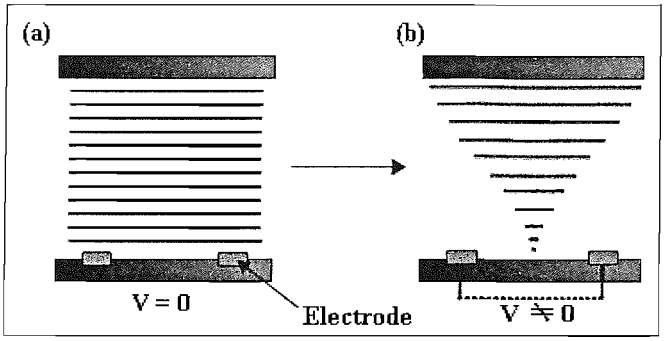

Figure 19: Alignment of the director in an in-plane switching nematic device (a) before and (b) after the application of an electric field.

The voltage versus transmission curve is much steeper than for the TN and VA devices indicating sharper switching behaviour i.e. better switching between black and white. The interdigitated electrodes, however, limit the aperture ratio giving rise to poor brightness. It has, therefore, been a primary concern to achieve high brightness in combination with good contrast [18]. The nematogens used in this type of display must have a high dielectric anisotropy because of the low voltages from the interdigitated electrodes. A rotational viscosity of tens of mPa s is needed for fast switching times.

The switching times in the IPS mode are dependent on the rotational viscosity coefficient and only the twist elastic constant, and are given by [19,20]

$$\tau_{on} = \frac{\gamma_1 d^2}{\varepsilon_0 \Delta\tilde{\varepsilon} V^2 - \pi^2 K_2}, \tag{60}$$

and

$$\tau_{off} = \frac{\gamma_1 d^2}{\pi^2 K_2}, \tag{61}$$

These equations illustrate the fact that for fast switching times a large $\Delta\tilde{\varepsilon}$ and a small γ_1 are needed, but a compromising value of the twist elastic constant is required as it effects the two response times differently. The IPS display is currently the most promising display in competition with traditional CRT monitors for PCs.

1.9 Synopsis of Thesis

This Thesis is mainly concerned with the physical properties of liquid crystals, in particular the relaxation time and rotational viscosity coefficient, and how molecular factors influence these properties. The main aim of the PhD was to find dopants that would lower the rotational viscosity of a nematic mixture in order to produce super low viscosity

nematic liquid crystals for display applications, without affecting the other physical properties too much. In the design of the dopants the focus was put on materials that yielded the lower viscosities rather than materials that were necessarily mesogenic. It would have been very difficult to design a molecule that has all of its properties optimised to produce an ideal display material. There is already a wide range of materials with the desired optical and dielectric properties for use in mixtures for display applications. The synthesis of the dopants was carried out and then their effect on the relaxation time and order parameters of a commercial host mixture, ZLI-4792, was measured using electron spin resonance (ESR) spectroscopy. A series of dopants all with the same basic molecular structure were investigated to give a qualitative insight into the relationship between molecular structure and viscosity of liquid crystals. A novel ESR experiment was designed to yield the relaxation times of the mixtures quickly and relatively easily in comparison with previous techniques. The strategy adopted in the design of the dopants which were investigated was successful in lowering the relaxation time of the host mixture and hence reducing the rotational viscosity. During the research some unexpected results were obtained concerning some of the dopants investigated. Four of the dopants were found to act as gelators in the host mixture, ZLI-4792 and in a variety of other host mixtures. These findings are reported in Chapter 5.

The next Chapter describes in detail the rotational viscosity of nematic liquid crystals and its important role in the improvement of display devices. The relationship between the molecular structure of the nematogens and the rotational viscosity will also be explored. Chapter 3 will explain ESR spectroscopy and detail the novel experimental design to determine the relaxation time of nematic liquid crystals with positive magnetic susceptibility. The results of the ESR investigation into the relaxation times of all the doped systems are given in Chapter 4 along with the corresponding analysis.

As mentioned above Chapter 5 explores the unexpected behaviour of four of the doped systems as well as describing the nature of previously studied gelled systems. Finally, in Chapter 6, the synthetic methods and characterisation of the compounds used as dopants are detailed.

1.10 References

[1] H. Zocher; Physik, **28**, (1927), 790.

[2] C. W. Oseen; Arkiv Matematik Astron. Fysik, **A19**, (1925), 1.; Fortschr. Chem. Physik u. Physik Chem. **20**, (1929), 1.; Trans. Faraday Soc., **29** (1933), 883.

[3] F. C. Frank; Disc. Faraday Soc.; **59**, (1958), 958.

[4] W. Haase in *Physical Properties of Liquid Crystals: Nematics,* eds. D. A. Dunmur, A. Fukuda and G. R. Luckhurst, (INSPEC London 2001), Chapter 6.3, 288.

[5] W. H. de Jeu; *Physical Properties of Liquid Crystalline Materials,* Chapter 5, (1980), Gordon and breach, London.

[6] A. Saupe; Z. Naturforsch, **15a**, (1960), 815.

[7] W. H. de Jeu; *Physical Properties of Liquid Crystalline Materials,* Chapter 6, (1980), Gordon and breach, London.

[8] M. Schadt and F. Muller; Revue Phys. Appl., **14**, (1979), 265.

[9] F. Leenhouts, A. J. Dekker and W. H. de Jeu; Phys. Lett., **72A**, (1979), 155.

[10] W. H. de Jeu and W. A. P. Claassen; J. Chem. Phys., **67**, (1977), 3705.

[11] W. H. de Jeu; *Physical Properties of Liquid Crystalline Materials,* Chapter 7, (1980), Gordon and breach, London.

[12] E. Ciampi, J. W. Emsley, G. R. Luckhurst and B. A. Timimi; J. Chem. Phys., **107**, (1997), 5907: S. M. Fan, G. R. Luckhurst and S. J. Picken; J. Chem. Phys., **101**, (1994), 3255.

[13] G. Meier, E. Sackmann and J. G. Grabmaier; *Applications of Liquid Crystals,* Chapter 2, (1975), 125, Springer-Verlag, Berlin.

[14] T. Scheffer and J. Nehring in *Liquid Crystals: Applications and Uses,* ed. B. Bahadur **1**, (World Scientific, 1990), **1**, 231.

[15] M. F. Grebyonkin, G. A. Beresnev and V. V. Belyaev; Mol. Cryst. Liq. Cryst., **103**, (1983), 1.

[16] M. Schadt and W. Helfrich; Appl. Phys. Lett., **18**, (1971), 127.

[17] K. Ohmuro, S. Kataoka, T. Sasaki and Y. Koike; SID Dig. Tech. Pap., (1997), 845.

[18] D. Pauluth and K. Tarumi; J. Mater. Chem., **14**, (2004), 1219.

[19] M. Oh-e and K. Kondo; Appl. Phys. Lett., **69**, (1996), 623.

[20] H. J. Coles, D. A. Dunmur, H. Kagawa, K. Kondo, N. Kunimatsu, G. R. Luckhurst and C. Schott; Mol. Cryst. Liq. Cryst., **347**, (2000), 157.

Chapter 2

Rotational Viscosity Coefficient

2.1 Introduction

This Chapter describes in detail the rotational viscosity coefficient, γ_1, which is one of the fundamental physical properties to affect the switching performance of display devices [1,2].

2.2 Theory of viscoelastic behaviour

According to the theory of Leslie [3], Ericksen [4] and Parodi [5] the rotational viscosity, γ_1, and the four shear viscosity coefficients described by Miesowicz [6] form a complete set of viscosity coefficients for a nematic liquid crystal; these can be obtained experimentally. The rotational viscosity coefficient is a measure of the viscous torque associated with a director rotation in the absence of flow in a nematic liquid crystal. For display application purposes it is the only viscosity of interest as it relates to the reorientation process of the director. The flow properties of nematic liquid crystals are complicated due to the anisotropy of the materials, the viscosities measured are therefore different depending on the direction of measurement. Miesowicz employed a pragmatic approach to define the viscosity coefficients of a nematic liquid crystal and introduced three Miesowicz viscosity coefficients η_1, η_2 and η_3. Consider a liquid crystal sample between two parallel plates with its director aligned by an external force. Miesowicz defined three relative orientations of the director, $\hat{n}$, with respect to the flow velocity, v, and the flow velocity gradient, ∇v. The three Miesowicz viscosities are each dependent on the particular geometry of the cell. These are known as the flow geometries. Figure 1 and Figure 2 show the orientation of the director with respect to the flow velocity and flow velocity gradient, with (a) the director parallel to the flow velocity gradient and perpendicular to the flow which gives the viscosity coefficient, $\eta_1, (\phi = 0°, \beta = 90°)$ (b) the director parallel to the flow velocity and perpendicular to the velocity gradient which gives the viscosity coefficient, η_2, $(\phi = 0°, \beta = 0°)$ and (c) the director perpendicular to the flow velocity and the flow velocity gradient which gives the viscosity coefficient, η_3, $(\phi = 90°, \beta = 90°)$. If the director is fixed in an arbitrary direction with respect to the flow viscosity and the flow viscosity gradient, then the effective viscosity coefficient is given by

a linear combination of the Miesowicz viscosities, and another viscosity coefficient, η_{12}, is described, see Figure 2(d), which can not be visualised by pure shear flow.

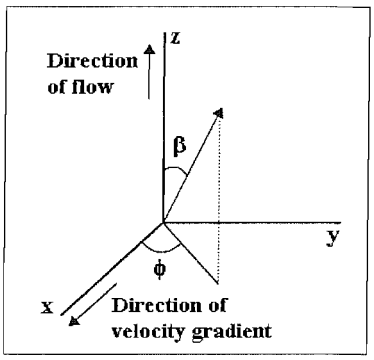

Figure 1: Definition of the orientation of the director with respect to the shear plane.

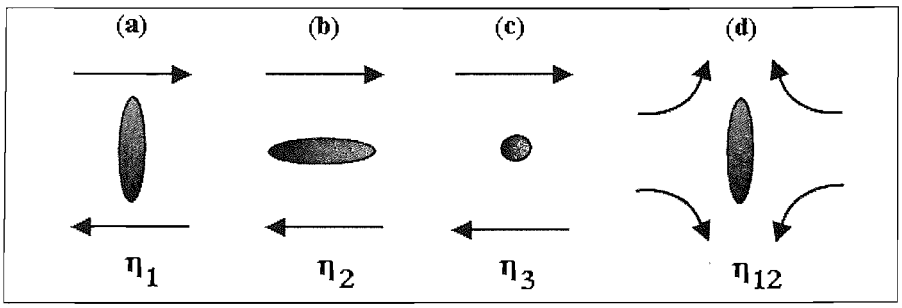

Figure 2: The flow geometries that give the Miesowicz viscosity coefficients of a nematic liquid crystal.

The most crucial viscosity coefficient in the application of LCDs is the rotational viscosity, γ_1, as it is this viscosity that governs the switching speed of devices based on the twisted nematic (TN) and super twisted nematic (STN) cells, see Chapter 1. The switching times of these cells are given by [7]

$$\tau_{on} = \frac{\gamma_1 d^2}{\varepsilon_0 \Delta\tilde{\varepsilon} V^2 - \pi^2 K_{eff}}, \tag{1}$$

$$\tau_{off} = \frac{\gamma_1 d^2}{\pi^2 K_{eff}}, \tag{2}$$

where d is the cell thickness, V is the applied voltage and K_{eff} is the effective elastic constant and for the twisted nematic modes is given by

$$K_{eff} = K_1 + \frac{(K_3 - 2K_2)}{4}. \tag{3}$$

Equations (1) and (2) show that the switching times are proportional to the rotational viscosity coefficient. As long as flow effects are not significant, the nematic director is subject only to rotational motion in the operation of typical LCD devices.

2.3 Rotational viscosity and molecular structure

The viscosity coefficients like many other physical properties of nematic liquid crystals show strong temperature dependence. The variation of viscosity of an isotropic liquid with temperature is given by the following exponential expression;

$$\eta_{iso} = \eta_0 \exp(E / k_B T), \tag{4}$$

where E is the activation energy for diffusion, η_0 is a constant and k_B is the Boltzmann constant. For liquid crystals however, due to their anisotropy, the order parameter, $\overline{P}_2$, should also be considered as it represents the order of the molecules which will influence the viscosity coefficients. In the case of the rotational viscosity it has been found experimentally that the temperature dependence is given by [8]

$$\gamma_1 \propto \overline{P}_2 \exp(E_a / k_B T). \tag{5}$$

This dependence is not unique but is the one that seems to fit best the experimental results. For liquid crystal display applications it is almost impossible to design a single nematogen that matches the many physical requirements of a real display. It is for this reason that mixtures of several liquid crystalline compounds are used to obtain the desired properties. In order to design these mixtures it is of importance to investigate and understand what molecular factors influence particular properties.

The relationship between molecular structure and the viscosities of liquid crystals is a difficult problem and no quantitative theories have yet been developed. The collection of experimental data does however permit some qualitative principles to be established. It is useful to distinguish between two types of effects; intramolecular and intermolecular, both of which depend on the size, shape, chemical functionality and the flexibility of the molecule. As the viscosity depends on the transfer of momentum through a fluid it is important to consider the intermolecular forces. In mixtures these forces act not only between like molecules but between all the components of the mixture, therefore it is important to consider the interaction of the molecules with other components of the mixture when designing low viscosity dopants.

At a basic level the rotational viscosity depends on molecular size and shape. As a general rule γ_1 increases as the molecular length increases. For example, γ_1 increases as the length of an alkyl chain substituent increases, although there is an observed odd-even effect. Consider the mesogens 5CB (4-pentyl-4'-cyanobiphenyl) and 8CB (4-octyl-4'-cyanobiphenyl). The longer 8CB has higher values for the rotational viscosity at the same shifted temperatures in comparison to the shorter mesogen 5CB [9], see Figure 3(b).

Unfortunately data for the whole homologous series is unavailable but these two illustrate the trend nevertheless.

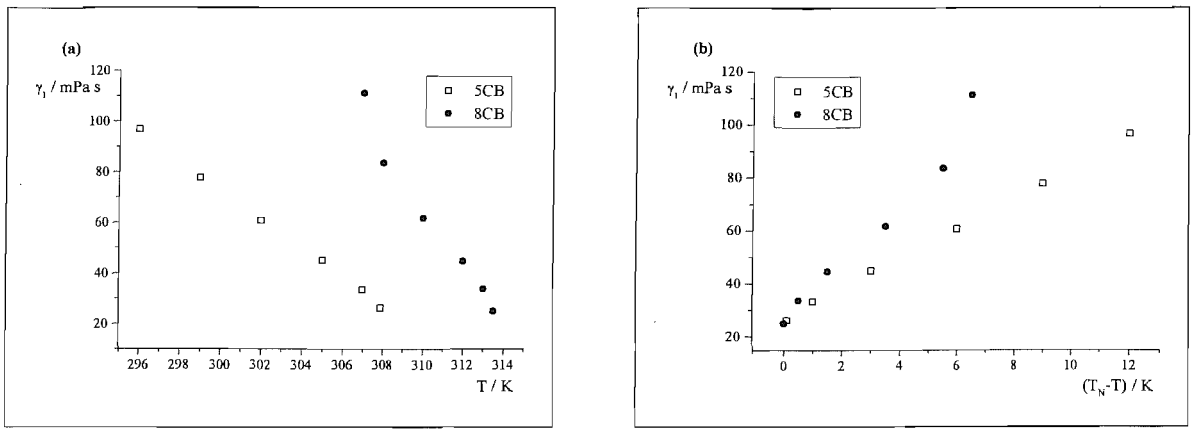

Figure 3: Rotational viscosities for 5CB and 8CB compared on (a) the absolute temperature scale and (b) the shifted temperature scale.

8CB has higher nematic-isotropic transition temperature than 5CB, also 8CB has a smectic A phase and the pre-transitional onset of this smectic phase is indicated by the sudden increase in viscosity shown by the two points at the highest viscosity in Figure 3(a). This increase in the rotational viscosity for 8CB is probably due to the increase in the order parameter.

The only simple connection between rotational viscosity and molecular structure is the geometrical free volume, v_{fg}, which is given by

$$v_{fg} = 1 - k_p, \tag{6}$$

where k_p is the Kitaigorodsky packing coefficient and is given by

$$k_p = \left(N_A v_0 \rho / M\right), \tag{7}$$

where N_A is the Avagadro constant, v_0 is the van der Waals volume of a single molecule, ρ is the density and M is the molar mass. From Equation (6) it is clear to see that the larger the packing coefficient, the smaller the geometrical free volume and vice versa. Belyaev [10] showed that the larger the geometrical free volume the lower the rotational viscosity, see Figure 4. Consequently for low viscosity systems a small packing coefficient is required. The relationship between the rotational viscosity and the geometrical free volume is given by [11]

$$\gamma_1 = bS^x exp\left(\frac{1}{v_{fg}}\right) = bS^x exp\left(\frac{B}{T - T_0}\right), \tag{8}$$

where b and B are material parameters, S is the order parameter raised to a power of x between 0 and 2 and T_0 is the temperature at which the free volume becomes zero and the rotational viscosity infinite i.e. a glass transition.

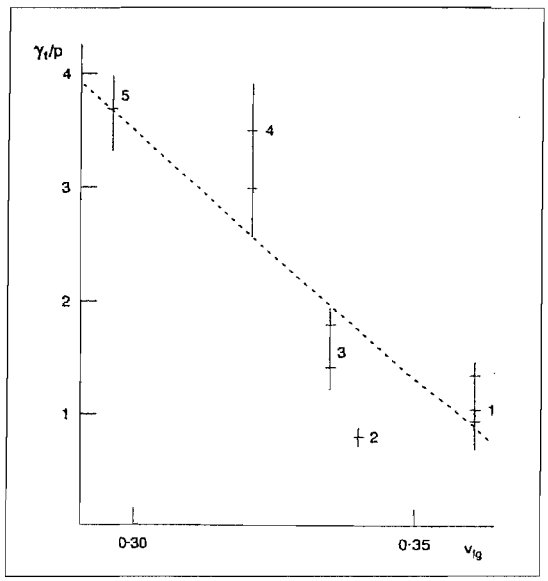

Figure 4: Relationship between the rotational viscosity (Poise) of bicyclic polar compounds and the geometrical free volume at 298K. **1** = C_nH_{2n+1}-Cy-Ph-CN, **2** = C_nH_{2n+1}-Ph-Ph-CN, **3** = C_nH_{2n+1}-Pyr-Ph-CN, **4** = C_nH_{2n+1}-BCO-Ph-CN and **5** = C_nH_{2n+1}-O-Ph-Ph-CN [10].

Table 1 compares a range of nematogens, which only differ slightly in their molecular composition, and their corresponding rotational viscosities. The values of γ_1 given are not directly measured values of the pure nematogen, instead a certain quantity (~10 wt%) of the compound is mixed with the commercially available host ZLI-4792 and the single value γ_1 is obtained by extrapolating from the measured values of γ_1 for ZLI-4792 and for the doped system. This is because it is the effect of the nematogens on the mixture which is of real interest for application purposes. However, the values obtained are only good for comparison with each other as the values will have large associated errors due to the long extrapolation and the use of only two data points (γ_1 at 0wt% and 10wt%). For this set of data the shift in the value of the nematic-isotropic transition temperature has been taken into account to enable direct comparisons to be made.

If the length of the molecule is increased by the addition of ring systems, an increase in γ_1 is observed, compare compounds 3 and 4 with 7 in Table 1 for example. The insertion of either a phenyl ring or cyclohexyl ring into compound 7 dramatically increases the viscosity. These general rules do not always hold. It would be expected that compound 5 would have a higher viscosity than compounds 4 and 6 considering this trend; however this is not the case and its rotational viscosity is somewhat lower than the other two.

Replacement of a cyclohexyl ring with a phenyl ring lowers the viscosity as can be seen when comparing compound 1 with 2 and 3 with 4. This may be due to a free volume effect; the molecular volumes of bicyclohexyl compounds (1 and 3) will be greater than the biphenyl compounds (2 and 4), this along with the assumptions that the densities are approximately the same and their molecular weights differ only slightly means that the packing coefficients for the bicyclohexyl compounds will be larger leading to a smaller free volumes and larger rotational viscosities as observed. The substitution pattern of the terminal group also affects the rotational viscosity; substitution of a functional group in the lateral position usually increases the viscosity in comparison to substitution in the terminal position (along the long axis), compare compound 8 with 2, however in this case there is only a small effect.

	Mesogen	γ_1 / mPa s
1	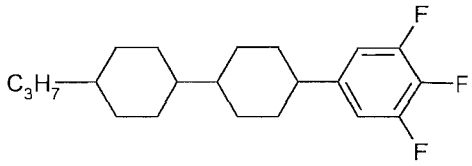	171
2	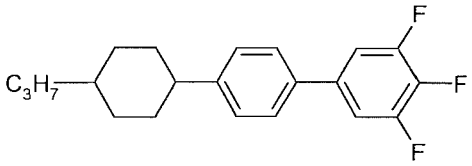	151
3	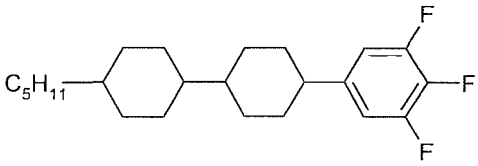	233
4	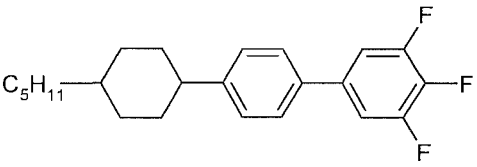	191
5	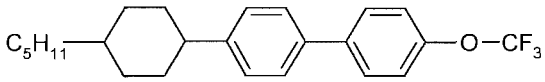	180
6	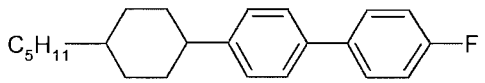	252
7	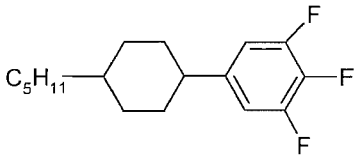	42
8	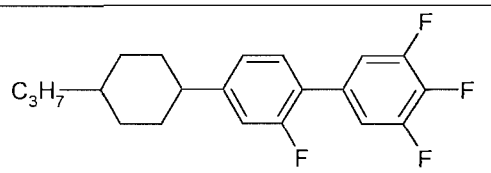	173

Table 1: The rotational viscosities of some mesogens, all values are extrapolated using ZLI-4792 as host [7].

Long range dipolar forces cause highly polar groups to contribute to high viscosity. These forces promote strong pair correlations, which increases the effective length of pairs of molecules and therefore decreases the free volume leading to the increase in viscosity. There is a link between increasing dielectric anisotropy and increasing rotational viscosity which may be due the increase in local dipolar intermolecular forces which would hinder

the end over end rotation of the molecules. Comparing mesogens containing cyano substituents with ones containing fluorine substituents, which have a smaller dipole, in the terminal position, corroborates this link. The cyano substituted mesogens have higher dielectric anisotropies due to their larger dipole and relatively high viscosities whereas the fluorine substitution does not have such a detrimental effect on the viscosity. It is for this reason that fluorine is increasingly being preferred as a functional group for display mixtures. Therefore, the larger the dipole the greater the dielectric anisotropy and the resultant large dipolar interactions lead to an increase in the rotational viscosity.

	Mesogen	$\Delta\tilde{\varepsilon}$
9	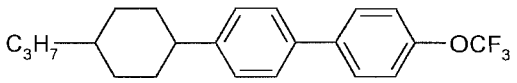	8.7
10	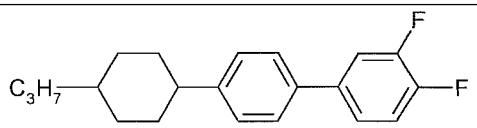	7.8
11	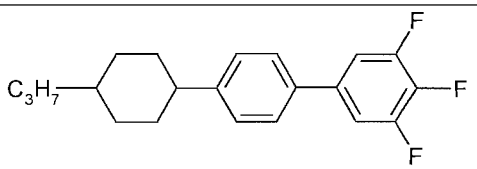	12.6
12	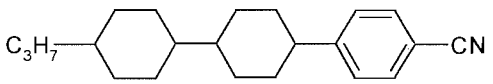	14.8
13	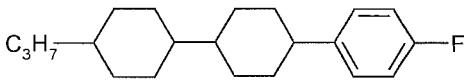	3.0
14	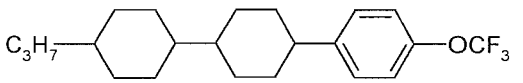	6.9
15	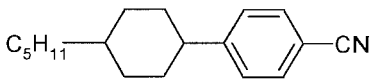	18.0
16	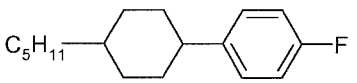	4.0
17	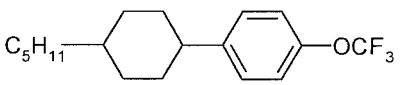	5.6

Table 2: Comparison of the extrapolated values of the dielectric anisotropies for different functional group substitutions at 20°C [12].

Table 2 highlights the fact that cyano substituted mesogens (compounds 12 and 15) have higher dielectric anisotropies than corresponding fluorine (compounds 13 and 16) and trifluoro-methoxy (compounds 14 and 17) mesogens. Compound 10 has a lower dielectric anisotropy than compound 11, due to the lateral substitution of the fluorine despite the fact that compound 11 has two laterally substituted fluorine atoms. However, the effective dipoles of the two laterally substituted fluorine atoms cancel due to the symmetry of the mesogen. Lateral substitution of polar functional groups tends to yield lower dielectric anisotropies, which becomes obvious if Equation 14 from Chapter 1 is considered. The introduction of a dipole at some angle, θ, to the molecular long axis will cause a reduction of the term $\left(\mu^2 / k_B T\right)\left(3\cos^2\theta - 1\right)/2$ in Equation 14, leading to a decrease in the dielectric anisotropy. Lateral substitution in combination with, for example, cyclohexyl rings, instead of phenyl rings, can lead to mesogens with negative dielectric anisotropies. Mesogens with negative values of dielectric anisotropy are of importance in display applications that use the vertical alignment (VA) and in-plane switching (IPS) modes. This is in contrast with most active matrix displays that use liquid crystal mixtures with positive dielectric anisotropy e.g. TN and STN. Table 3 shows a range of mesogenic materials with negative dielectric anisotropies and their corresponding rotational viscosities [13], again these values have been obtained by extrapolation from 10wt% solutions in the host ZLI-4792 for γ_1 and in the host ZLI-2857 (which is dielectrically negative) for $\Delta\tilde{\varepsilon}$. The variation in the mesophase behaviour has been taken into account to allow direct comparisons to be made. It is clear that the compounds with the biphenyl units have significantly lower rotational viscosities than the corresponding compounds with the bicyclohexyl units due to the free volume effect discussed earlier. For example the rotational viscosity is 45% lower for compound 21 than it is for compound 24. As the terminal chain length within a homologous series (18- 20, 21- 23 or 24-26) is increased the rotational viscosity also increases and in most cases so does the dielectric anisotropy.

	Mesogen	$\Delta\tilde{\varepsilon}$	γ_1 / **mPa s**
18	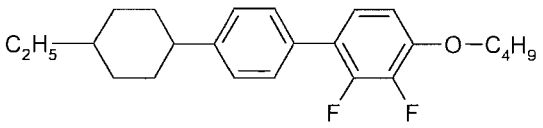	-5.6	202
19	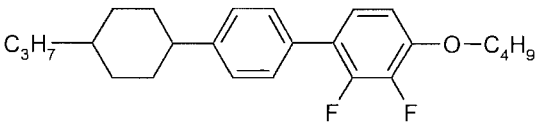	-5.4	245
20	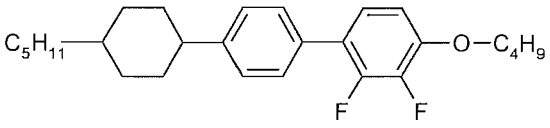	-5.0	307
21	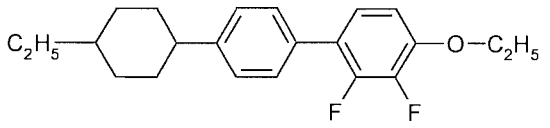	-6.0	207
22	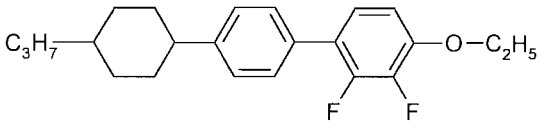	-5.9	233
23	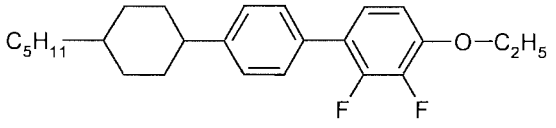	-5.3	345
24	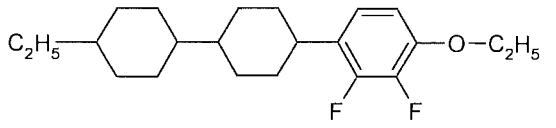	-5.7	383
25	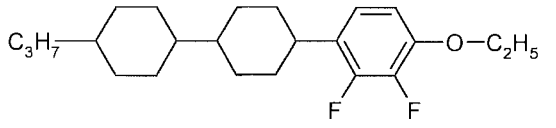	-6.0	413
26	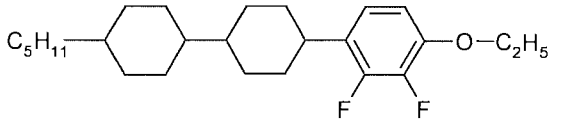	-5.3	469
27	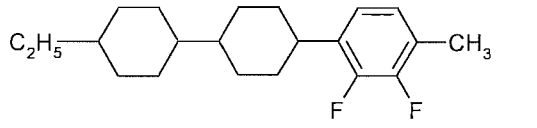	-2.1	165
28	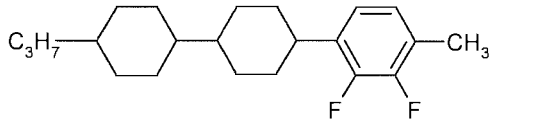	-2.8	217

Table 3: Comparison of the dielectric anisotropies and rotational viscosities for different core structures and different terminal chain substitutions at 20°C, all values are extrapolated [13].

The mesogens with the lowest rotational viscosities in Table 3 are the ones with the shortest molecular length (compounds 27 and 28). The ether linked chains in compounds 26 and 27 have been replaced by methyl groups producing a reduction of 57% and 47% respectively in the rotational viscosity. This reduction in the viscosity can also be attributed to the change in the dipole strength on removal of the ether linkage which will cause a reduction in the polarity of the terminal group. A marked decrease in the dielectric anisotropy is also observed, this can also be explained by considering Equation 14 in Chapter 1. The larger the dipole the greater the term $(\mu^2 / k_B T)(3\cos^2\theta - 1)/2$ becomes leading to larger values of the dielectric anisotropy. Another feature of a molecule that can dramatically affect the viscosity is the internal flexibility. Increased viscosity due to increased terminal chain length is probably a result of an increase in chain entanglements, which are caused by the flexibility of the chain. It has been shown that introducing double bonds into the terminal chain can reduce the rotational viscosity of the liquid crystal [14,15]. The positioning of the double bond is important; when it is placed at the end of chain a marked decrease in the viscosity is observed, probably due to the reduction in the end chain entanglements promoting free motion of the molecules. A similar effect on the viscosity is observed when the double bond is placed at a specific site in the chain, but the reason for the reduction is different. This time it can be attributed to the change in conformational distribution which affects the shape of the molecule. Schadt *et al.* found that the relationship between the double bond position and the rotational viscosity is dependent on an odd-even effect. There is a marked difference in the rotational viscosity if the double bond is placed at an odd alkyl position than if it is placed at an even alkyl position, see Figure 5.

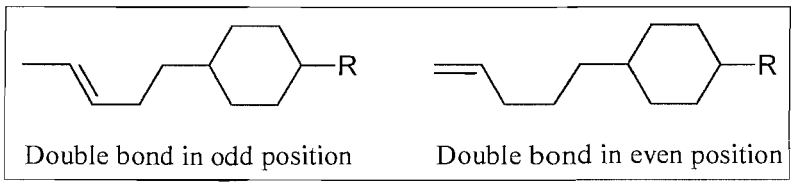

Figure 5: Structures illustrating positioning of double bonds.

Mesogens with the double bond in the even position were found to have lower rotational viscosities than there odd counterparts. It was also shown that the rotational viscosity is independent of the double bond position, provided equally long terminal chains are compared and the double bond positions are either even or odd only.

2.4 Dopant design

In designing nematic mixtures with low viscosity a strategy that focussed on materials that yield low viscosity rather than materials that are necessarily mesogenic was adopted. It would be almost impossible to design a material possessing all the mesogenic properties that are required for an ideal display material combined with a low viscosity. Display materials that already possess the required physical properties are commercially available and it is just the switching times of such materials that need to be optimised. This is achieved by lowering the rotational viscosity of the liquid crystal. The starting point for the design of the dopants to be used in this study was spherical molecules, which would undoubtedly lower the rotational viscosity of a host mixture dramatically. The spheres would allow the molecules in the mixture to slide over each other easily due to the free motion and rotation. However, the lack of anisotropy of spherical molecules would affect the other physical properties, necessary for display applications, detrimentally. The next step in the design process was to try and incorporate the idea of these spherical molecules in dopants with increased anisotropy. This can be achieved by linking two spherical-like moieties together using a flexible chain. The flexibility of the chain should allow the dopant molecules to move freely, whilst allowing the molecules in the mixture to slide over each other with ease promoting a reduction in the rotational viscosity. The chains being capped by the two spherical-like moieties will prevent end chain entanglements, which leads to an increase in the rotational viscosity, observed with terminal chains. This research work, therefore, concentrated on low polarity liquid crystal dimers, in which two rigid moieties are connected by a flexible alkyl spacer. The affect on the rotational viscosity of the dimers has not yet been investigated, but it is thought that because the flexible chain is capped at both ends by the dipolar head group the chain entanglements will be greatly reduced, thus reducing the viscosity. The increased molecular weight of the dimers may cause a decrease in free volume, however when used as a dopant (additive) in mixtures, it is possible that the dimers will reduce the chain entanglements throughout the mixture without detrimentally effecting the other physical properties too much. Phenyl rings with different substituents and substitution patterns were chosen as the rigid moieties and the flexible spacer was an ether linked alkyl chain. The ether linkage was adopted for ease of synthesis.

2.5 Measurement of the rotational viscosity coefficient

The rotational viscosity coefficient, γ_1, is the most frequently measured viscosity coefficient of liquid crystals. There are a number of ways both direct and indirect to

measure the rotational viscosity of a nematic liquid crystal experimentally. However, this section will describe only a few of the more common methods.

2.5.1 Rotating magnetic field method

In 1939 Tsvetkov reported an experiment in which a liquid crystal sample was placed in a rotating magnetic field [16]. In the early 1970's this experiment was used, almost unchanged, to determine the rotational viscosity [17,18]. One variation of this method is to rotate the sample instead of the magnetic field, which some investigators chose to do [19,20], see Section 2.5.2. The basic principal of the rotating magnetic field method is that the nett torque exerted on the nematic (frictional torque) created by the rotating field is assumed to be transmitted completely to the sample container and the torque on the container is then measured directly. However, this method is unable to monitor whether the director moves as a monodomain or not as required by the theory, and also it requires large amounts of sample to obtain accurate values of γ_1.

When a cylindrical nematic sample is subjected to a uniform magnetic flux density, $\boldsymbol{B}$, the director will want to align parallel to the field in order to minimise its magnetic energy. When the field is slowly rotated the director will follow the field but with a certain phase lag.

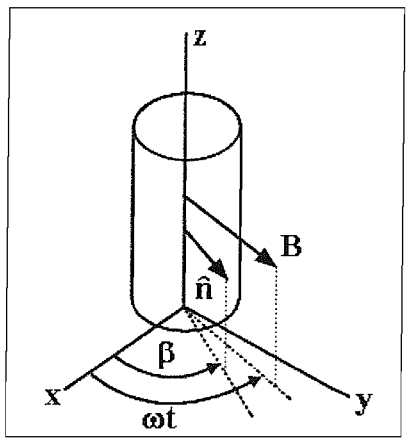

Figure 6: A nematic sample in a rotating magnetic field.

This phase lag is such that the frictional torque and the magnetic torque balance, allowing the measurement of the rotational viscosity, γ_1. Figure 6 illustrates this lag and gives

$$\boldsymbol{B} = (B_0 \cos \omega t, B_0 \sin \omega t, 0), \tag{9}$$

and

$$\hat{\boldsymbol{n}} = (\cos \beta, \sin \beta, 0), \tag{10}$$

leading to

$$N = \frac{d\hat{n}}{dt} = (-\sin\beta, \cos\beta, 0)\frac{d\beta}{dt}, \tag{11}$$

Assuming the elastic forces are negligible the magnetic and shear torque in the z direction balance and the torque-balance equation is

$$\gamma_1 \frac{d\beta}{dt} = \frac{1}{2}\mu_0^{-1}\Delta\tilde{\chi}B_0^2 \sin 2(\omega t - \beta). \tag{12}$$

The solution to this differential equation depends on the values of

$$\omega_0 = (\mu_0^{-1}\Delta\tilde{\chi} / 2\gamma_1)B_0^2. \tag{13}$$

For the situation where $\omega < \omega_0$ a steady state is reached for which there is a constant phase lag between the director and the field, this is given by

$$\tan(\omega t - \beta) = \omega_0 / \omega - (\omega_0^2 / \omega^2 - 1)^{\frac{1}{2}}. \tag{14}$$

Assuming that the torque exerted on the nematic is fully transmitted to the sample container then the torque on the container is

$$\Gamma_{cont} = V\gamma_1\omega, \tag{15}$$

where V is the volume of the sample. Γ_{cont} may be obtained by suspending the sample on a quartz fibre in a magnetic field and measurement of the torsion on the application of the field allows the determination of the rotational viscosity coefficient directly. A plot of Γ_{cont} / V versus ω gives a straight line with γ_1 as the slope.

If $\omega > \omega_0$ the situation is more complicated and will not be discussed here. There are however, some fundamental problems with this experiment [21] regarding the anchoring of the molecules at the boundary walls. This means that the rotation of B does not give a real steady state region, but a twist between diametrically opposed surfaces. This twist must relax via disclination loops. The success of this method is probably due to the fact that for a bulk sample at low frequencies this effect is negligible and so the fraction of the sample which is perturbed by the disclinations is relatively small.

2.5.2 Rotating sample in a magnetic field

This method differs both theoretically and experimentally from the rotating magnetic field method. In this experiment the sample tube is spun in a magnetic field and the sample experiences two types of torque [19]. The first is the torque associated with the preferential director orientation which aligns the director parallel to the magnetic field. The second torque is associated with the motion of the director when the sample tube is spun about its long axis, which is orthogonal to the field. As the sample is spun in the magnetic field the director is moved continually away from its equilibrium position parallel to the field. This

motion of the director is opposed by the magnetic field trying to pull the director back to be parallel with it. At constant angular velocity the magnetic and viscous torques balance leaving the director at some angle,β, to the magnetic field. The torque balance equation is then

$$\gamma_1 \omega = \frac{\Delta\tilde{\chi}B^2}{2\mu_0}\sin 2\beta, \tag{16}$$

rearrangement gives

$$\sin 2\beta = -\left(\frac{2\mu_0\gamma_1}{\Delta\tilde{\chi}B^2}\right)\omega = \omega/\Omega_c, \tag{17}$$

where Ω_c is the critical angular velocity

$$\Omega_c = -\left(\mu_0^{-1}\Delta\tilde{\chi}/2\gamma_1\right)B^2. \tag{18}$$

A plot of $\sin 2\beta$ vs. ω yields a straight line with the slope equal to Ω_c and providing the diamagnetic susceptibility is known and the angular velocity is equal to the critical angular velocity the rotational viscosity can be determined using Equation (18).

2.5.3 ESR field-time experiment

A different class of experiment in which the determination of the director orientation is possible can also yield a value for the rotational viscosity and one such experiment has been devised by Luckhurst *et al.* [22] using electron spin resonance (ESR) spectroscopy. This technique is able to assess the uniformity of the director by monitoring the field-induced director dynamics of the sample, i.e. it can monitor whether the director is moving as a monodomain during relaxation. Significantly smaller samples can be used in comparison with the methods in Sections 2.5.1 and 2.5.2. A nematic sample of positive diamagnetic susceptibility is step-rotated from being parallel to a magnetic field to an angle of 45° using a rotary solenoid, and the relaxation behaviour observed. It was found to be impossible to capture a single ESR spectrum in a time short enough that the director orientation remained constant, so a procedure in which the spectral intensity was acquired in a time domain for a fixed value of the magnetic field was adopted. In this the director is first aligned parallel to the magnetic field before the sample tube is rotated through 45°; the intensity is monitored as a function of time over a period long enough for the director to be realigned parallel to the magnetic field. The field is then increased by a small amount, and the sample tube is rotated again through 45° and the time dependence of the spectral intensity determined. This procedure is repeated until a field range has been covered which is sufficient to record the entire spectrum of the specific spin probe for all director

orientations. By assembly of these time decays into a matrix of time-field intensities it is then possible to obtain a conventional field sweep spectrum at given times by taking a cross-section of the stack plot, see Figure 7.

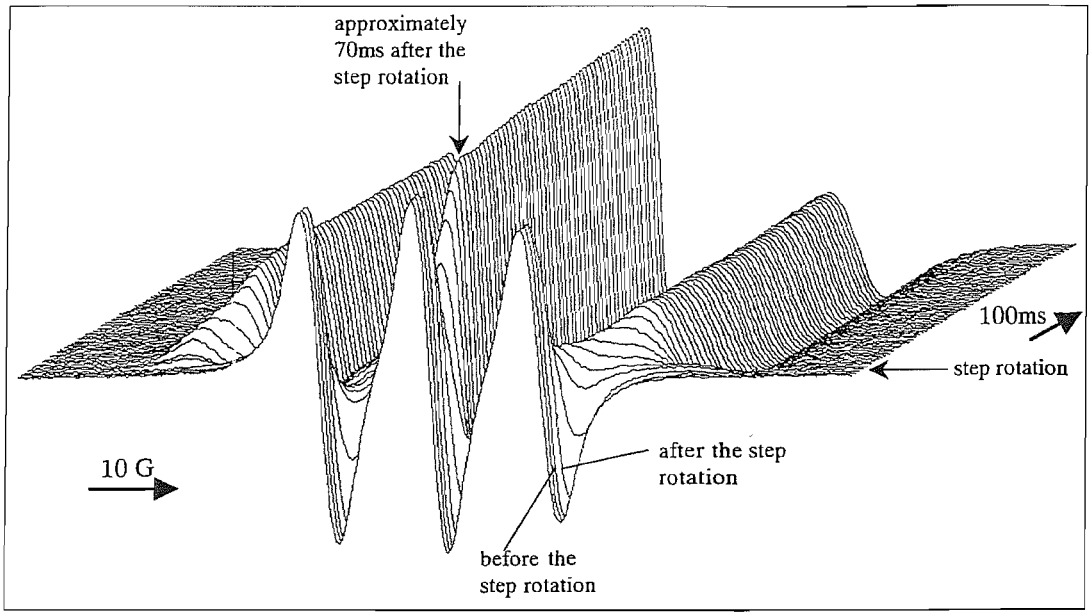

Figure 7: The stack plot of time-sweeps for cholestane in ZLI-4792.

The time taken to acquire the data for a complete time-domain stack plot is approximately 2 h. The relaxation time, τ, could then be determined from the cross section of the time-domain stack plot and providing the diamagnetic susceptibility is known the rotational viscosity can then be calculated.

Another method to gain information on the viscous properties of nematic liquid crystals is the study of the response to a sudden change in an applied field, this is known as the Freedericksz transition and details were given in Chapter 1.7.

2.6 References

[1] E. Jakeman and E. P. Raynes; Phys. Lett. A, **39**, (1972), 69.

[2] H. J. Coles, D. A. Dunmur, H. Kagawa, K. Kondo, N. Kunimatsu, G. R. Luckhurst and C. Schott; Mol. Cryst. Liq. Cryst., **347**, (2000), 157.

[3] F. M. Leslie; Arch. Rati. Mech. Anal., **28**, (1968), 265.

[4] J. L. Ericksen; Mol. Cryst. Liq. Cryst., **7**, (1969), 153.

[5] O. Parodi; J. Phys. Paris, **31**, (1970), 581.

[6] J. K. Moscicki in *Physical Properties of Liquid Crystals: Nematics,* eds. D. A. Dunmur, A. Fukuda and G. R. Luckhurst, (INSPEC London 2001), Chapter 8.2, 387: M. Miesowicz; Bull. Intern. Acad. Polon. Ser., **A**, (1936), 228: M. Miesowicz; Nature UK, **158**, (1946), 27.

[7] K. Tarumi and M. Heckmeier in *Physical Properties of Liquid Crystals: Nematics,* eds. D. A. Dunmur, A. Fukuda and G. R. Luckhurst, (INSPEC London 2001), Chapter 11.

[8] W. H. de Jeu; *Physical Properties of Liquid Crystalline Materials,* Chapter 7, (1980), Gordon and Breach, London.

[9] H. Kneppe, F. Schneider and N. K. Sharma; J. Chem. Phys., **77**, (1982), 3203.

[10] V. V. Belyaev in *Physical Properties of Liquid Crystals: Nematics,* eds. D. A. Dunmur, A. Fukuda and G. R. Luckhurst, (INSPEC London 2001), Chapter 8.4, 414: V. V. Belyaev, Russian Chem. Rev. (UK), **16**, (1989), 917.

[11] Hp. Schad and H. R. Zeller, Phys. Rev. A. **26**, (1982), 2940.

[12] M. Klasen, M. Bremer, A. Gotz, A. Manabe, S. Naemura and K. Tarumi; Jpn. J. Appl. Phys., **37**, (1998), No. 8A, L945.

[13] M. Klasen, M. Bremer and K. Tarumi; Jpn. J. Appl. Phys., **39**, (2000), No. 11B, L1180.

[14] M. Schadt, M. Petrzilka, P. R. Gerber and A. Villiger; Mol. Cryst. Liq. Cryst., **122**, (1985), 241.

[15] R. Buchecker and M. Schadt; Mol. Cryst. Liq. Cryst., **149**, (1987), 359.

[16] V.V. Belyaev; Phys. Uspekhi, **44**, (2001), 255: V. N. Tsvetkov; Zh. Eksp. Teor. Fiz., **9**, (1939), 602: V. N. Tsvetkov; Acta Physicochem. URSS, **10**, (1939), 555.

[17] J. Prost and H. Gasparoux; Physics. Lett. A, **36**, (1971), 245.

[18] H. Gasparoux and J. Prost; J. Phys. (Paris), **32**, (1971), 953.

[19] F. M. Leslie, G. R. Luckhurst and H. J. Smith; Chem. Phys. Lett., **13**, (1972), 368.

[20] A. Polimeno and A. F. Martins; Liq. Cryst., **25**, (1998), 545.

[21] P. G. de Gennes; *Physics of Liquid Crystals*, (1974), Clarendon Press, Oxford.

[22] C. J. Dunn, D. Ionescu, N. Kunimatsu, G. R. Luckhurst, L. Orian and A. Polimeno; J. Phys. Chem. B, **104**, (2000), 10989.

Chapter 3

Electron Spin Resonance Spectroscopy

3.1 Basic theory of ESR

This Section is going to describe the basic theory of electron spin resonance (ESR) spectroscopy, which is the method used to investigate the field-induced director dynamics of doped nematic liquid crystals in this research. ESR spectroscopy can only be carried out on species with one or more unpaired electrons. Most liquid crystals are diamagnetic and therefore do not contain an unpaired electron, and to overcome this problem small quantities of a paramagnetic spin probe are doped into the liquid crystal sample, see next Section. The energy differences studied using ESR are predominantly due to the interaction of unpaired electrons with a magnetic field; this is known as the Zeeman effect. An electron, by virtue of the fact that it is a moving charge, will generate a magnetic moment, which has two possible values associated with $m_s = \pm 1/2$. The magnetic moment for an electron is much larger than the magnetic moment generated by a nucleus; this is because the Bohr magneton is much greater than the nuclear magneton, which means that the energy gap between the ground and excited states is much larger for the electron. This large energy gap changes the Boltzmann distribution between the two states which makes ESR spectroscopy a much more sensitive technique than NMR spectroscopy, and consequently smaller magnetic fields can be used. The most commonly studied compounds are radical ions and transition metal complexes.

The basis of the experiment is that when a paramagnetic sample is placed in a magnetic field, splitting of the electron-spin energy levels occurs provided the resonance condition is satisfied, see Figure 1, and the energy difference is given by

$$\Delta E = \mathrm{h}\nu = g\mu_B B, \qquad (1)$$

where h is the Planck constant, ν is the frequency of the radiation, μ_B is the Bohr magneton ($9.274 \times 10^{-24} \mathrm{JT}^{-1}$), B is the magnetic flux density and g is a factor of proportionality. For a free electron (one that is not associated with any orbital motion within a molecule) g = 2.00232. Generally most organic radicals have g-factors between 1.99 and 2.01.

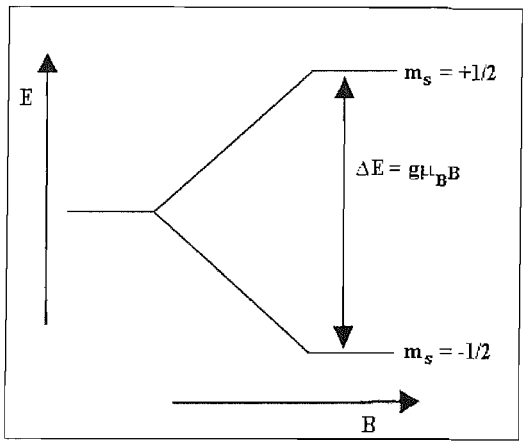

Figure 1: The energy levels for an unpaired electron in a magnetic field.

The ESR spectrum is recorded at a fixed frequency with the magnetic field varying. The frequency is not varied as the cavity is tuned for one frequency. The spectrum obtained is usually displayed as the first derivative of the absorption peak against magnetic field. This derivative curve corresponds to a measure of the gradient of the original peak. As the absorption increases so does the derivative, but as the maximum absorption is approached the rate of change of the absorption starts to fall and the derivative passes through zero when this rate of change is zero. These two lineshapes are shown in Figure 2. The spectrum is recorded as the first derivative because the detector is tuned to the frequency of the oscillation field.

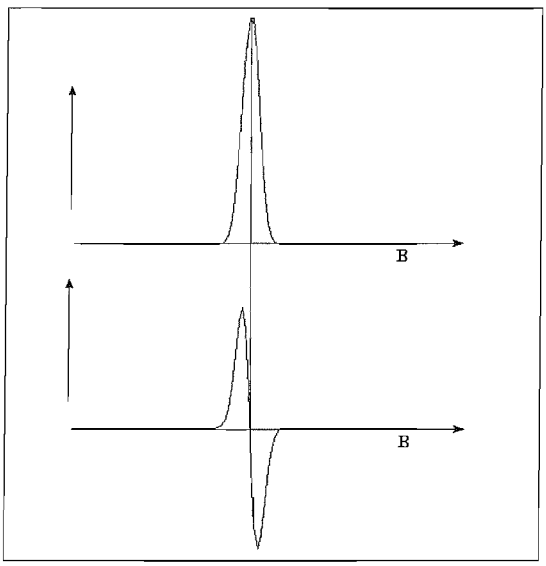

Figure 2: An absorption peak and its first derivative.

In ESR spectroscopy spin interactions can result from two different sources; electron-electron coupling and electron-nucleus coupling or hyperfine coupling. Electron-electron coupling as the name suggests arises from the interaction of electrons in a system which has more than one unpaired electron, a number of possible spin states then arise. For

example, if there are two unpaired electrons then the spin of the electrons may be aligned parallel or anti-parallel in four different combinations corresponding to M_S= 1, 0, 0 and -1. Here M_S is the sum of the individual m_s states. Three of these combinations are symmetric and are allowed but the other is anti-symmetric and transitions to or from it are disallowed. These three components would be split in a magnetic field and a number of transitions will be observed in the ESR spectrum due to the different energies of the Zeeman spin states. The second type of coupling; hyperfine coupling arises from the electron interacting with the spin of surrounding nuclei. The ESR spectrum of a single electron with no coupling would result in one spectral line corresponding to the transition shown in Figure 1, with its position determined by the value of the g-factor. However, if the electron is surrounded by n equivalent nuclei with spin each with a spin quantum number I, then a $(2nI+1)$ line spectrum results. For spin-½ nuclei the relative intensities of the line observed will follow the binomial distribution and the energy difference is now given by

$$\Delta E = g\mu_B B + MA, \tag{2}$$

where A is the hyperfine coupling constant and M is the total spin quantum number of n nuclei.

The layout of the ESR spectrometer is shown in Figure 3. The klystron is the microwave source and the microwave power on the sample is controlled by an attenuator. The circulator allows the microwaves to pass in a certain direction as indicated by the arrows in the diagram.

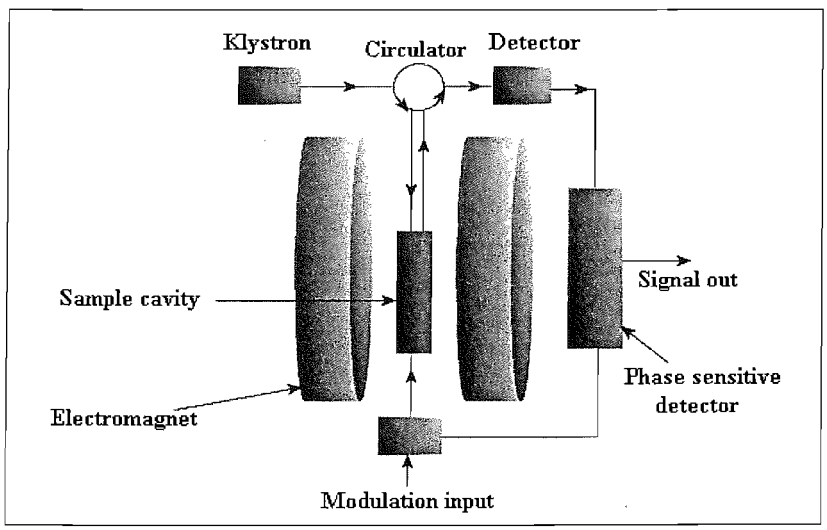

Figure 3: The ESR spectrometer setup.

The reflected microwaves are detected by the diode detector which converts the microwave power to an electric current. A reference arm supplies the detector with a bias microwave power to enable the signal intensity to be measured quantitatively. Phase sensitive

detection enhances the sensitivity of the spectrometer by eliminating noise and interference. This is achieved by varying the magnetic field strength at the modulation frequency and then the reflected microwaves from the cavity are amplitude modulated at the same frequency. The phase sensitive detector then filters any signals which do not possess the same frequency and phase as the field modulation and gives the first derivative spectra.

3.2 Spin probes in ESR

Since the majority of nematogenic liquid crystals are diamagnetic they need to be doped with a paramagnetic spin probe if they are to be studied with ESR. The usual spin probes are organic nitroxides [1] in which the spin of the unpaired electron interacts predominantly with the spin of the nitrogen nucleus: as a consequence the ESR spectrum contains three nitrogen hyperfine lines as for nitrogen I=1.

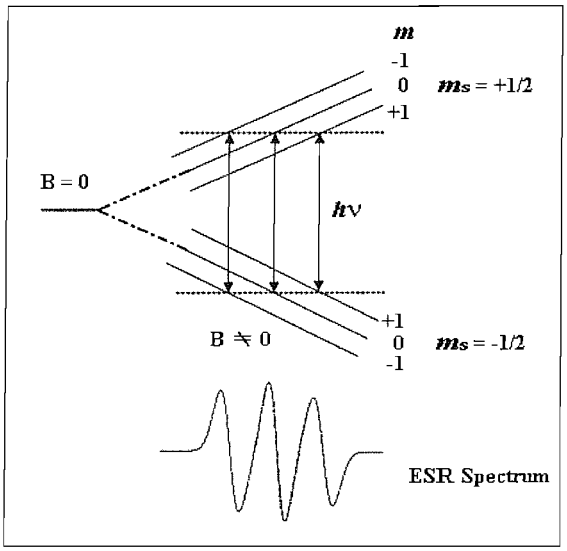

Figure 4: Allowed transitions and the corresponding ESR spectrum.

The allowed transitions, following the selection rules $\Delta m_s = \pm 1$ and $\Delta m = 0$, and the corresponding ESR spectrum are shown in Figure 4.

The chosen spin probe for this investigation was the nitroxide 4,4'-dimethylspiro(5-α-cholestane-3,2'oxazolidin)-3'-yloxy or cholestane for short, see Figure 5. This nitroxide was chosen due to its high solubility and stability in the liquid crystal. The long backbone increases the anisotropy of the nitroxide and allows strong anisotropic interactions with the liquid crystal host, ZLI-4792.

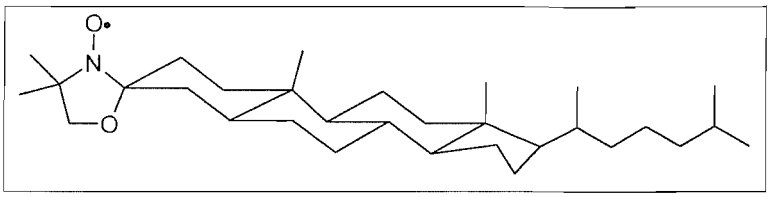

Figure 5: The molecular structure of the spin probe cholestane.

The ESR spectrum for nitroxide spin probes doped in a nematic liquid crystal exhibits three hyperfine lines in the isotropic phase as well as in the nematic phase, but with a distinct difference in the hyperfine spacings. In the isotropic phase the hyperfine lines are separated by a spacing of ~15G, which is the average value of the hyperfine spacing resulting from the three principal axes of the nitrogen hyperfine tensor. When a magnetic field is applied along these three axes in a crystal, the two axes in the plane of the oxazolidine ring yield a value for the spacing of 5G and along the axis perpendicular to this plane gives a value of 35G. In the nematic phase the hyperfine spacing varies depending on the director orientation and for an aligned sample with the director parallel to the magnetic field can range from 7-10G depending on the degree of order in the system, see Figure 6.

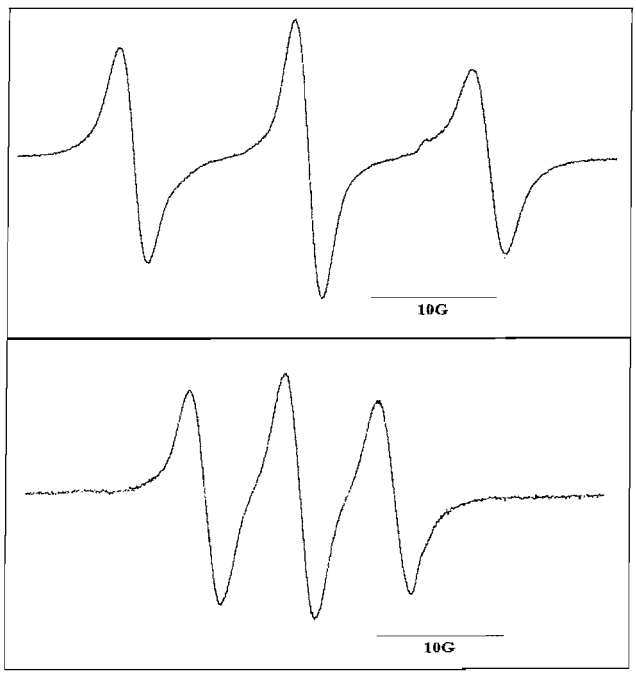

Figure 6: The ESR spectrum of the cholestane spin probe in the isotropic (top) and nematic (bottom) phase of ZLI-4792.

Although the information in the ESR spectrum is obtained from the paramagnetic dopant, it can be treated as if it were from the liquid crystal host, since the paramagnetic dopant is orientationally ordered by its anisotropic interaction with the liquid crystal and so the directions of alignment are the same i.e. the director. The two tensors, which determine the

positions of the spectral lines, are the g-tensor and the nitrogen hyperfine tensor, $\tilde{A}$. In the fast motion limit of approximately 10^{-7}s the principal components of these partially averaged tensors have the cylindrical symmetry of the nematic phase. The components parallel to the director are denoted by $\tilde{g}_{\parallel}$ and $\tilde{A}_{\parallel}$ while those perpendicular to the director are indicated by $\tilde{g}_{\perp}$ and $\tilde{A}_{\perp}$; as with other properties the tilde shows the value in the liquid crystal phase as opposed to the crystal.

The concentration of cholestane used for this investigation was $1x10^{-2}$wt% of the host. This might seem weak but too high a concentration can induce a change to a chiral nematic phase with a helical director distribution which would cause a powder like pattern in the ESR spectrum. This five-line pattern arises from the director being parallel and perpendicular to the magnetic field, with the outer two spectral lines resulting from the perpendicular components of the director and the inner two from the parallel components, see Figure 7.

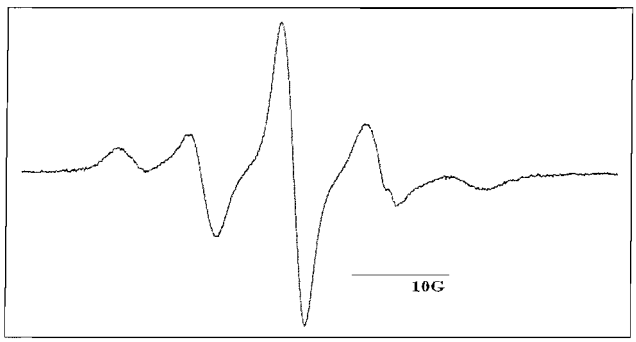

Figure 7: ESR spectrum for ZLI-4792 containing five-lines caused by the formation of chiral nematic due to high concentration of cholestane.

3.3 Novel ESR experiment

3.3.1 Background theory and spectral simulations

The response times of liquid crystal displays based on nematics are controlled by a variety of factors, as it has been shown previously the rotational viscosity coefficient is of special importance. As a consequence the determination of this viscosity coefficient has attracted considerable attention and a range of techniques is now available to do this [2]. Of particular value are a class of experiments in which the director orientation is changed by the application of an external magnetic or electric field. Then, provided the nematic director rotates as a monodomain, the relationship between the time dependence of the director orientation and the rotational viscosity coefficient is straightforward. Although several techniques, such the methods described in Chapter 2, can be used to determine the

director orientation they do not all monitor the distribution in the director during alignment. However, magnetic resonance experiments, both NMR and ESR, allow the director distribution to be determined since the observed spectrum is usually a sum of spectra from all director orientations in the sample [3, 4]. It has already been shown that ESR can be utilised to give the instantaneous director orientation [4] by first determining the time dependent spectral intensity for a given field strength. By assembly of these time decays into a matrix of time-field intensities it is then possible to obtain a conventional field sweep spectrum at given times by taking a cross-section of the stack plot. The field-induced relaxation time could then be obtained from this method [5]. An aim of this research was to see if sufficient information could be obtained to determine the field-induced relaxation time by scanning the magnetic field to record the spectrum in a time comparable to that required for the director orientation to change significantly. First the theoretical analysis based on the simulation of this novel experiment is reported, followed by the experimental results.

In an ESR experiment the frequency, ν, is held fixed and the resonance condition is satisfied by scanning the magnetic field. The values of the resonance fields depend on the angle made by the director with the magnetic field, which is why ESR spectroscopy is such a powerful tool for the study of the macroscopic behaviour in liquid crystals. The form of this angular dependence is given, in general, by [1]

$$\begin{aligned}\widetilde{B}_m(\beta) = {} & h\nu/\widetilde{g}\mu_B B - h\widetilde{K}m/\widetilde{g}\mu_B - \left(h^2\widetilde{A}_\perp/4\widetilde{g}^2\mu_B B^2\right) \\ & \times\left[\left(\widetilde{A}_{||}+\widetilde{K}^2\right)/\widetilde{K}^2\right]\left[\left(I(I+1)-m^2\right)\right] \\ & -\left(h^2m^2/2\widetilde{g}^2\mu_B^2B^2\right)\left[\left(\widetilde{A}_{||}^2-\widetilde{A}_\perp^2\right)/\widetilde{K}\right]^2 \\ & \times\left(\widetilde{g}_{||}^2\widetilde{g}_\perp^2/\widetilde{g}^4\right)cos^2\beta\,sin^2\beta;\end{aligned} \tag{3}$$

in this expression h is the Planck constant, I is the nuclear spin quantum number and m is the magnetic quantum number. The quantities $\widetilde{K}$ and $\widetilde{g}$ also depend on the director orientation according to

$$\widetilde{g} = \left[\widetilde{g}_\perp^2 + \left(\widetilde{g}_{||}^2 - \widetilde{g}_\perp^2\right)cos^2\beta\right]^{1/2}, \tag{4}$$

and

$$\widetilde{K} = \left[\widetilde{A}_\perp^2\widetilde{g}_\perp^2 + \left(\widetilde{A}_{||}^2\widetilde{g}_{||}^2 - \widetilde{A}_\perp^2\widetilde{g}_\perp^2\right)cos^2\beta\right]^{1/2}/\widetilde{g}, \tag{5}$$

In order to simplify the calculations and to make the basic physics of the experiment more apparent it is useful to make a number of approximations; these are valid for the nitroxide spin probe that is used in the experiments. The first is to ignore the second order correction terms represented by the last two terms on the right hand side of Equation (3). This has the

effect of making the hyperfine spacing between the first and second spectral lines equal to that between the second and third lines. The other approximation is that the anisotropy in the g tensor vanishes; that is $\tilde{g}_{\parallel} = \tilde{g}_{\perp}$ which means that the central line in the spectrum for which $m = 0$ does not depend on the director orientation. With these approximations the resonance field in Equation (3) becomes

$$\tilde{B}_m(\beta) = B_0 - (h/\tilde{g}\mu_B)\left[\tilde{A}_{\perp}^2 + \left(\tilde{A}_{\parallel}^2 - \tilde{A}_{\perp}^2\right)cos^2\beta\right]^{1/2} m, \tag{6}$$

where the factor $h/\tilde{g}\mu_B$ converts the hyperfine tensor components which are in frequency units to field units.

This expression together with Equation (32) (from Chapter 1) was used to calculate how the positions of the three hyperfine lines vary with time during the director rotation. To do this $\tilde{A}_{\parallel}$ and $\tilde{A}_{\perp}$ for the commercially available host mixture ZLI-4792 were assigned the values of 2.162MHz (7.70G) and 5.081MHz (18.10G), respectively, where the parallel hyperfine tensor is measured from the spacings of a static spectrum and the perpendicular hyperfine tensor was calculated from

$$\tilde{A}_{\perp} = \frac{3a_{iso} - \tilde{A}_{\parallel}}{2}, \tag{7}$$

in which a_{iso} is the isotropic hyperfine splitting and is equal to 14.6G for cholestane in ZLI-4792. The scalar g factor was 2.0056 and the position of the central line was arbitrarily set equal to zero. The dependence of the angle between the director and the magnetic field on the scaled time, t^*, was calculated from Equation (32) (from Chapter 1) with the initial director orientation, β_0, set equal to 45°. Figure 8 shows the resulting line positions as a function of the scaled time where the horizontal axis gives the position of the resonance fields and the vertical axis is the scaled time. In our experiments the director is initially parallel to the magnetic field and so the nitrogen hyperfine spacing is $\tilde{A}_{\parallel}$ which has a value of 7.70G. After the director has been rotated, essentially instantaneously, through 45° the hyperfine splitting has increased to about 14.9G, and then is seen to decrease as a function of time until it reaches its equilibrium value of $\tilde{A}_{\parallel}$, when the director is again parallel to the magnetic field. Although the outer two lines change their positions with time the central line remains fixed because of the assumptions that $\tilde{g}_{\parallel} = \tilde{g}_{\perp}$ and that the second order terms are negligible.

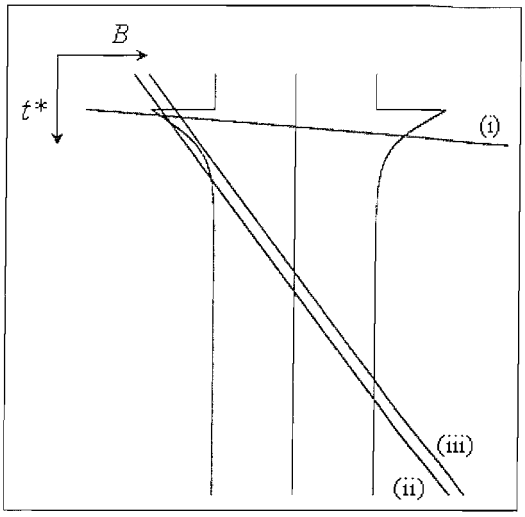

Figure 8: The dependence of the resonance fields for the three spectral lines on the scaled time, t^*, following the increase of the angle between the director and the magnetic field from 0° to 45°. The straight lines ((i)-(iii)) indicate a selection of scanning field profiles used to record the spectra.

To record the ESR spectrum the magnetic field is now scanned through the resonance fields: the field changes linearly with time, which is due to the spectrometer's capabilities. The straight lines in Figure 8 indicate how this field might vary. The particular form of the time dependence of the director orientation is determined by the value of the magnetic field at which the director orientation is changed and the rate at which the field is scanned. More strictly it is the value of the magnetic field relative to that at which the central spectral line occurs which is of relevance. To see how these factors affect the spectrum which is recorded, consider the three calculated results for the 45° experiment shown in Figure 8. For scan (i), which has the fastest rate, the line cuts each of the resonance field lines while the director orientation is still changing. The resultant spectrum is predicted, therefore, to contain three hyperfine lines with unequal spacings. It will be shown that these two hyperfine spacings allow the determination of the field-induced relaxation time. For the scan corresponding to line (ii) the field changes at a much slower rate, and in addition the field at which the director orientation is changed is closer to the central field, meaning the first hyperfine line is recorded earlier than in scan (i). As a consequence of the change in the scan profile, the field line cuts the $m = 1$ resonance field twice, the central resonance field ($m = 0$) once and the $m = -1$ resonance field once. The spectrum should, therefore, contain four hyperfine lines. In this case the spacings between the first three lines in the spectrum are unequal and they should be determined by the relaxation time, τ. In contrast, by the time the final line is recorded the director has returned to being parallel to the magnetic field and so the hyperfine spacing is simply $\widetilde{A}_{\|}$ and contains no information about the director dynamics. The observation of four spectral lines for a nitroxide spin probe is

clearly intriguing as is the final case to be considered for the 45° experiment. The scan profile for this experiment is shown by line (iii) in Figure 8, it has the same slope as for the previous case but the initial field difference is slightly smaller. Now it can be seen that this field does not cut the $m = 1$ resonance field but does for the other two ($m = 0$ and -1). It would seem, therefore, that the spectrum will contain just two lines and that the spacing between them would be $\widetilde{A}_{\|}$, as in the previous example.

It has been assumed so far that the spectral linewidth is zero. This assumption is clearly not true and so the discussion needs to be extended to include the finite width of the lines. To do this the lineshape was taken to be Gaussian, largely as a result of inhomogeneous broadening caused by unresolved proton hyperfine structure [1]. The expression for the first derivative lineshape is

$$L(B, B_m, T_2) = \left(T_2^3 / \sqrt{2\pi}\right)(B_m - B)\exp\left\{-T_2^3 (B_m - B)^2 / 2\right\}, \qquad (8)$$

where $2T_2^{-1}$ is the separation between the maximum and minimum peaks of the derivative lineshape. In addition, B_m is the resonance field (see Equation (6)) and B is the field scanned to record the spectrum; in the experiments just described both of these fields vary with time. It is convenient to take the variable in the spectral simulations to be the field B. Given the field difference at the time origin and the slope, dB/dt^*, it is then possible to replace the scaled time by the field and hence determine the director orientation as a function of the field. Also this allows the resonance fields to be evaluated as a function of B. The results of these spectral simulations for the three 45° experiments are shown in Figure 9; the linewidth, $2T_2^{-1}$, was assumed to be the same for the three lines and was set equal to 0.6G which is smaller than that of the nitroxide spin probe obtained from experiment but this value does allow the variation in the spectra to be clearly distinguished.

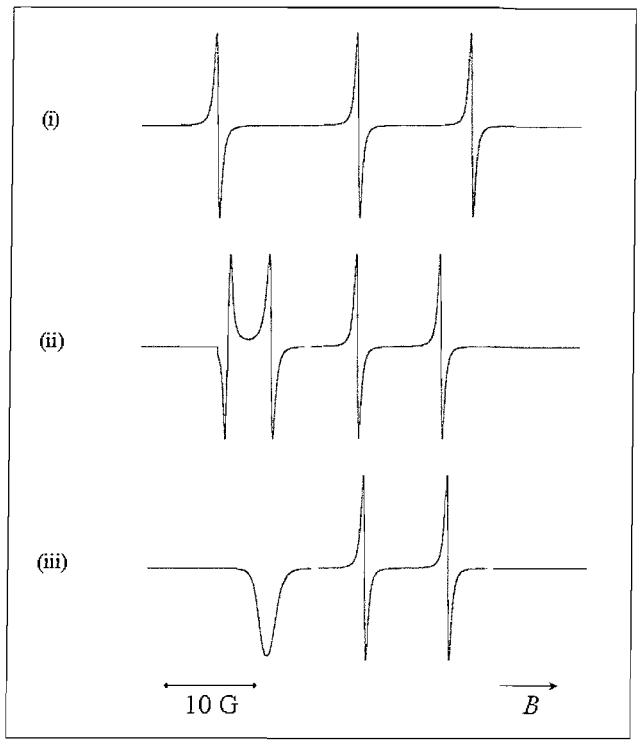

Figure 9: ESR spectra simulated for a nitroxide probe following the increase in the angle between the director and the magnetic field from 0° to 45° for the three scanning field profiles shown in Figure 8.

The spectrum corresponding to the fastest scan rate is shown in Figure 9(i) and as anticipated it contains three hyperfine lines with unequal spacings. The second experiment with the slower scan rate which was predicted to give four spectral lines is shown in Figure 9(ii) and does indeed contain four hyperfine lines. The unequal spacings between these are clearly observed; however, what had not been anticipated was the reversal of phase for the spectral line at the lowest field. This occurs because unlike the other three lines B_m is smaller than B before the line centre at B_m is reached. As a consequence $(B_m - B)$ in Equation (8) is, initially, negative and so a negative phase is observed. In the final 45° experiment just two lines were expected to be observed but as the simulations demonstrate the spectrum contains three (see Figure 9(iii)). The central and high field lines have the usual first derivative form but in contrast the unexpected line at low field has an unusual shape. It appears as an absorption-like lineshape, and not its derivative, but with negative amplitude, as if in emission. In fact this shape is obtained because although the scanning field and the resonance field lines do not cross they approach sufficiently close that the negative region of the spectral line (see Figure 9(ii) and Figure 8(iii)) is sampled by the scanning field. These simulations suggest that the ESR spectra recorded with a field scan time comparable to the time taken for the director reorientation to change should indeed exhibit some novel features from which aspects of the field-induced director dynamics could be deduced.

3.3.2 Experimental

The nematic liquid crystal used to explore these ideas for this novel ESR experiment was the commercial material ZLI-4792 which is available from Merck and is a mixture of fluorinated compounds. A few of the major components of the mixture ZLI-4792 are shown in Figure 10.

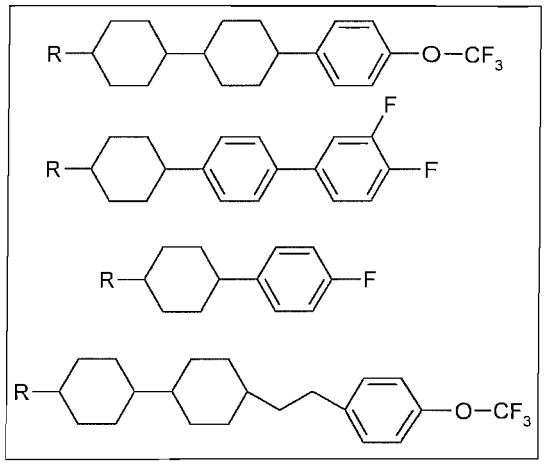

Figure 10: The chemical structures of only a few of the components of ZLI-4792.

This particular nematic liquid crystal was chosen because its dynamic behaviour has been well-studied with ESR spectroscopy [4, 5]. It also has a long nematic range, and at room temperature, where the measurements are made, the orientational order is high so that the anisotropy in $\tilde{A}$ is large which makes the ESR experiments easier. The cholestane spin probe 4,4'-dimethylspiro(5-α-cholestane-3,2'oxazolidin)-3'-yloxy was used because its large length-to-breadth ratio also helps to enhance the anisotropy in $\tilde{A}$. The concentration of the cholestane spin probe in ZLI-4792 was approximately $1x10^{-2}$wt% which gives a good signal-to-noise ratio without causing any concentration broadening of the spectral lines. The sample was placed in a pyrex tube with a 4mm internal diameter, and was degassed to remove dissolved oxygen which can also broaden the lines. The sample tube was placed in the TE_{102} microwave cavity of a Bruker ECS 106 spectrometer. The tube was connected, through a flexible coupling, to a rotary solenoid (Radio Spares; 439-997, rotation angle 45°) which was used to rotate the sample tube and hence the director [4] in order to change the angle between the director and the magnetic field from 0° to 45°. This is necessary because it is not possible to change the orientation of the magnetic field with this ESR spectrometer.

In the initial experiment the scan range was fixed at 50G which covers the spectral width for this particular spin probe in ZLI-4792 at room temperature. Following the start of the

scan the rotary solenoid was activated to change the director orientation more or less instantaneously (~12ms). The maximum time difference between starting the scan and rotating the director which could be used was 0.5s due to the spectrometer's limitations. Since this time controls the initial value of the field, it would be useful to be able to increase this value. However, this is not possible, and instead the position of the central spectral line is varied with respect to the field at which the director is rotated. The remaining parameter is the scan time which controls the rate at which the field is changed. The smallest scan time available that gives a spectrum with a good signal-to-noise ratio is 0.66s and this can only be increased in powers of two, which again limits the range of experiments achievable with this particular ESR spectrometer. In the following experiments the scan time was fixed at 5.24s.

3.3.3 Results and discussion

The first experiment to be optimised was the dynamic experiment that yielded a spectrum containing three hyperfine lines with unequal spacings.

To simulate the spectrum, the separation between the central field and the initial field was 21.75G and the scan time was 5.24s corresponding to a scan rate of 9.54Gs^{-1}. The resultant spectrum is shown in Figure 11(a) and clearly contains three unequally spaced hyperfine lines. The spacing between the low field line is $\tilde{a}_1$ and the spacing between the high field line is $\tilde{a}_2$. The spacing, $\tilde{a}_2$, between the high field line and the central peak is 8.28G. This value is greater than that of 7.61G measured for $\tilde{A}_{\|}$ from the static spectrum and shows that the director has not been aligned parallel to the magnetic field when the high field line was recorded. The low field line is clearly incomplete and results from the fact that the scanning field has reached a value close to the centre of the low field line after the director had been rotated by 45°.

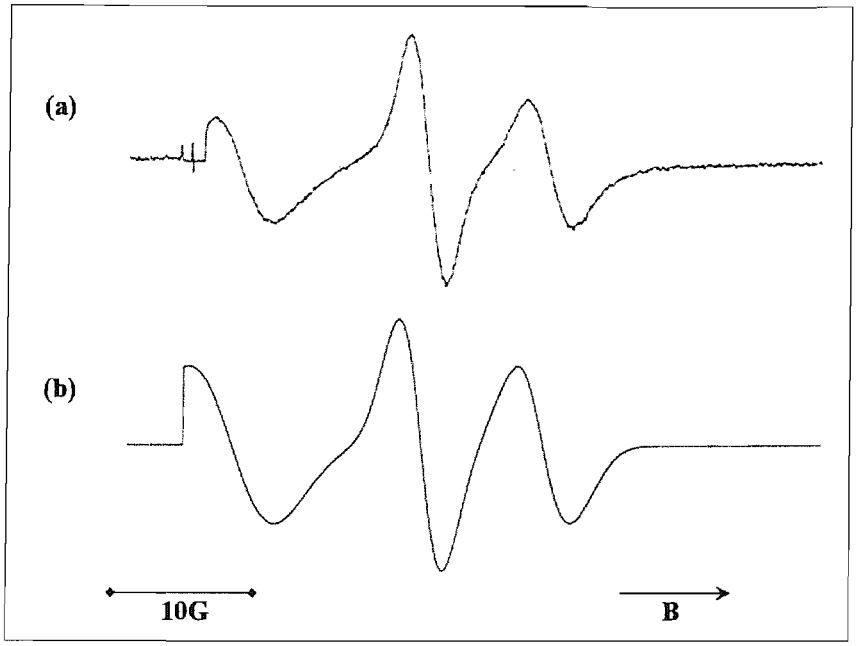

Figure 11: The ESR spectrum of the cholestane nitroxide spin probe dissolved in the nematic host ZLI-4792 following the rotation of the director by 45° (a) measured with the conditions described in the text and (b) simulated via Equations (6) and (8) and from Chapter 1 Equation (32) using the parameters given in the text.

The other spectral features which should be noted relate to the linewidths. First, they are significantly broader than those used in the spectral simulations shown in Figure 9, and secondly the widths of the three lines are not quite the same, although this differential broadening in an anisotropic environment is well understood [6]. To show that the real spectrum is well-accounted for by the theory which has been developed, the spectrum was simulated using values of $(B(m = 0) - B)$ of 21.75G, where B is the value of the field when the sample is rotated and $B(m = 0)$ is the value of the field at which the central resonance line occurs, τ of 1.46s and the three linewidths equal to 3.8G ($m = 1$), 3.0G ($m = 0$) and 3.8G ($m = -1$). The simulation is shown in Figure 11(b) and is clearly in good but not perfect agreement with experiment. The line positions are in quantitative agreement with experiment and shows that the estimation of the field-induced relaxation time, τ, from the hyperfine spacings can be achieved. Since, to a good approximation, the central line position does not depend on the director orientation, the hyperfine spacing associated with the low field line gives, via Equation (6), the director orientation at time t_1. This time is determined from the scan rate and the field position of the low field line relative to the field value at which the director was rotated. Similarly, the hyperfine spacing associated with the high field line gives the director orientation at time t_2, which is again evaluated from the field position of the high field line, see Figure 12. Each of these director orientations could, with knowledge of t_1 and t_2, together with the initial director orientation

be used to estimate two values for the field-induced relaxation times from Equation (32) from Chapter 1.

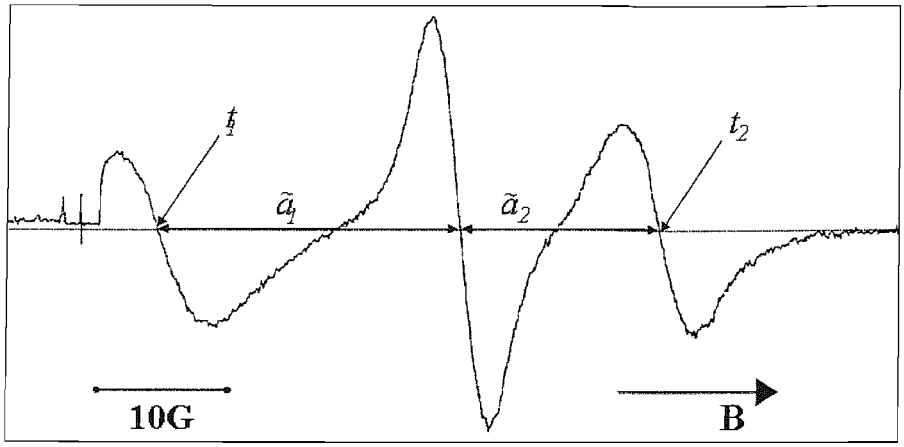

Figure 12: ESR spectrum showing the hyperfine spacings, $\tilde{a}_1$ and $\tilde{a}_2$.

Experimentally, however, it proved difficult to determine the time at which the director orientation is changed and the rotation angle with sufficient accuracy. Fortunately both these problems could be solved by taking the ratio of the tangents of the two angles, which gives

$$\tan\beta_1 / \tan\beta_2 = \exp\left[-(t_1 - t_2)/\tau\right], \tag{9}$$

rearrangement gives

$$\tau = \frac{-t_1 - t_2}{\ln\tan\beta_2 - \ln\tan\beta_1}, \tag{10}$$

where

$$t_m = \tilde{a}_m \times \frac{sweep\,time}{sweep\,width}, \tag{11}$$

and

$$\tan\beta_m = \left(\frac{\tilde{a}_m^2 - \tilde{A}_{\|}^2}{\tilde{A}_{\perp}^2 - \tilde{a}_m^2}\right)^{1/2}. \tag{12}$$

Equation (10) can now be rewritten in terms of the two hyperfine splittings giving

$$\tau = \frac{2(\tilde{a}_1 - \tilde{a}_2)}{b\,ln\left(\tilde{a}_1^2 - \tilde{A}_{\|}^2\right)\left(\tilde{A}_{\perp}^2 - \tilde{a}_2^2\right)/\left(\tilde{A}_{\perp}^2 - \tilde{a}_1^2\right)\left(\tilde{a}_2^2 - \tilde{A}_{\|}^2\right)}, \tag{13}$$

where b is the rate at which the field is scanned (b = 50G/5.24s = 9.54Gs^{-1} in this case). In order to estimate the experimental error in the relaxation time determined from the two hyperfine splittings the experiment was repeated ten times. This gives the value of the relaxation time for ZLI-4792 at room temperature (~25°C) of 1.44 ± 0.09s, which is in

very close agreement with the value of 1.42s determined from a complete set of time-resolved ESR spectra [5]. The error in this new determination is approximately 6%, which is necessarily higher than that, 1%, resulting from the use of a dramatically larger data set. The error in the value of τ determined from the single spectrum clearly depends on how close the director is to being aligned parallel to the magnetic field when the low and high spectral lines are measured. Assuming that the error in measuring the hyperfine spacing is 0.1G, although it can be somewhat smaller than this, the error in τ is found to be in the range 4-8% provided the hyperfine spacing, $\widetilde{a}_2$, is greater than $\widetilde{A}_{\|}$ by about 0.6G and $\widetilde{a}_1$ is greater than $\widetilde{a}_2$ by at least 1.0G. This error in τ does not seem to be unreasonably high in comparison with other methods, and this new ESR technique certainly has the advantage of being rapid, as once the sample is set up and the parameters optimised the measurement of the relaxation time only takes about ten minutes.

This next part is concerned with the verification of the predictions of the unusual spectral features made by the analysis presented in section 3.3.2. To do this a series of experiments were performed in which, the rate at which the magnetic field is changed is held constant at 9.54Gs^{-1} but the difference between the field value when the director is rotated and the field at the central line is varied. The experimental spectra for the cholestane spin probe dissolved in ZLI-4792 for a selection of field differences are shown in Figure 13(i). To appreciate these experiments and their results the field plots along with the resonance fields calculated using the same parameters as those used to construct Figure 8 are shown in Figure 13(ii). The first scan profile shown in Figure 13(ii a) has the largest field difference and so the scanning field cuts all three resonance fields after the director has returned to being parallel to the magnetic field. The spectrum is expected to contain three hyperfine lines with both spacings equal to $\widetilde{A}_{\|}$; this is certainly the case as the experimental spectrum shows (see Figure 13(i a)). In Figure 13(ii b) the field difference has decreased and so the scanning field first approaches the $m = 1$ resonance field before cutting it after the director is once more parallel to the magnetic field. It is expected, therefore, that the spectrum will again contain three hyperfine lines with two equal spacings of $\widetilde{A}_{\|}$. However, there might also be an initial spectral line with an unusual shape depending on the width of the low field line. This feature is indeed observed in the experimental spectrum as a decaying tail just after the start of the scan, together with the three equally spaced hyperfine lines (see Figure 13(i b)).

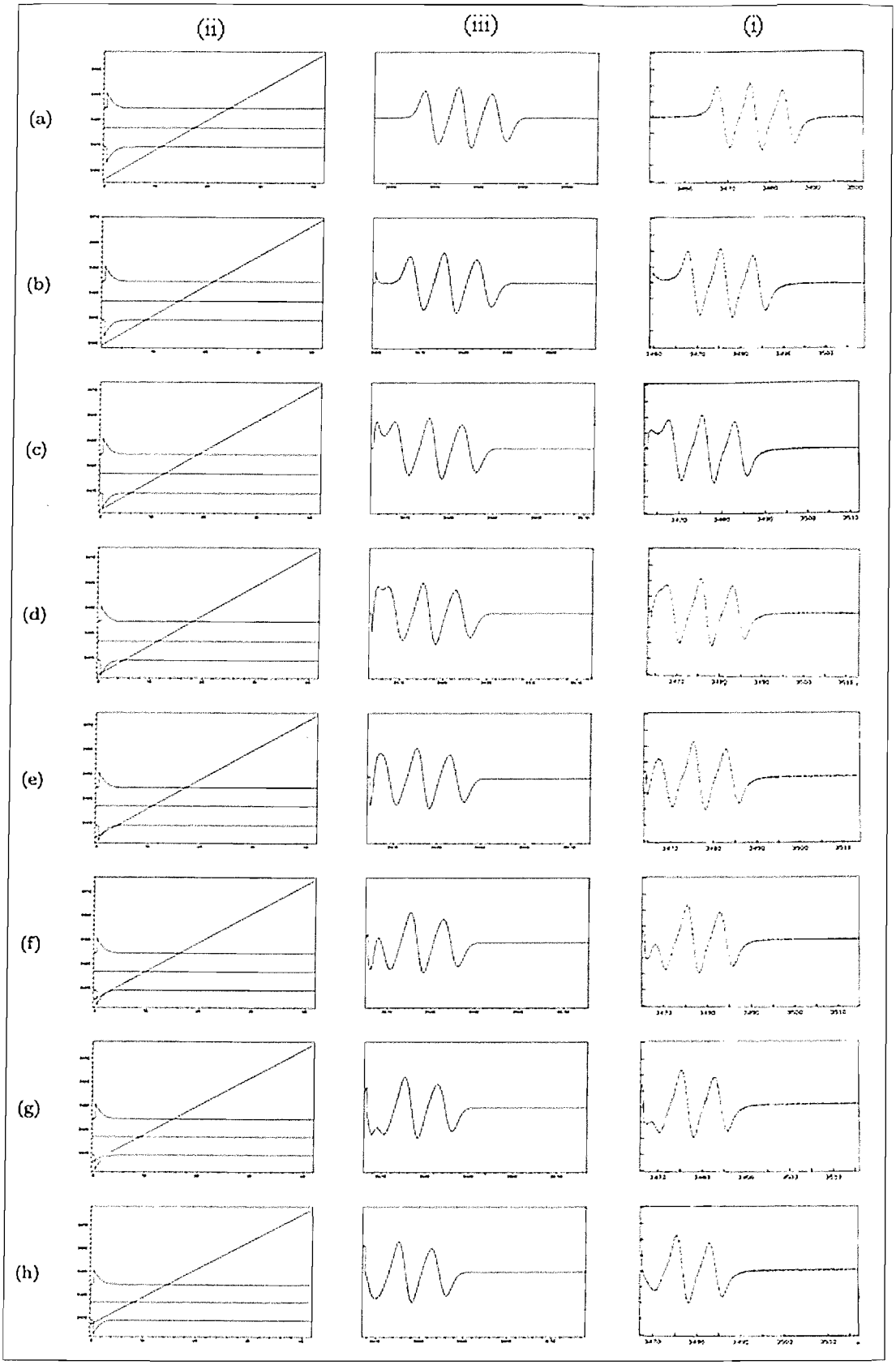

Figure 13: (i) The experimental ESR spectra of the cholestane spin probe dissolved in the nematic ZLI-4792 recorded after the rotation of the director by 45° for a series of scan profiles differing in the initial field relative to that for the central peak. To understand the nature of the spectra and their variation the time dependence of the resonance lines together with the scan profiles with their differing initial field values are shown in (ii). The simulated spectra obtained for the various scan profiles are shown in (iii). The horizontal axes in Figures (i) and (iii) are in gauss and that in Figure (ii) is in seconds.

As the field difference is further reduced, the scanning field approaches more closely to the initial stage of the $m = 1$ resonance field (see Figure 13(ii c)). It was expected, therefore, to see a stronger feature in the spectrum before the normal three line spectrum appears, and this proves to be the case (see Figure 13(i c)). In addition, the extra spectral feature has become closer to the low field line, as it might have anticipated from the field plot in Figure 13(ii c). The next reduction in the field difference now causes the scanning field to cut the resonance field for $m = 1$ twice (see Figure 13(ii d)). It is expected, therefore, to see an additional hyperfine line at low field but with the opposite phase to that for the other three spectral lines. The extra line is clearly apparent in the experimental spectrum but not all of the line is observed, partly because the large linewidths cause the spectral lines to overlap. In addition, the difference between the scanning field and the resonance field does not become sufficiently small in comparison with the linewidth, for the entire lineshape to be observed (see Equation (8)). As the field difference is decreased further, so the fields at which the scanning field cuts the $m = 1$ resonance field become more similar (see Figure 13(ii e)), and because of the large linewidth, the two lines which should be observed at low field merge into a single peak (see Figure 13(i e)). However, the opposite phase of the two peaks means that there is a reduction in the overall line intensity, and a negative region at the start of the spectrum. This behaviour is more apparent for the experimental spectrum shown in Figure 13(i f), where the low field peak is very small and has an unusual shape. The reason for this behaviour is clearly apparent from the associated field plot in Figure 13(ii f), where the scanning field is essentially tangential to the $m = 1$ resonance field curve; that is the points at which the lines intersect are virtually identical. Further decrease in the field difference means that the scanning field does not intersect the $m = 1$ resonance line (see Figure 13(ii g)). The low field line should then vanish, but because the two fields approach within a distance comparable to the linewidth, some spectral feature is observed at low field (see Figure 13(i g)). In the final experiment the field difference has been decreased still further so that the scanning field does not pass so close to the $m = 1$ resonance field. The difference between these fields, $(B_m\text{-}B)$, is always negative (see Figure 13(ii h)), and so this contributes an emission-like feature to the spectrum (see Figure 9(iii) and Figure 13(i h)). The experimental spectrum also shows a positive intensity for a small field range at the very beginning of the scan. This is also apparent in the other spectra (see, for example, Figure 13(i d)-(i h)), although the intensity decreases as the field difference between the initial field and the field at the central line increases. This feature originates from the low field spectral line before the director orientation changes. As the scan profiles

in Figure 13(ii a)-(ii h) show, the scanning field approaches closer to the $m = 1$ resonance field in this sequence and so the spectral intensity also increases.

As has been illustrated in this Chapter, the scan profiles provide an excellent means of designing the experiment and in understanding the essential features of the spectrum obtained. However, they do not provide a quantitative interpretation of the experimentally observed spectra. To achieve this it is necessary to simulate the spectra allowing for the finite linewidths and the differential line broadening. The spectra have, therefore, been simulated using parameters almost identical to the ones used experimentally. The overall agreement between the simulations (see Figure 13(iii)) and the experimental spectra (see Figure 13(i)) is seen to be excellent. Of particular importance is the comparison in the low field region where the director dynamics have the greatest influence. Indeed in this series of experiments, the dominant hyperfine lines are associated with the director after it has returned to being parallel to the magnetic field. The features of the low field spectral region are surprisingly well-accounted for by the simulation, although the intensities are not perfectly reproduced. This may result from the variation of the linewidths with the director orientation [7], which has not been allowed for in the simulations. In spite of this minor mismatch, the agreement in this low field region indicates that the model that has been developed to simulate the spectra is reliable, and can be used with confidence to extract the field-induced relaxation time from the experimental spectra.

3.4 References

[1] G. R. Luckhurst in *Liquid Crystals and Plastic Crystals* eds. G. W. Gray and P. A Winsor (Ellis Hordwood Ltd, Chichester, 1974) Vol. 2, Chap. 7.

[2] J. K. Moscicki in *Physical Properties of Liquid Crystals: Nematics* eds. D. A. Dunmur, A. Fukuda and G. R. Luckhurst, (INSPEC London 2001), Chap. 8.2.

[3] C. J. Dunn, G. R. Luckhurst, T. Miyamoto, H. Naito, A. Sugimura and B. A. Timimi; Mol. Cryst. Liq. Cryst. A, **347**, (2000), 167.

[4] C. J. Dunn, D. Ionescu, N. Kunimatsu, G. R. Luckhurst, L. Orian and A. Polimeno; J. Phys. Chem. B, **104**, (2000), 10989.

[5] N. Kunimatsu; *Ph.D. Thesis*, University of Southampton, (2000).

[6] G. R. Luckhurst and A. Sanson; *Mol. Phys.* **24**, (1972), 1297.

[7] A. Kantola, G. R. Luckhurst, A. Sugimura and B. A. Timimi; *Mol. Cryst. Liq. Cryst. A*, **402**, (2003), 117.

Chapter 4

Doped nematic systems

4.1 Dopants

The dopants used for this research were mostly dimers containing two rigid moieties (phenyl rings) linked together by a flexible alkyl chain, the design of these dopants was outlined in Chapter 2. An ether linkage was incorporated for geometrical reasons. This ether linkage increases the angle made between the phenyl rings and the alkyl chain from ~109° for a methylene linked dimer to ~120° and also brings the chain and phenyl ring into the same plane. The advantage of these ether linked dimers from a synthetic point of view is that they are easier to synthesise than the equivalent methylene linked dimers. The substitution patterns of the phenyl rings were varied together with the length of the alkyl chain linking unit. The predominant substituent used was fluorine due to the widespread use of fluoro-mesogens in display materials. The basic molecular structure of the dopants is shown in Figure 1.

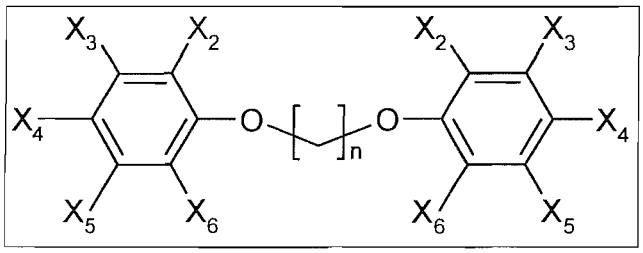

Figure 1: Basic molecular structure of the dopants.

The majority of the dimers investigated were symmetric. Table 1 lists the dopants synthesised and investigated along with their mnemonics; these will be used in the remainder of the text. The mnemonics can be understood as follows; C*n* indicates the spacer length i.e. the number of CH_2 groups linking the two phenyl rings. This will be prefixed with a letter dependent on the type of substituent on the phenyl ring i.e. if the substituent is fluorine, FC*n* is the mnemonic. The mnemonic C*n* indicates that the phenyl ring is fully protonated and no substituents on the phenyl ring are present. If the ring has multiple substituents the number of the position at which the substituent occurs prefixes the rest of the mnemonic i.e. 23FC9, there are fluorine substituents at the 2 and 3 position on the phenyl ring and a spacer length of 9. The mnemonics prefixed with a 'P' indicate the phenyl rings are penta-fluorinated. The mnemonics prefixed with a 'N' indicate the dimer is non-symmetric and the substituents on each phenyl ring are given in the table.

Mnemonic	X_2	X_3	X_4	X_5	X_6	n	Name
DFS33	/	/	/	/	/	/	*1,2-difluoro-1,2-bis-(4-propyl-phenyl)ethene*
C7	H	H	H	H	H	7	*1,7-bis-(phenyl-1-yloxy)heptane*
C8	H	H	H	H	H	8	*1,8-bis-(phenyl-1-yloxy)octane*
C9	H	H	H	H	H	9	*1,9-bis-(phenyl-1-yloxy)nonane*
C10	H	H	H	H	H	10	*1,10-bis-(phenyl-1-yloxy)decane*
C11	H	H	H	H	H	11	*1,11-bis-(phenyl-1-yloxy)undecane*
C12	H	H	H	H	H	12	*1,12-bis-(phenyl-1-yloxy)dodecane*
MeC9	H	H	CH_3	H	H	9	*1,9-bis-(4-methyl-phenyl-1-yloxy)nonane*
MeC10	H	H	CH_3	H	H	10	*1,10-bis-(4-methyl-phenyl-1-yloxy)decane*
FC7	H	H	F	H	H	7	*1,7-bis-(4-fluorophenyl-1-yloxy)heptane*
FC9	H	H	F	H	H	9	*1,9-bis-(4-fluorophenyl-1-yloxy)nonane*
FC10	H	H	F	H	H	10	*1,10-bis-(4-fluorophenyl-1-yloxy)decane*
CF3C9	H	H	CF_3	H	H	9	*1,9-bis-(4-trifluoro-methyl-phenyl-1-yloxy)nonane*
CF3C10	H	H	CF_3	H	H	10	*1,10-bis-(4-trifluoro-methyl-phenyl-1-yloxy)decane*
23FC9	F	F	H	H	H	9	*1,9-bis-(2,3-fluorophenyl-1-yloxy)nonane*
24FC7	F	H	F	H	H	7	*1,7-bis-(2,4-fluorophenyl-1-yloxy)heptane*
24FC8	F	H	F	H	H	8	*1,8-bis-(2,4-fluorophenyl-1-yloxy)octane*
24FC9	F	H	F	H	H	9	*1,9-bis-(2,4-fluorophenyl-1-yloxy)nonane*
24FC10	F	H	F	H	H	10	*1,10-bis-(2,4-fluorophenyl-1-yloxy)decane*
34FC7	H	F	F	H	H	7	*1,7-bis-(3,4-fluorophenyl-1-yloxy)heptane*
34FC10	H	F	F	H	H	10	*1,10-bis-(3,4-fluorophenyl-1-yloxy)decane*
234FC7	F	F	F	H	H	7	*1,7-bis-(2,3,4-fluorophenyl-1-yloxy)heptane*
234FC9	F	F	F	H	H	9	*1,9-bis-(2,3,4-fluorophenyl-1-yloxy)nonane*
345FC7	H	F	F	F	H	7	*1,7-bis-(3,4,5-fluorophenyl-1-yloxy)heptane*
345FC9	H	F	F	F	H	9	*1,9-bis-(3,4,5-fluorophenyl-1-yloxy)nonane*
PFC7	F	F	F	F	F	7	*1,7-bis-(2,3,4,5,6-fluorophenyl-1-yloxy)heptane*
PFC9	F	F	F	F	F	9	*1,9-bis-(2,3,4,5,6-fluorophenyl-1-yloxy)nonane*
NC8	H / F	H / F	H / F	H / F	H / F	8	*1-(2,3,4,5,6-fluorophenyloxy)-8-(phenyl-1-yloxy)octane*
NC9	H / F	H / F	H / F	H / F	H / F	9	*1-(2,3,4,5,6-fluorophenyloxy)-9-(phenyl-1'-yloxy)nonane*
NC10	H / F	H / F	H / F	H / F	H / F	10	*1-(2,3,4,5,6-fluorophenyloxy)-10-(phenyl-1-yloxy)decane*

Table 1: Dopant mnemonics and names.

4.2 Synthesis

The ether linked dimers were made using a procedure known as the Williamson synthesis [1]. This involves the deprotonation of the phenol to produce a phenate anion which is then reacted with a dibromoalkane to produce the dimer. The reaction is stoichiometric with the molar ratio 2:1 of the phenol:dibromoalkane, sometimes however a slight excess of phenol was used to ensure complete reaction of the dibromoalkane. This is due to the fact that the dibromoalkane is quite difficult to separate from the product whereas the phenol can be washed away using a basic work-up. The base used was potassium carbonate (K_2CO_3) and the solvent was dimethylformamide (DMF). This solvent was chosen because of its polarity which stabilises the phenate anion and because of its high boiling point and therefore low volatility. In some of the reactions sodium iodide was used to catalyse the reaction [2], this substitutes iodide for the bromide in the dibromoalkane, which is a better leaving group than bromide and hence speeds up the reaction. The work-up and purification procedures varied considerably for the dimers. For some of the reactions the addition of water to the reaction mixture precipitated the product and only washing and recrystallisation was needed for purification while in other cases an aqueous work-up was required followed by column chromatography, for further purification and the removal of DMF.

4.2.1 Synthesis of the symmetric dimers

The general reaction scheme for the symmetric dimers is shown in Reaction Scheme 1.

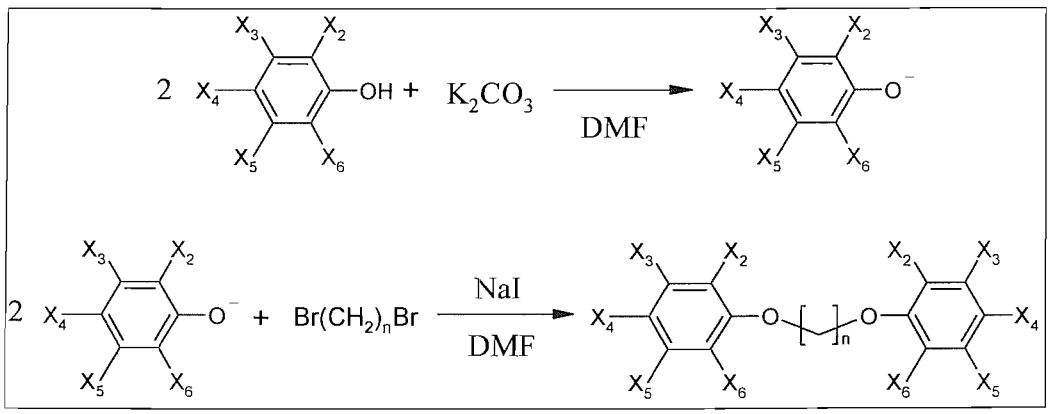

Reaction Scheme 1: Synthesis of the symmetric ether linked dimers.

4.2.2 Synthesis of the non-symmetric dimers

The reaction for the non-symmetric dimers has two stages, the first is the synthesis of the monomer and the second is the reaction of the monomer with a second phenol, in this case the pentafluorophenol to form the non-symmetric dimer, see Reaction Scheme 2.

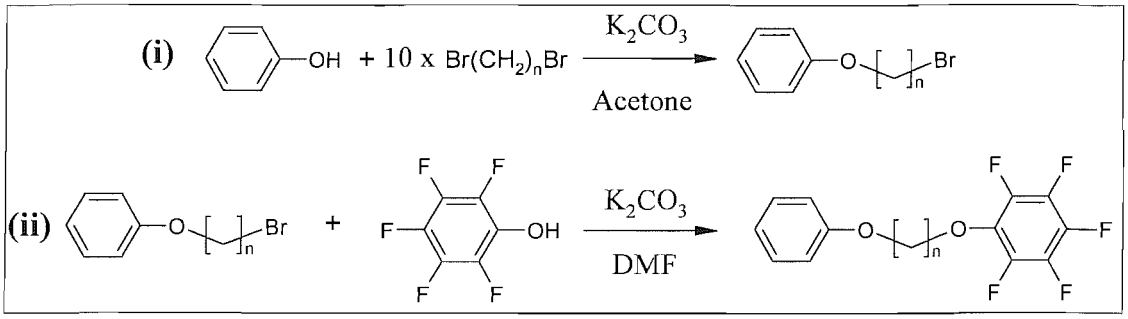

Reaction Scheme 2: Synthesis of the non-symmetric ether linked dimers, 1-(2,3,4,5,6-fluorophenyl-1-yloxy)-n'-(phenyl-1-yloxy)alkane.

4.2.3 Synthesis of 4,4`-bis-pentyloxy-biphenyl

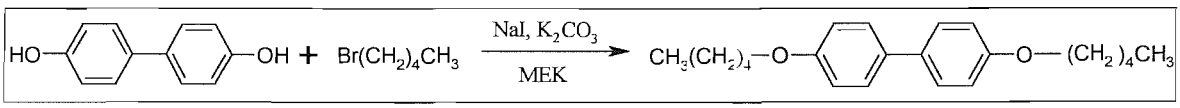

Reaction Scheme 3: Synthesis of 4,4`-bis-pentyloxy-biphenyl.

The synthetic pathways for all the compounds are summarised in Table 2, the dimers in red are novel compounds, meaning no literature could be found on the synthesis of these materials.

The ^{1}H NMR and ^{13}C NMR were recorded on a Bruker DPX 400 or Bruker 300 spectrometer in deuteriated chloroform. Melting points were measured on an electrothermal melting point apparatus. Thin Layer Chromatography was carried out on aluminium-backed Merck Si 60/F_{254} sheets. All the chemicals used were reagent grade and were supplied by Aldrich Chemical Company.

Mnemonic	Name	Reaction Scheme	Reference
C7	*1,7-bis-(phenyl-1-yloxy)heptane*	1	[3]
C8	*1,8-bis-(phenyl-1-yloxy)octane*	1	[3]
C9	*1,9-bis-(phenyl-1-yloxy)nonane*	1	[3]
C10	*1,10-bis-(phenyl-1-yloxy)decane*	1	[4]
C11	*1,11-bis-(phenyl-1-yloxy)undecane*	1	[5]
C12	*1,12-bis-(phenyl-1-yloxy)dodecane*	1	[4]
MeC9	*1,9-bis-(4-methyl-phenyl-1-yloxy)nonane*	1	/
MeC10	*1,10-bis-(4-methyl-phenyl-1-yloxy)decane*	1	/
FC7	*1,7-bis-(4-fluorophenyl-1-yloxy)heptane*	1	/
FC9	*1,9-bis-(4-fluorophenyl-1-yloxy)nonane*	1	/
FC10	*1,10-bis-(4-fluorophenyl-1-yloxy)decane*	1	/
CF3C9	*1,9-bis-(4-trifluoro-methyl-phenyl-1-yloxy)nonane*	1	/
CF3C10	*1,10-bis-(4-trifluoro-methyl-phenyl-1-yloxy)decane*	1	/
23FC9	*1,9-bis-(2,3-fluorophenyl-1- yloxy)nonane*	1	/
24FC7	*1,7-bis-(2,4-fluorophenyl-1-yloxy)heptane*	1	/
24FC8	*1,8-bis-(2,4-fluorophenyl-1-yloxy)octane*	1	/
24FC9	*1,9-bis-(2,4-fluorophenyl-1-yloxy)nonane*	1	/
24FC10	*1,10-bis-(2,4-fluorophenyl-1-yloxy)decane*	1	/
34FC7	*1,7-bis-(3,4-fluorophenyl-1-yloxy)heptane*	1	/
34FC10	*1,10-bis-(3,4-fluorophenyl-1-yloxy)decane*	1	/
234FC7	*1,7-bis-(2,3,4-fluorophenyl-1-yloxy)heptane*	1	/
234FC9	*1,9-bis-(2,3,4-fluorophenyl-1-yloxy)nonane*	1	/
345FC7	*1,7-bis-(3,4,5-fluorophenyl-1-yloxy)heptane*	1	/
345FC9	*1,9-bis-(3,4,5-fluorophenyl-1-yloxy)nonane*	1	/
PFC7	*1,7-bis-(2,3,4,5,6-fluorophenyl-1-yloxy)heptane*	1	/
PFC9	*1,9-bis-(2,3,4,5,6-fluorophenyl-1-yloxy)nonane*	1	/
NC8	*1-(2,3,4,5,6-fluorophenyloxy)-8-(phenyl-1-yloxy)octane*	2	/
NC9	*1-(2,3,4,5,6-fluorophenyloxy)-9-(phenyl-1'-yloxy)nonane*	2	/
NC10	*1-(2,3,4,5,6-fluorophenyloxy)-10-(phenyl-1-yloxy)decane*	2	/
DC8	*1,8-bis-(phenyl-1-yloxy)octane-d10*	1	[5]
DC10	*1,10-bis-(phenyl-1-yloxy)decane-d10*	1	[5]
Ref	*4,4`-bis-pentyloxy-biphenyl*	3	[6]

Table 2: Synthesis of the symmetric and non-symmetric dimers together with the reference compound.

4.3 Mesophase behaviour

This section describes the investigation of the mesophase behaviour of the doped nematic systems. The desired effect of the dopant is to lower the viscosity of the base mixture without lowering the phase transition temperatures too drastically. The effect of the dopants on the phase behaviour of the host is studied using polarising microscopy. This

technique allows the transition temperatures of liquid crystal to be accurately measured and then phase diagrams are used to visualise the effect.

4.3.1 Polarising microscopy

ZLI-4792 does not have a sharp transition from the nematic to isotropic phase, but exhibits a biphasic region over ~8K due to the fact that it is a mixture of mesogenic compounds. The transition temperatures of the dopants dissolved in the base liquid crystal, ZLI-4792, were measured using polarising microscopy, and phase diagrams were produced to see to what degree the dopant depresses the transition temperatures of the liquid crystal. There are two transition temperatures as the mixture is inherently biphasic, as is the host. The lower transition temperature T_N is when the isotropic phase first appears indicated by black spots in the optical texture, and the upper transition temperature T_I is when the nematic phase disappears completely (completely black). The region between T_N and T_I is the biphasic region in which the nematic and isotropic phases co-exist, see Figure 3 and Figure 4. The liquid crystal samples were prepared using a total weight of 100mg, with 5mg (5wt%) or 10mg (10wt%) of the dopant in the base mixture ZLI-4792. To ensure complete dissolution of the dopant approximately 1ml of dichloromethane (DCM) was added. On complete dissolution the dichloromethane was removed by careful heating and the sample was then left at RT for a few hours to ensure complete evaporation of the solvent. Small drops of the sample mixtures were then placed onto slides on the hot stage of the polarising microscope and the phase transitions observed with a polarising microscope. The transition temperatures were measured using three heating and cooling cycles on the same sample at a rate of 1°C/min to ensure the results were consistent, which indicated that no DCM remained. The presence of DCM would lower the transition temperatures and on successive heating the DCM would be evaporated and an increase of the transition temperatures would be observed. The polarising microscopy results for each doped system are shown in Table 3 for concentrations of 5wt% and 10wt% along with the nematic transition temperature, T_N, obtained from variable temperature ESR. The ESR spectrum at this transition consists of the three hyperfine lines from the aligned nematic with a spacing of ~10G and two outer spectral features which correspond to the isotropic phase, which have a spacing of ~15G, see Figure 5. These outer two peaks grow in intensity as the temperature is increased, until the nematic has essentially disappeared and the isotropic phase is dominant. The values of the transition temperature obtained using these two techniques vary slightly due to the use of different temperature control units which were calibrated independently.

Figure 2: Polarising microscope texture of the nematic phase of ZLI-4792 containing four brush defects.

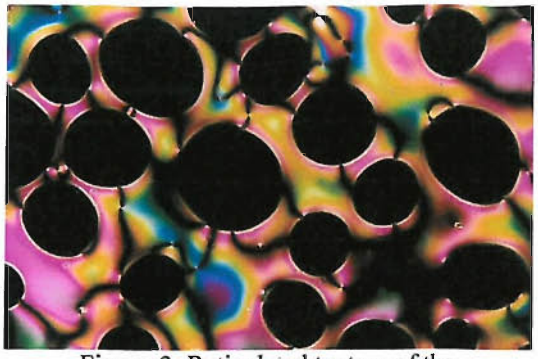

Figure 3: Reticulated texture of the biphasic region of ZLI-4792 on heating at a higher temperature than the texture in Figure 2.

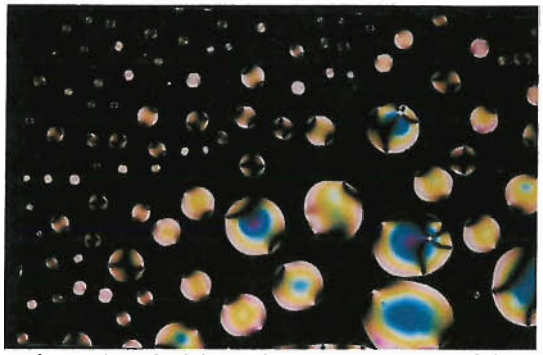

Figure 4: Polarising microscope texture of the biphasic region of ZLI-4792 on heating at a higher temperature than the texture in Figure 3.

The texture shown in Figure 2 shows the nematic phase of ZLI-4792 and the textures in Figure 3 and Figure 4 show the biphasic region of the same sample on heating.

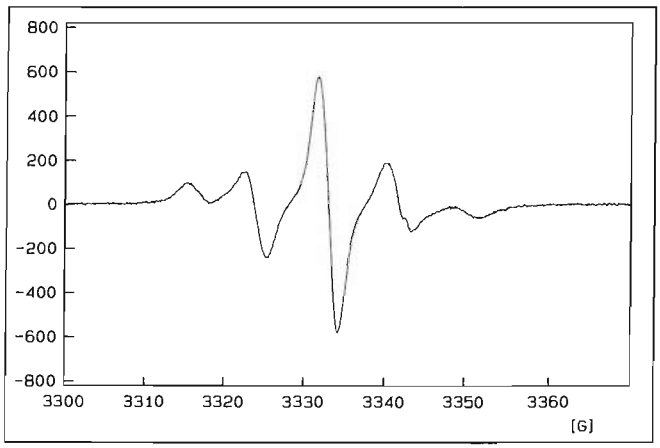

Figure 5: ESR spectrum showing the onset of the biphasic region.

Dopant	Concentration of dopant in ZLI-4792 / wt%	T_N / K (± 0.5K)	T_N / K (± 1.0K) ESR	T_I / K (± 0.5K)
ZLI-4792	0	366.0	366	373.5
C7	5	350.0	/	360.4
	10	335.6	337	346.5
C8	5	347.7	/	359.3
	10	333.0	/	346.1
C9	2	365.2	/	369.9
	8	346.2	/	354.2
	10	340.3	340	350.2
C10	5	346.0	/	355.2
	10	334.9	/	344.7
C11	5	352.8	/	363.1
	10	341.2	341	354.1
C12	5	350.0	/	360.3
	10	335.7	/	348.9
MeC9	5	361.1	/	367.8
	10	350.9	348	359.4
MeC10	5	362.2	/	368.8
	10	353.2	/	362.2
FC7	5	354.5	/	365.1
	10	346.1	346	355.6
FC9	5	354.6	/	363.1
	10	343.2	346	352.6
FC10	5	361.1	/	369.5
	10	Insoluble	/	Insoluble
CF3C9	5	354.2	/	363.5
	10	343.4	344	353.5
CF3C10	5	351.9	/	362.1
	10	342.4	340	352.2
23FC9	5	353.1	/	361.9
	10	341.4	340	351.1
24FC7	5	353.8	/	362.3
	10	340.4	341	350.1
24FC8	5	355.4	/	364.3
	10	343.9	346	353.3
24FC9	5	355.3	/	363.2
	10	344.6	343	353.6
24FC10	5	351.8	/	361.0
	10	340.1	347	349.9
34FC7	5	353.5	/	361.8
	10	342.9	343	352.3
34FC10	5	355.3	/	364.0
	10	343.6	344	352.9
234FC7	5	359.1	/	366.9
	10	352.0	345	359.5
234FC9	5	355.2	/	363.4
	10	343.2	345	353.0
345FC7	5	355.1	/	363.1
	10	345.8	345	354.5

Dopant	Concentration of dopant in ZLI-4792 / wt%	T_N / K (± 0.5K)	T_N / K (± 1.0K) ESR	T_I / K (± 0.5K)
345FC9	5	350.5	/	360.3
	10	338.9	340	348.7
PFC7	5	354.0	/	362.1
	10	344.6	343	353.8
PFC9	5	356.0		364.4
	10	346.7	346	356.7
NC8	5	354.4	/	361.7
	10	346.2	345	354.1
NC9	5	355.7	/	362.6
	10	345.8	348	353.5
NC10	5	356.1	/	364.4
	10	346.5	347	356.6
DFS33	10	363.7	362	371.2

Table 3: Transition temperatures for ZLI-4792 + 5wt% and 10wt% of dopant.

4.3.2 Phase diagrams

The transition temperatures, measured using polarising microscopy, are plotted in the following phase diagrams to illustrate the effect of the dopants on the transition temperatures of the host mixture, ZLI-4792.

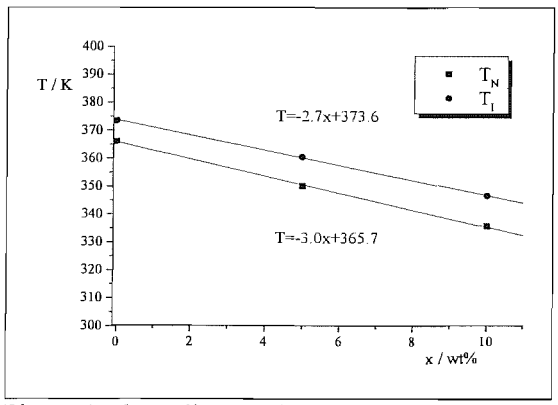

Figure 6: Phase diagram for ZLI-4792 + C7.

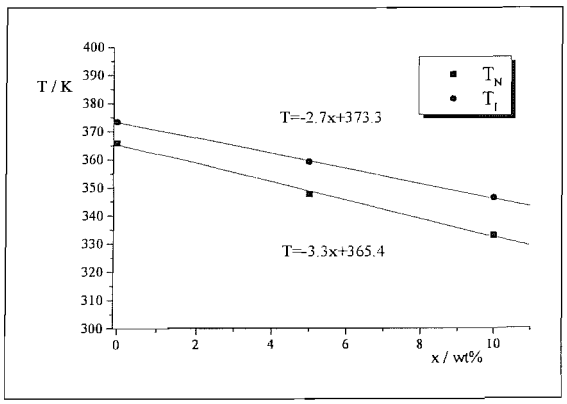

Figure 7: Phase diagram for ZLI-4792 + C8.

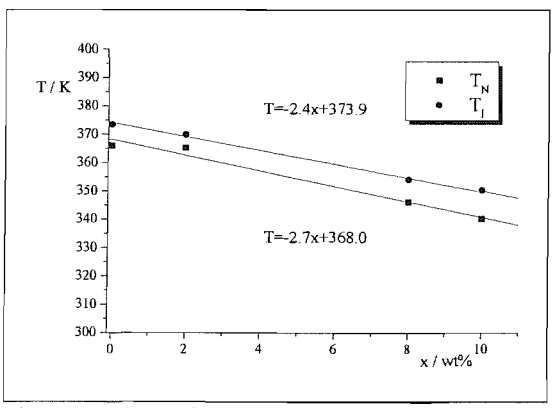

Figure 8: Phase diagram for ZLI-4792 + C9.

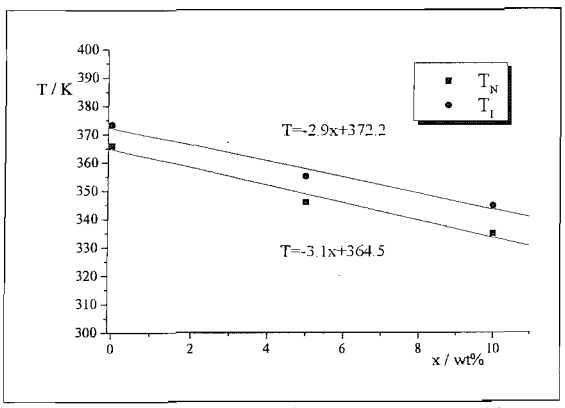

Figure 9: Phase diagram for ZLI-4792 + C10.

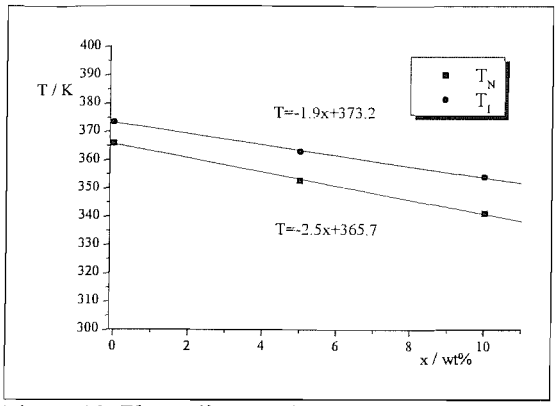

Figure 10: Phase diagram for ZLI-4792 + C11.

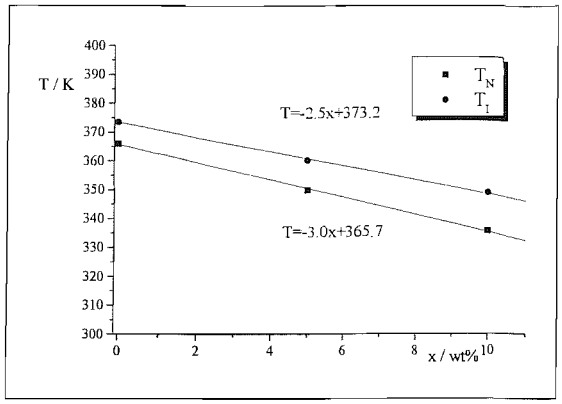

Figure 11: Phase diagram for ZLI-4792 + C12.

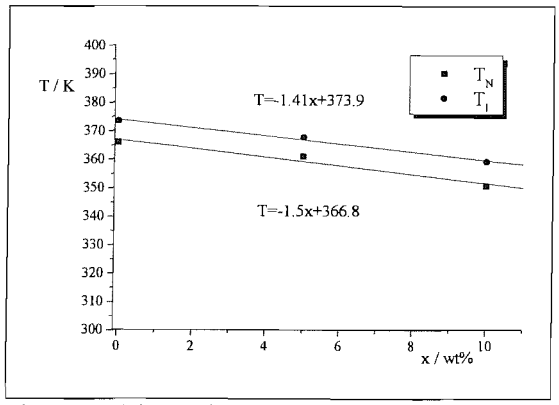

Figure 12: Phase diagram for ZLI-4792 + MeC9.

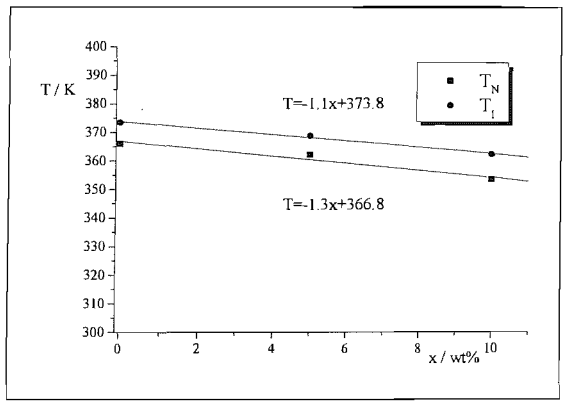

Figure 13: Phase diagram for ZLI-4792 + MeC10.

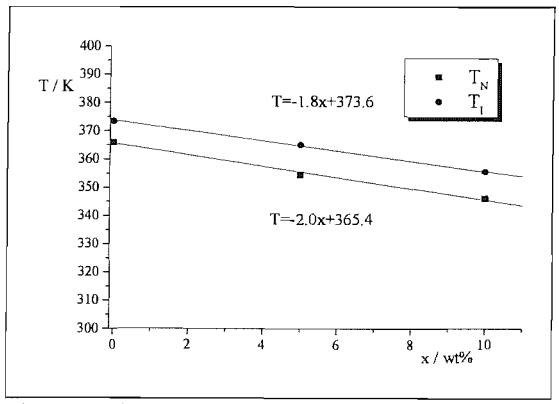

Figure 14: Phase diagram for ZLI-4792 + FC7.

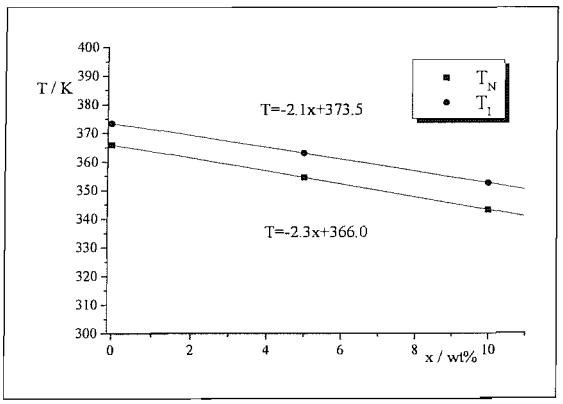

Figure 15: Phase diagram for ZLI-4792 + FC9.

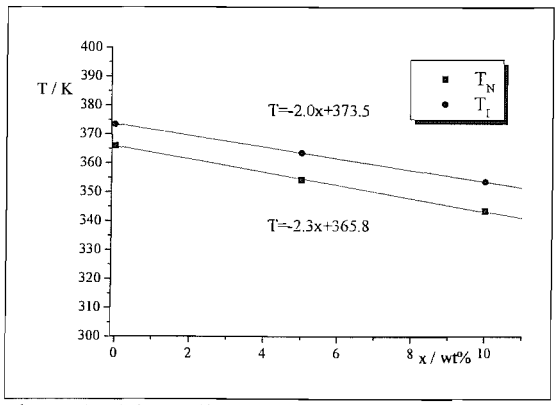

Figure 16: Phase diagram for ZLI-4792 + CF3C9.

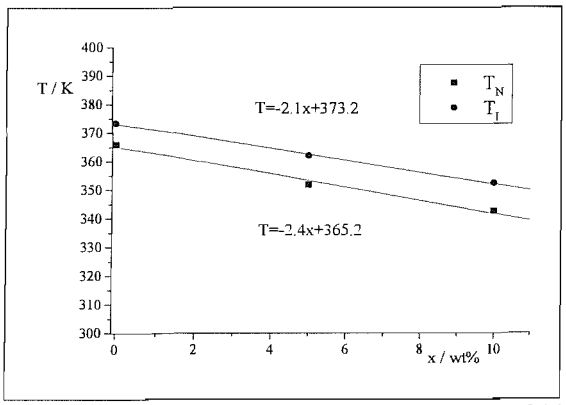

Figure 17: Phase diagram for ZLI-4792 + CF3C10.

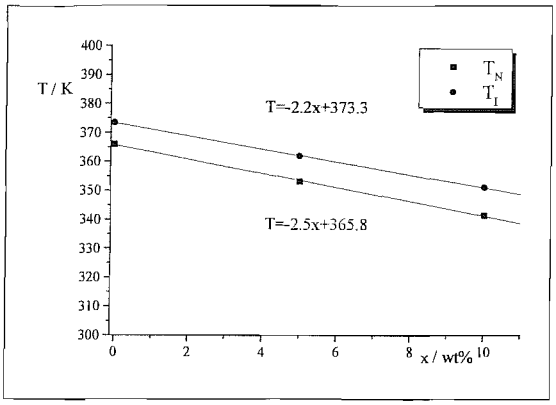

Figure 18: Phase diagram for ZLI-4792 + 23FC9.

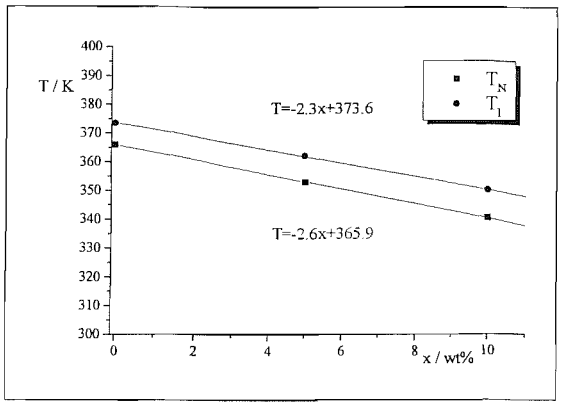

Figure 19: Phase diagram for ZLI-4792 + 24FC7.

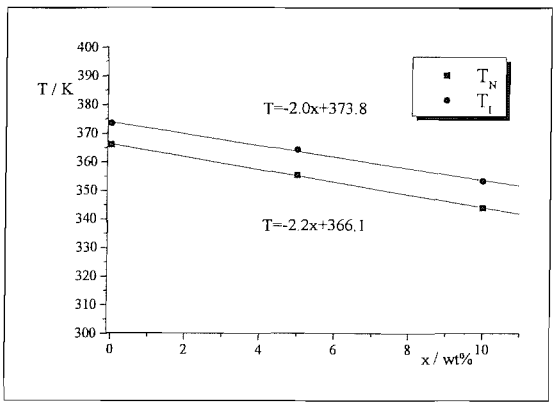

Figure 20: Phase diagram for ZLI-4792 + 24FC8.

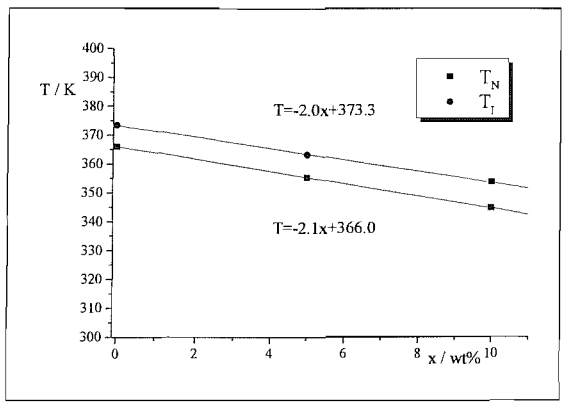

Figure 21: Phase diagram for ZLI-4792 + 24FC9.

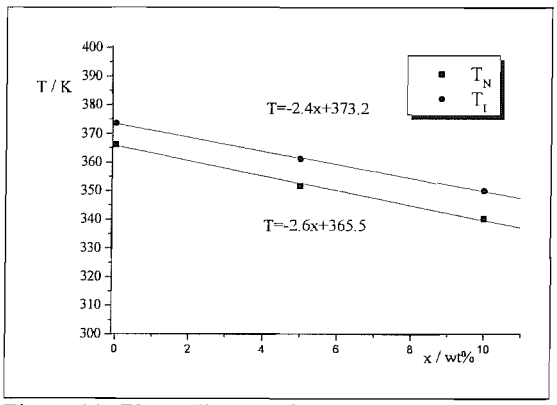

Figure 22: Phase diagram for ZLI-4792 + 24FC10.

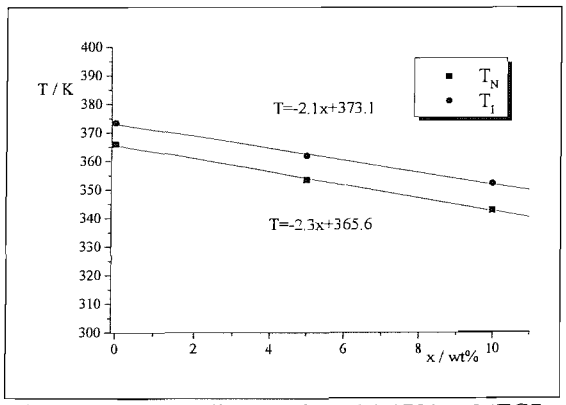

Figure 23: Phase diagram for ZLI-4792 + 34FC7.

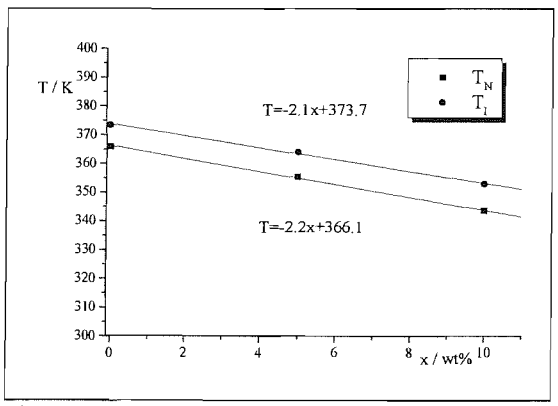

Figure 24: Phase diagram for ZLI-4792 + 34FC10.

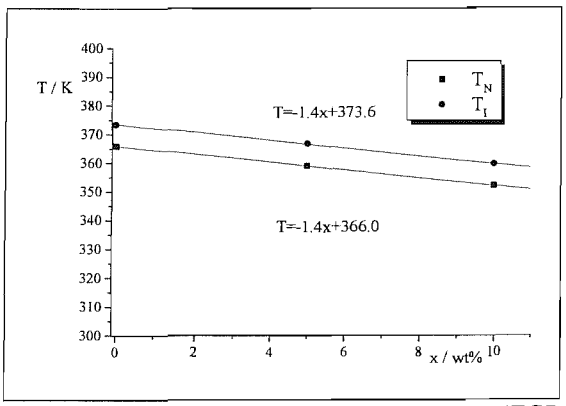

Figure 25: Phase diagram for ZLI-4792 + 234FC7.

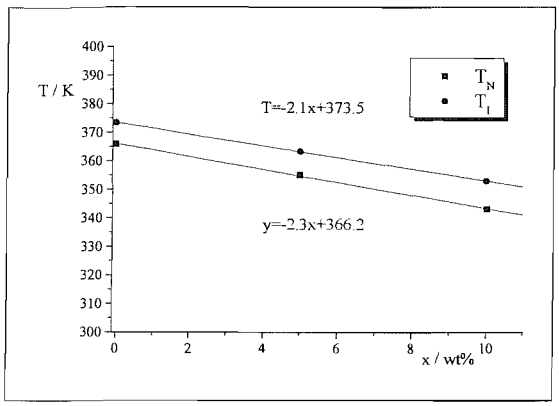

Figure 26: Phase diagram for ZLI-4792 + 234FC9.

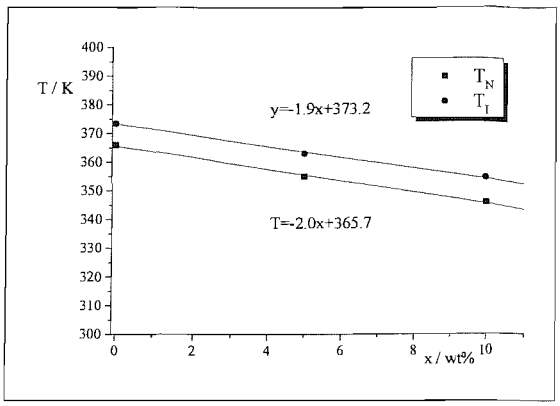

Figure 27: Phase diagram for ZLI-4792 + 345FC7.

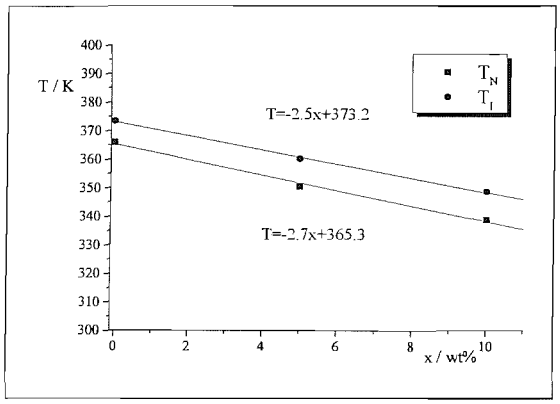

Figure 28: Phase diagram for ZLI-4792 + 345FC9.

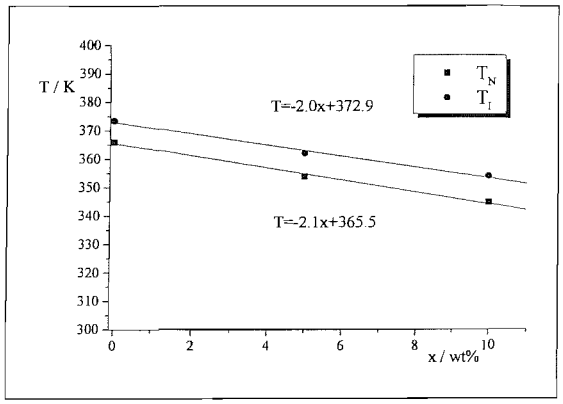

Figure 29: Phase diagram for ZLI-4792 + PFC7.

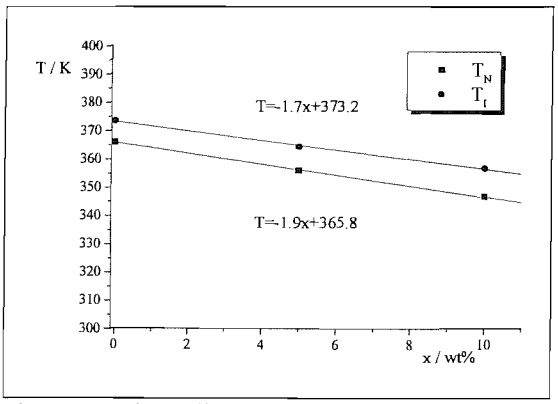

Figure 30: Phase diagram for ZLI-4792 + PFC9.

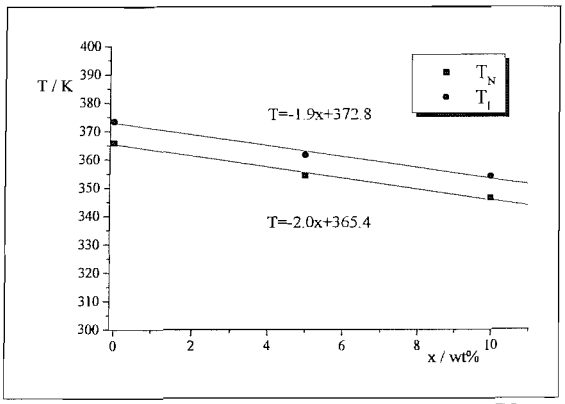

Figure 31: Phase diagram for ZLI-4792 + NC8.

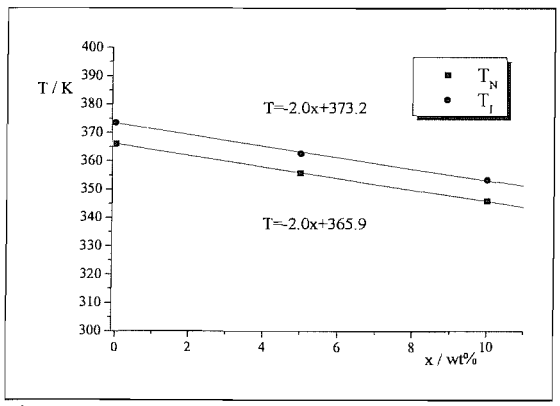

Figure 32: Phase diagram for ZLI-4792 + NC9.

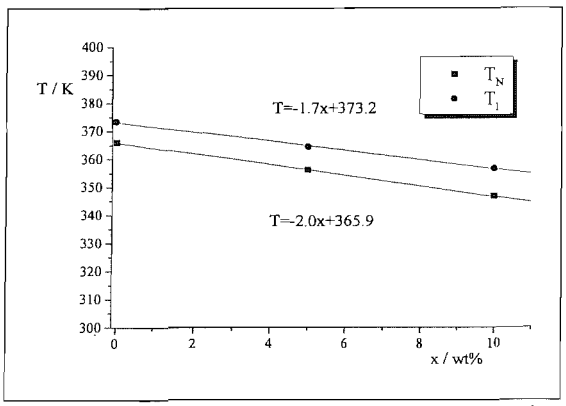

Figure 33: Phase diagram for ZLI-4792 + NC10.

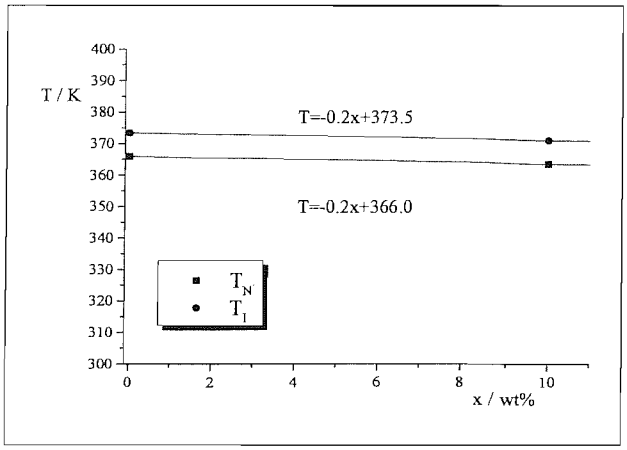

Figure 34: Phase diagram for ZLI-4792 + DFS33.

The error in the intercepts range from 0.1-3.0K and the error in the slopes range from 0.01-0.3K/wt%. The error in measuring the melting points is ±1K.

It is clear that all of the dopants investigated lower the transition temperatures of the host nematic mixture, ZLI-4792. This is not desirable for display applications, as the operating temperature of a display generally has to be within a specified range of approximately -40°C to 100°C. However, the dopants do not depress the transition of the host far enough so that they are totally unusable in certain types of display devices. The FC10 dopant was insoluble at a concentration of 10wt%, so the phase diagram was not plotted. The DFS33 is the only dopant to have a minimal affect on the transition temperatures, T_N and T_I. Table 4 compares the slopes of the lines from each phase diagram for each of the dopants at both transitions and the extrapolated transition temperatures of the dopants i.e. virtual T_{NI}. The slopes of the lines associated with the nematic transition temperature, T_N, have been sorted into ascending order with the dopants that depress the transition temperature T_N the most at the top of the table.

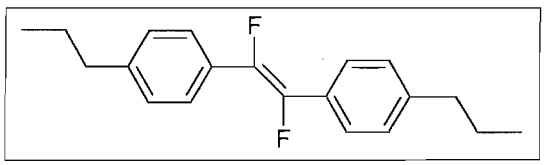

Figure 35: Structure of DFS33.

Dopant	Melting Point / K	Slope, m_N / (K/wt%)	Slope, m_I / (K/wt%)	Virtual T_N for 100% of dopant / K	Virtual T_I for 100% of dopant / K
C8	357.2	-3.3	-2.7	35	103
C10	358.2	-3.1	-2.9	54	82
C7	327.2	-3.0	-2.7	66	103
C12	359.2	-3.0	-2.5	66	123
C9	333.2	-2.7	-2.4	98	134
345FC9	322.4	-2.7	-2.5	95	123
24FC7	< 288.2	-2.6	-2.3	106	144
24FC10	333.2	-2.6	-2.4	105	133
C11	337.2	-2.5	-1.9	116	183
23FC9	333.7	-2.5	-2.2	116	153
CF3C10	335.7	-2.4	-2.1	125	163
FC9	337.7	-2.3	-2.1	136	163
CF3C9	316.7	-2.3	-2.0	136	173
34FC7	301.2	-2.3	-2.1	136	163
234FC9	309.7	-2.3	-2.1	136	163
24FC8	325.2	-2.2	-2.0	146	174
34FC10	314.7	-2.2	-2.1	146	164
24FC9	< 288.2	-2.1	-2.0	156	173
PFC7	< 288.2	-2.1	-2.0	155	173
FC7	328.7	-2.0	-1.8	165	194
345FC7	332.3	-2.0	-1.9	166	183
NC8	304.2	-2.0	-1.9	165	183
NC9	< 288.2	-2.0	-2.0	166	173
NC10	313.2	-2.0	-1.7	166	203
PFC9	< 288.2	-1.9	-1.7	176	203
MeC9	336.7	-1.5	-1.4	217	234
234FC7	318.7	-1.4	-1.4	226	233
MeC10	358.2	-1.3	-1.1	234	264

Table 4: The melting points, slopes of the transition temperatures and the virtual transition temperatures for the dopants.

The error in measuring the melting points is ±1K.

The fully protonated, C7-C12, compounds depress the transition temperature to a greater degree than the other dopants and therefore posses lower virtual transitions. There is also an odd-even effect where the odd spacer linked dimers have higher virtual transitions compared to the even spacer linked dimers which are next to them in the homologous series i.e. the C10 dopant has a much lower virtual transition than the C9 and C11 dopants. This odd-even effect is the reverse of what would be expected as the T_N for the even spacer linked dimers should be higher as it is with other liquid crystal dimers. The methylated dopants have the least effect on the transition temperatures compared to the other dopants and possess high virtual transition temperatures. These dopants would therefore be the best for display applications when considering mesophase behaviour.

4.4 Temperature dependence of the relaxation time

It is clearly necessary to compare the relaxation times on an appropriate temperature scale. Deciding whether to use the absolute or shifted temperature scale is a difficult problem. For display applications it is the absolute temperature scale which is of most importance, because it is at this temperature that the displays will operate, and the mixture chosen will be optimised to work efficiently within an operating temperature range. However, for the optimisation of mixtures, when comparing different doped systems with varying transition temperatures the reduced or shifted temperature scales will show the effect of the dopant on the host mixture more accurately than comparisons using the absolute temperature scale. The order parameter is dependent on the shifted temperature and because the order parameter is proportional to the rotational viscosity this too is dependent on the shifted temperature scale. It is therefore, necessary to use both temperature scales when comparing new mixtures for display applications. It was shown in Chapter 2 that the temperature dependence of the rotational viscosity is given by both Arrhenius behaviour and by that of the order parameter [7],

$$\gamma_1 \propto \overline{P}_2 \exp(E_a / RT). \tag{1}$$

The relaxation time, τ, is proportional to $\gamma_1 / \Delta\tilde{\chi}$ which in turn is expected to be proportional to $\gamma_1 / \overline{P}_2$, since $\Delta\tilde{\chi} \propto \overline{P}_2$ and so

$$\tau \propto \gamma_1 / \overline{P}_2 \propto \exp(E_a / RT). \tag{2}$$

Therefore the relaxation time should be given by simple Arrhenius behaviour

$$\tau = \tau^{\infty} \exp(E_a / RT), \tag{3}$$

where τ^{∞} is the relaxation time which is obtained by extrapolating to infinite temperature, however due to the system becoming isotropic at T_I this relaxation time constant cannot be determined directly. The value of τ^{∞} is obtained indirectly from a plot of $\ln\tau$ vs. T^{-1}, which also yields the value of the activation energy for director relaxation.

$$ln\tau = ln\tau^{\infty} + (E_a / R)T^{-1}. \tag{4}$$

4.5 Parameters for the ESR variable temperature step-rotation experiments

The samples of ZLI-4792 and 10wt% of dopant with approximately $1x10^{-2}$wt% of cholestane were prepared in an ESR tube. The ESR tube is made of pyrex with an internal diameter of ~2mm, which has been established to be the optimum diameter to ensure a uniform director distribution when the sample is rotated i.e. the director moves essentially as a monodomain [8]. The cholestane was dissolved in DCM and pipetted into the ESR tube, the concentration was tested on the spectrometer for acceptable signal-to-noise ratio

and then the DCM was carefully removed on a high vacuum line. The doped nematic liquid crystal ZLI-4792 (ca.0.1ml) was added to the cholestane and then the sample was degassed by a repeat freeze-thaw cycle in order to avoid line broadening caused by dissolved oxygen, which is paramagnetic. The samples were placed in the microwave cavity of the ESR spectrometer and the rotary solenoid was fitted. The sample was rotated by the rotary solenoid by an angle of ~45° and the spectra were recorded over a time comparable to the director relaxation time. The experimental parameters were optimised for each ESR experiment in order to obtain the most accurate values of the relaxation time. This was achieved by varying the sweep time, pulse time and centre field if necessary. The following table gives the parameters used for the experimental study of the pure host ZLI-4792.

4.5.1 Parameters for ZLI-4792

Temperature / K	Centre Field / G	Sweep width / G	Sweep Time / s	Rotation time / s
293	3335	40	2.62	0.100
298	3335	40	2.62	0.100
305	3335	40	2.62	0.100
310	3335	40	1.31	0.030
315	3335	40	1.31	0.010
320	3335	40	1.31	0.010
325	3335	40	1.31	0.010
330	3336	50	0.66	0.070
335	3336	50	0.66	0.070

Table 5: Parameters for the variable temperature step-rotation experiment with ZLI-4792.

The rotation time is the time after the scan has started when the rotary solenoid is triggered to rotate the sample, and not the time taken for the sample to be rotated. The highest temperature possible for most of the systems was 325K, this is due the fact that as the temperature increases the rotational viscosity decreases and so the relaxation behaviour becomes faster and the scan time is not fast enough to prevent the director relaxing back to being parallel to the magnetic field by the end of the scan. This could be overcome if we could scan at a faster rate, but 0.66s is the fastest scan time available and 40G was found to be the optimum sweep width for obtaining small errors.

4.5.2 Parameters for ZLI-4792 + 10wt% Dopant

The experimental parameters for all the doped systems are given in Tables A.1-A.29 in Appendix A.

4.6 ESR variable temperature step-rotation results

4.6.1 Calculation of the relaxation time from an ESR spectrum

It was shown in Chapter 3 that the relaxation time can be calculated using

$$\tau = \frac{2(\tilde{a}_1 - \tilde{a}_2)}{bln\left(\tilde{a}_1^2 - \tilde{A}_{||}^2\right)\left(\tilde{A}_{\perp}^2 - \tilde{a}_2^2\right)/\left(\tilde{A}_{\perp}^2 - \tilde{a}_1^2\right)\left(\tilde{a}_2^2 - \tilde{A}_{||}^2\right)}, \tag{5}$$

where $\tilde{a}_1$ and $\tilde{a}_2$ are the two hyperfine spacings.

The following equation allows the calculation of the angle the director makes with the magnetic field at times, t_1 and t_2;

$$\tan\beta_m = \left(\frac{\tilde{a}_m^2 - \tilde{A}_{||}^2}{A_{\perp}^2 - \tilde{a}_m^2}\right)^{1/2}, \tag{6}$$

where β_m is the angle at time, t_m. The angle difference, $\beta_1 - \beta_2$, can then be calculated which is the angle over which the director is seen to relax. The lowest angle during director relaxation observed for these measurements was 8° and the error in the relaxation time is still low (below ± 0.1s). The errors associated with the relaxation times were found to be low (4-8%) providing the hyperfine spacing, $\tilde{a}_1$, is greater than the hyperfine spacing, $\tilde{a}_2$, by at least 1.0G and the hyperfine spacing, $\tilde{a}_2$, is greater than the parallel hyperfine spacing, $\tilde{A}_{||}$, by about 0.6G. The percentage error in the relaxation time was then calculated using the two extreme cases in the measurement of the hyperfine spacings, $\tilde{a}_1$ and $\tilde{a}_2$. The error in measuring these spacings was taken to be ± 0.25mm, which equates to ~0.05G for a sweep width of 40G and ~0.06G for a sweep width of 50G. The relaxation times were then calculated using values of $\tilde{a}_1$ + 0.05G with $\tilde{a}_2$ -0.05G and $\tilde{a}_1$ -0.05G with $\tilde{a}_2$ +0.05G. The percentage difference from the measured relaxation time was then calculated to give the associated error.

The order parameter of the spin probe, cholestane, was calculated using [9]

$$\overline{P}_2 = 2(a_{iso} - \tilde{A}_{||})/\tilde{A}'_{33}, \tag{7}$$

where the isotropic hyperfine splitting, a_{iso} = 14.6G and $\tilde{A}'_{33}$ = 18.3G [8]which is the anisotropic hyperfine spacing perpendicular to the plane of the oxazolidine ring measured from the spectrum of the probe in a glass phase. It must be noted that this is the order parameter of the molecular long axis of the spin probe with respect to the director and not the orientational order parameter of the director with respect to the magnetic field. Although the order parameters are for the spin probe they can be taken to be from the liquid crystal due to the spin probes interaction with the liquid crystal host.

4.6.2 Results for ZLI-4792

Temperature / K	τ / s	Error in τ / s	$\overline{P_2}$	β_1 / °	β_2 / °	$\beta_1 - \beta_2$ / °
293	1.82	± 0.07	0.77	35.1	18.1	17.0
298	1.49	± 0.06	0.76	33.0	14.8	18.2
305	1.07	± 0.06	0.73	31.7	10.4	21.3
307*	1.06					
310	0.93	± 0.04	0.71	34.5	17.9	16.6
312*	0.91					
315	0.80	± 0.04	0.70	34.3	15.9	18.4
317*	0.78					
320	0.68	± 0.04	0.68	32.9	13.2	19.7
325	0.62	± 0.03	0.67	33.0	12.1	20.9
330	0.54	± 0.04	0.66	31.7	20.2	11.5
335	0.49	± 0.04	0.63	28.6	15.6	13.0

Table 6: Relaxation times, order parameters and rotation angles for ZLI-4792 at varying temperatures. *Interpolated values.

4.6.3 Results for ZLI-4792 + 10wt% Dopant

The results for all the doped systems are given in tables in the Sections B.1-B.25 in Appendix B. The relaxation times for the even members of the C*n* homologous series (C8, C10, C12) and the MeC10 dopant could not be investigated using this novel ESR method due to unexpected gelling behaviour of these dopants in ZLI-4792. They are, however, the topic of Chapter 5.

4.7 Comparison of results for the doped systems

The following results concerning the dynamic behaviour and order of the systems are obviously from the spin probe, cholestane, but in order to simplify the discussion this will be neglected from now on and only the doped systems will be discussed.

The nematic transition temperatures used, when comparing the order parameters on the shifted temperature scale, were obtained from the variable temperature ESR experiment and not polarising microscopy. These values of the transition temperature differ slightly from the values obtained by polarising microscopy, with some dopants showing larger differences than others. These differences are due to the different temperature control units used for the two experiments. Both values of this transition temperature are given in Table 3. The transition temperature used for comparison of the relaxation times is the value obtained from polarising microscopy.

For display applications comparison on the absolute temperature scale is necessary, as it is the ambient temperature at which the display is used. However, for direct comparison of the dopants with each other and the host it is important to consider the shift in the transition temperatures caused by the addition of the dopants, this is achieved by comparison on the shifted temperature scale ($T_N - T$).

4.7.1 Relaxation times and order parameters for the DFS33 doped system

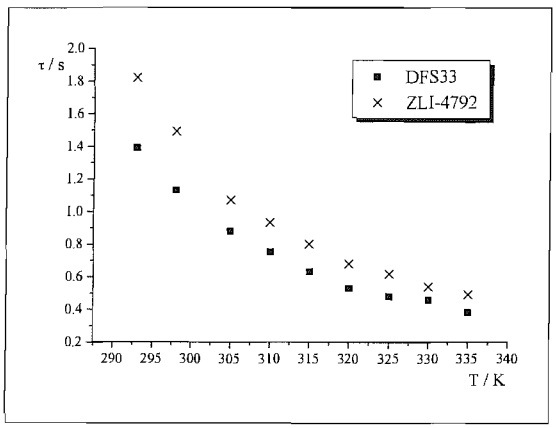

Figure 36: Comparison of the relaxation times for the DFS33 doped system on the absolute temperature scale.

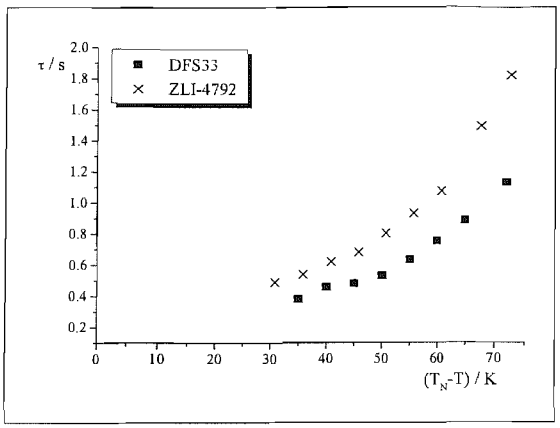

Figure 37: Comparison of the relaxation times for the DFS33 doped system on the shifted temperature scale.

Figure 36 clearly illustrates that the addition of DFS33 to ZLI-4792 reduces the relaxation time of this host significantly. Therefore this is a very effective dopant at lowering the rotational viscosity of the host nematic mixture when compared at the same absolute temperature. If they are compared on the shifted temperature scale then DFS33 is still an effective dopant at reducing the relaxation time of the host, illustrated in Figure 37. This is due to the fact that the addition of DFS33 does not change the transition temperature of ZLI-4792.

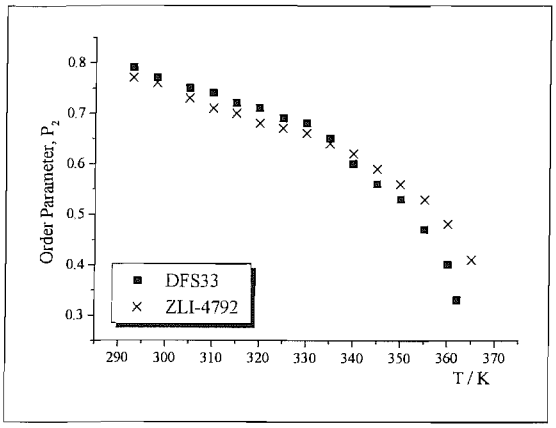

Figure 38: Comparison of the order parameters for the DFS33 doped system on the absolute temperature scale.

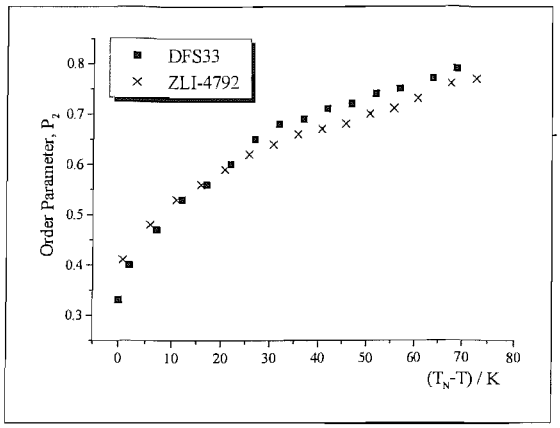

Figure 39: Comparison of the order parameters for the DFS33 doped system on the shifted temperature scale.

The order parameter curves are typical for a nematic liquid crystal with a sharp decrease at the nematic-isotropic transition, see Chapter 1. The order parameters are not affected significantly by the addition of this dopant when compared on the absolute and shifted temperature scales. This dopant would be an ideal dopant for display applications providing it does not affect the other physical properties, such as the diamagnetic susceptibility, dielectric anisotropy and the birefringence, of the mixture detrimentally.

4.7.2 Relaxation times and order parameters for the Cn and MeC9 doped systems

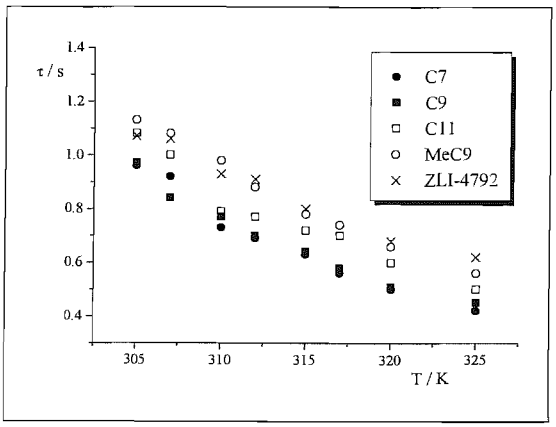

Figure 40: Comparison of the relaxation times for the C*n* and MeC9 doped systems on the absolute temperature scale.

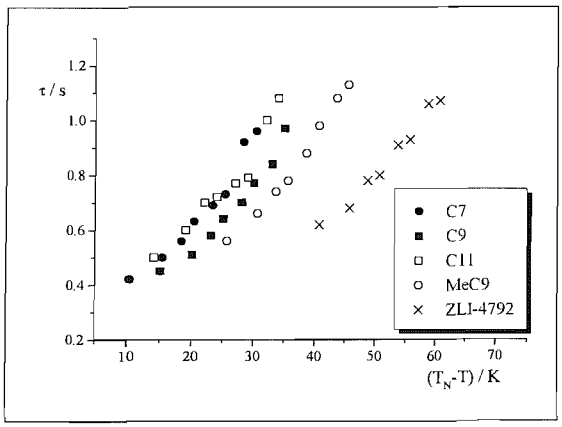

Figure 41: Comparison of the relaxation times for the C*n* and MeC9 doped systems on the shifted temperature scale.

The shifted temperature scale groups the doped systems together which are separated from the pure host. Values for the relaxation time close to the transition for the pure host were not obtainable due to the limitations of the ESR experiment. Comparisons of the doped systems with the host at the same shifted temperature are therefore not possible in most cases, dependent on the variation in T_N.

The MeC9 dopant has little effect on the relaxation behaviour of the host mixture when compared on the absolute temperature scale. This dopant however affects the mesophase behaviour of the host the least, so when the shift in transition temperature is considered and the dopants are compared at the same shifted temperature the MeC9 dopant actually has better relaxation dynamics than the other dopants. The C*n* dopants all lower the relaxation time of the host, with the short-spacer length dimers having a greater effect than the longer C11. This observation fits with the theory that the rotational viscosity increases with increasing alkyl chain length, see Figure 40 and Figure 41. The order parameter, at absolute temperatures below 345K, is lowered by the addition of the dopants, see Figure 42, with greater decreases at high temperatures due to the lower nematic transition temperatures of the doped systems. The order decreases more sharply near the transition to an approximate value of 0.4. This decrease in the order parameter when nearing the transition temperature for C*n* dopants is not as sharp as it is for the MeC9 doped system and the pure host. Obviously comparisons of the order parameter cannot be made for all values of the absolute temperature due to the fact that at the transition temperatures of the dopants the order vanishes. However, Figure 43 shows there is little effect on the order parameter when the shift in the transition temperatures is considered.

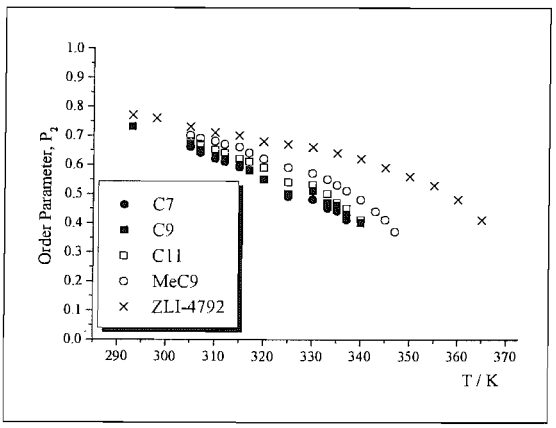

Figure 42: Comparison of the order parameters for the C*n* and MeC9 doped systems on the absolute temperature scale.

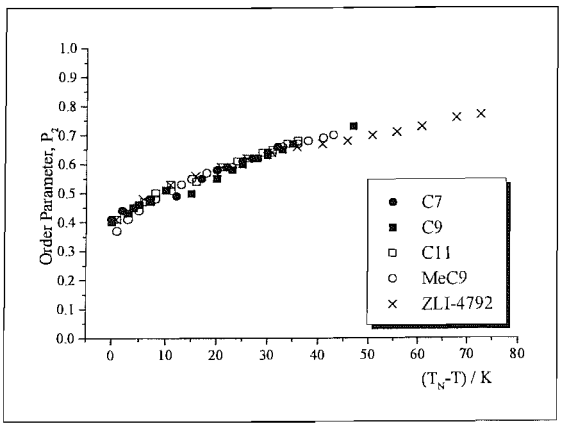

Figure 43: Comparison of the order parameters for the C*n* and MeC9 doped systems on the shifted temperature scale.

4.7.3 Relaxation times and order parameters for the FCn and CF3Cn doped systems

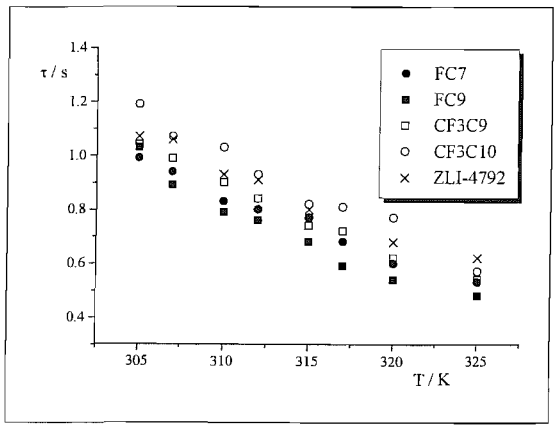

Figure 44: Comparison of the relaxation times for the FC*n* and CF3C*n* doped systems on the absolute temperature scale.

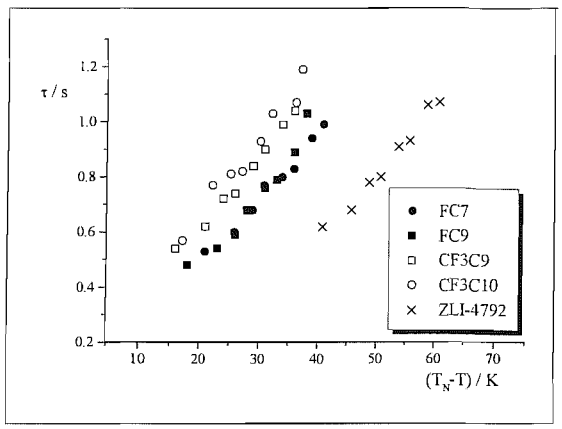

Figure 45: Comparison of the relaxation times for the FC*n* and CF3C*n* doped systems on the shifted temperature scale.

Figure 44 shows that the CF3C10 dopant actually increases the relaxation time of the host, which is undesirable. This may be due to the parity of the linking unit. Even dimers in the nematic phase tend to adopt, on average, linear conformations which are able to pack more efficiently than their odd counterparts [10,11]. This increase in packing strength leads to higher melting points, transition temperatures and slower relaxation behaviour due to higher viscosities. The FC*n* dopants are the better dopants in all respects when compared to the CF3C*n* dopants as they speed up the relaxation behaviour, see Figure 45, and also decrease the transition temperature by the least amount, see Table 3. This may be due to the trifluoromethyl group of the CF3C*n* dopants being bulkier substituents than the fluoro-substituents and because of steric hindrance, due to the unfavourable interaction of fluorine with hydrogen, prevents the motion of the molecules as they slide passed one another.

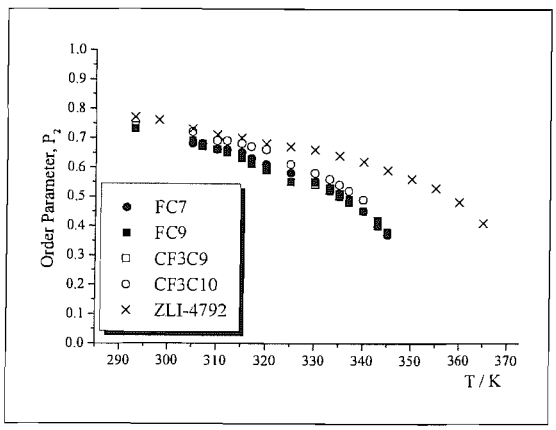

Figure 46: Comparison of the order parameters for the FC*n* and CF3C*n* doped systems on the absolute temperature scale.

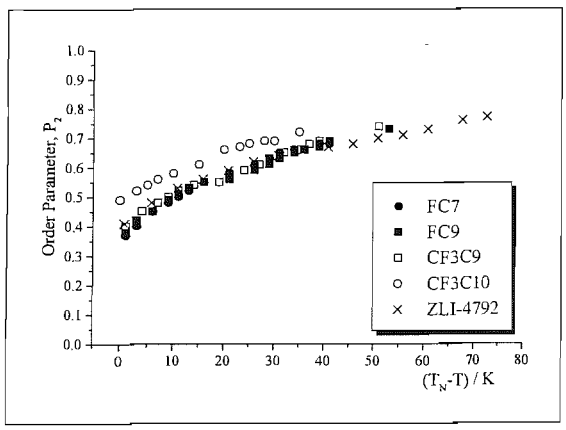

Figure 47: Comparison of the order parameters for the FC*n* and CF3C*n* doped systems on the shifted temperature scale.

Figure 46 shows that on the absolute temperature scale all the dopants lower the order of the system by approximately the same amount; however on the shifted temperature scale there is little to no effect of the addition of the dopants on the order of the system, except for the CF3C10 dopant which actually appears to increase the order of the system probably due to the long 'trans' chain, see Figure 47.

4.7.4 Relaxation times and order parameters for the 24FCn doped systems

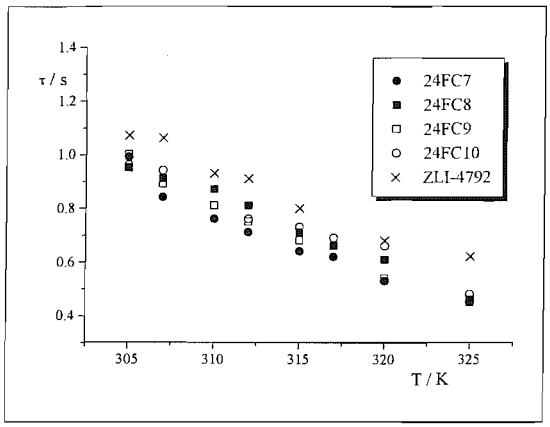

Figure 48: Comparison of the relaxation times for the 24FC*n* doped systems on the absolute temperature scale.

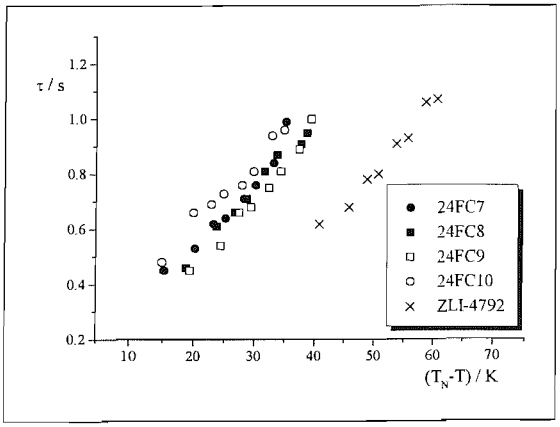

Figure 49: Comparison of the relaxation times for the 24FC*n* doped systems on the shifted temperature scale.

From Figure 48 it is clear that all four dopants decrease the relaxation time of the host mixture with the 24FC7 dopant showing the fastest relaxation behaviour, however when compared on the shifted temperature scale, which takes into account the effect the dopants have on the nematic-isotropic transition temperature of the host, the 24FC9 dopant exhibits the fastest relaxation times compared to the other doped systems, see Figure 49, but all the doped systems have slower dynamics than for the pure host at the same shifted temperature.

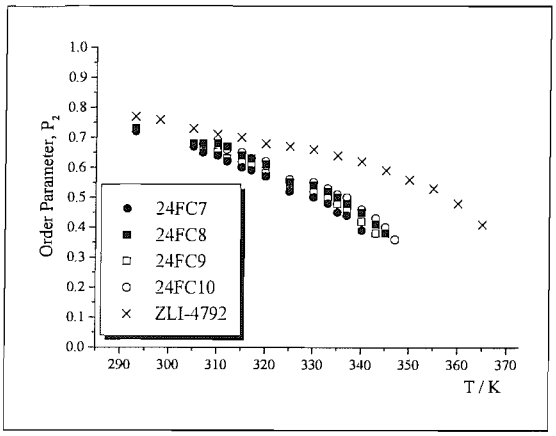

Figure 50: Comparison of the order parameters for the 24FC*n* doped systems on the absolute temperature scale.

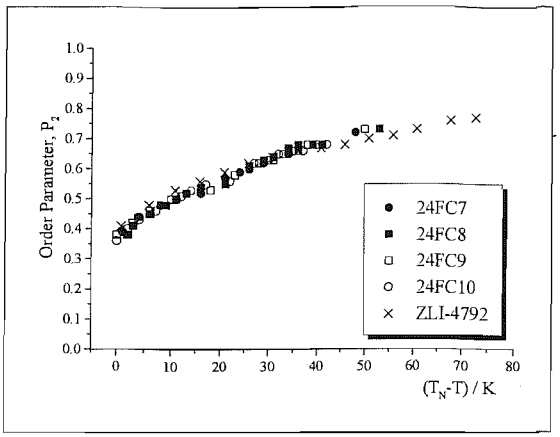

Figure 51: Comparison of the order parameters for the 24FC*n* doped systems on the shifted temperature scale.

In this series the odd-spacer length dopants, 24FC7 and 24FC9, affect the order slightly more than the even-spacer length dopants on the absolute temperature scale, see Figure 50, however this difference essentially vanishes when compared on the shifted temperature scale.

4.7.5 Relaxation times and order parameters for the 34FCn and 345FCn doped systems

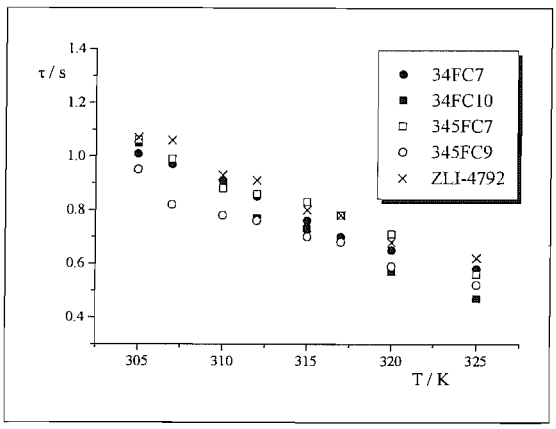

Figure 52: Comparison of the relaxation times for the 34FC*n* and 345FC*n* doped systems on the absolute temperature scale.

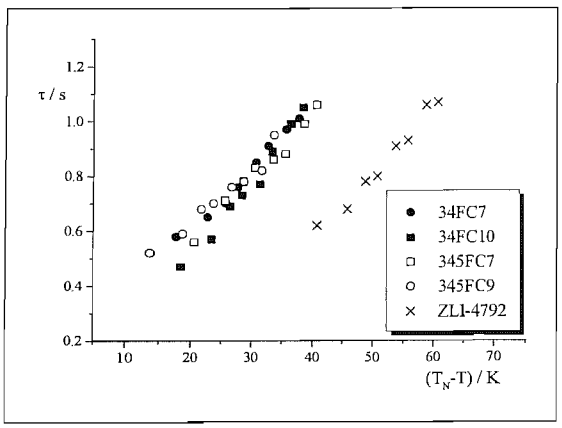

Figure 53: Comparison of the relaxation times for the 34FC*n* and 345FC*n* doped systems on the shifted temperature scale.

The data point for the 345FC9 dopant at 307K seems to be out of place. The dopants are all grouped together quite tightly when compared on the shifted temperature scale with the pure host separated. All the dopants lower the relaxation time when compared on the absolute temperature scale, see Figure 52. However, if the shift in transition temperature is taken into account they actually increase the relaxation behaviour of the pure host, ZLI-4792, see Figure 53.

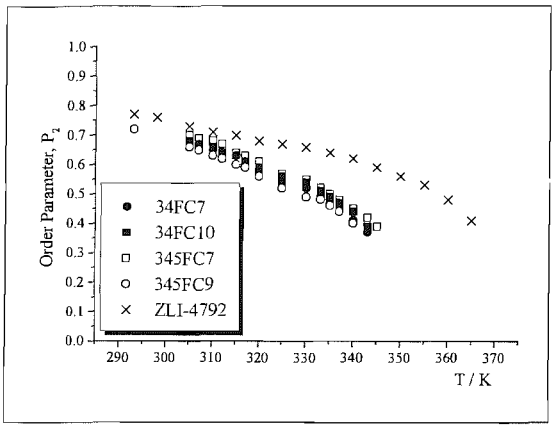

Figure 54: Comparison of the order parameters for the 34FC*n* and 345FC*n* doped systems on the absolute temperature scale.

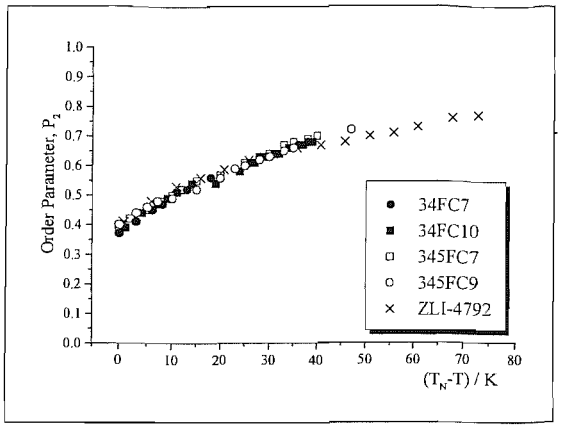

Figure 55: Comparison of the order parameters for the 34FC*n* and 345FC*n* doped systems on the shifted temperature scale.

On the absolute temperature scale the dopants seem to affect the order of the system by approximately the same amount, see Figure 54, however there is little effect on the order of the pure system when compared on the shifted temperature scale, Figure 55.

4.7.6 Relaxation times and order parameters for the 234FCn and 23FC9 doped systems

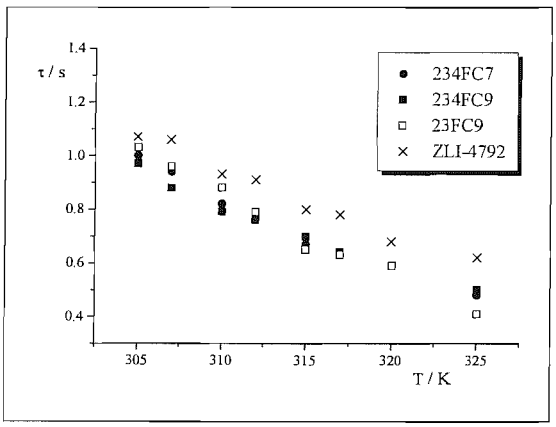

Figure 56: Comparison of the relaxation times for the 234FC*n* and 23FC9 doped systems on the absolute temperature scale.

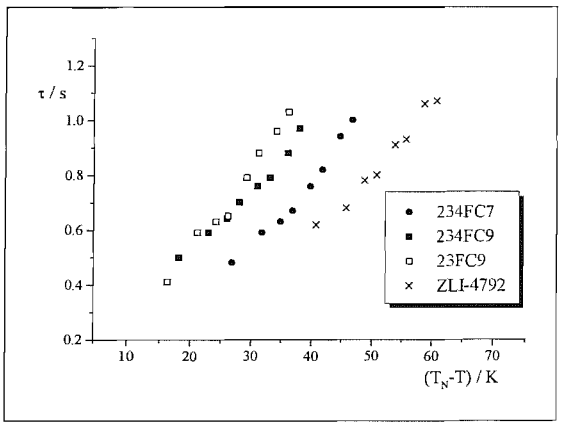

Figure 57: Comparison of the relaxation times for the 234FC*n* and 23FC9 doped systems on the shifted temperature scale.

Again it is clear to see from Figure 56 that all the dopants lower the relaxation time of the host significantly on the absolute temperature scale but on the shifted temperature scale the relaxation time actually increases, see Figure 57.

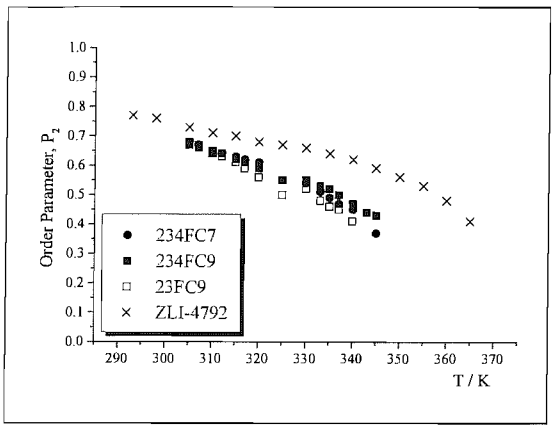

Figure 58: Comparison of the order parameters for the 234FC*n* and 23FC9 doped systems on the absolute temperature scale.

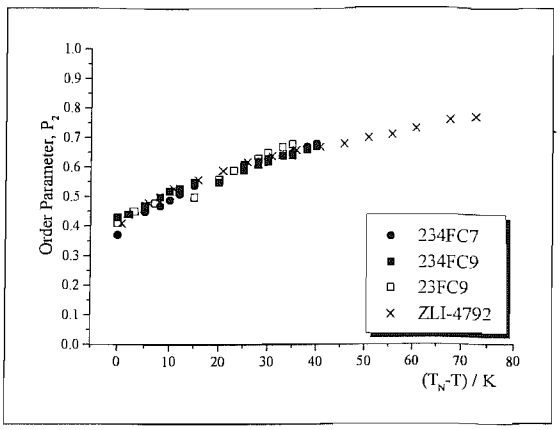

Figure 59: Comparison of the order parameters for the 234FC*n* and 23FC9 doped systems on the shifted temperature scale.

The order parameter is lowered on the absolute temperature scale but is hardly altered if the shift in transition temperature is considered see Figure 58and Figure 59. At low shifted temperatures it appears that there could be a reduction of the relaxation time for the 23FC9 system, this combined with the unaffected order parameter shows that this dopant is possibly effective at fulfilling the objective of this research.

4.7.7 Relaxation times and order parameters for the PFCn and NCn doped systems

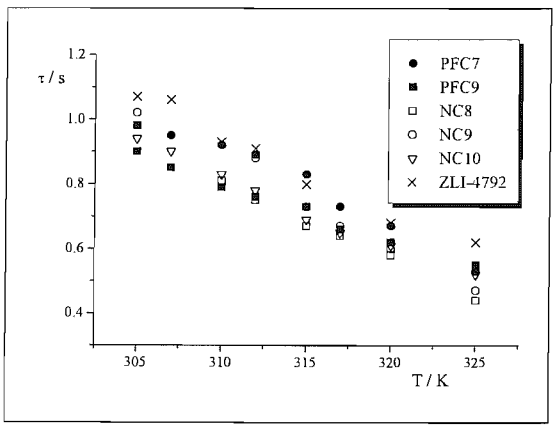

Figure 60: Comparison of the relaxation times for the PFC*n* and NC*n* doped systems on the absolute temperature scale.

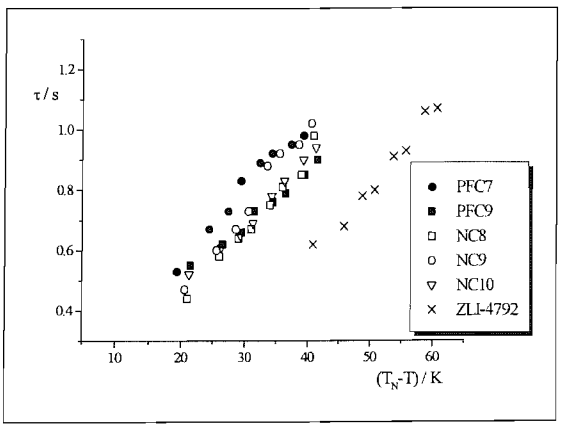

Figure 61: Comparison of the relaxation times for the PFC*n* and NC*n* doped systems on the shifted temperature scale.

The PFC7 dopant is the least effective at reducing the relaxation time and has little effect on the dynamics of the host mixture when compared on the absolute temperature scale. This is surprising as it has the shortest chain length which should by theory lead to faster relaxation behaviour than its longer chain counterpart. All of these dopants could possibly exhibit faster relaxation behaviour than the host when compared close to their transition temperatures, see Section 4.7.8. On the absolute temperature scale all the dopants lower the

order parameter, see Figure 62, but when the shift in transition temperature is accounted for there is little effect, Figure 63.

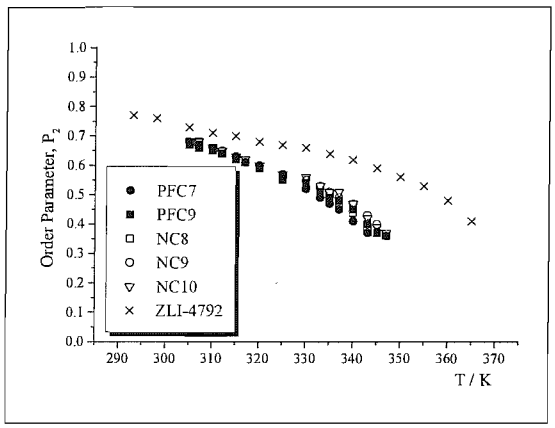

Figure 62: Comparison of the order parameters for the PFC*n* and NC*n* doped systems on the absolute temperature scale.

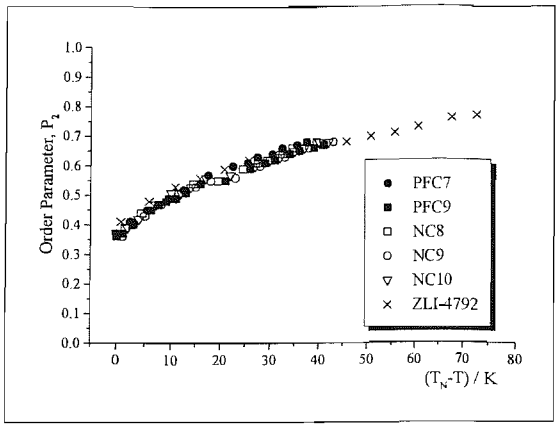

Figure 63: Comparison of the order parameters for the PFC*n* and NC*n* doped systems on the shifted temperature scale.

Most of the studied systems have lower relaxation times, which is desirable, and lower order parameters, which is not good, than the host mixture on the absolute temperature scale. This is the necessary temperature scale for comparison of mixtures for display applications. However, the dynamics of the systems are governed by both the absolute and shifted temperature scale. The dopants, due to the change in mesophase behaviour, exhibit slower relaxation times when compared on the shifted temperature scale, whereas the order remains unchanged.

4.7.8 Activation energy

The activation energy associated with the relaxation process can be obtained from the slope of the line from a plot of ln τ vs. $1/T$. The slope being equal to E_a/R, where R is the gas constant and the intercept is τ^{∞}.

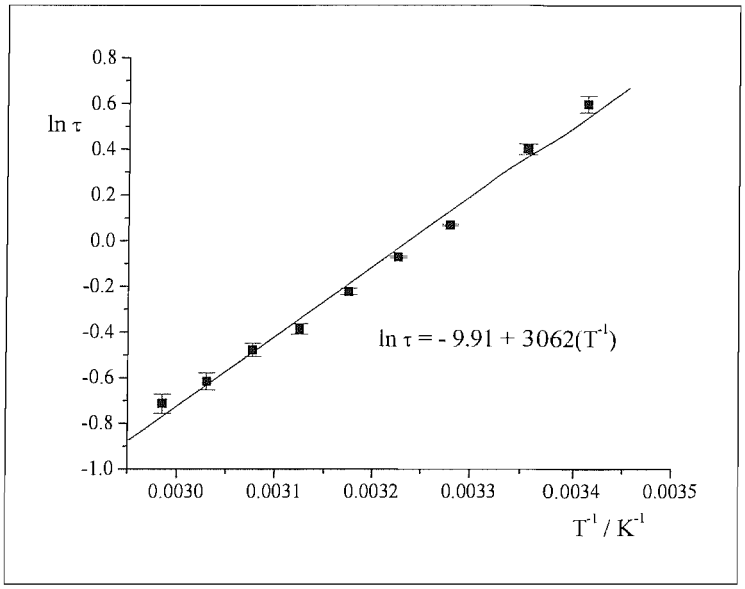

Figure 64: Arrhenius plot for ZLI-4792 to determine the activation energy for the field-induced director alignment process.

The slight deviation from linearity observed in Figure 64 may be caused by experimental error or some dependence of the activation energy on the order parameter.

The activation energies for each system are given in Table 7 along with the relaxation times at infinite temperature, the relaxation times at the transition temperature, T_N of the system and the relaxation times at 298K. All of these relaxation times have been interpolated from the corresponding Arrhenius plots. The data has been tabulated so that the relaxation times at the nematic transitions are in ascending order.

Dopant	Activation energy, E_a, / kJmol^{-1}	τ^{∞} /$\times 10^{-5}$ s	τ^{N} ± 0.05 s	τ^{298K} ± 0.05 s
DFS33	24.7 ± 0.9	5.20 ± 1.42	0.16	1.13
FC9	31.4 ± 1.7	1.87 ± 1.40	0.16	1.32
ZLI-4792*	***25.5 ± 1.0***	***5.0 ± 1.5***	***0.21***	***1.49***
234FC7	30.1 ± 0.8	0.70 ± 0.14	0.21	1.32
23FC9	36.6 ± 2.5	0.06 ± 0.08	0.23	1.50
NC8*	30.2 ± 1.9	0.64 ± 0.21	0.24	1.29
24FC9	31.7 ± 1.5	0.37 ± 0.18	0.24	1.34
NC9*	32.1 ± 2.4	0.34 ± 0.25	0.24	1.45
MeC9	29.9 ± 0.8	3.48 ± 1.72	0.25	1.52
34FC10	33.2 ± 1.6	0.23 ± 0.18	0.25	1.46
C9	31.4 ± 1.2	0.71 ± 0.24	0.26	1.25
24FC8	29.3 ± 2.3	0.97 ± 0.24	0.27	1.32
24FC7	30.6 ± 1.4	0.54 ± 0.17	0.27	1.25
C7	34.8 ± 1.5	0.40 ± 0.16	0.28	1.32
NC10*	24.9 ± 0.7	5.13 ± 1.31	0.30	1.20
FC7	26.0 ± 1.4	0.42 ± 0.19	0.30	1.28
234FC9	26.4 ± 0.7	2.89 ± 1.32	0.30	1.22
C11	30.2 ± 2.2	0.88 ± 0.13	0.30	1.38
CF3C9	27.8 ± 0.9	2.07 ± 2.30	0.31	1.37
PFC7	24.9 ± 2.8	5.71 ± 2.93	0.34	1.32
24FC10	26.2 ± 2.6	3.24 ± 2.69	0.34	1.26
PFC9	20.1 ± 0.8	32.43 ± 13.7	0.35	1.09
345FC7	23.8 ± 2.0	8.80 ± 2.17	0.35	1.33
34FC7	24.2 ± 1.0	7.30 ± 1.46	0.36	1.29
CF3C10	27.8 ± 2.2	0.11 ± 0.03	0.36	1.54
345FC9	22.9 ± 1.6	11.07 ± 1.84	0.37	1.14

Table 7: Activation energies, and relaxation times at infinite temperature, room temperature and the nematic transition temperatures for all of the mixtures. * Pure host data.

It has been shown previously that most of the dopants speed up the relaxation behaviour of the host system, ZLI-4792 at the same absolute temperature. Table 7 shows that the activation energy of the relaxation process for most of the doped systems is higher than that for the pure host mixture. High values of the activation energy mean the relaxation

time is more strongly temperature dependent and the amount of energy required for the relaxation process is greater.

The three dopants which stand out from the rest and affect the relaxation behaviour most dramatically at room temperature are DFS33, PFC9 and 345FC9. All of which have lower activation energies than that of the pure host. The relaxation time at the nematic transition temperature for the DFS33 doped system is lower than that of the host while the values for the other two doped systems are higher, this is due to the fact that DFS33 does not affect the mesophase behaviour of the host, so the nematic transition temperature is close to the value for the host mixture. The PFC9 dopant lowers the nematic transition temperature by 19.3K to 346.5K and the 345FC9 dopant lowers T_N by 27.1K to 338.7K, it is at these temperatures that this relaxation time is calculated. At low shifted temperatures the dopants DFS33 and FC9 exhibit a reduction in the relaxation time and this combined with the unaffected order parameters indicates that these dopants are effective at fulfilling the objective of this research

4.8 Solubility Parameters

The solubility of some of the dopants has been calculated using a method described by K. Araya *et al.* [12]. This allows an approximation of how much of the dopant would be soluble in the host mixture at specified temperatures.

Differential Scanning Calorimetry (DSC) was performed on some of the dopants using a Hewlett Packard DSC 7 to enable the evaluation of the solubility of certain dopants in the host ZLI-4792. This is because the enthalpy of melting is needed for the solubility calculations. The values for the enthalpies of melting obtained from DSC are given in Table 8 along with the melting points which are also taken from the DSC traces. The dimensionless entropies were calculated using

$$\Delta S / R = \Delta H /(T_{mp} R). \qquad (8)$$

Compound	ΔH / Jg^{-1}	ΔH / $kJmol^{-1}$	ΔH / $calmol^{-1}$	T_{mp} / K	ΔS / R
345FC7	119.4	39.7	9478.7	332.3	14.4
345FC9	105.8	44.5	10631.1	322.4	16.6
24FC10	151.8	60.5	14455.8	334.5	21.8
34FC10	137.6	54.8	13103.6	312.0	21.1
23FC9	130.5	50.2	11989.5	335.2	18.0

Table 8: Values of the melting points, enthalpies of melting and dimensionless entropies for the listed dopants.

The solubility parameters of the dopants were calculated using the method described by Araya *et al.*[12], where the solubility parameter, δ, is defined as the square root of the cohesive energy density. Since the cohesive energy density is defined as the ratio of the molar enthalpy of vaporisation (ΔE) to the molar volume (V), δ can be written as

$$\delta = (\Delta E / V)^{1/2}. \tag{9}$$

The enthalpy and molar volume changes at the nematic liquid crystal-isotropic liquid transition are negligibly low compared with those of the nematic liquid crystal-solid transition [13,14] and so the solubility parameter defined in Equation (9) can be applied to a nematic liquid crystal as well as an isotropic liquid.

According to the Fedors method [15], ΔE and V can be estimated by assuming the additivity rules;

$$\Delta E = \sum \Delta e_i, \tag{10}$$

and

$$V = \sum \Delta v_i, \tag{11}$$

where Δe_i and Δv_i are the atomic and group contributions for the energy of vaporisation and molar volume, respectively. Table 9 gives values of Δe_i and Δv_i used to calculate the energy of vaporisation and the molar volume for the dopants; 345FC7, 345FC9, 24FC10, 34FC10 and 23FC9.

Atom or Group	Δe / **calmol^{-1}**	Δv / **cm^{3}mol^{-1}**
Phenyl	7630	71.4
Phenyl (Disubstituted)	7630	52.4
Phenyl (Trisubstituted)	7630	33.4
-CH_2-	1180	16.1
-O-	800	3.8
-F-	800	22.0

Table 9: Atomic and group contributions to energy of vaporisation and molar volume at 25°C.

Table 10 shows the calculated values of the solubility parameters, molar volumes and the energies of vaporization.

Compound	δ / $(calcm^{-3})^{1/2}$	ΔE / $calmol^{-1}$	V / cm^3mol^{-1}
ZLI-4792	9.00	/	307.6
345FC7	9.68	29920	319.1
345FC9	9.59	32280	351.3
24FC10	9.39	31860	361.4
34FC10	9.39	31860	361.4
23FC9	9.43	30680	345.3

Table 10: Solubility parameters, molar volumes and the energies of vaporization for the dopants.

This data along with the melting points, T_1, of the dopants and their associated enthalpies of melting, ΔH_1, have been used to calculate the mole fractions of the dopant soluble in ZLI-4792 at various temperatures using the Schröder-van Laar equation described by Araya *et al.*[12]

$$T = \frac{\Delta H + V_1\left(\left(1-x_1\right)V_2 / x_1V_1 + \left(1-x_1\right)V_2\right)^2\left(\delta_1-\delta_2\right)^2}{\left(\Delta H_1 / T_1\right) - R\ln x_1}, \qquad (12)$$

where V_1 and V_2 are the molar volumes of the dopant and the host, ZLI-4792, respectively, δ_1 and δ_2 are the solubility parameters for the dopant and host, respectively, where δ_2 for ZLI-4792 is 9.0$(cal / cm^3)^{1/2}$, and x_1 is the mole fraction of the solid dopant. From Equation (12) the temperatures at which the mole fractions are just completely soluble are calculated for all mole fractions of the solid solute from 0 to 1. These calculations were carried out for only five dopants in ZLI-4792, see Figure 65.

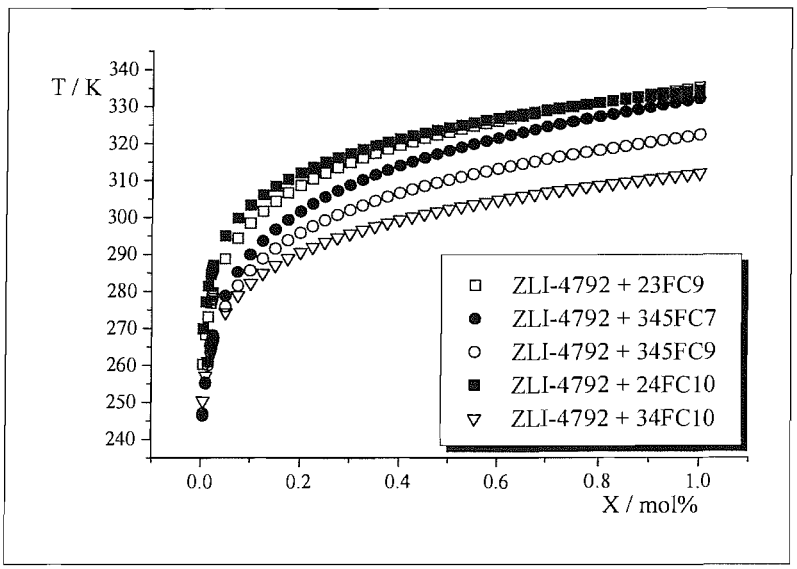

Figure 65: A plot of mole fraction vs. temperature for five doped systems.

Figure 65 shows that the mole fraction of dopant soluble in ZLI-4792 increases as the temperature increases. At low temperatures up to zero degrees (273.15K) the change in the mole fraction is small, and then at values above room temperature a sudden increase in mole fraction is observed. The temperature at which the start of this sharp increase is observed is dependent on the doped system. The 23FC9 and 24FC10 dopants are less soluble than the other three dopants when compared at the same temperature. The 24FC10 dopant is less soluble than the 34FC10 dopant, indicating a dopant with a substituent in the 2-position leads to worse solubility.

For the ESR experiments a molar fraction of 10wt% was used and the lowest temperature at which measurements were made was 305K. The plot shows for all five doped systems a mole fraction greater than 10wt% would be soluble at this temperature. According to the solubility calculations at 305K the 24FC10 dopant would be soluble up to 12.5wt%, the 23FC9 dopant would be soluble up to 15wt%, the 345FC7 dopant would be soluble up to 25wt%, the 345FC9 dopant would be soluble up to 37.5wt% and the 34FC10 would be soluble up to 60wt%.

4.9 Field-balance experiment to find the rotational viscosity

In order to calculate the rotational viscosity coefficient from the experimentally obtained relaxation times, the diamagnetic susceptibility must be known. Deuterium NMR can be used to obtain a value for $\Delta\tilde{\varepsilon}/\Delta\tilde{\chi}$ and from an independent experiment an accurate value of $\Delta\tilde{\varepsilon}$ can be obtained. These two experiments in combination lead to a value for $\Delta\tilde{\chi}$.

4.9.1 Background and theory of deuterium NMR

Deuterium NMR is analogous to ESR in that it allows the determination of the director orientation in a liquid crystal sample. The theoretical background to this technique is now described. Deuterium possesses a quadrupole moment due to the fact that it has a nuclear spin of one (I=1). This quadrupole moment interacts with the electric field gradient at the nucleus to produce a tensorial quadrupolar interaction. In an isotropic phase the deuterium NMR spectrum for a single deuteron contains just one line made up of a pair of degenerate transitions because of the rapid tumbling of the molecules averages this quadrupolar interaction to zero. However, in a nematic liquid crystal phase this degeneracy is removed due to the long range orientational order of the phase combined with the quadrupolar interaction of the deuterium nuclei. The deuterium NMR spectrum for a single deuteron in a monodomain nematic phase exhibits two equally intense lines which originate from the orientational order and quadrupolar interaction. The splitting between these two lines is

known as the quadrupolar splitting, $\Delta\tilde{\nu}$, which is dependent on the angle, β, made between the director and the magnetic field and is given by

$$\Delta\tilde{\nu}(\beta) = \Delta\tilde{\nu}_0 P_2(\cos\beta), \tag{13}$$

where $\Delta\tilde{\nu}_0$ is the splitting when the director is parallel to the magnetic field and $P_2(\cos\beta)$ is the second Legendre polynomial. As the director moves away from its equilibrium position parallel to the magnetic field (assuming $\Delta\tilde{\chi} > 0$) the quadrupolar splitting decreases until it passes through zero at the magic angle ($\beta = 54.74°$) and then it increases to a maximum value of one half of the original splitting, $\Delta\tilde{\nu}_0$, when the director is orthogonal to the magnetic field. Once the director has passed through the magic angle the quadrupolar splitting changes sign, however, this is not directly available from the spectrum. The major advantage of this type of NMR is that it monitors whether the director moves as a monodomain or not. When the director is not uniformly aligned the observed spectrum is a weighted sum of the spectra from all director orientations. In this respect this NMR technique is directly analogous to ESR experiments on liquid crystals. This sensitivity to the director orientation makes deuterium NMR a good experimental technique for investigating the response of the director to competing magnetic and electric fields.

4.9.2 Theory for the field-balance experiment

The nematic liquid crystal doped with a deuterated probe is uniformly aligned in a thin sandwich cell in a magnetic field, B. The electric field is then applied at some angle, α, to the magnetic field. The director will move towards the electric field and equilibrate at some angle, β, to the magnetic field which is dependent on the electric field strength, see Figure 66. If the electric field is strong enough β will become equal to α.

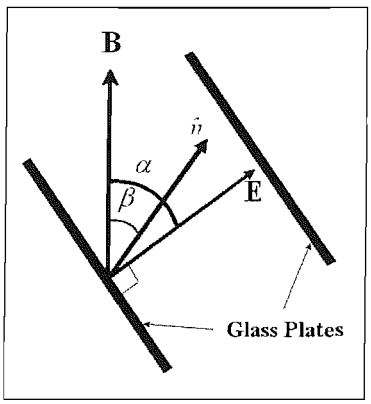

Figure 66: Experimental geometry for the field-balance experiment.

For a monodomain sample, ignoring surface anchoring effects, a Leslie-Ericksen based theory gives the time dependence of the director relaxation when the director is subject to both magnetic and electric fields.

The rate of change of the director orientation for the turn-on process is then given by the torque-balance equation [16]

$$\gamma_1 \frac{d\beta(t)}{dt} = -\frac{\Delta\tilde{\chi}}{2\mu_0} B^2 sin2\beta(t) + \frac{\varepsilon_0 \Delta\tilde{\varepsilon}}{2} E^2 sin2(\alpha - \beta(t)), \tag{14}$$

where ε_0 is the dielectric permittivity of a vacuum. The solution to this equation is obtained analytically as [17]

$$\beta(t) = \beta_\infty + tan^{-1}[tan(\beta_0 - \beta_\infty) exp(-t/\tau)], \tag{15}$$

where β_0 is the initial angle, τ is the relaxation time and β_∞ is the limiting value of $\beta(t)$ when t tends to infinity and is given by

$$cos2\beta_\infty = \frac{1 + \rho cos 2\alpha}{(1 + 2\rho cos 2\alpha + \rho^2)^{1/2}}, \tag{16}$$

where ρ is given by the ratio of the magnetic and electric anisotropic energies, U_M and U_E, respectively. These are given by

$$U_M = \frac{\Delta\tilde{\chi}}{2\mu_0} B^2, \tag{17}$$

and

$$U_E = \frac{\varepsilon_0 \Delta\tilde{\varepsilon}}{2} E^2, \tag{18}$$

and so

$$\rho = \frac{U_E}{U_M} = \mu_0 \varepsilon_0 \left(\frac{E}{B}\right)^2 \left(\frac{\Delta\tilde{\varepsilon}}{\Delta\tilde{\chi}}\right). \tag{19}$$

From Equations (16) and (19) it is clear that the limiting value of the director orientation depends on the material property $\Delta\tilde{\varepsilon}/\Delta\tilde{\chi}$, as well as the experimental parameters E/B and α. Figure 67 illustrates the dependence of the limiting values of the director orientation, β_∞, on ρ for varying values of α. This dependence becomes stronger on increasing the angle between the two fields. The limiting values of the director orientation do not exactly match the values of α because the value of ρ is insufficient to align the director parallel to the electric field. An analogous variation with ρ is observed for the quadrupolar splitting due to the relationship between this splitting and the director orientation, see Equation (13).

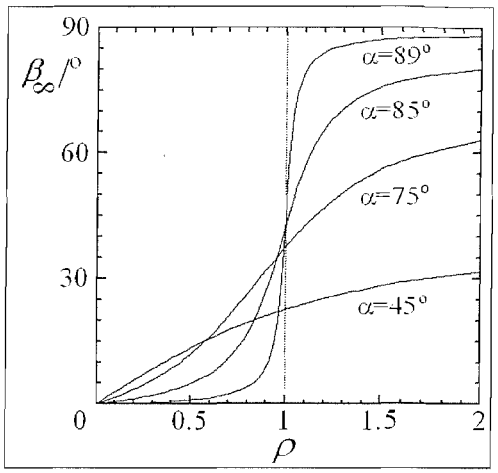

Figure 67: A plot showing the limiting value of the director orientation, β_∞, vs. ρ for various values of α.

4.9.3 Variable temperature ^2H NMR for ZLI-4792 and ZLI-4792 + 10wt% C7

The experimental work in this section was carried out by Azizah Mainal of Southampton University.

In this experiment p-xylene-d_{10} was used as a probe molecule which is orientationally ordered by the host mixture ZLI-4792. Work by Emsley *et al.*[18] on the orientational order of p-xylene-d_{10} dissolved in a series of 4-alkyloxy-4'-cyanobiphenyls has shown that the orientational order of the guest molecule reflects that of the host. So, by analogy to the ESR experiment, the information obtained from the probe can be assumed to parallel that of the liquid crystal host itself. This probe, p-xylene-d_{10}, was chosen as it gives a well resolved NMR spectrum and it is commercially available. The molecular structure of p-xylene-d_{10} is shown in Figure 68 along with its symmetry axes.

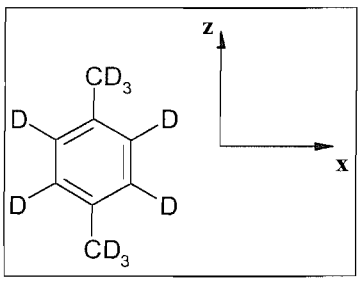

Figure 68: Molecular structure of p-xylene-d_{10} with its symmetry axes.

The reason for this variable temperature experiment was to test the signal-to-noise ratio of the sample and to determine the temperature dependence of the quadrupolar splittings. The samples of 4wt% p-xylene-d_{10} in ZLI-4792 and ZLI-4792 + 10wt% C7 were made and inserted into a 3.5cm length of a 5mm outer diameter and 4mm inner diameter NMR glass tube. A Teflon vortex plug was used to prevent the sample from escaping. The sample was

placed in the probe of the NMR spectrometer. The deuterium NMR (^{2}H NMR) measurements were performed on a Varian Infinity Plus 300 spectrometer with SPINSIGHT software for data acquisition and processing, using the Solaris Operating Environment on a SUN microsystem workstation. The temperature was controlled using a thermocouple in the probe head connected to a Varian temperature control unit. The accuracy of this unit is ±0.1K. The ^{2}H NMR spectra of this probe in ZLI-4792 contain two pairs of peaks, see Figure 69. The peaks have the lineshape of absorption in contrast to ESR where the first derivative lineshapes are observed. The outer two peaks correspond to methyl deuterons whilst the inner two peaks correspond to the aromatic deuterons. This assignment can be determined from the integration of each set of respective peaks with the ratio of the areas under the peaks equivalent to 6:4. The fine splittings of the peaks due to dipolar couplings between neighbouring deuterons confirm this assignment. The splitting of the outer two peaks results from the dipolar couplings of the three deuterons of the methyl group and the splitting of the inner peaks results from the dipolar couplings of the nearest two deuterons on the aromatic ring.

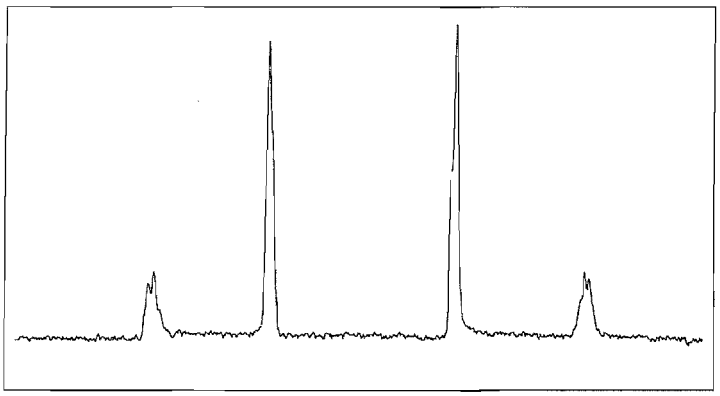

Figure 69: ^{2}H NMR spectrum of 4wt% p-xylene-d_{10} in ZLI-4792 at 298K.

A selection of spectra from the variable temperature experiment on ZLI-4792 are shown in Figure 70 and a plot of the variation of the quadrupolar splittings with temperature is shown in Figure 71. As the temperature is decreased the quadrupolar splitting increases as does the intensity of the spectral lines. The quadrupolar splitting associated with the methyl deuterons is related to the orientational order according to [19]

$$-\Delta\tilde{\nu}_{Me} = \frac{3}{4} q_{CD}^{Me} S_{zz} \left(3\cos^2\xi - 1\right), \tag{20}$$

where q_{CD}^{Me} is the quadrupolar coupling constant for the methyl deuterons and is equal to 168kHz, S_{zz} is the orientational order parameter of the z-axis and ξ is the angle between the C-D bonds (in the CD_3 group) and the z-direction, which is 70.5° assuming a tetrahedral

geometry. The quadrupolar splitting associated with the aromatic deuterons is related to the orientational order according to [19]

$$\Delta\tilde{\nu}_{Ar} = \frac{3}{4} q_{CD}^{Ar}\left[S_{zz}\left(3\cos^2\phi - 1\right) + \left(S_{xx} - S_{yy}\right)\sin^2\phi\right], \tag{21}$$

where q_{CD}^{Ar} is the quadrupolar coupling constant for the aromatic deuterons and is equal to 186kHz, ϕ is the angle made between the aromatic C-D bonds and the z-direction, which is 60° assuming a regular hexagonal structure and S_{xx} and S_{yy} are the orientational order parameters of the x-axis and y-axis, respectively and therefore (S_{xx}- S_{yy}) is the biaxial order parameter.

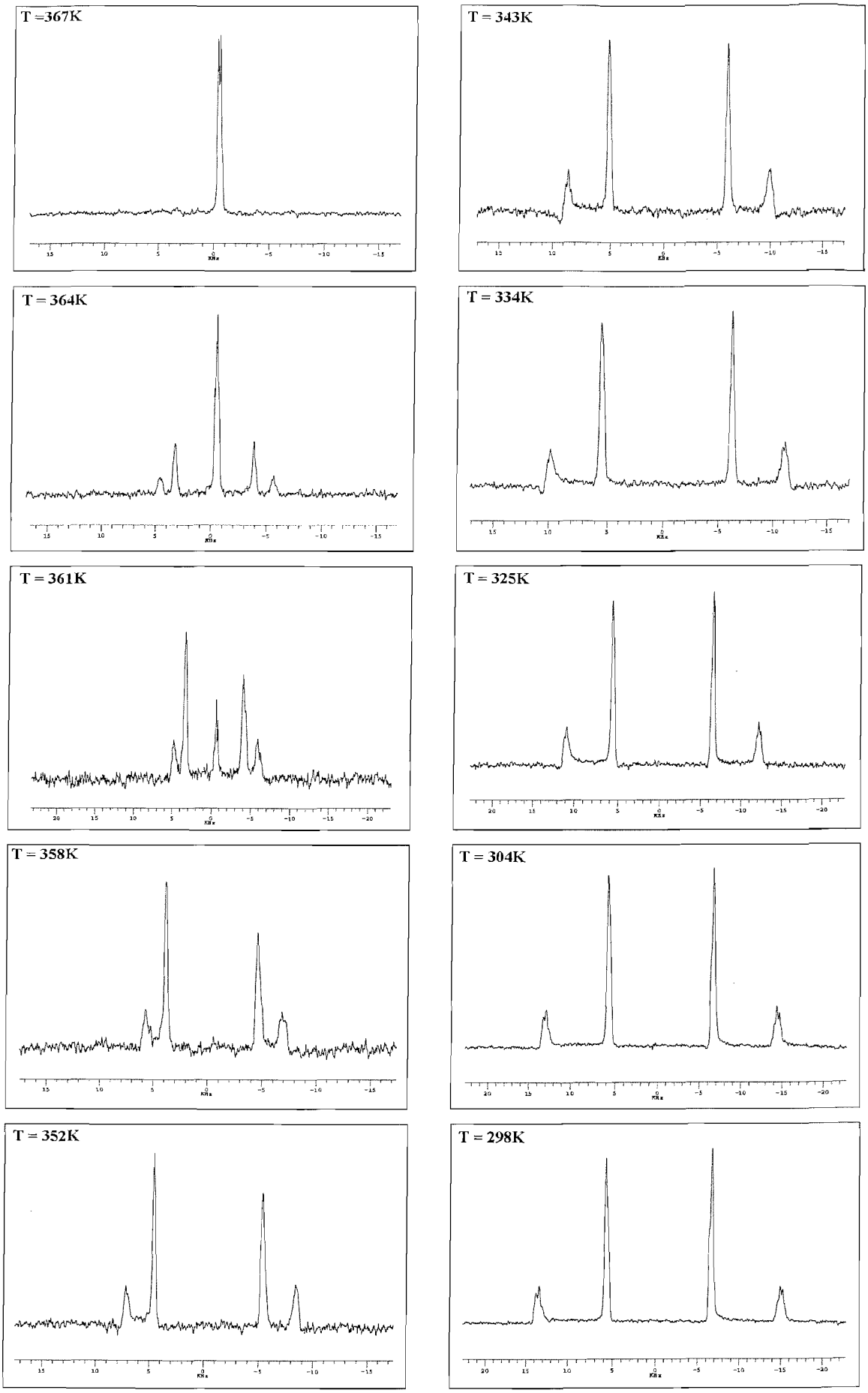

Figure 70: Variable temperature ^{2}H NMR for 4wt% p-xylene-d_{10} in ZLI-4792 on cooling from the isotropic.

The first spectrum in Figure 70 shows that the system is isotropic at 367K and as the temperature is decreased two sets of peaks start to appear indicating the system has become biphasic. On lowering the temperature further these peaks grow in intensity and the isotropic peak decreases in intensity as more nematic phase forms. At 358K the system has become fully nematic. The quadrupolar splittings remain constant in the biphasic region but in the nematic phase they increase on decreasing the temperature indicating an increase in the orientational order of the probe. From Figure 71 it is clear that the splittings of the methyl deuterons are affected to a greater extent than the splittings for the aromatic deuterons on decreasing the temperature.

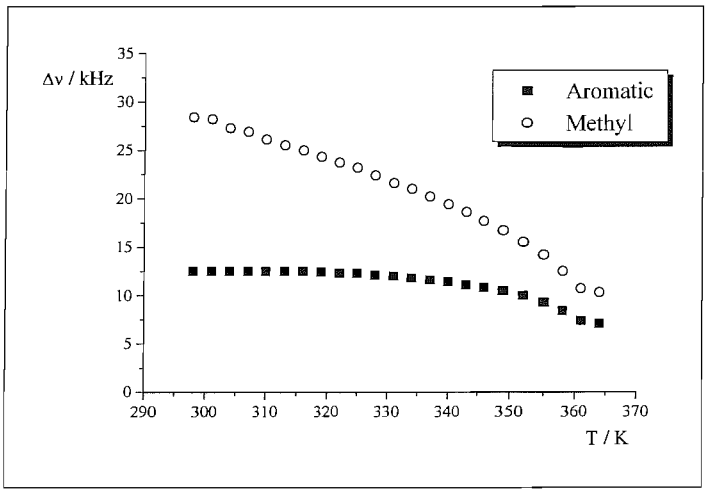

Figure 71: Plot showing the variation of the quadrupolar splittings with temperature for 4wt% p-xylene-d_{10} in ZLI-4792.

As the sample is cooled through the biphasic region something unusual is observed in the spectrum; the outer doublet starts to spread out and the quadrupolar splittings of both sets of doublets increase. This phenomenon has been observed previously and is due to the formation of a concentration gradient as the sample is cooled from the isotropic phase [20]. On cooling through the biphasic region droplets of nematic form, drop to the bottom of the sample and coalesce to form a layer of nematic phase and as the rate of molecular diffusion is slow in comparison to the experimental timescale the sample ends with several layers of nematic phase all with different concentrations.

The addition of p-xylene-d_{10} lowers the transition temperatures of the systems slightly, see Table 11.

System	T_N / K Polarising microscopy	T_I / K Polarising microscopy	T_N / K ^{2}H NMR	T_I / K ^{2}H NMR
ZLI-4792	366.0	373.5	/	/
ZLI-4792 + 4wt% p-xylene-d_{10}	358.0	365.8	361.2	367.2
ZLI-4792 + 10wt% C7	335.6	346.5	/	/
ZLI-4792 + 4wt% p-xylene-d_{10} + 10wt% C7	332.6	343.7	330.2	349.2

Table 11: Transition temperatures for ZLI-4792 + 4wt% p-xylene-d_{10} and ZLI-4792 + 4wt% p-xylene-d_{10} + 10wt% C7 obtained from polarising microscopy and ^{2}H NMR.

The transition temperatures obtained from the ^{2}H NMR experiments differ from the values measured using polarising microscopy. This is due to the different temperature control units used, which are calibrated separately. The orientational order parameters for 4wt% p-xylene-d_{10} in ZLI-4792 have been calculated and Figure 72 shows the variation with temperature.

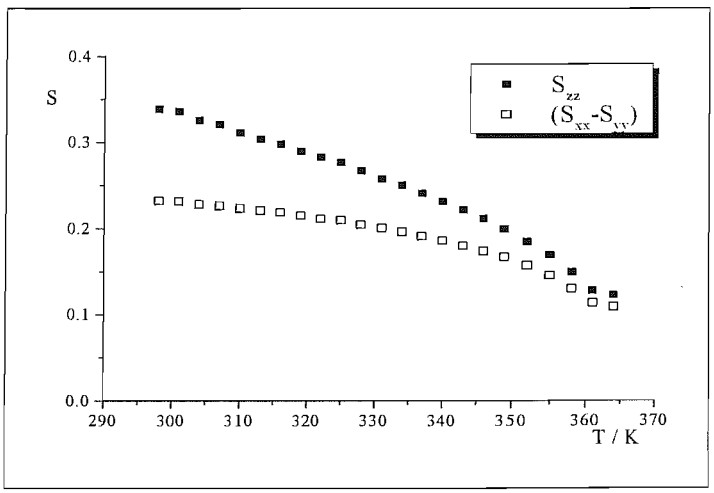

Figure 72: Plot showing the variation of the orientational order parameter with temperature for 4wt% p-xylene-d_{10} in ZLI-4792.

The orientational order increases on decreasing the temperature and the orientational order of the z-axis, S_{zz}, being larger than biaxial orientational order parameter, (S_{xx}- S_{yy}).

The order parameter S_{zz} is larger than the biaxial order parameter because it is the order parameter of the long axis of the probe. The value of S_{zz} at room temperature is ~0.35 which is indicative of the nematic phase.

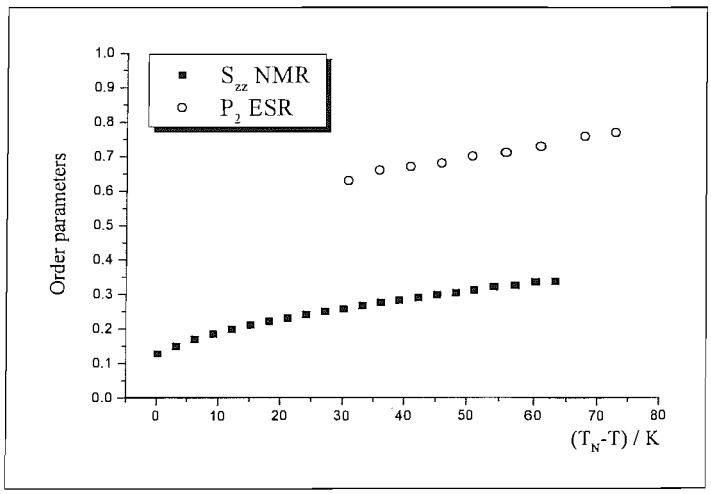

Figure 73: Comparison of the orientational order parameters S_{ZZ} and $\overline{P_2}$ from ^{2}H NMR and ESR respectively for 4wt% p-xylene-d_{10} in ZLI-4792.

The orientational order parameter S_{zz} is much lower than the order parameter $\overline{P_2}$ because p-xylene-d_{10} is a much smaller molecule, and hence less anisotropic, than cholestane. Therefore, cholestane is more ordered by the nematic phase than p-xylene-d_{10}.
The resultant spectra from the variable temperature experiment on ZLI-4792 + 10wt% C7 are shown in Figure 74 and a plot of the variation of the quadrupolar splitting with temperature is shown in Figure 75. As the temperature is decreased from the isotropic phase at 350K two sets of peaks begin to appear at 348K indicating the start of the biphasic region in which isotropic and nematic phases coexist. These peaks increase in intensity as the temperature is lowered further until the isotropic peak has vanished and the system is completely nematic at 328K. Again the line broadening observed is due to the formation of a concentration gradient [20]. This broadening is particularly apparent in the spectrum at 330K.

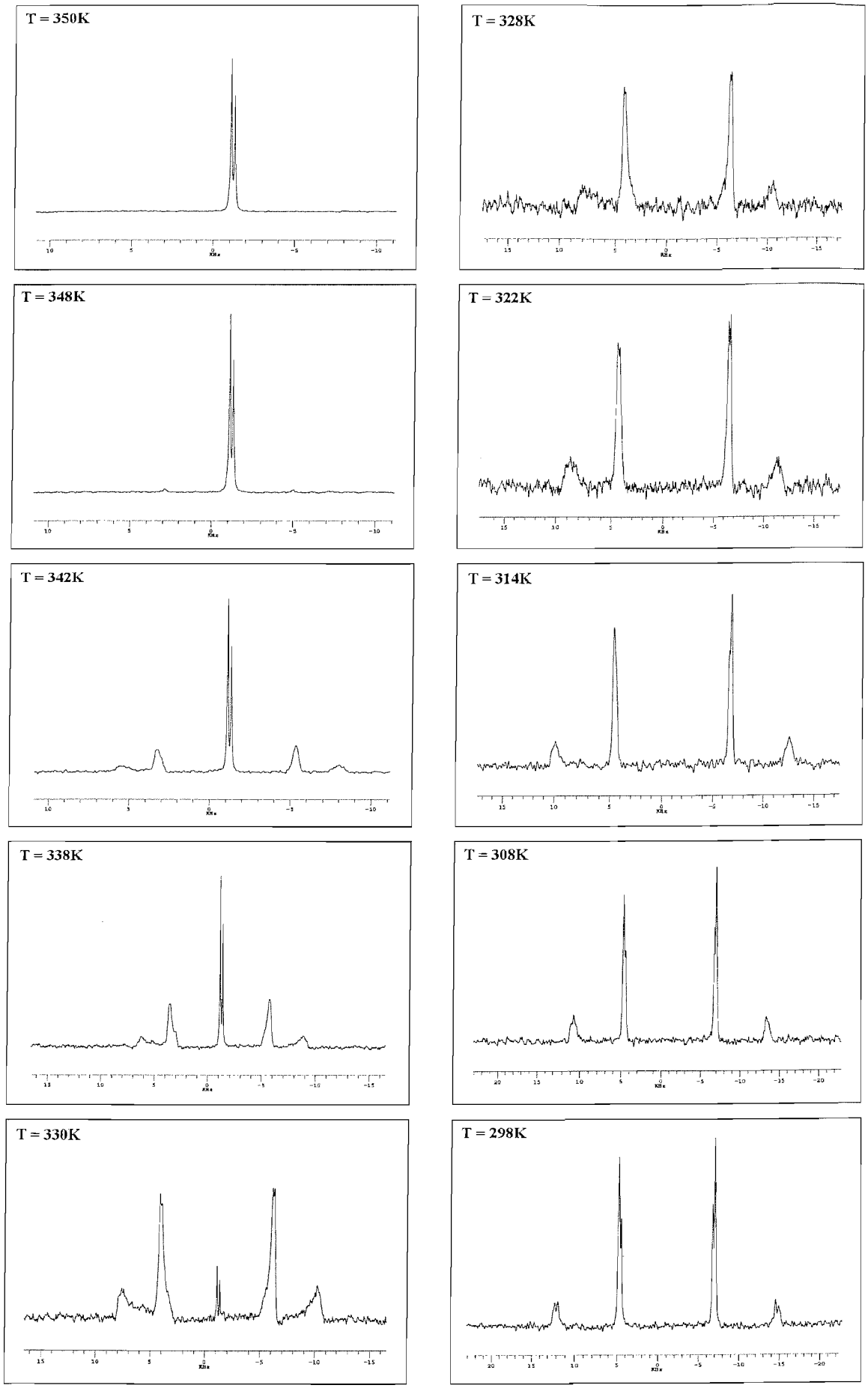

Figure 74: Variable temperature ^{2}H NMR for 4wt% p-xylene-d_{10} in ZLI-4792 + 10wt% C7.

From Figure 75 it is clear that the splittings of the methyl deuterons are affected to a greater extent than the splittings for the aromatic deuterons on decreasing the temperature.

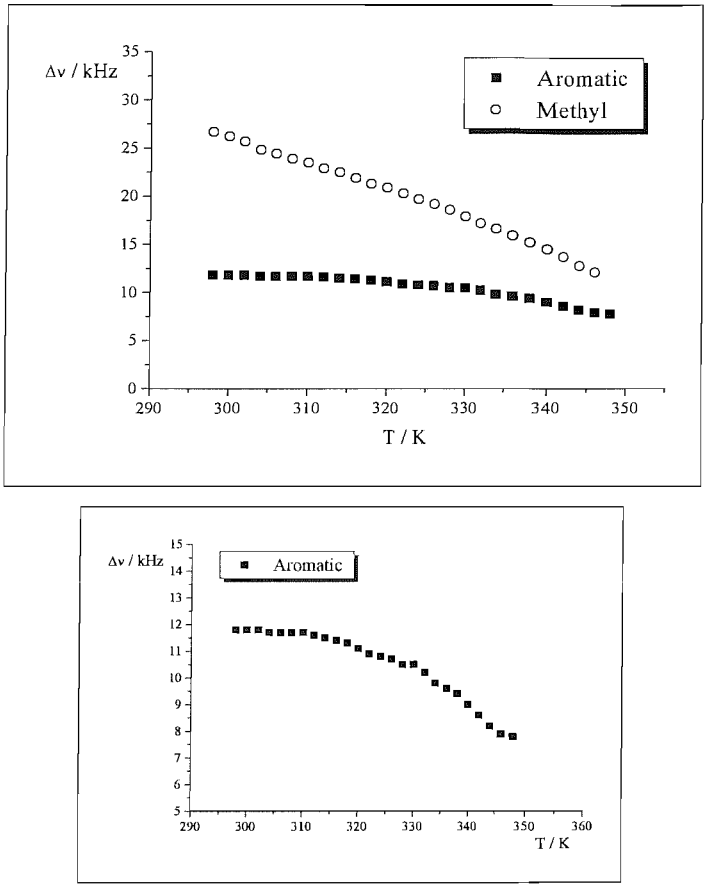

Figure 75: Plots showing the variation of the quadrupolar splittings with temperature for 4wt% p-xylene-d_{10} in ZLI-4792 +10wt% C7.

The orientational order parameters for 4wt% p-xylene-d_{10} in ZLI-4792 have been calculated and Figure 76 shows the variation with temperature.

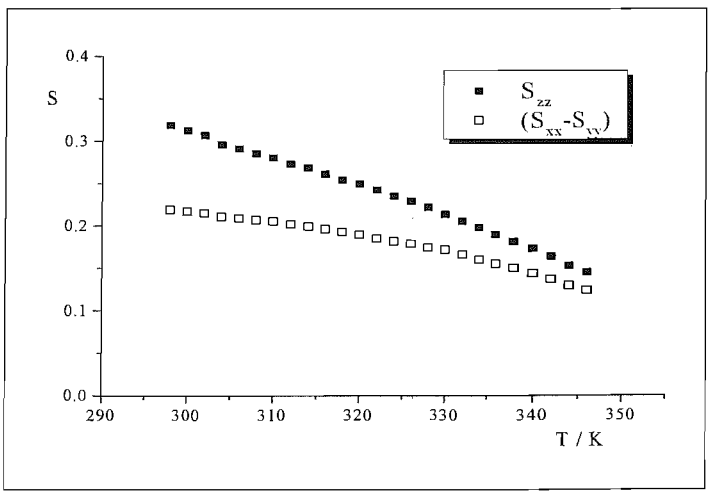

Figure 76: Plot showing the variation of the orientational order parameter with temperature for 4wt% p-xylene-d_{10} in ZLI-4792 + 10wt% C7.

The orientational order increases on decreasing the temperature and the orientational order of the z-axis, S_{zz}, being larger than biaxial orientational order parameter, $(S_{xx}- S_{yy})$. The order parameter S_{zz} is larger than the biaxial order parameter because it is the order parameter of the long axis of the probe. The value of S_{zz} at room temperature is ~0.32 which is indicative of the nematic phase.

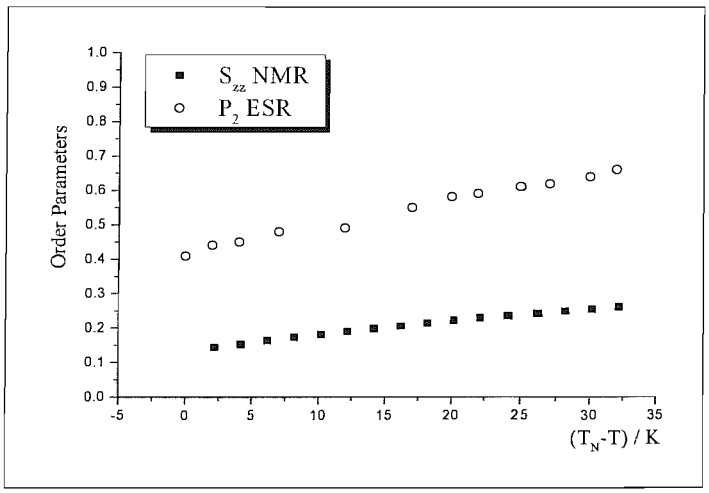

Figure 77: Comparison of the orientational order parameters S_{ZZ} and $\overline{P}_2$ from ^{2}H NMR and ESR respectively for 4wt% p-xylene-d_{10} in ZLI-4792 + 10wt% C7.

The orientational order parameter S_{zz} is much lower than the order parameter $\overline{P}_2$ because p-xylene-d_{10} is a much smaller molecule, and hence less anisotropic, than cholestane. Therefore, cholestane is more ordered by the nematic phase than p-xylene-d_{10}.
The quadrupolar splittings compared on the shifted temperature scale for both of the systems ZLI-4792 and ZLI-4792 + 10wt% C7 are shown in Figure 78. The nematic transition temperatures used in the calculations of the shifted temperatures are the ones obtained from the NMR experiments and not polarising microscopy. When compared at the same shifted temperature the mixture doped with the C7 dopant has larger splittings than for the pure host mixture, ZLI-4792, indicating that it has larger orientational order than the pure host at the same shifted temperature. However, when compared at the same absolute temperature the quadrupolar splittings and hence the orientational order for 4wt% p-xylene-d_{10} in ZLI-4792 are larger than the doped ZLI-4792, see Figure 79.

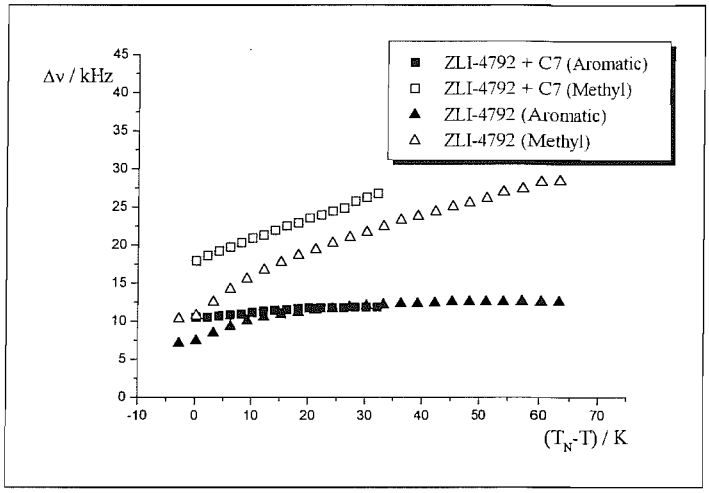

Figure 78: Plot showing the variation of the quadrupolar splittings with shifted temperatures for 4wt% p-xylene in ZLI-4792 and ZLI-4792 + 10wt% C7.

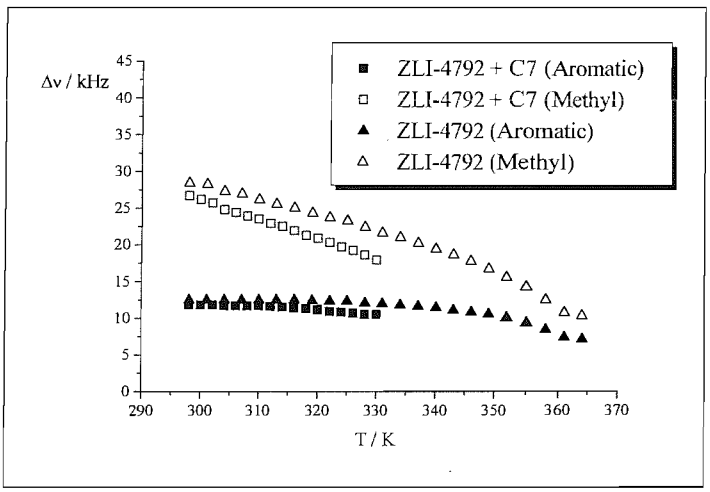

Figure 79: Comparison of the quadrupolar splittings for 4wt% p-xylene-d_{10} in ZLI-4792 and ZLI-4792 + 10wt% C7 on the absolute temperature scale.

4.9.4 Determination of $\Delta\tilde{\varepsilon}/\Delta\tilde{\chi}$ and γ_1 for 4wt% p-xylene-d_{10} in ZLI-4792 from the static field-balance experiment

The experimental work in this section was carried out by Professor A. Sugimura and his research group from the Osaka Sangyo University in Japan.

This experiment is the static field-balance experiment to determine $\Delta\tilde{\varepsilon}/\Delta\tilde{\chi}$ and α. This angle, α could be determined directly from a goiniometer, however, the value obtained is not very accurate. A uniformly aligned sample of 4wt% p-xylene in ZLI-4792 in a thin sandwich cell of thickness, $d = 97\mu m$ placed in a magnetic field is subjected to an electric field of varying strength at an angle close to 90° to the magnetic field. The spectra are then recorded when the director has realigned at some angle, β, to the magnetic field which is dependent on the voltage applied. The results for this system at 293K using a frequency of 5kHz for the electric field are shown in Figure 80. The splittings from the aromatic

deuterons are used in the following calculations. The splitting at 0V is the splitting when the director is parallel to the magnetic field and is $\Delta\tilde{\nu}_0$. As the voltage is increased the quadrupolar splitting is seen to decrease until at 85V the splitting has almost reached zero indicating that β is almost at the magic angle of 54.74°. After this, the splitting is seen to increase until a voltage of 130V when the director is almost parallel to the electric field and the splitting associated with this voltage is approximately half that of $\Delta\tilde{\nu}_0$, this only applies for values of α close to 90°.

The angle between the electric and magnetic fields, α, is an important parameter in investigating the director orientation and the precise value of this angle is determined from this static experiment. A combination of Equations (13) and (16) gives

$$g\left(\Delta\tilde{\nu}/\Delta\tilde{\nu}_0\right)=\frac{1}{a\sin 2\alpha}\cdot\frac{1}{V^2}+\cot 2\alpha, \tag{22}$$

where

$$g\left(\Delta\tilde{\nu}/\Delta\tilde{\nu}_0\right)=\frac{4\left(\Delta\tilde{\nu}/\Delta\tilde{\nu}_0\right)-1}{2\sqrt{\left[2-2\left(\Delta\tilde{\nu}/\Delta\tilde{\nu}_0\right)\right]\left[1+2\left(\Delta\tilde{\nu}/\Delta\tilde{\nu}_0\right)\right]}}, \tag{23}$$

and

$$a=\frac{\mu_0\varepsilon_0}{B^2d^2}\left(\frac{\Delta\tilde{\varepsilon}}{\Delta\tilde{\chi}}\right). \tag{24}$$

The function $g\left(\Delta\tilde{\nu}/\Delta\tilde{\nu}_0\right)$ is found to be linear in $\frac{1}{V^2}$ with the slope equal to $\frac{1}{a\sin 2\alpha}$ and the intercept equal to $\cot 2\alpha$, and hence $\Delta\tilde{\varepsilon}/\Delta\tilde{\chi}$ can be determined by a linear least squares fit of the experimental NMR data to Equation (22).

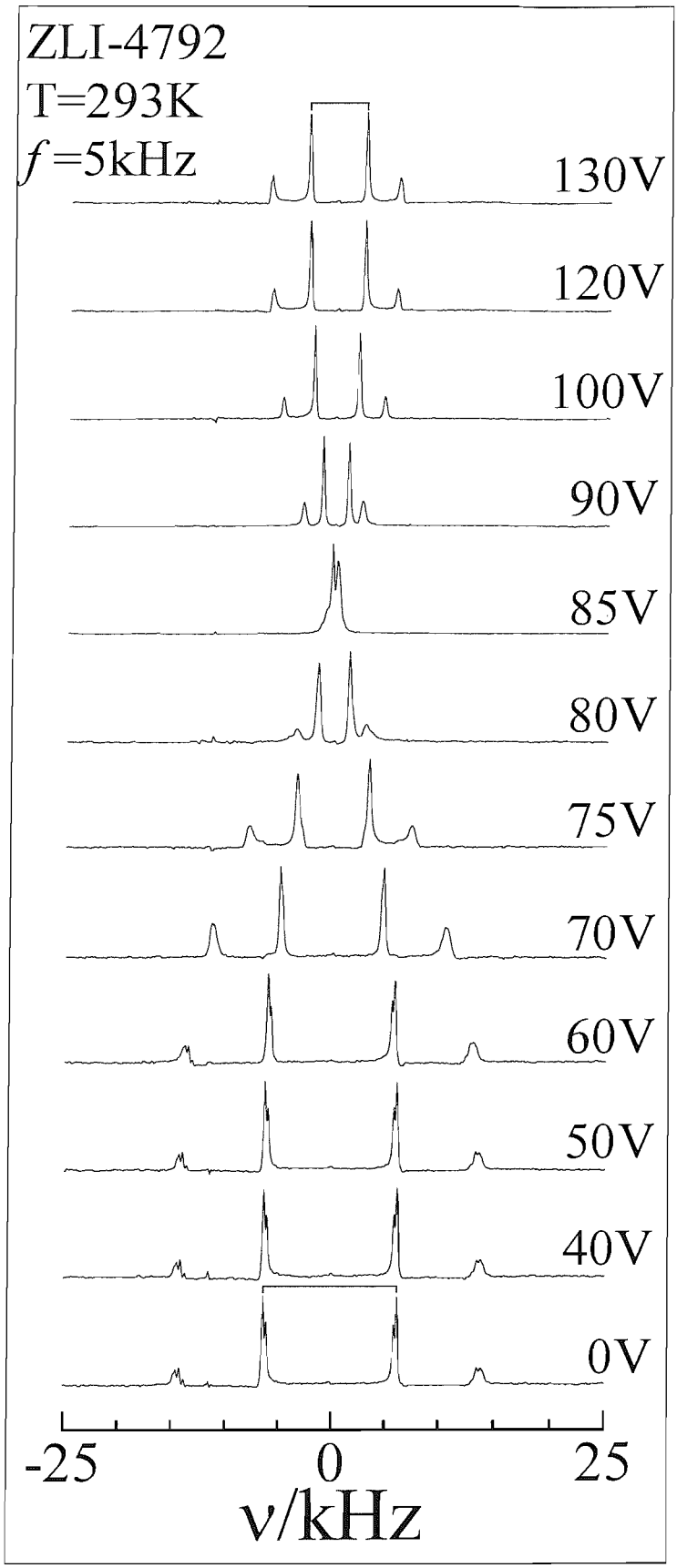

Figure 80: ^{2}H NMR spectra from the static field-balance experiment for 4wt% p-xylene-d_{10} in ZLI-4792.

The least squares fit of the experimental NMR data to Equation (22) is shown in Figure 81.

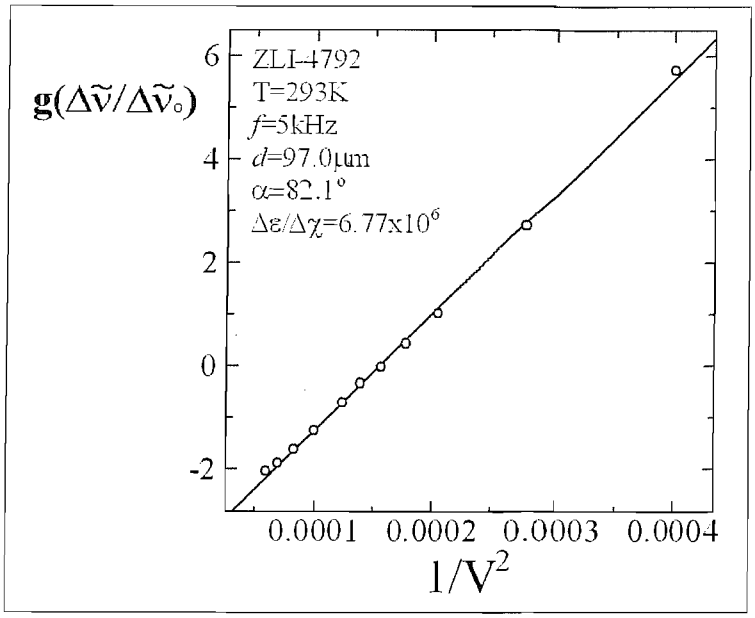

Figure 81: Linear least squares fit of the experimental data to Equation (16) for 4wt% p-xylene-d_{10}.

The voltage dependence of $(\Delta\tilde{\nu}/\Delta\tilde{\nu}_0)$ for the experimental geometry of $\alpha = 82.1°$ is shown in Figure 82. The solid line shows the prediction for values of $\Delta\tilde{\varepsilon}/\Delta\tilde{\chi}$ and α determined from the linear plot in Figure 81.

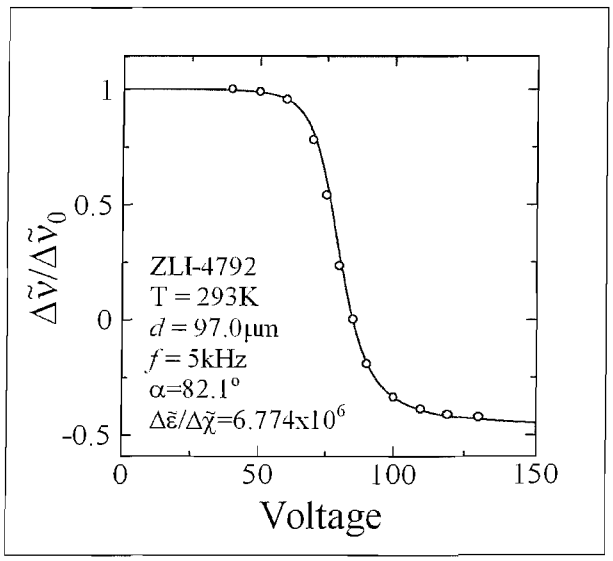

Figure 82: The voltage dependence of $\Delta\tilde{\nu}/\Delta\tilde{\nu}_0$ for the experimental geometry of $\alpha = 82.1°$.

The value of $\Delta\tilde{\varepsilon}/\Delta\tilde{\chi}$ was found to be 6.77×10^6 with an error of approximately 0.04×10^6 [21] and the value of $\alpha = 82.1°$. The diamagnetic susceptibility anisotropy at 293K for ZLI-4792 can now be determined using values of the dielectric anisotropies for ZLI-4792 supplied by Merck, which are given in Table 12. These are plotted in Figure 83 and the values for the dielectric anisotropy in Table 13 are interpolated values. The assumption that the relationship between the dielectric anisotropy and the temperature is linear in this range

is acceptable as the highest temperature (333K) is 33K below the nematic transition temperature.

Temperature / K	$\Delta\tilde{\varepsilon}$
273	6.1
293	5.3
298	5.1
333	3.8

Table 12: Values of the dielectric anisotropy for ZLI-4792, supplied by Merck.

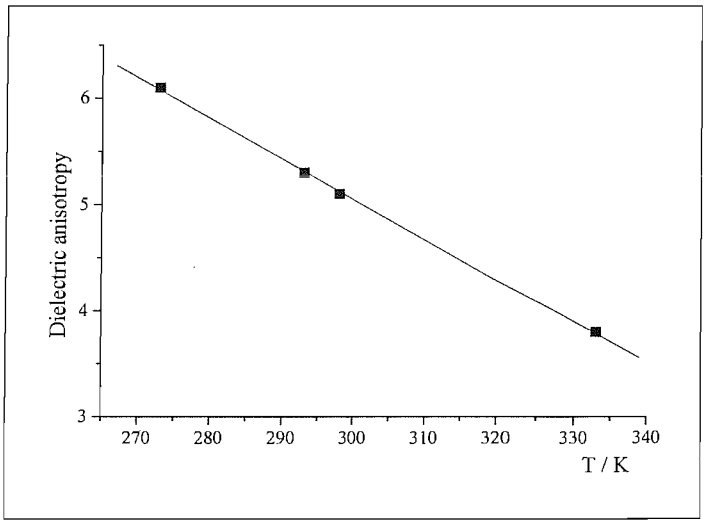

Figure 83: Plot of dielectric anisotropy, $\Delta\tilde{\varepsilon}$, vs. temperature for ZLI-4792.

Assuming that the ratio of $\Delta\tilde{\varepsilon}/\Delta\tilde{\chi}$ is temperature independent as found for other nematics [22], the values of the diamagnetic susceptibility at various temperatures can be calculated. The rotational viscosities for ZLI-4792 at various temperatures can also be calculated from the relaxation times obtained by the dynamic ESR experiments and the calculated values of the diamagnetic susceptibilities using

$$\gamma_1 = \frac{\tau \Delta\tilde{\chi} B^2}{\mu_0}. \qquad (25)$$

The assumption that the probe, p-xylene-d_{10}, does not affect the dynamic behaviour of the host has also been made.

Temperature / K	$\Delta\tilde{\varepsilon}$	$\Delta\tilde{\chi}$ x10^{-7}	τ / s	Centre Field, B / T	γ_1 / mPas
293	5.20	7.68	1.82	0.3335	124
298	5.12	7.56	1.49	0.3335	100
305	4.86	7.18	1.07	0.3335	68
310	4.67	6.90	0.93	0.3335	57
315	4.48	6.62	0.80	0.3335	47
320	4.28	6.32	0.68	0.3335	38
325	4.09	6.04	0.62	0.3335	33
330	3.90	5.76	0.54	0.3336	28

Table 13: Values of the dielectric anisotropy, relaxation times and magnetic flux and the calculated values of the diamagnetic susceptibility and rotational viscosity at various temperatures for ZLI-4792.

The value of 124 mPas for the rotational viscosity at 293K is in good agreement with the value of 133mPas supplied by Merck.

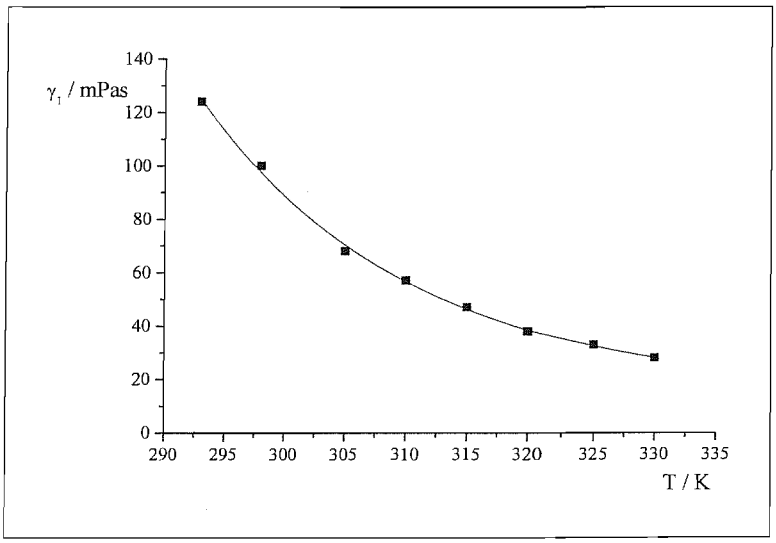

Figure 84: Plot of the rotational viscosity vs. temperature for ZLI-4792.

Figure 85 shows the exponential behaviour of the rotational viscosity. The orientational order parameter has been accounted for by dividing the rotational viscosity with the quadrupolar splitting from the methyl deuterons $(\gamma_1 / \Delta\tilde{\nu}_{Me})$.

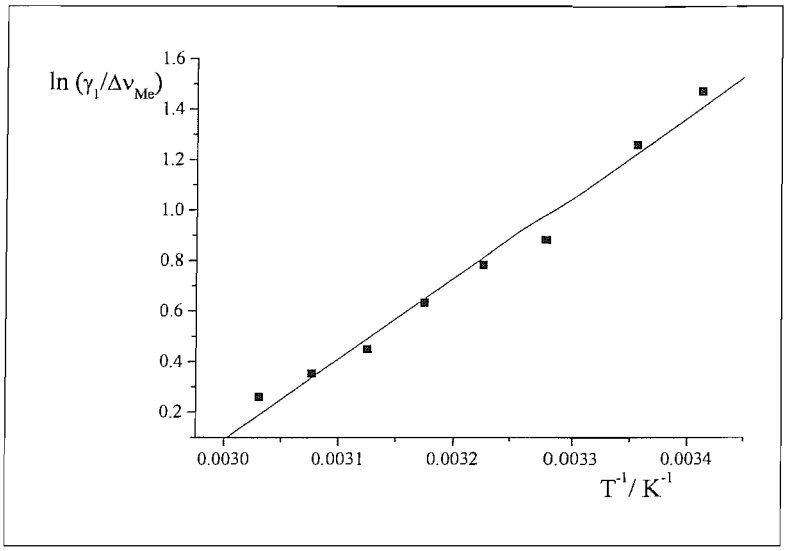

Figure 85: A plot showing the exponential behaviour of the rotational viscosity.

4.9.5 Determination of the relaxation time from the time-averaged experiments for 4wt% p-xylene-d_{10} in ZLI-4792

This experiment allows the determination of the field-induced relaxation time for the turn-on process. The nematic cell was placed in the NMR probe with the same geometrical setup as in Section 4.9.2. The angle between the electric and magnetic field of $\alpha = 82.1°$ was measured in the static experiment. The sample temperature was set to 293K. A sinusoidal electric field, see Figure 86, of 78.8V was applied continuously to the sample and the director oscillates uniformly between the electric and magnetic fields [23].

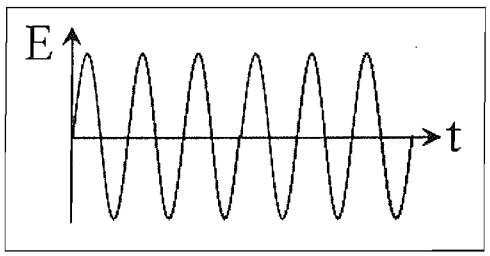

Figure 86: Sinusoidal electric field.

With a sinusoidal electric field the E^2 in Equation (14) has to be replaced by

$$E(t^*)^2 = E_0^2 \sin^2 2\pi f^* t^*, \tag{26}$$

where f is the frequency of the sinusoidal field. The torque-balance equation can then be rewritten in terms of scaled coordinates as

$$\frac{d\beta}{dt^*} = -\frac{1}{2}\sin 2\beta + (\rho/2)\sin^2(2\pi f^* t^*) \times \sin 2(\alpha - \beta). \tag{27}$$

The scaled time coordinate is given by

$$t^* = t / \tau_M, \tag{28}$$

where τ_M is the magnetic relaxation time. The scaled frequency is

$$f^* = f / \tau_M^{-1}. \tag{29}$$

For a given value of α the time dependence of the director orientation will be determined by ρ and the scaled frequency. This dependence was obtained by numerically solving the torque balance equation. The results of these calculations are shown in Figure 87 for α=44.7°. At too high frequencies the director does not oscillate because the field varies too rapidly for the director to follow see Figure 87, but at lower frequencies the director oscillates uniformly [23].

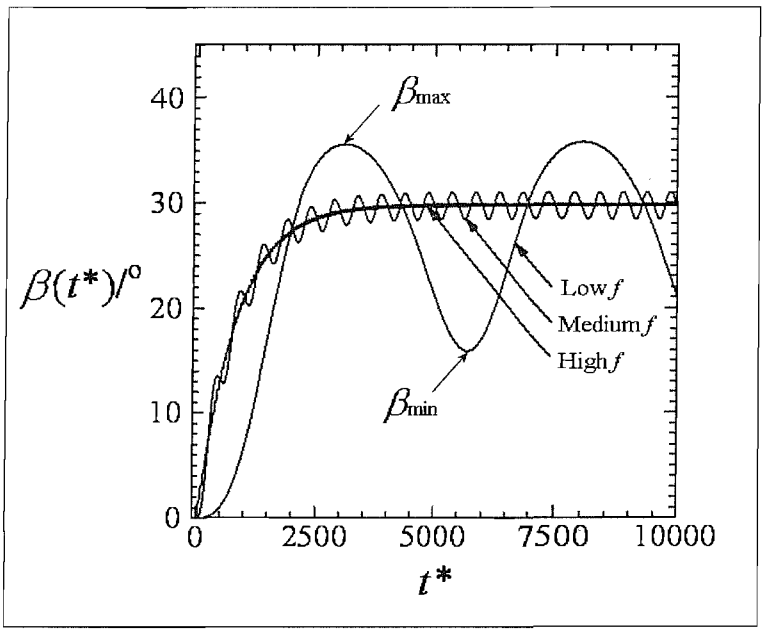

Figure 87: Variation of the director orientation with the scaled time as a function of frequency for α = 44.7°.

The acquired spectrum is a time averaged and so samples all points including β_{max} and β_{min}. From the time averaged spectra limiting values of β_{max} and β_{min} can be obtained for different frequencies, see Figure 88. These limiting values of β_{max} and β_{min} for the range of frequencies are then plotted as indicated by the open and closed circles in Figure 89. A fit to this data then results in a value for the magnetic relaxation time for the system.

It is clear from Figure 88 that at low frequencies the director is oscillating between β_{max} and β_{min} and the resultant spectra are the time averaged spectra of all orientations. As the frequency is increased the angle the director makes with the magnetic field increases indicated by the reduction in the quadrupolar splittings. At 500 Hz, the frequency is high enough so, the director does not oscillate but is just orientated parallel to the electric field.

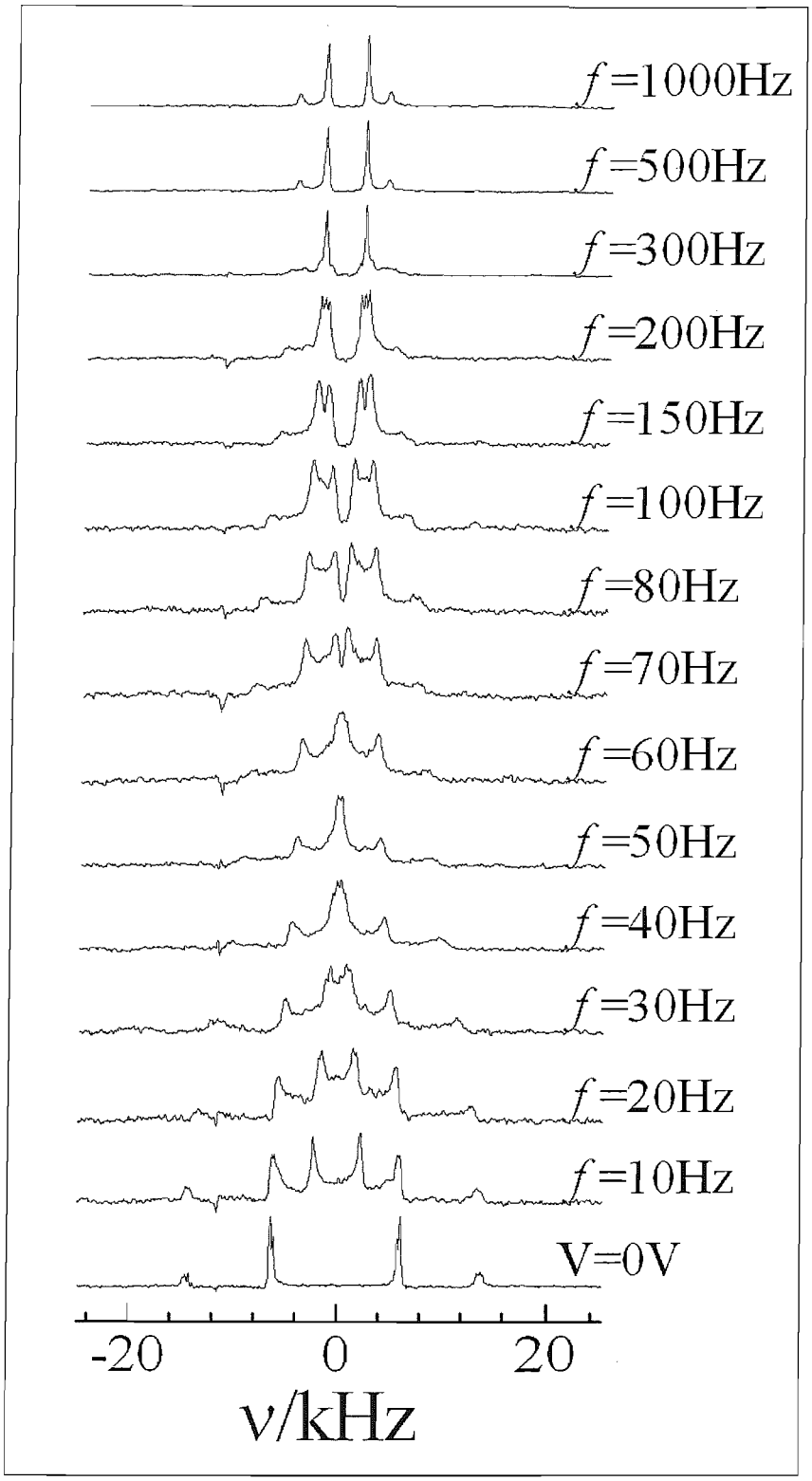

Figure 88: Time-averaged spectra at different frequencies for 4wt% p-xylene-d_{10} in ZLI-4792.

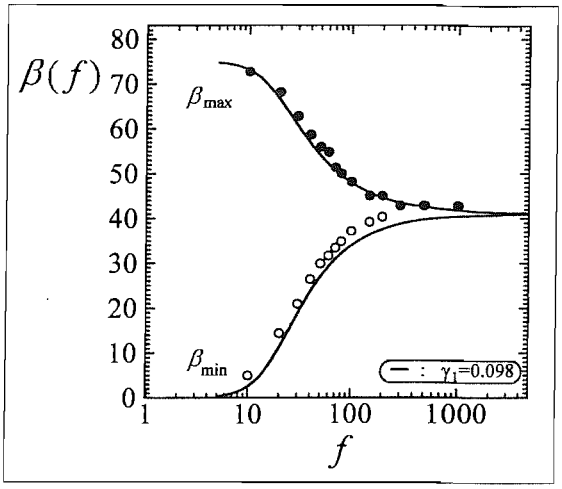

Figure 89: Variation of the extreme director orientations at different frequencies.

The variation of $\Delta\tilde{\nu}/\Delta\tilde{\nu}_0$ with frequency is shown in Figure 90.

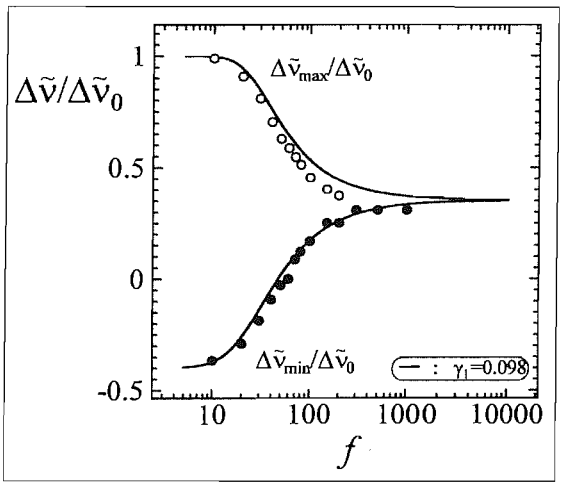

Figure 90: Variation in the quadrupolar splittings at different frequencies.

The value of the magnetic relaxation time obtained via this method is 3.2ms.

To compare the relaxation times obtained from the NMR experiment and ESR experiment the difference in field strength needs to be considered.

$$\tau = \left(\frac{7.05}{0.3335}\right)^2 \times 3.2\,\text{ms} = 1.43\text{s}$$

The ESR step-rotation experiment for ZLI-4792 + 4wt% p-xylene gave a relaxation time of 1.31s at 293K, which is in good agreement with the value of 1.43s obtained via the NMR method given the dramatic difference in the fields and hence the relaxation times.

4.10 Conclusion

A range of techniques have been used to study the effect of dimeric dopants on the commercial host mixture ZLI-4792. The mesophase behaviour of the doped systems was examined using polarising microscopy. The dynamic response, of doped ZLI-4792, to a magnetic field has been investigated using electron spin resonance (ESR) spectroscopy and nuclear magnetic resonance (NMR) spectroscopy. The solubility of a few of the dimeric dopants has been calculated with aid of differential scanning calorimetry.

It was found that all of the dimeric dopants lower the transition temperatures, T_N and T_I, of the host mixture by at least 15K. However, for display applications, the majority of the doped systems remain within the operating temperature range. The only dopant to have no significant effect on the mesophase behaviour of the host was DFS33, which was supplied by Hitachi. This dopant, however, is light sensitive and isomerises to the cis-isomer on prolonged exposure to light. This could prove to be a problem if used in display mixtures.

All of the doped nematic mixtures studied by ESR have faster relaxation times than the pure host mixture, ZLI-4792, when compared on the absolute temperature scale. This temperature scale is probably the most important when considering mixtures for use in displays. However, if the shift in the nematic transition temperature is considered, the relaxation times obtained for the pure host mixture are faster than the doped mixtures when compared on the shifted temperature scale. The addition of the dopants appear to decrease the order of the pure host when compared on the absolute temperature scale but on the shifted temperature scale there is little effect on the order of the systems. The only dopant to have faster dynamic behaviour than the pure host on both temperature scales is DFS33 and this is because this dopant has little effect on the nematic transition temperature of ZLI-4792.

The static field-balance NMR experiment yielded a value for $\Delta\tilde{\varepsilon}/\Delta\tilde{\chi}$. This then allowed the determination of the diamagnetic susceptibility at varying temperatures because the dielectric anisotropy was already known and the ratio $\Delta\tilde{\varepsilon}/\Delta\tilde{\chi}$ is assumed to remain constant. These values of the diamagnetic susceptibility and the values of the relaxation times for the host mixture obtained by the ESR experiments then allowed the determination of the rotational viscosity at varying temperatures. The rotational viscosity at 293K calculated by this method was 124 mPas and this is in very good agreement with the literature value of 133 mPas. The dynamic NMR field-balance experiment allowed the determination of the magnetic relaxation time, τ_M. This relaxation time was then

compared to the relaxation time obtained using ESR spectroscopy and allowing for the difference in the field strengths the two values appear to be in extremely good agreement.

4.11 References

[1] A. I. Vogel; *Practical Organic Chemistry*, 665, (1957), Longmans, Green and Co.

[2] C. T. Imrie; *Ph.D. Thesis*, University of Southampton, (1988).

[3] S. Solonina, Zh. Russ. Fiz.-Khim. O-va; (1898), **30**, 618.

[4] V. Braun, Chem. Ber.; (1909), **42**, 4548.

[5] T. W.Cheung; *Ph.D. Thesis*, University of Southampton, (1990), 59.

[6] H. O. Wirth, F. U. Herrmann, G. Herrmann and W. Kern, Mol. Cryst., **4**, 321, (1968).

[7] W. H. de Jeu; *Physical Properties of Liquid Crystalline Materials,* Chapter 7, (1980), Gordon and breach, London.

[8] N. Kunimatsu; *Ph.D. Thesis*, University of Southampton, (2000).

[9] G. R. Luckhurst; *Magnetic Resonance Spectroscopy of Liquid Crystals - Non-Amphiphilic Systems, Liquid Crystals and Plastic Crystals*, **Vol. 2**, Chapter 7, (1974), Ellis Horwood, Chichester.

[10] A. Emerson, G. R. Luckhurst and R. W. Phippen; Liq. Cryst., **10**, (1991), 1.

[11] M. J. Duer and C. Roper; Phys. Chem. Chem. Phys., **5**, (2003), 3034.

[12] K. Araya and K. Iwasaki; Mol. Cryst. Liq. Cryst., **392**, (2002), 49.

[13] G. W. Gray; *Molecular structure and the properties of liquid crystals*, Chapter 6, (1962), Academic Press, London, 112.

[14] H. Kelkar and R. Hats; *Handbook of liquid crystals*, Chapter 8, (1980), Verlag Chemie, Weinheim, 357.

[15] R. F. Fedors; Polym. Eng. Sci., **14**, (1974), 147.

[16] P. J. Collings and M. Hird; Introduction to Liquid Crystals, Chemistry and Physics, (1997), Taylor & Francis, 197.

[17] C. J. Dunn, G. R. Luckhurst, T. Miyamoto, H. Naito, A. Sugimura and B. A. Timimi; Mol. Cryst. Liq. Cryst. A, **347**, (2000), 167.

[18] J. W. Emsley, G. R. Luckhurst and H. S. Sachdev; Liq.Cryst., **5**, (1989), 953.

[19] A. Borštnik, H. Stark and S. Žumer; Phys. Rev. E, **61**, (2000), 2831.

[20] T. W. Cheung, S. Fan, G. R. Luckhurst and D. L. Turner; J. Chem.Soc., Faraday Trans., **93**, (1997), 3099.

[21] G. R. Luckhurst, A. Sugimura, B. A. Timimi and H. Zimmermann; Liq. Cryst., in press.

[22] G. R. Luckhurst, T. Miyamoto, A. Sugimura and B. A. Timimi; J. Chem. Phys., **117**, (2002), 5899.

[23] G. R. Luckhurst, T. Miyamoto, A. Sugimura, B. A. Timimi and H. Zimmermann; J. Chem. Phys., **121**, (2004), 1928.

Chapter 5

Liquid Crystal Gels

5.1 Introduction

During the investigation into dopants for super-low viscosity nematics a novel and unexpected discovery was made. It was found that four of the dopants studied act as gelators in a range of liquid crystals with positive, zero and negative dielectric anisotropies, corresponding to quite different charge distributions within the mesogenic molecules. The gelled systems were investigated using ESR spectroscopy, polarising microscopy and DSC. The ESR spectra were also simulated using an appropriate director orientational distribution function to give some insight into the ability of the field to align the director of the gelled systems. This Chapter summarises the results of this investigation as well as to compare them with previous work on liquid crystal gels carried out by Kato *et al.* [1-2]. Low molecular mass compounds have previously been found to gel liquid crystals; work by Kato *et al.* [1] has shown that amino acid derivatives act as gelators in the same kind of liquid crystals. These gels were found to exhibit novel behaviour not only as a consequence of their high viscosity but also because of the strong interactions of the director with the fibrous network forming the gel. The formation of hydrogen bonds in these amino acid derivatives is thought to play a major role in the formation of the gel. Our new class of gelators are, however, unable to form hydrogen bonds and some other mechanism must be responsible for the gel formation. The next Section introduces types of gels starting with normal gels followed by liquid crystal gels. Section 5.3 describes the novel gelators discovered during this research and Sections 5.4 and 5.5 present the experimental findings starting with polarising microscopy and then ESR spectroscopy which includes spectral simulations. Section 5.6 discusses the solubility parameters for these gelators to determine their solubilities, and Section 5.7 details deuterium NMR experiments which were carried out for the deuteriated gelators in ZLI-4792.

5.2 Gels

5.2.1 Normal gels

Different kinds of gels are all around us; from cosmetics (hair gel), to food (jelly), to toys (silly putty) and in life itself (living organisms are made up of aqueous gels). Hydrophilic (water loving) colloids, under certain conditions, are capable of partially coagulating to a mass of interconnecting filaments which may enclose all of the solvent (dispersion medium) to produce a pseudo-solid which is an easily deformable mass or jelly [3]. Such gels may be formed when they contain as little as 1% of gelling agent and generally appear to be heterogeneous under a microscope. In other words a gel is a biphasic system of semi-solid nature which is still rich in liquid. Gels are classified as macromolecular colloids [3,4]. A colloid consists of a dispersed phase (in this case the gelling agent) which is distributed uniformly in a finely divided form within a dispersion medium. In a gel a 3D-network, which is generally fibrous in nature, immobilises the liquid preventing flow at the macroscopic level. The most commonly known gelling agents are gelatines which are used to gel water to form jelly; they are also used in photography and in the manufacture of glue. Gelatines are insoluble in cold water but dissolve in hot water to form viscous solutions. A solution containing more than 1% of gelatine solidifies to a jelly on cooling. A gelatine gel may be converted back to the disperse solution (sol) on heating and is, therefore, known as a thermo-reversible gel. Silica gel on the other hand is known as an irreversible gel as it cannot be converted back to the sol due to the formation of covalent bonds on creation of the gel. The process of gelation can occur in three different ways; first by changing the temperature of the colloid, secondly by the addition of a precipitant and finally by the formation of salt gels resulting from a chemical reaction. An example of the first gelation process is gelatine which forms a jelly on cooling a solution of gelatine and water. This type of gel is similar to the novel gels described later in this Chapter. The second gelation process is critically dependent on the concentration of precipitant and an example is the rapid mixing of saturated calcium acetate with a ten-fold excess of alcohol to yield 'solid alcohol'. An example of the final process is the chemical reaction between barium thiocyanate and magnesium sulphate to form the gel of barium sulphate. Gels can be broadly classified into two groups; chemical gels and physical gels. Chemical gels are made up of a network which is held together entirely through covalent bonds, an example of which is cross-linked polymers. These gels can be swollen or shrunk by the addition or removal of solvent and by change in temperature and pressure. Silica is another example of this type of gel. The formation of chemical gels is generally irreversible. Physical gels on

the other hand are formed entirely from non-covalent interactions such as hydrogen bonds, aromatic interactions (π-π interactions), ionic and London dispersion interactions. It is this weaker non-covalent nature of the bonding which allows the physical gels to be reversible.

5.2.2 Liquid crystal gels

Phase segregation which occurs in gelled liquid crystals can lead to the formation of materials suitable for electro-optic displays. Liquid-crystalline chemical gels have been prepared by the dispersion of covalently cross-linked polymers and are utilised in polymer dispersed liquid crystal displays (PDLCs), in which droplets of nematic liquid crystal (20-70wt%) on the scale of micrometers or less are dispersed in polymer matrices (30-80wt%). These phase segregated structures appear milky white in the off-state, but switch to being transparent on the application of an electric field. No liquid crystal physical gel equivalents had been reported until studies by Kato *et al.* [1] showed that they were easily obtained by the self-aggregation of *trans*-(1R,2R)-bis(dodeconoylamino)-cyclohexane. Recent work by Kato *et al.* [1-2] has illustrated that liquid crystal physical gels can exhibit faster electro-optic response times in TN cells than the corresponding pure host, providing the concentration of the gelator is below 1wt%. He reports the gelation of room temperature nematic liquid crystals by self-aggregation or crystallisation of low molecular weight molecules through hydrogen bonding. The gelling agents (gelators for liquid crystal physical gels) used are all amino acid derivatives which have high melting points and so low solubilities, presumably as a result of the intrinsic hydrogen bonding. However, the chirality of the molecules is also thought to play an essential role in the function of the gelator [5]. Thus the tapes, fibrils or fibres stabilising the gel are twisted because of the chirality, but to self-organise to form the crystal they would need to untwist. The twist elastic energy required would have to be matched by the gain in attractive energy on crystallisation of the gelator. Clearly for the amino acid gelators this is not the case.
The network of fibres which make up the gel can then pin the director at their surface and this pinning competes with applied electric or magnetic fields for the director alignment. These systems are prepared by the addition of the gelator to a room temperature nematic liquid crystal at the desired concentration. Concentrations of above 1wt% of gelator are of no use for TN displays due to the increased light scattering caused by the increased amount of the phase segregated gelators; however, they are being investigated for use in light scattering display devices. The gelator Kato first investigated is shown in Figure 1 and had been developed as a gelator of common organic solvents [6].

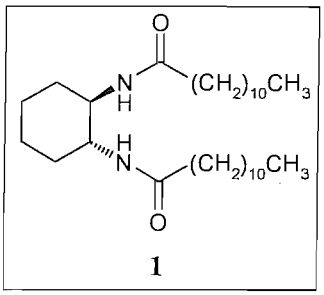

1

Figure 1: Gelling agent *trans*-(1R,2R)-bis(dodeconoylamino)cyclohexane used to gel the room temperature nematic liquid crystal 5CB [1].

When a mixture of 1 mol% of gelator **1** in 5CB (4-pentyl-4'-cyanobiphenyl, T_{NI}=34°C) is cooled from the isotropic phase a transition to a *normal* gel is observed at 74°C. This is a phase in which the gelator molecules do not dissolve in the liquid crystal and the gel is an isotropic gel because the liquid crystal is still in its isotropic phase. On further cooling a transition from the isotropic gel phase to a liquid crystal gel phase is observed at 34°C. These transitions are thermally reversible. As the concentration of the gelator is increased the isotropic gel- isotropic transition temperature increases but the LC gel-isotropic gel transition temperature remains unchanged. Kato *et al.* [1] then went on to find materials which exhibited improved director alignment and electro-optic properties, see Section 5.2.3. Two chiral amino acid derivatives which were used to gel 5CB are shown in Figure 2.

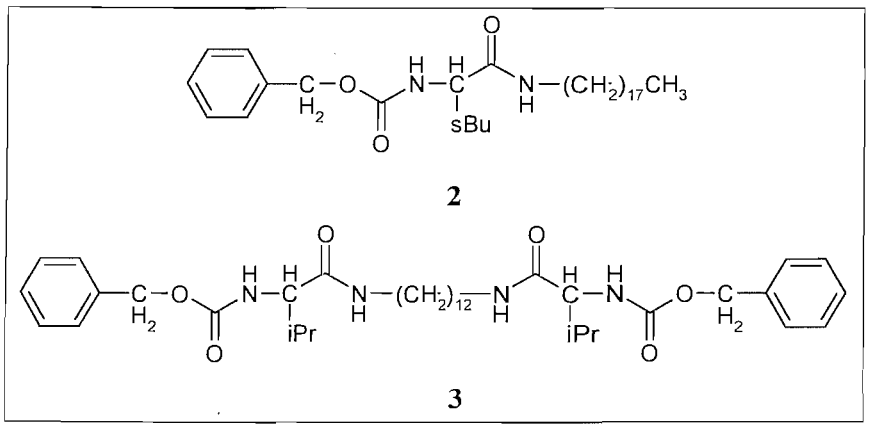

2

3

Figure 2: Gelling agents used to gel the room temperature nematic liquid crystal 5CB [2].

Compound **3** is a dimeric gelator as are the new class of gelators discovered during this research. Both **2** and **3** efficiently gel the liquid crystal 5CB and once the gel forms it does not flow. Again two gel phases are observed; the isotropic gel (normal gel) and the liquid crystal gel. The transition temperature between the isotropic gel and anisotropic gel remains constant at 35°C on increasing the concentration of the gelator which shows that the nematic transition is unchanged by the addition of the gelator. By contrast the isotropic

gel-isotropic transition temperature increases with increasing concentration of gelator. This isotropic gel-isotropic transition temperature is greater for the mixture containing gelator **3** than for the mixture containing gelator **2** when compared at the same concentration, for example the minimum concentration of gelator **3** needed to gel 5CB is 0.15 mol% whereas the minimum concentration of gelator **2** needed to gel 5CB is 0.25 mol%. This may be due to the increased number of moieties able to form hydrogen bonds in gelator **3** which would create stronger molecular associations in the network. The melting point of gelator **3** is expected to be higher than for gelator **2.**

5.2.3 Liquid crystal gels and electro-optic response

Kato *et al.* [1] investigated a mixture of 1 mol% of gelator **1** in 5CB placed between two plates coated with polyimide with parallel rubbing directions. No director alignment at room temperature was observed unlike the pure host 5CB for which uniform planar alignment is usually obtained. The system responded to an electric field but gave results for the threshold voltage and response times which were much greater than for 5CB. These results indicate that the fibres and liquid crystal interact and the dynamics of the mesophase is restricted by the gel. This suggested that these systems could be used as electro-optic materials. This is in contrast to *normal* gels of common solvents in which orientational ordering of the solvent molecules cannot be achieved.

The electro-optic response times for the gelled systems made up of gelators **1, 2** and **3** in 5CB from a twisted nematic cell were obtained using a cell thickness of 16μm, an applied voltage of 10V and a frequency of 300Hz [7]. The results are given in Table 1.

Gelling agent	**Concentration / mol%**	**Turn-off response time / ms**	**Threshold voltage / V**
None	0	12	1.0
1	0.50	19	1.5
2	0.25	6	0.8
2	0.50	7	1.7
3	0.25	n/a*	n/a*

Table 1: Electro-optic behaviour of the nematic gel of 5CB containing gelators **1, 2** and **3** in a twisted nematic cell at 20°C. * No TN alignment or response observed [7].

The same effect on the alignment and response times was observed for gelators **2** and **3** in 4-(*trans*-4'-pentylcyclohexyl)benzonitrile (PCH5, T_{NI}=54°C, see Figure 3) [8].

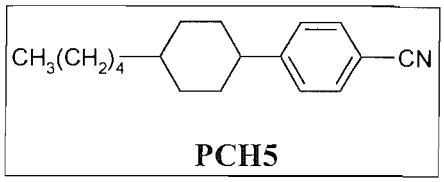

Figure 3: Molecular structure of the nematic liquid crystal PCH5.

No TN director alignment was achieved for the system containing gelator **3** and so no electro-optic response was measured. The gelled system containing less than 0.5 mol% of gelator **2** exhibits faster electro-optic response times than for the liquid crystal alone because the surface area has been increased by the network of fibres which are more efficient at aligning the director. At a concentration of 1 mol% of gelator **2** no TN alignment was observed.

The main common characteristic of these gelators is their ability to form hydrogen bonds which was thought to be essential for physical gel formation. This allows networks of the gelling agents to build up and trap the surrounding solvent (water, liquid crystal etc). Kato provided a small quantity of gelator **3** which was used to compare with the behaviour of the new class of gelators.

5.3 Novel low molecular mass gelators

The new class of gelators discovered in this research belong to the 1,n-bis-(phenyl-1-yloxy)alkane homologous series with spacer lengths ranging from n=7 to n=12; 1,10-bis-(4-methylphenyl-1-yloxy)decane was also found to be a gelator. Only the even-spaced members of this homologous series are gelators at room temperature.

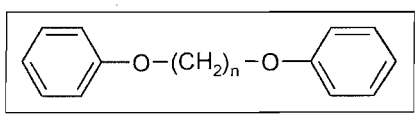

Figure 4: Molecular structure of 1,n-bis-(phenyl-1-yloxy)alkane.

These gelators were first found to gel the liquid crystal host ZLI-4792, which is a mixture of fluorinated mesogens. The crystallisation of these gelators cannot be due to the formation of hydrogen bonding and it was first thought that electrostatic interactions with the host played an important role in the formation of the fibrous network. The electrostatic quadrupoles of the gelators were thought to interact with the opposite electrostatic quadrupole of the host. This theory, however, was dismissed when it was found that these gelators are able to gel liquid crystal host mixtures which contained no polar substituents and hence did not possess an opposite electrostatic quadrupole to the gelator. The other

host mixtures studied were; ZLI-1565 which is a mixture of cyano-substituted mesogens, I22 which is an essentially non-polar liquid crystal, 5CB which is a single component cyano-substituted mesogen, ZLI-3086 which is a non-polar mixture and MDA-03-4596 which is also a non-polar mixture. The gels formed are found to be thermally reversible but do exhibit hysterisis in that they only form on cooling when left for at least ten minutes. The ability of these compounds to form a gel is observed to be critically dependent on whether the spacer contains an odd or an even number of methylene units. The gelators with even-numbered spacers form gels at room temperature whereas the gelators having odd-numbered spacers do not, see Figure 5. The gels (C8 and C10 in Figure 5) are milky white and viscous so they do not flow, which is illustrated by the inversion of the bottles for the gelled systems, where as the C7 and C9 systems do not form gels but are turbid because of the liquid crystal and readily flow.

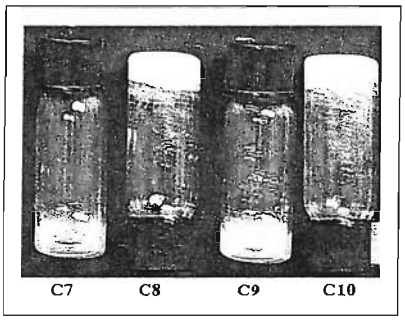

Figure 5: Samples C7, C8, C9 and C10 in ZLI-4792 illustrating the nematic gel phase for C8 and C10.

The melting points of these gelators also exhibit an odd-even effect, see Table 2. This parity dependence is illustrated in Figure 6 where it can be clearly seen that the even-spacer dopants possess higher melting points than their odd counterparts.

Dopant	**T_{mp} / K**
C7	327.2
C8	357.2
C9	333.2
C10	358.2
C11	337.2
C12	358.2

Table 2: Melting points for the 1,n-bis-(phenyl-1-yloxy)alkane homologous series.

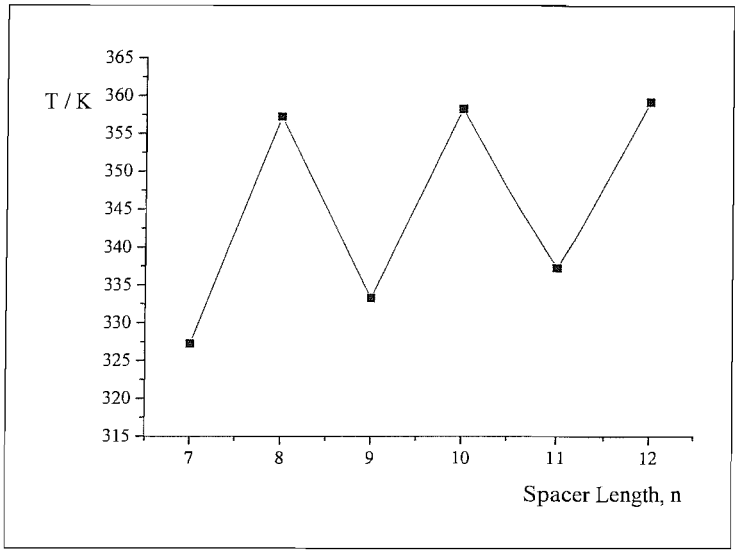

Figure 6: Melting points for the 1,n-bis-(phenyl-1-yloxy)alkane homologous series as a function of the spacer length.

This parity dependence is, presumably, due to the differences in molecular shape of the molecules at least in their all trans-conformations. Even dimers are on average more linear than the odd-conformers which are bent. This allows them to pack more efficiently and so the crystal structures have a higher stability leading to higher melting points. Crystal structure analysis of the C7 and C8 gelators show that the C8 dimer is linear with an angle between the para-axis of the phenyl rings of 39.9°, whilst the C7 dimer is bent with an angle between the para-axis of the phenyl rings of 101.2°, see Figure 7 and Figure 11. The unit cells for the C7 and C8 dimers are shown in Figure 8 and Figure 12 respectively. These show that the dimers with an odd-numbered spacer packs far less efficiently than the even-numbered spacer, which fits with the lower melting point observed. This unusual parity dependence of the melting point is well-known in liquid crystal science [9].

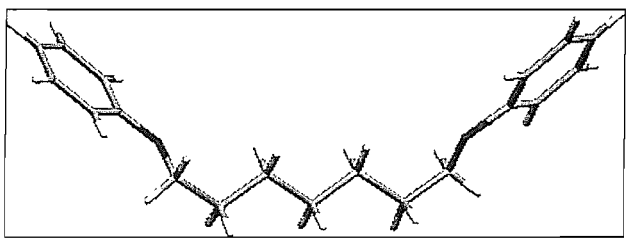

Figure 7: Molecular structure of 1,7-bis-(phenyl-1-yloxy)heptane (C7) dimer.

The molecular structure of the 1,7-bis-(phenyl-1-yloxy)heptane (C7) dimer shows that the alkyl chain is not in the all trans conformation and in fact there are two gauche links at either end of the chain. Whereas the molecular structure of the 1,8-bis-(phenyl-1-yloxy)octane (C8) dimer shows that the alkyl chain is all trans.

The crystal structure analysis was performed by James Orton from the University of Southampton.

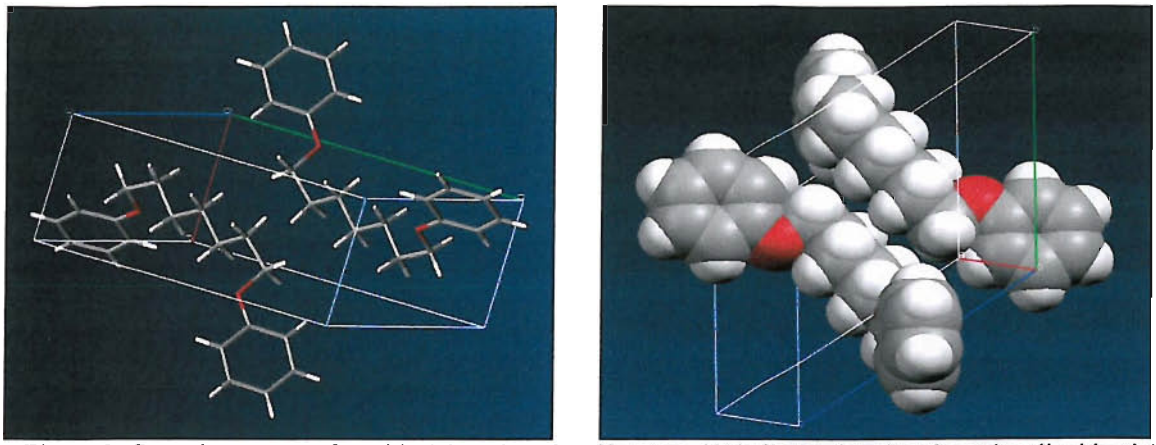

Figure 8: Crystal structure of 1,7-bis-(phenyl-1-yloxy)heptane (C7) dimer showing the unit cell with stick model (left) and space filling model (right).

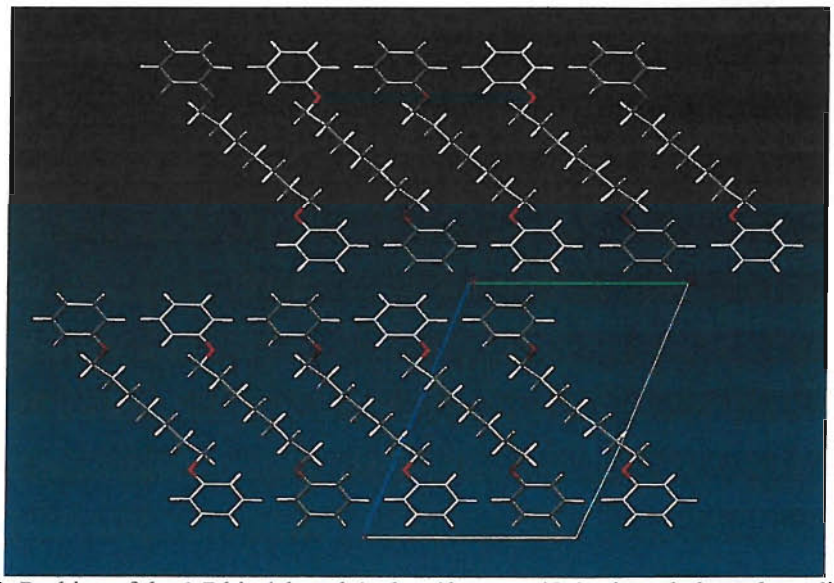

Figure 9: Packing of the 1,7-bis-(phenyl-1-yloxy)heptane (C7) viewed along the *a*-direction.

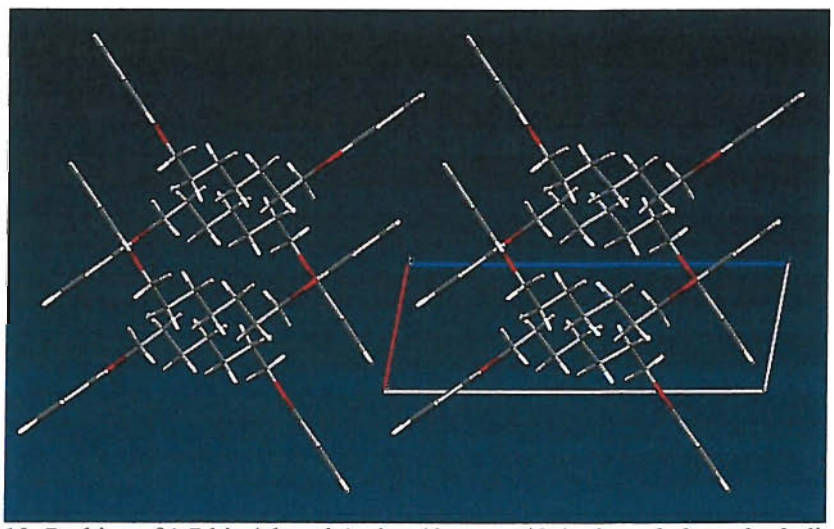

Figure 10: Packing of 1,7-bis-(phenyl-1-yloxy)heptane (C7) viewed along the *b*-direction.

The packing of the C7 dimer is shown from two perspectives in Figure 9 and Figure 10. These show that they pack in a sheet array. This is consistent with the plate-like crystals formed for this dimer on crystallisation from hot methanol.

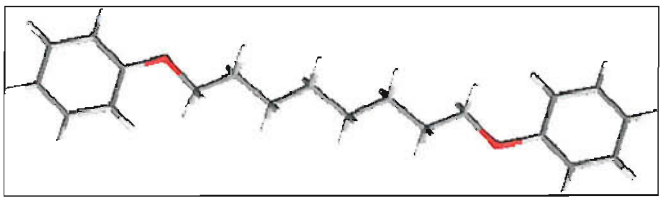

Figure 11: Molecular structure of 1,8-bis-(phenyl-1-yloxy)octane (C8) dimer.

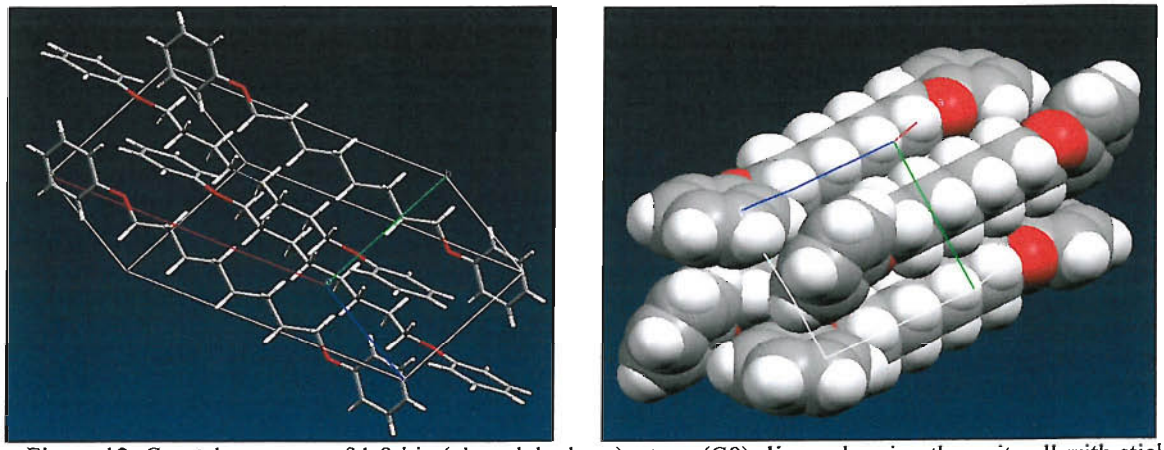

Figure 12: Crystal structure of 1,8-bis-(phenyl-1-yloxy)octane (C8) dimer showing the unit cell with stick model (left) and space filling model (right).

The relative orientation of the phenyl rings is similar to the packing observed for free benzene in that each phenyl ring is orthogonal to its neighbour i.e. they pack in a side-on-face orientation, see Figure 12.

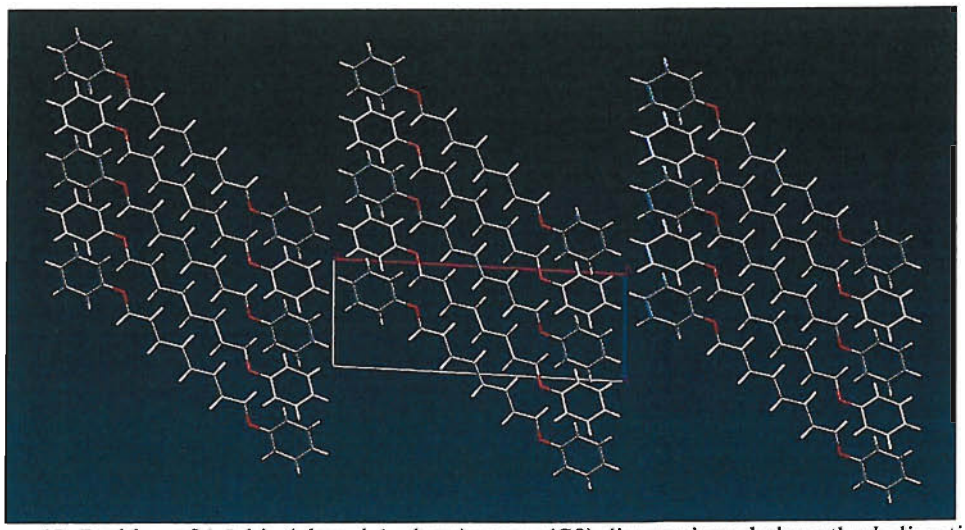

Figure 13: Packing of 1,8-bis-(phenyl-1-yloxy)octane (C8) dimer viewed along the *b*-direction.

The packing of the C8 dimer is shown from two perspectives in Figure 13 and Figure 14. These show that they pack in a sheet array. This is consistent with the plate-like crystals formed for this dimer on crystallisation from hot methanol.

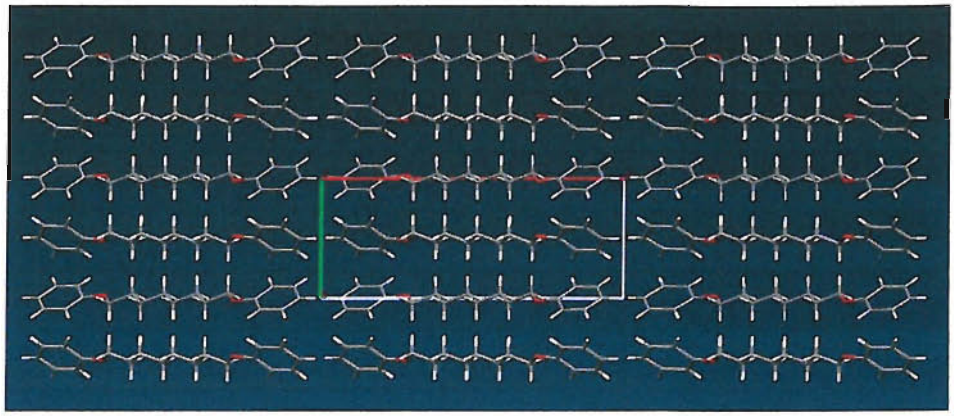

Figure 14: Packing of 1,8-bis-(phenyl-1-yloxy)octane (C8) dimer viewed along the *c*-direction.

We have suggested that the gel formation results from differences in the solubility of the gelators. The even-numbered spacer dopants have higher melting points than the corresponding odd-numbered spacer dopants indicating that their solubility is likely to be less. The solubility parameters for these dopants are calculated and discussed in Section 5.6. However, insolubility alone is not enough to be the sole cause for the formation of the gel phase, because gel formation requires the creation of a network capable of trapping pockets of liquid crystal. Kato gels are formed due to the insolubility of the gelators in the host liquid crystal which as a consequence form a network of fibres held together by hydrogen bonding. The dimeric gelators studied here, however, are unable to form hydrogen bonds and so another type of interaction must be responsible for the formation of the network which traps the liquid crystal. The packing of these dimers into sheets on crystallisation could be responsible for the gel formation and hence the network that traps of the liquid crystal host.

5.4 Polarising microscopy

The liquid crystal physical gels were prepared by mixing the liquid crystal, ZLI-4792, and the gelators, heating to the isotropic state when a simple solution is formed, followed by cooling to the required temperatures. The phase behaviour of the gelled systems was studied using a Zeiss Universal polarising microscope fitted with a Linkam hot stage using a heating rate of 1.0°C/min around the transitions and 5°C/min in between them. The transition temperatures, T_N and T_I of all the gels are given in Table 3. It should be noted

that a greater concentration of these dimeric gelators is needed to gel ZLI-4792 than the concentration of the gelator used by Kato *et al.* to gel 5CB.

Mixture	T_N / K	T_I / K
ZLI-4792	366.0	373.5
ZLI-4792 + 10wt % C8	333.0	346.1
ZLI-4792 + 5wt % C10	346.0	355.2
ZLI-4792 + 10wt % C10	334.9	344.7
ZLI-4792 + 10wt % C12	335.7	348.9
ZLI-4792 + 10wt % MeC10	353.2	362.2

Table 3: Transition temperatures for the gelled systems obtained by polarising microscopy.

The optical textures observed for ZLI-4792 + 10wt% C10 are shown in Figure 15. The textures at room temperature show the gel phase with pockets of nematic indicating coexistence of the nematic gel phase and the nematic phase, as the temperature is increased the fibres of the gelator gradually breakdown and the pockets of nematic liquid crystal grow until eventually all of the gel phase has been destroyed. These novel gelled systems differ from the hydrogen bonded physical gels discussed in Section 5.2.2 in that this system does not posses an isotropic gel phase (so no normal gel phase is observed) and in fact breaks down in the nematic phase of the liquid crystal host. This indicates that these gelators are not as effective as the Kato gelators and the interactions holding the network together are not as strong as the hydrogen bonded fibres of Kato's gels.

The optical textures observed for ZLI-4792 + 10wt% C12 are shown in Figure 16. The texture observed at room temperature is very similar to a texture observed for a crystalline sample. There are, however, small areas of nematic phase which grow in size on heating until the entire gelator network has dissolved and the system has become fully nematic. At 66°C the isotropic phase starts to appear and the system has become biphasic.

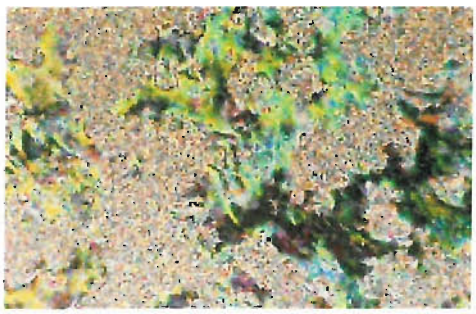

Room Temperature (x20) [N_{Gel}]

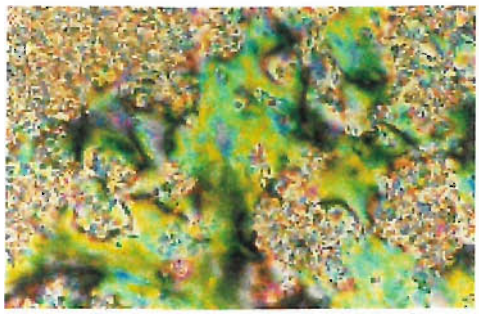

Room Temperature (x50) [N_{Gel}]

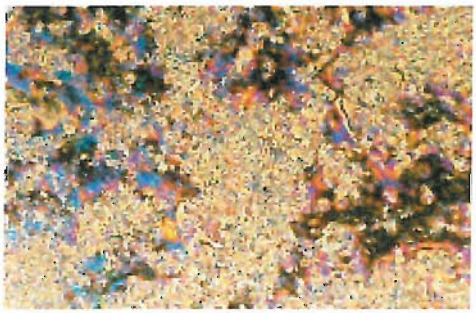

T = 19.0°C (x20) [N_{Gel}]

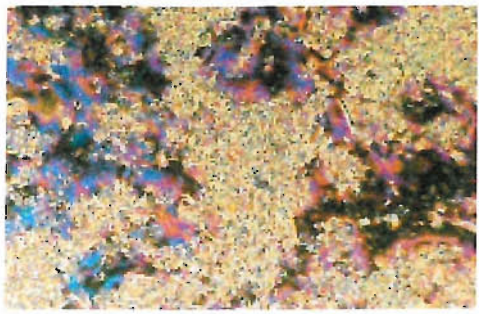

T = 26.5°C (x20) [N_{Gel}]

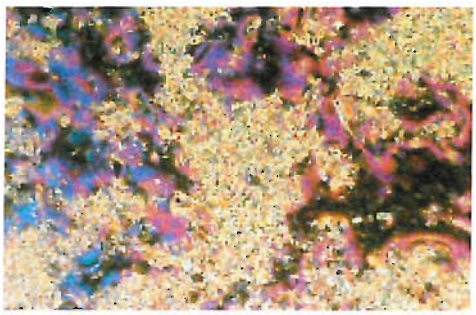

T = 34.0°C (x20) [N_{Gel}]

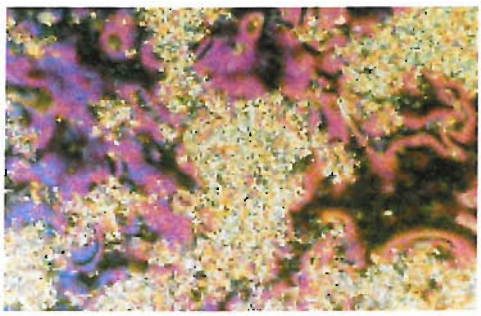

T = 42.2°C (x20) [N_{Gel}]

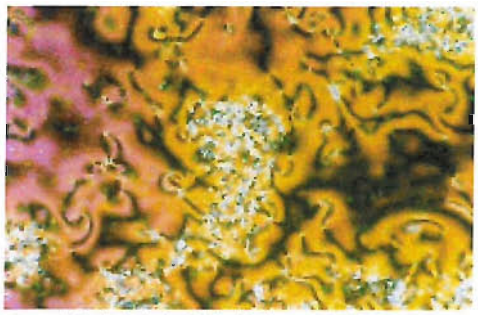

T = 49.2°C (x20) [N_{Gel} + N]

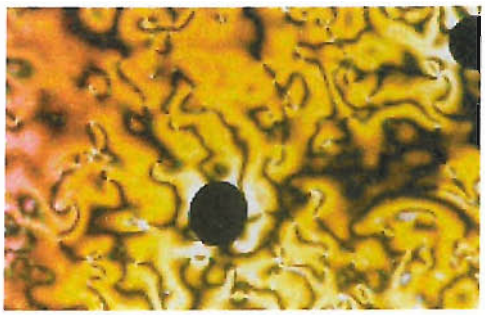

T = 58.2°C (x20) [N + I]

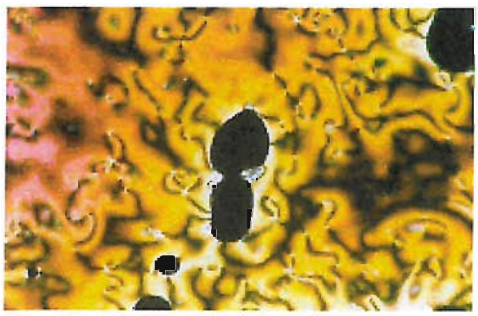

T = 61.1°C (x20) [N + I]

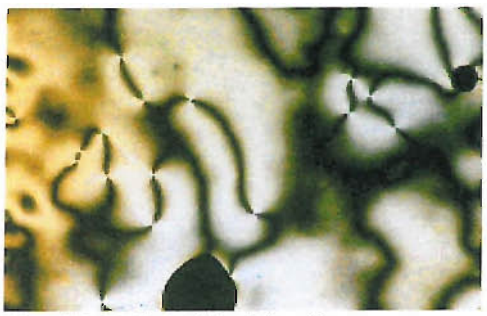

T = 65.5°C (x20) [N + I]

Figure 15: Polarising microscopy textures of ZLI-4792 + 10wt% C10.

T = 30.0°C (x20) [N_{Gel}]

T = 40.0°C (x20) [N_{Gel}]

T = 50.0°C (x20) [N_{Gel}]

T = 55.0°C (x20) [N_{Gel}]

T = 60.0°C (x20) [N]

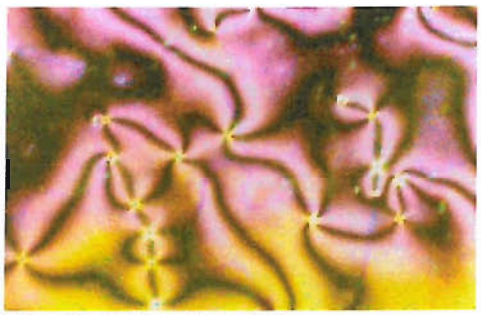

T = 62.0°C (x20) [N]

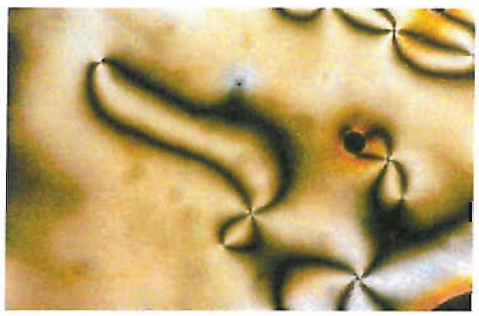

T = 66.0°C (x20) [N + I]

T = 68.0°C (x20) [N + I]

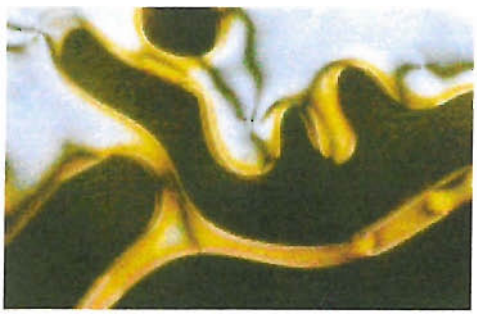

T = 70.0°C (x20) [N + I]

T = 72.0°C (x20) [N + I]

Figure 16: Polarising microscopy textures of ZLI-4792 + 10wt% C12.

5.5 ESR spectroscopy and spectral simulations

ESR spectroscopy was used to study the director alignment of the gels when subjected to a magnetic field. The distribution of the director was then calculated using an appropriate distribution function and the spectra were simulated using this distribution function.

The liquid crystal physical gels were prepared by mixing the liquid crystal, ZLI-4792, and the gelators, heating to the isotropic phase, followed by cooling to the required temperatures. Cholestane ($1x10^{-2}$ wt%) in DCM was pipetted into an ESR tube, the signal tested for a good signal-to-noise ratio on the spectrometer, and the DCM was then removed under vacuum. The gelled sample was then heated into the isotropic phase and pipetted into the ESR tube containing the cholestane to a depth of 1cm. The ESR spectra were recorded on a Bruker ECS 106 spectrometer as a function of temperature. The time waited once the temperature was set for the sample to equilibrate was approximately ten minutes. The spectrum for the gelled system at room temperature contains five lines corresponding to a three-dimensional distribution with the fibres or sheets, which are randomly distributed, pinning the director at their surfaces so the magnetic field is unable to align the director, see Figure 17. The outer two spectral lines correspond to the director being perpendicular to the magnetic field and the inner two spectral lines result from the director being parallel to the magnetic field.

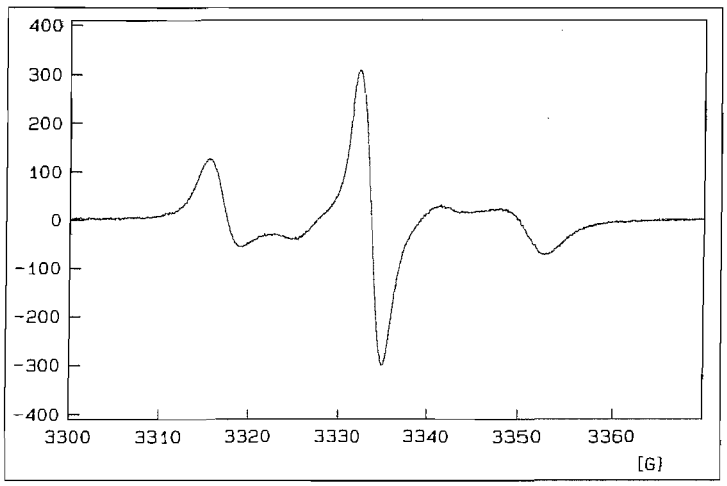

Figure 17: Typical ESR spectrum for the novel gel, ZLI-4792 + 10wt% C10, at room temperature showing a three-dimensional distribution of the director.

The model director distribution function which is obtained from the solution of the torque-balance equation for a system in which the director is initially random and is given by [10]

$$f(x) = \frac{a^2}{\left[a^2 + (a^2 - 1)x^2\right]^{3/2}}, \qquad (1)$$

where x is equal to $\cos\beta$ (with β being the angle between the director and its average position) and is defined in the half range from 0 to 1, and $f(x)$ is normalised over this range. The parameter a is a measure of order for the system and is equal to unity for a three dimensional distribution (zero order) and in the other limit as a tends to infinity the distribution becomes a delta function centred at $\beta = 0$ (complete director order). The second rank director order parameter is related to the distribution function by

$$\overline{P}_2^n = \int_0^1 \frac{(3x^2-1)}{2} f(x)dx, \tag{2}$$

can be obtained analytically and is

$$\overline{P}_2^n = \frac{a^2}{2}\left\{\left(\frac{2a^2+1}{a^2(a^2-1)}\right) - \left(\frac{3arctan(a^2-1)^{1/2}}{(a^2-1)^{3/2}}\right)\right\}. \tag{3}$$

The variation of $\overline{P}_2^n$ with a is shown in Figure 18. The order of the system is zero when a =1 and as a increases to 10 the order rapidly increases, then as a increases from 10 to 100 the change in the order slows until a plateaux is reached.

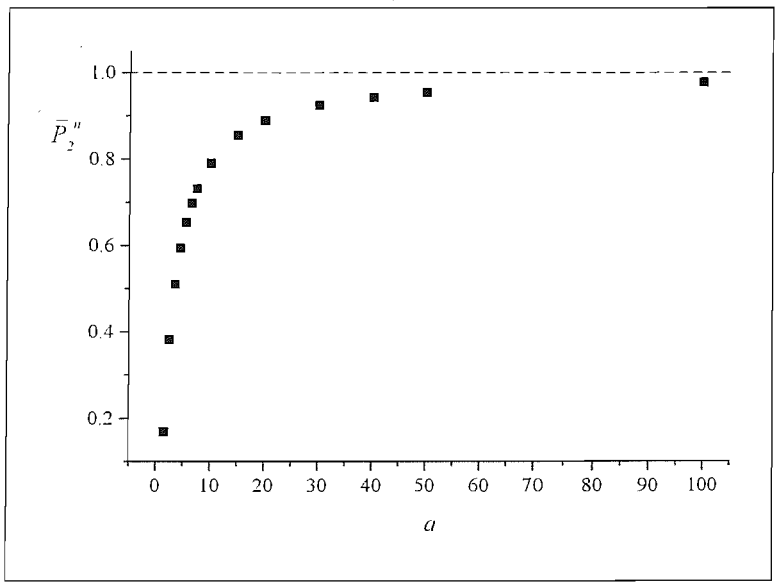

Figure 18: The director orientational order parameter, $\overline{P}_2^n$, versus the distribution parameter a.

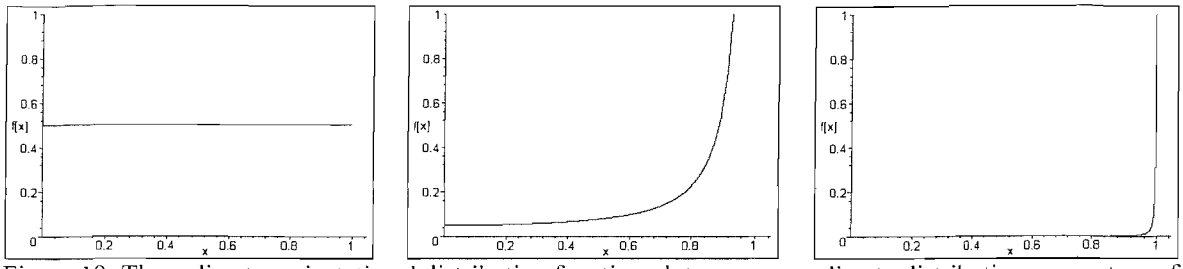

Figure 19: Three director orientational distribution function plots corresponding to distribution parameters of a=1.0 (left), a=10.0 (middle) and a=2000 (right).

Figure 19 shows three director orientational distribution function plots corresponding to distribution parameters of a =1.0, a =10.0 and a =2000. The area corresponds to the total probability and is equal to 1. For a = 1 the director is completely disordered and there is equal probability of the director being at any angle from 0° to 90°. For a = 2000 the director is normally completely ordered and is at 0° to the magnetic field. The following results concerning the behaviour and order of the systems are obviously obtained from the spin probe, cholestane, but as this probe is orientationally ordered by its anisotropic interaction with the host liquid crystal, and in order to simplify the discussion, this will be neglected from now on and only the doped systems will be discussed.

The spectra were simulated by varying a, which gives the director order, and using

$$I(B,\beta) = \sum_{m=1,0,-1} L(B,\tilde{B}_m,T_2^{-1}), \tag{4}$$

where B_m, the resonance field, is given by

$$\tilde{B}_m(\beta) = B_0 - (h/\tilde{g}\mu_B)[\tilde{A}_\perp^2 + (\tilde{A}_{||}^2 - \tilde{A}_\perp^2)cos^2\beta]^{1/2}m. \tag{5}$$

$I(B,\beta)$ is the spectral intensity for a single spectrum for a single value of β, which is the angle made by the director with the magnetic field, and so the total spectral intensity is then

$$I_{tot}(B) = \sum_{\beta} I(B,\beta)f(\cos\beta), \tag{6}$$

for values of β in the half range from 0° to 90° (i.e. this repeats from 90° to 180°).

$f(\cos\beta) = f(x)$ is the model director distribution function.

The variable parameters used to simulate the ESR spectra were the linewidths, T_2^{-1}, the parallel hyperfine tensor, $\tilde{A}_{||}$, the perpendicular hyperfine tensor, $\tilde{A}_\perp$, and a. The first three of these parameters are taken from the spectra themselves with slight alterations at times and then a suitable value of a is found by trial and error. The spectroscopy experimental ESR parameters used to record the ESR spectra for all the gels are given in Table 4.

Gel	Centre Field / T	Sweep Width / G	Modulation Amplitude / G	Sweep Time / s	Power / mW	Frequency / GHz
10wt% C8	0.3335	70	1.0	5.24	12.7	9.34
5wt% C10	0.3335	70	2.0	5.24	12.7	9.34
10wt% C10	0.3335	70	2.0	5.24	12.7	9.34
10wt% C12	0.3337	70	2.0	5.24	12.7	9.34
10wt% MeC10	0.3335	70	2.0	5.24	12.7	9.34

Table 4: ESR experimental parameters for the gelled systems.

The ESR variable temperature experiment was performed for both the heating cycle and cooling cycle.

5.5.1 ESR variable temperature results for ZLI-4792 + 10wt% C8

The results given are for the heating cycle starting at 305K. The cooling cycle for this and the rest of the gels are not shown because the gel does not reform on cooling in the time taken to run the experiment. In fact the gel phase takes ten minutes at room temperature to reform, and as a result the ESR spectra from the cooling cycle contain three hyperfine lines with a spacing which indicates full alignment of the director with respect to the magnetic field. The first spectrum at 305K is typical for a three-dimensional distribution in which the director is unaligned by the magnetic field. This indicates that the randomly arranged sheets of the gel network are pinning the director at their surfaces and the magnetic field of 0.335T is not strong enough to compete with this surface elastic force. As the temperature is increased the network gradually dissolves allowing more of the director to be aligned by the magnetic field. This gradual alignment of the director is shown by the increasing intensity of the two inner spectral lines and the decreasing intensity of the two outer spectral lines. For this system the network has completely dissolved and the director is fully aligned at 323K as is apparent from the three line spectrum at 323K. The values of a, the parallel, $\widetilde{A}_{\|}$, and perpendicular, $\widetilde{A}_{\perp}$, hyperfine spacings together with the values for the linewidths of the three hyperfine lines used to simulate the spectra for cholestane dissolved in ZLI-4792 doped with 10wt% of the 1,8-bis-(phenyl-1-yloxy)octane (C8) gelator are given in Table 5. The corresponding director orientational order parameters are also given in Table 5 and the experimental spectra along with the corresponding simulated spectra and the associated director distribution function plots are shown in Figure 20.

T / K	a	$\widetilde{A}_{\|}$ / G	$\widetilde{A}_{\perp}$ / G	ΔB_0 / G	ΔB_2 / G	ΔB_1 / G	$\overline{P}_2^n$
305	1.40	6.96	18.42	1.50	1.80	1.50	0.14
310	1.60	7.57	18.11	1.50	1.80	1.50	0.20
315	3.30	9.21	17.30	1.50	1.70	1.50	0.49
323	2000	9.36	17.22	1.54	1.69	1.38	0.99

Table 5: The values for the distribution parameter a, and the corresponding director orientational order parameters for ZLI-4792 + 10wt% of the C8 gelator together with the hyperfine spacings and linewidths used to simulate the spectra.

As the temperature is increased the parallel hyperfine spacing increases indicating a decrease of order in the system, consequently the perpendicular hyperfine spacing decreases.

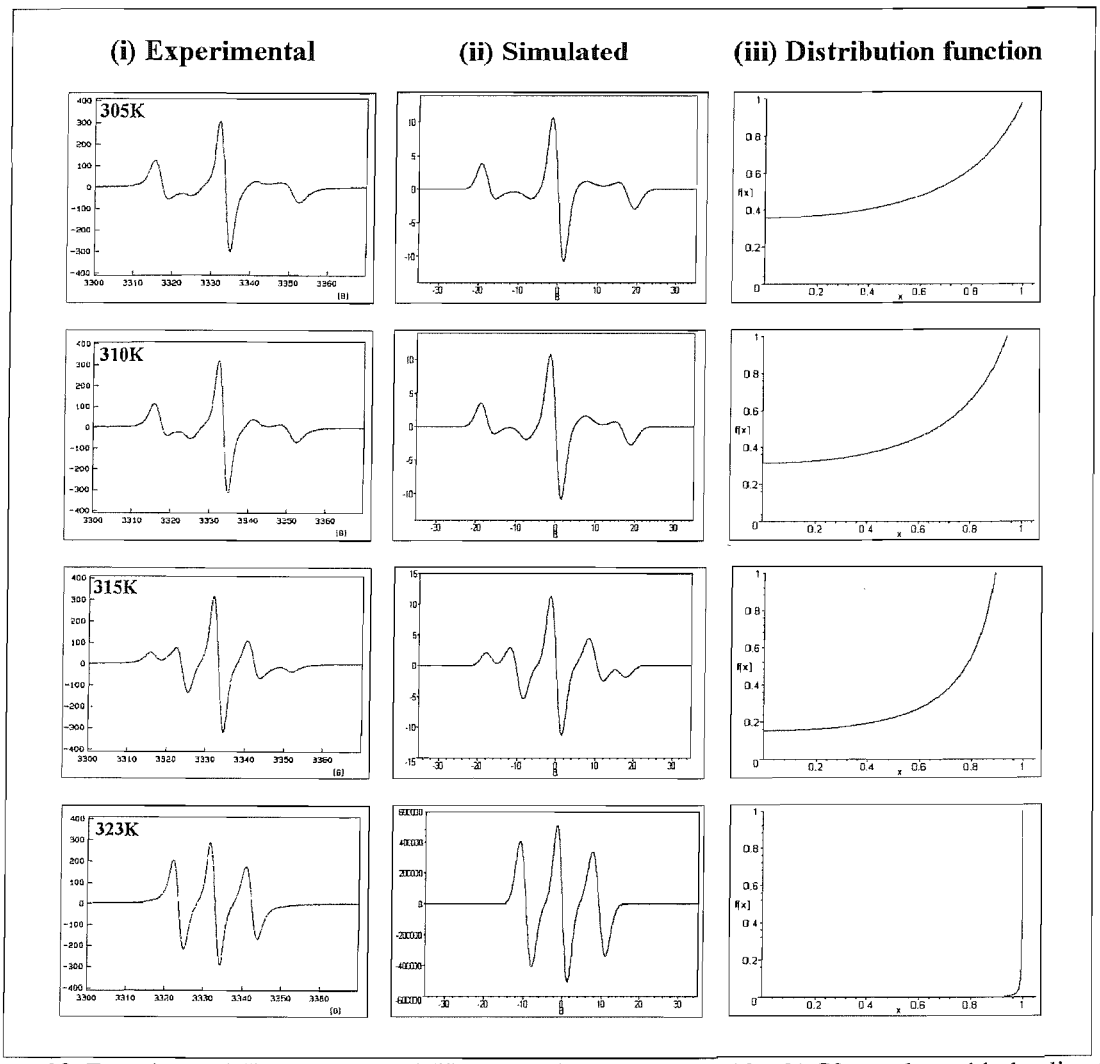

Figure 20: Experimental (i) and simulated (ii) spectra for ZLI-4792 + 10wt% C8 together with the director orientational distribution function (iii).

The simulated spectra are in good but not perfect agreement with their experimental counterparts. The director orientational distribution function plots indicate the range of angles the director makes with the magnetic field for the specific value of a. When $x = 1$ the director is parallel to the magnetic field and when $x = 0$ the director is orthogonal to the magnetic field.

5.5.2 ESR variable temperature results for ZLI-4792 + 5wt% C10

The first spectrum at 303K suggests a three dimensional distribution for the director because the magnetic field (0.34T) is unable to align it. The two outer spectral lines correspond to the director being perpendicular to the field and the two inner, less intense, lines correspond to the director being parallel to the field. This is indicative of the sheets trapping the liquid crystal and pinning the director at its surface. On increasing the temperature the outer spectral lines lose intensity and the inner spectral lines gain intensity, showing the gradual alignment of the director by the field as the sheets dissolve. At 313K the network of sheets has dissolved sufficiently to allow the director to be almost fully aligned parallel to the field. At 323K the network of sheets has dissolved so the director is fully aligned parallel to the field. The final spectrum is typical for the cholestane spin probe in a nematic liquid crystal with a positive diamagnetic susceptibility, which means the director will align parallel to the magnetic field.

The values of a, the parallel, $\widetilde{A}_{\|}$, and perpendicular, $\widetilde{A}_{\perp}$, hyperfine spacings together with the values for the linewidths of the three hyperfine lines used to simulate the spectra for cholestane dissolved in ZLI-4792 doped with 5wt% of the 1,10-bis-(phenyl-1-yloxy)decane (C10) gelator are given in Table 6. The corresponding director orientational order parameters are also given in Table 6 and the experimental spectra along with the corresponding simulated spectra and the director distribution function plots are shown in Figure 21.

T / K	a	$\widetilde{A}_{\|}$ / G	$\widetilde{A}_{\perp}$ / G	ΔB_0 / G	ΔB_2 / G	ΔB_1 / G	$\overline{P}_2^n$
303	3.00	6.34	18.73	1.30	1.60	1.80	0.45
313	8.00	6.96	18.42	1.50	1.30	1.50	0.75
318	10.00	7.57	18.11	1.40	1.20	1.50	0.79
323	2000	8.67	17.56	1.20	1.20	1.30	0.99

Table 6: The values for the distribution parameter a, the corresponding director orientational order parameters for ZLI-4792 + 5wt% of the C10 gelator together with the hyperfine spacings and linewidths used to simulate the spectra.

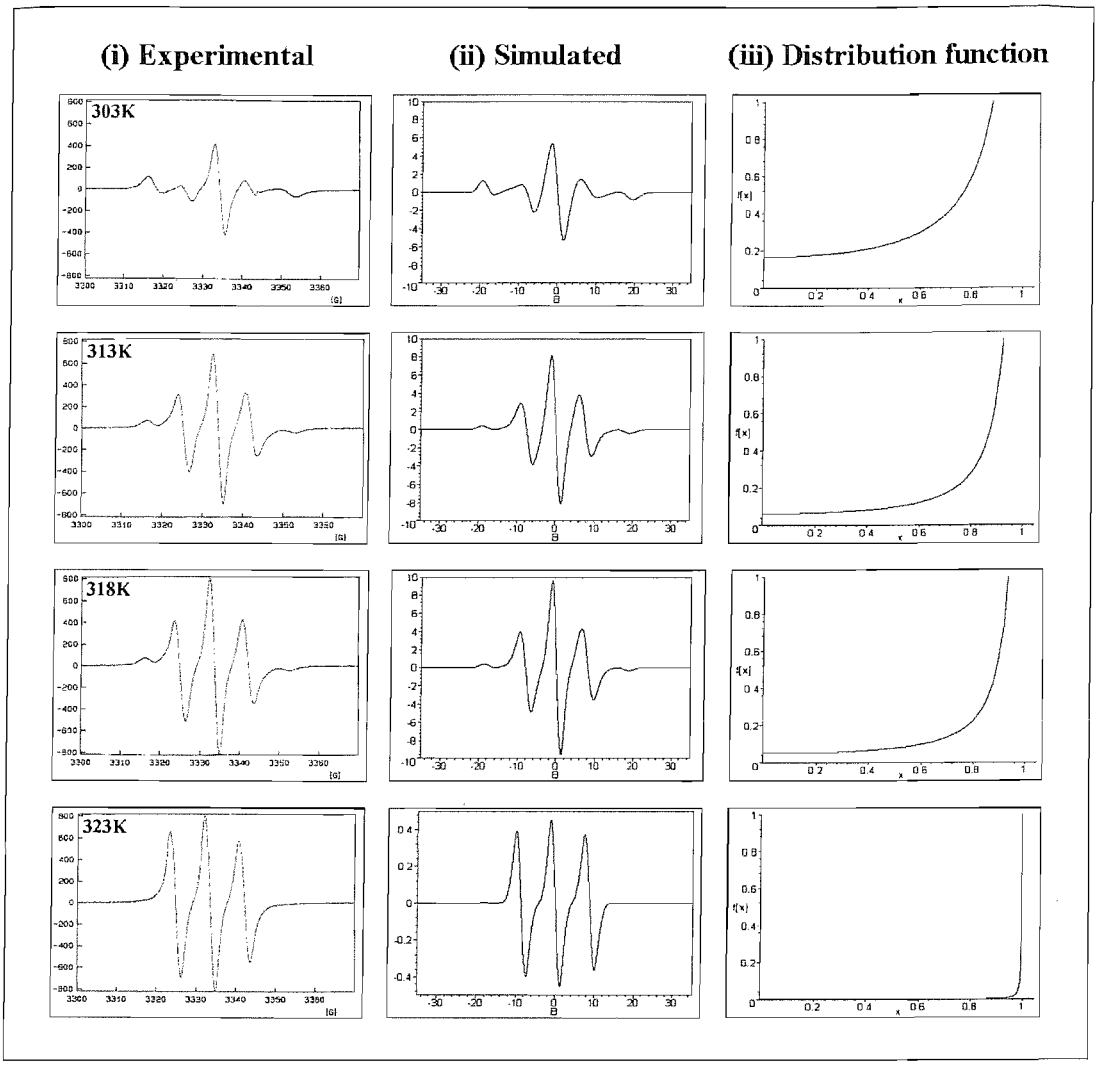

Figure 21: Experimental (i) and simulated (ii) spectra for ZLI-4792 + 5wt% C10 together with the director orientational distribution function (iii).

The simulated spectra are in good agreement with the experimentally obtained spectra.

5.5.3 ESR variable temperature results for ZLI-4792 + 10wt% C10

The spike observed on the high field line in the spectrum at 303K in Figure 22 is caused by paramagnetic impurities in the quartz heating jacket. This heating jacket was changed for the measurement of the other systems. The magnetic field is able to align fully the director at 326K for this doped sample. The network of sheets at this concentration is stronger than for the 5wt% gel which is indicated by the more random distribution of the director. For this gel the network gradually dissolves over a larger temperature range than for the 5wt% C10 gel and also full alignment of the director occurs at a slightly higher temperature. The values of a, the parallel, $\widetilde{A}_{\parallel}$, and perpendicular, $\widetilde{A}_{\perp}$, hyperfine spacings together with the values for the linewidths of the three hyperfine lines used to simulate the spectra for cholestane dissolved in ZLI-4792 doped with 10wt% of the 1,10-bis-(phenyl-1-

yloxy)decane (C10) gelator are given in Table 7. The corresponding director order parameters are also given in Table 7 and the experimental spectra along with the corresponding simulated spectra and the director distribution function plots are shown in Figure 22.

T / K	a	$\widetilde{A}_{\|}$ / G	$\widetilde{A}_{\perp}$ / G	ΔB_0 / G	ΔB_2 / G	ΔB_1 / G	$\overline{P}_2^n$
303	1.50	6.96	18.42	1.50	1.50	1.50	0.17
313	3.00	6.96	18.42	1.50	1.50	1.50	0.45
318	4.50	7.80	18.00	1.50	1.40	1.50	0.59
326	2000	9.06	17.37	1.20	1.15	1.30	0.99

Table 7: The values for the distribution parameter a, the corresponding director orientational order parameters for ZLI-4792 + 10wt% of the C10 gelator together with the hyperfine spacings and linewidths used to simulate the spectra.

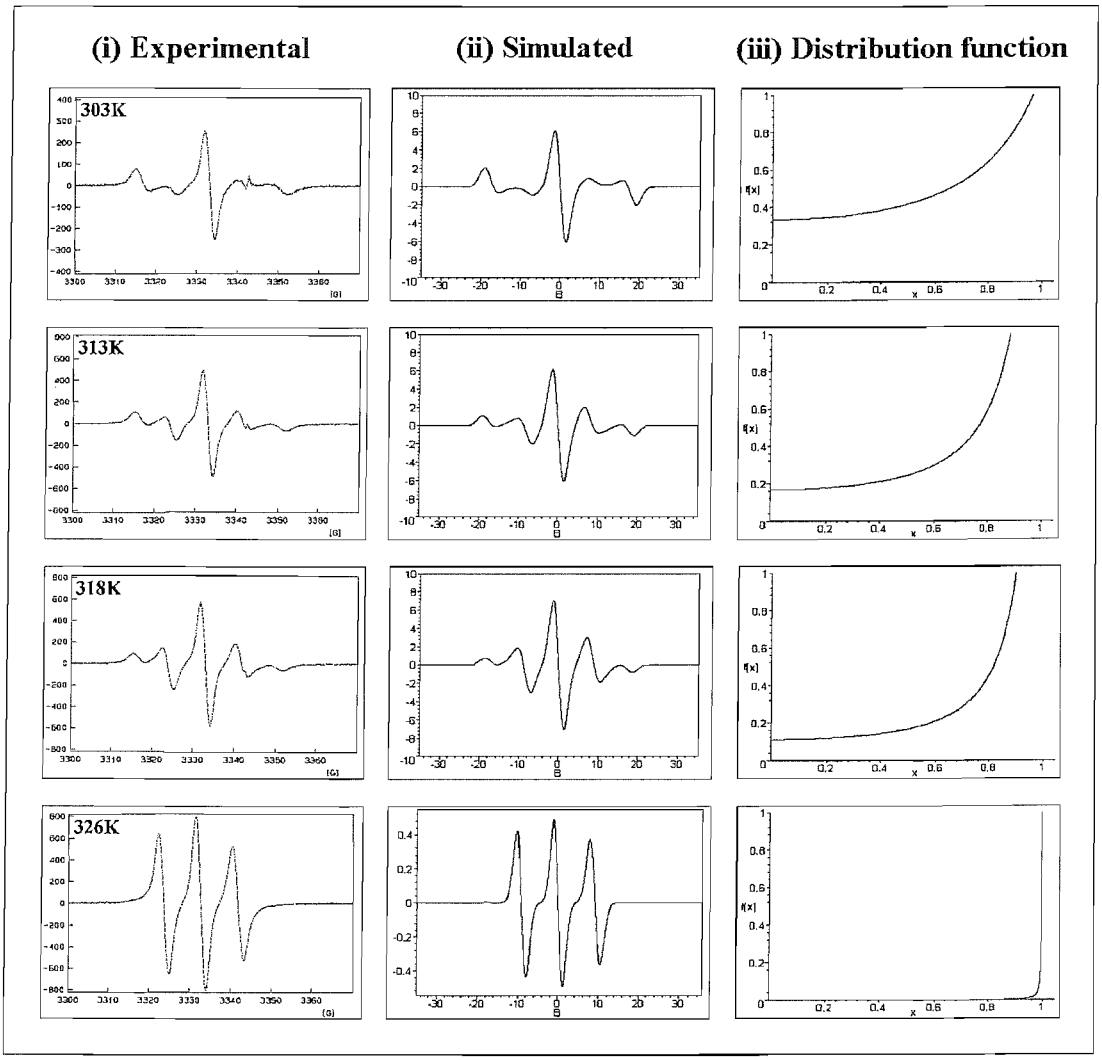

Figure 22: Experimental (i) and simulated (ii) spectra for ZLI-4792 + 10wt% C10 together with the director orientational distribution function (iii).

The simulated spectra are in good but not perfect agreement with their experimental counterparts.

5.5.4 ESR variable temperature results for ZLI-4792 + 10wt% C12

The first spectrum at 303K in Figure 19 suggests a three dimensional distribution for the director because the magnetic field (0.34T) is unable to align it. At 313K the sheet network of the gelator has dissolved sufficiently to allow the director to be almost fully aligned parallel to the field. At 323K the network has dissolved so the director is fully aligned parallel to the field. This gel is very similar to the 5wt% C10 gel. The spectral lines in these spectra are significantly broader than for the other samples and is probably due line broadening caused by dissolved oxygen as all the experimental parameters are the same as for the other experiments. The values of a, the parallel, $\widetilde{A}_{\|}$, and perpendicular, $\widetilde{A}_{\perp}$, hyperfine spacings together with the values for the linewidths of the three hyperfine lines used to simulate the spectra for cholestane dissolved in ZLI-4792 doped with 10wt% of the 1,12-bis-(phenyl-1-yloxy)dodecane (C12) gelator are given in Table 8. The corresponding director order parameters are also given in Table 8 and the experimental spectra along with the corresponding simulated spectra and the director distribution function plots are shown in Figure 23.

T / K	a	$\widetilde{A}_{\|}$ / G	$\widetilde{A}_{\perp}$ / G	ΔB_0 / G	ΔB_2 / G	ΔB_1 / G	$\overline{P}_2^n$
303	2.00	6.34	18.73	1.50	1.40	1.50	0.29
313	8.00	8.59	17.60	1.60	1.50	1.60	0.75
318	10.00	8.67	17.57	1.60	1.50	1.60	0.79
323	2000	8.90	17.45	1.60	1.50	1.60	0.99

Table 8: The values for the distribution parameter a, the corresponding director orientational order parameters for ZLI-4792 + 10wt% of the C12 gelator together with the hyperfine spacings and linewidths used to simulate the spectra.

The simulated spectra are again in good but not perfect agreement with their experimental counterparts. The baseline appears to be slightly distorted which is possibly due to a too weak a concentration of spin probe. This then allows the signal from the pyrex ESR tubes to be observed under the signal from the spin probe. Pyrex contains a variety of transition metal impurities which can be observed by ESR spectroscopy.

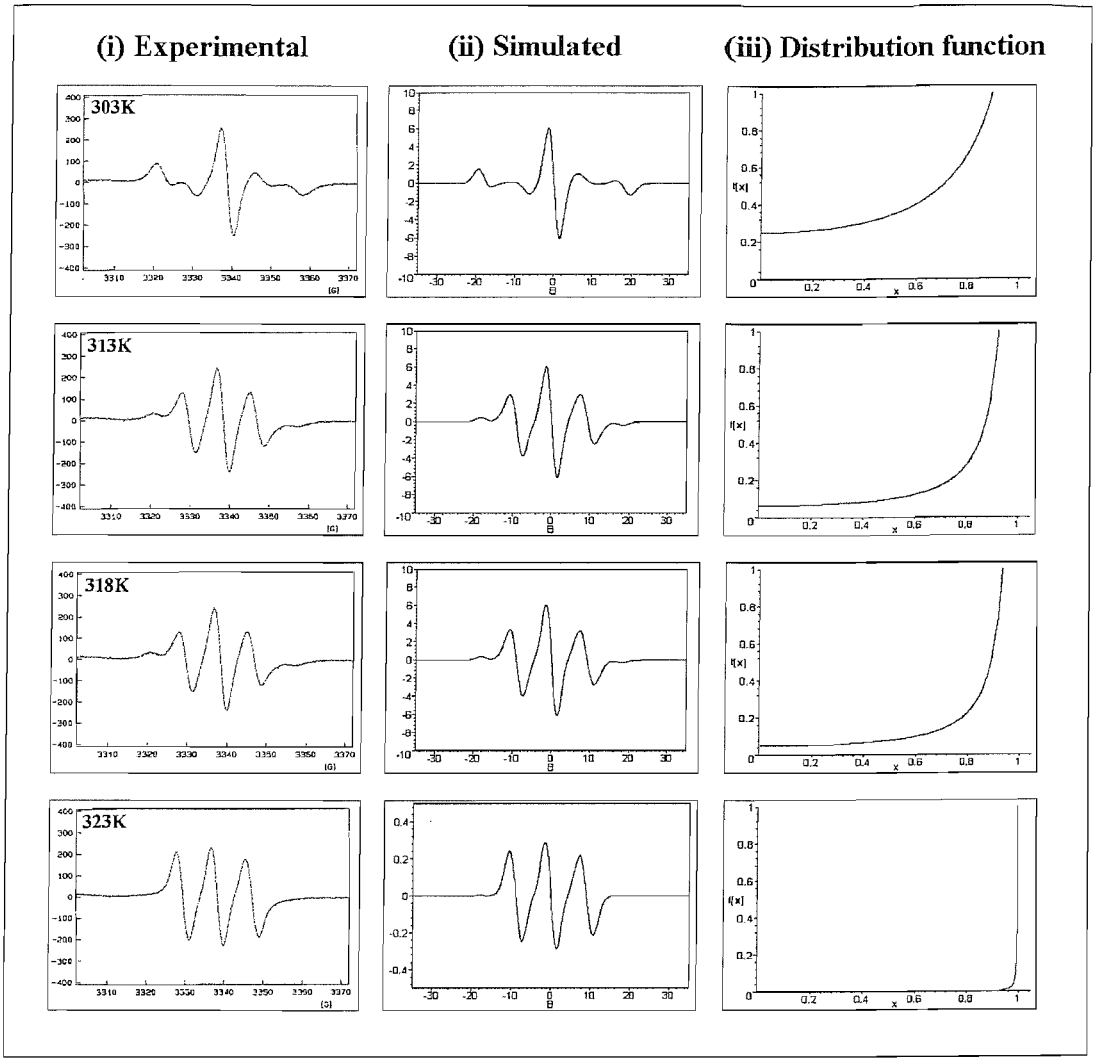

Figure 23: Experimental (i) and simulated (ii) spectra for ZLI-4792 + 10wt% C12 together with the director orientational distribution function (iii).

5.5.5 ESR variable temperature results for ZLI-4792 + 10wt% MeC10

The first spectrum at 303K in Figure 24 suggests a three dimensional distribution for the director because the magnetic field (0.34T) is unable to align it. This indicates that the gelator network is pinning the director at the surfaces of the network and the magnetic field of 0.335T is not strong enough to compete with this surface force. As the temperature is increased the network of sheets gradually dissolve allowing more of the director to be aligned by the magnetic field, this is because the average separation between the network of sheets increases allowing the field to align the director more readily. Full alignment by the magnetic field occurs at 328K, which is the highest temperature in comparison to all the gelators at which full alignment is achieved. The values of a, the parallel, $\widetilde{A}_{\|}$, and perpendicular, $\widetilde{A}_{\perp}$, hyperfine spacings together with the values for the linewidths of the three hyperfine lines used to simulate the spectra for cholestane dissolved in ZLI-4792 doped with 10wt% of the 10-bis-(4-methylphenyl-1-yloxy)decane (MeC10) gelator are

given in Table 9. The corresponding director order parameters are also given in Table 9 and the experimental spectra along with the corresponding simulated spectra and the director distribution function plots are shown in Figure 24.

T / K	a	$\tilde{A}_{\parallel}$ / G	$\tilde{A}_{\perp}$ / G	ΔB_0 / G	ΔB_2 / G	ΔB_1 / G	$\overline{P}_2^n$
303	3.00	6.65	18.57	1.30	1.60	1.80	0.45
313	5.50	6.96	18.42	1.50	1.50	1.50	0.65
318	10.00	7.26	18.27	1.50	1.50	1.50	0.79
328	2000	8.98	17.41	1.50	1.30	1.50	0.99

Table 9: The values for the distribution parameter a, the corresponding director orientational order parameters for ZLI-4792 + 10wt% of the MeC10 gelator together with the hyperfine spacings and linewidths used to simulate the spectra.

Again the simulated spectra are in good agreement with the equivalent experimental spectra.

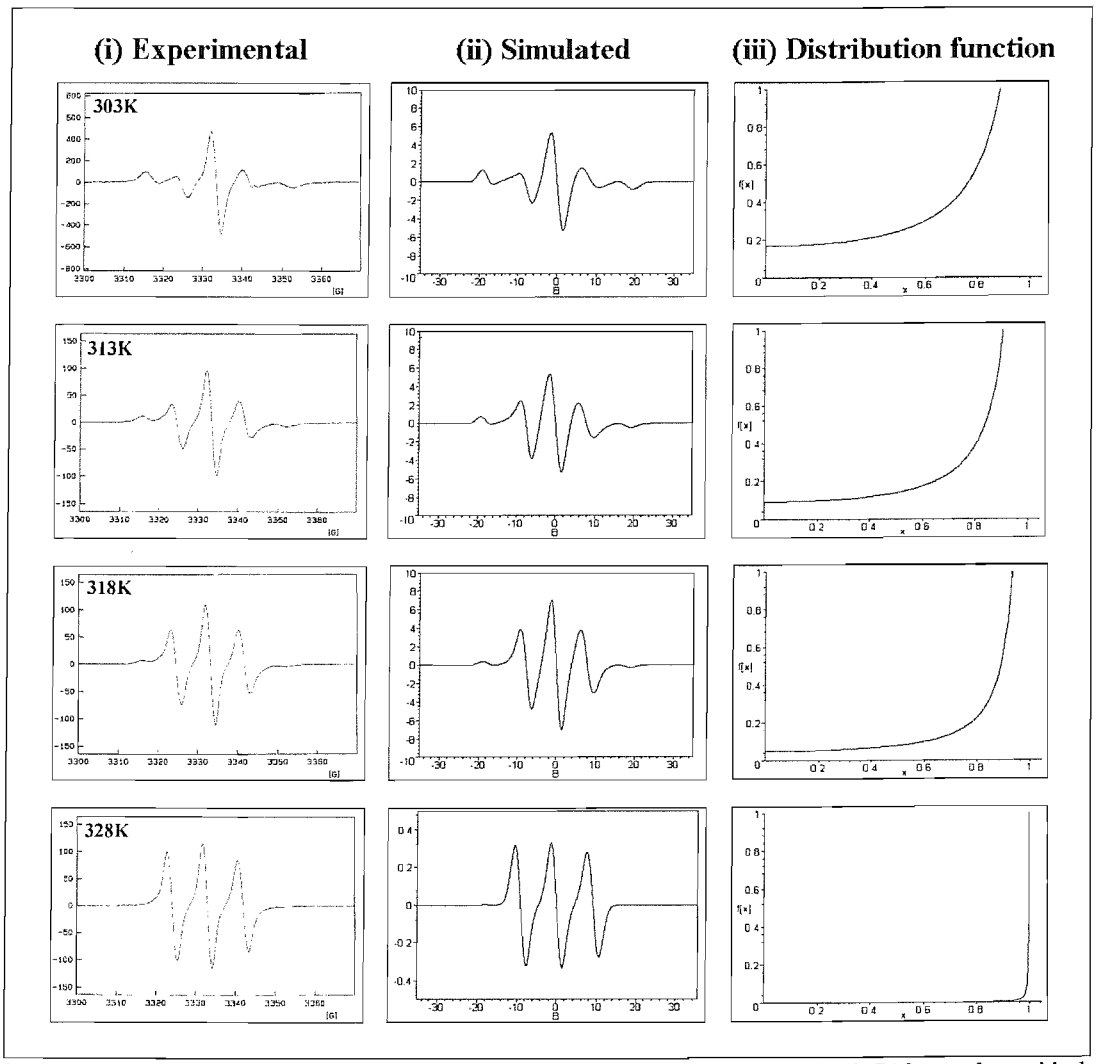

Figure 24: Experimental (i) and simulated (ii) spectra for ZLI-4792 + 10wt% MeC10 together with the director orientational distribution function (iii).

5.5.6 Comparison of the director orientational order parameters for all the gels

The director orientational order parameter, $\overline{P}_2^n$, has been plotted against the shifted temperatures for all of the gelled systems. This accounts for the difference in mesophase behaviour and allows direct comparison of the order parameters at the same shifted temperatures. The plot shown in Figure 25 indicates that the C8 and C10 gelled systems have much lower order than the other gels when compared at the same shifted temperatures. A lower director order parameter means that the gelator network is pinning the director at their surfaces more strongly preventing the magnetic field from aligning the director.

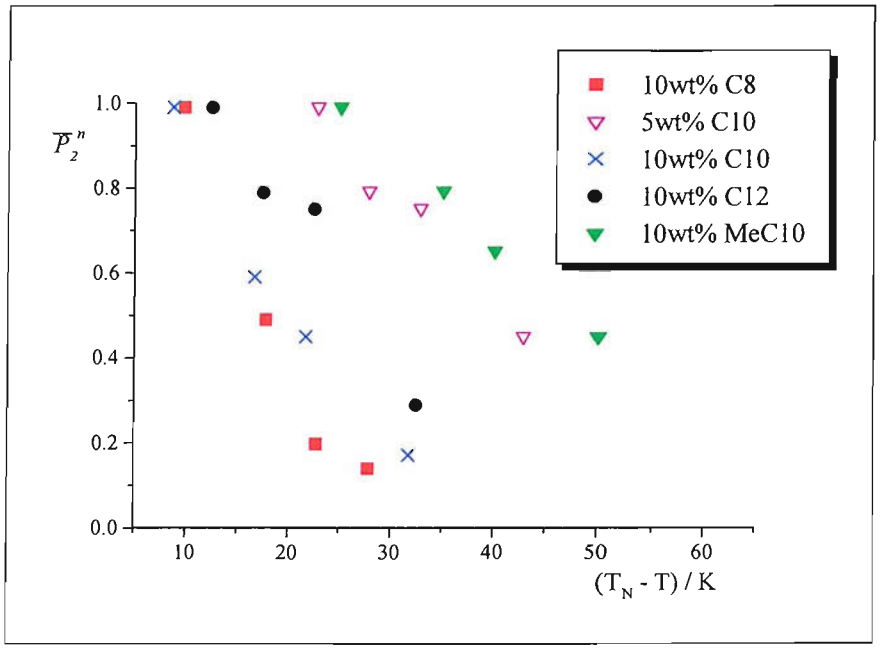

Figure 25: Comparison of the second rank director order parameter for the gelled systems on the shifted temperature scale.

5.5.7 ESR variable temperature results for 5CB + 0.25mol% Kato gelator 3

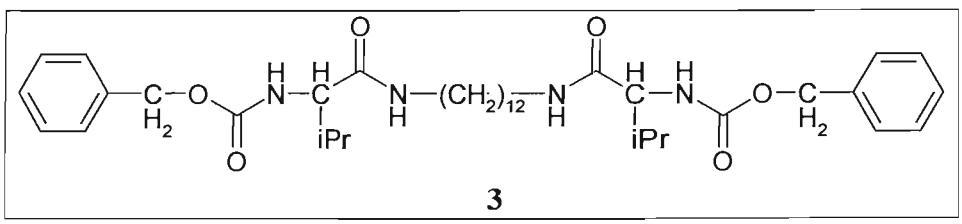

Figure 26: Structure of the Kato gelator [2].

The mixture of 5CB and 0.25mol% of gelator **3** was prepared as described in Section 5.5. This chiral hydrogen bonded gel was studied so that a comparison with the novel gelators, which are not chiral and cannot form hydrogen bonds, could be made.

T / K	a	$\widetilde{A}_{\parallel}$ / G	$\widetilde{A}_{\perp}$ / G	ΔB_0 / G	ΔB_2 / G	ΔB_1 / G	$\overline{P}_2^n$
293	1.00	9.06	17.37	2.30	1.69	4.40	0
303	1.00	9.70	17.05	2.07	1.69	2.92	0
313	/	14.74	/	1.54	1.37	2.07	/

Table 10: The values for the distribution parameter a, the corresponding director orientational order parameters for 5CB + 0.25mol% of the Kato **3** gelator together with the hyperfine spacings and linewidths used to simulate the spectra.

In this gel the network of fibres are held together via hydrogen bonding and do not gradually dissolve on heating like the C*n* gels. The spectra in general have broader lines compared with previous spectra because of the different host liquid crystal with its higher viscosity. The first spectrum at 293K in Figure 27 is indicative of a completely random distribution and as the temperature is increased the system does not become more ordered possibly due to the insolubility of the gelator. The distribution parameter, a, therefore remains constant at one. The final spectrum at 313K appears at first glance to be more ordered but is in fact due to the isotropic gel phase with a hyperfine spacing corresponding to ~15G. This gelator is dimeric like the novel gelators detailed previously, however, these novel gelators are not chiral and are unable to form hydrogen bonds like this gelator.

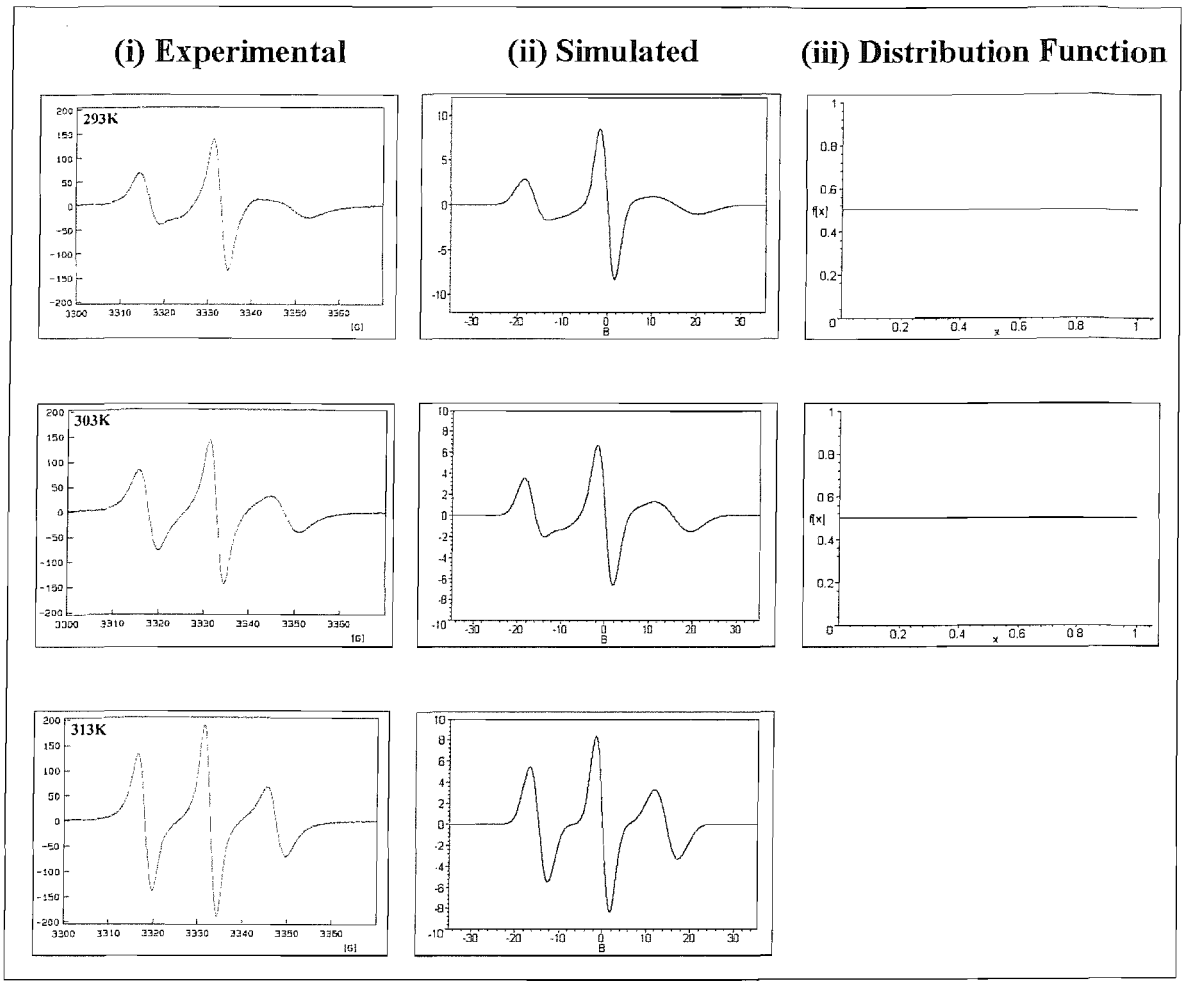

Figure 27: Experimental (i) and simulated (ii) spectra for 5CB + 0.25mol% Kato gelator **3** together with the director orientational distribution function (iii).

5.6 Solubility parameters of the Cn gelators

The formation of the gels is thought to be a result of low solubility combined with some kind of interaction between the gelator molecules and to explore this idea further the solubility of the gelators was investigated. The solubility of the dopants in ZLI-4792 has been estimated using the method described by Araya *et al.* [11]. In this the solubility parameter, δ, is defined as the square root of the cohesive energy density.

$$\delta = \left(\Delta E / V\right)^{1/2}, \tag{7}$$

where ΔE is the enthalpy of vaporisation and V is the molar volume. Using the solubility parameters, molar volumes and the melting points of the gelators along with their corresponding enthalpies the mole fractions of the dopant soluble in ZLI-4792 at various temperatures can be calculated using the Schroder-van Laar equation [11], see Chapter 4. In order for the solubility of the C*n* compounds to be calculated, the enthalpies of melting for each gelator are needed and were obtained from differential scanning calorimetry (DSC).

Compound	$\Delta H / Jg^{-1}$	$\Delta H / kJmol^{-1}$	$\Delta H / calmol^{-1}$	T_{mp} / K	$\Delta S / R$
C7	158.5	45.1	10762.4	327.2	16.8
C8	190.8	56.9	13599.9	357.2	19.2
C9	145.6	45.5	10867.5	333.2	16.5
C10	193.3	63.1	15076.2	358.2	21.2
C11	163.9	55.8	13334.8	337.2	20.1
C12	203.9	72.3	17266.2	359.2	24.1
Ref	101.0	33.0	7877.1	407.2	9.7

Table 11: Values of the melting points, enthalpies of melting and dimensionless entropies of melting for the 1,n-bis-(phenyl-1-yloxy)alkane, Cn, homologous series and 4,4'-bis-pentyloxybiphenyl (reference compound).

From Table 11 it is clear that as well as the melting points exhibiting an odd-even effect the enthalpies of melting and the dimensionless entropies do too.

Compound	$\delta / (calcm^{-3})^{1/2}$	$\Delta E / calmol^{-1}$	V / cm^3mol^{-1}
C7	9.77	25120	263.1
C8	9.71	26300	279.2
C9	9.65	27480	295.3
C10	9.59	28660	311.4
C11	9.55	29840	327.5
C12	9.50	31020	343.6
Ref	9.63	28550	308.2

Table 12: Solubility parameters, molar volumes and the energies of vaporization for the 1,n-bis-(phenyl-1-yloxy)alkane series and 4,4'-bis-pentyloxy-biphenyl.

The values for the enthalpies of vaporisation and the molar volumes together with the calculated solubility parameters for all of the gelators are given in Table 12.

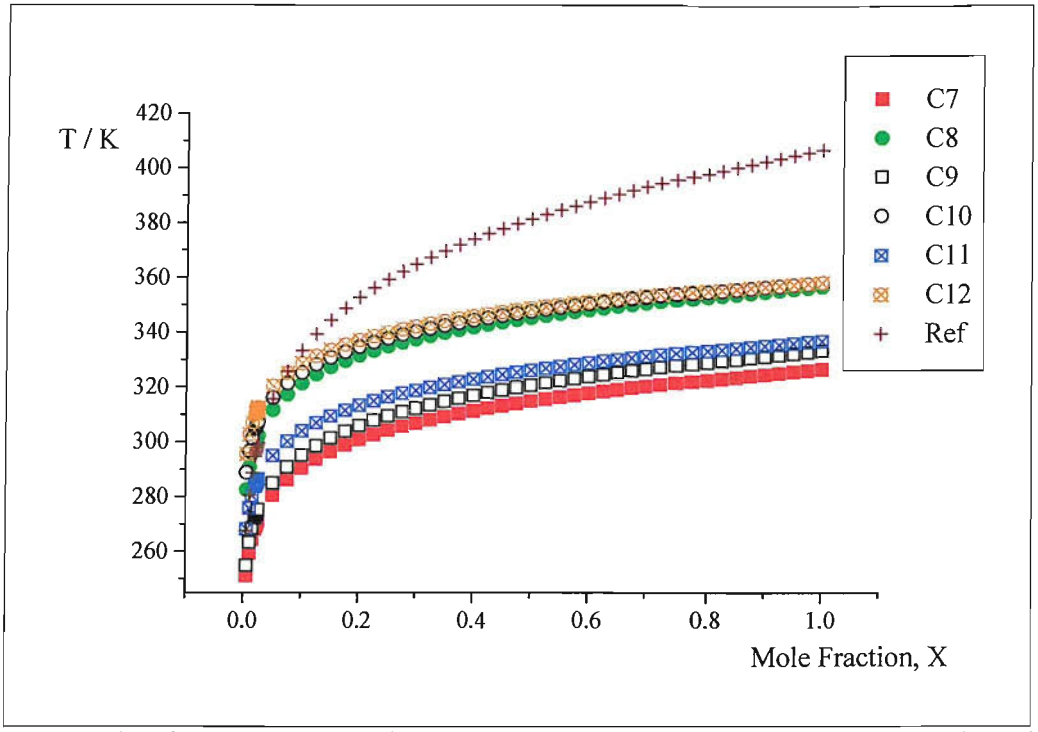

Figure 28: A plot of temperature vs. mole fraction for the 1,n-bis-(phenyl-1-yloxy)alkane series and the reference compound in ZLI-4792.

The mole fraction is the maximum concentration of dopant/gelator which will dissolve at the specified temperature. Figure 28 shows that at a given concentration (mole fraction) of the dopant, the temperature at which solubility in ZLI-4792 occurs is much higher for the even spaced dimers than for the odd. This is consistent with the observed odd-even effect in their melting points and enthalpies of melting, where the even gelators have higher melting points. The form of the plot indicates that the odd spaced dimers might form gels at lower temperatures below 290K. When samples of the odd spaced dimers in ZLI-4792 were placed in the refrigerator at 278K they all formed gels, which is consistent with this observation. It is also clear that changes in the temperature at low temperatures, (below 290K for the odd spacer length dimers and below 315K for the even), has little to no effect on the mole fraction which will dissolve i.e. the solubility.

The 4,4'-bis-pentyloxy-biphenyl (Ref), see Figure 29, was investigated because it is a structural isomer of the 1,10-bis-(phenyl-1-yloxy)decane (C10) dimer and it has a mesogenic structure. It was hoped that this compound would give some insight into the effect of the flexible spacers in the dimeric compounds.

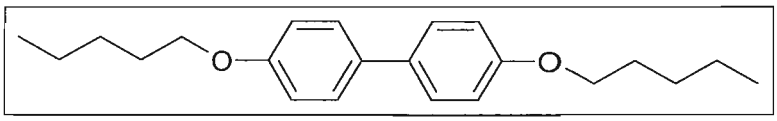

Figure 29: Structure of 4,4'-bis-pentyloxybiphenyl.

Unfortunately it was found to be insoluble in ZLI-4792. Figure 28 highlights this insolubility at temperatures below 320K.

5.7 ESR study of trimeric species

Three trimeric compounds were synthesised by M. Davis in order to study their behaviour when doped into ZLI-4792. The molecular structure of these trimers is similar to the dimeric compounds which act as gelators in a variety of liquid crystal hosts. It is of interest to see if these trimeric species also act as gelators.

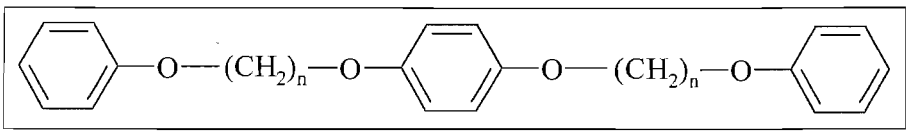

Figure 30: Molecular structure of trimeric compounds.

The chain lengths were n = 8 (TC8), n = 9 (TC9) and n = 10 (TC10). All three trimeric materials were found to gel ZLI-4792 at concentrations of 10wt% at room temperature. They were also found to gel deuteriated toluene which, like the Kato gels, shows that they can be used to gel conventional organic solvents too. Variable temperature ESR spectroscopy was carried out on these gels and the results compared to the dimeric gelled systems.

Samples of 10wt% of the trimers in ZLI-4792 were made as described in Section 5.5. The ESR spectroscopic experiment used to study the gelation was identical to that for the dimeric gelators.

5.7.1 Polarising microscopy

The transition temperatures for 10wt% of all three trimers in ZLI-4792 were measured using polarising microscopy as detailed in Section 5.4. The transition temperature $T_{N\text{-}Gel}$ is the temperature at which the gel phase has just fully dissolved on heating.

Mixture	$T_{N\text{-}Gel}$ / K	T_N / K	T_I / K
ZLI-4792	/	366.0	373.5
+ 10wt% TC8	/	362.7	384.2
+ 10wt% TC9	348.2	354.6	363.7
+ 10wt% TC10	/	364.3	380.2

Table 13: Mesophase behaviour of the trimeric gels.

The TC8 and TC10 gelators gel ZLI-4792 into the isotropic phase, whereas the gelator network of the TC9 dissolves just before the nematic transition leaving a range of approximately 7K in which the system is nematic. The increase in the isotropic transition temperature for the TC8 and TC10 doped systems indicates that these gelators have a higher anisotropy than the host mixture.

5.7.2 ESR variable temperature results for ZLI-4792 + 10wt% TC8

The first spectrum at 305K shows that the director is randomly distributed with the magnetic field unable to align it. As the temperature is increased the alignment of the director parallel to the magnetic field only increases slightly, indicating that the network of gelator is not dissolving. This is in contrast to the network of sheets of the dimeric gelators which dissolve into the nematic liquid crystal on heating allowing the alignment of the director by the magnetic field. This trimeric gelator is therefore a stronger gelator than the dimeric gelators.

The values of a used to simulate the spectra for cholestane dissolved in ZLI-4792 doped with 10wt% of the TC8 gelator are given in Table 14 together with the parallel and perpendicular hyperfine spacings and the linewidths for all three hyperfine lines. The corresponding director order parameters are also given in Table 14 and the experimental spectra along with the corresponding simulated spectra and the director distribution function plots are shown in Figure 31.

T / K	a	$\widetilde{A}_{\parallel}$ / G	$\widetilde{A}_{\perp}$ / G	ΔB_0 / G	ΔB_2 / G	ΔB_1 / G	$\overline{P}_2^n$
305	1.25	6.65	18.57	1.60	1.54	1.99	0.09
320	1.30	7.58	18.11	1.69	1.56	1.84	0.11
345	1.40	9.11	17.35	1.18	1.23	1.69	0.14
353	/	11.26	16.27	1.84	1.54	1.69	0

Table 14: The values for the distribution parameter a, the corresponding director orientational order parameters for ZLI-4792 + 10wt% of the TC8 gelator together with the hyperfine spacings and linewidths used to simulate the spectra.

The distribution parameter, a, only increases slightly over the 40K temperature range, therefore, the order parameters only change slightly indicating poor alignment by the magnetic field. The simulated spectra are in good agreement with the equivalent experimentally obtained spectra.

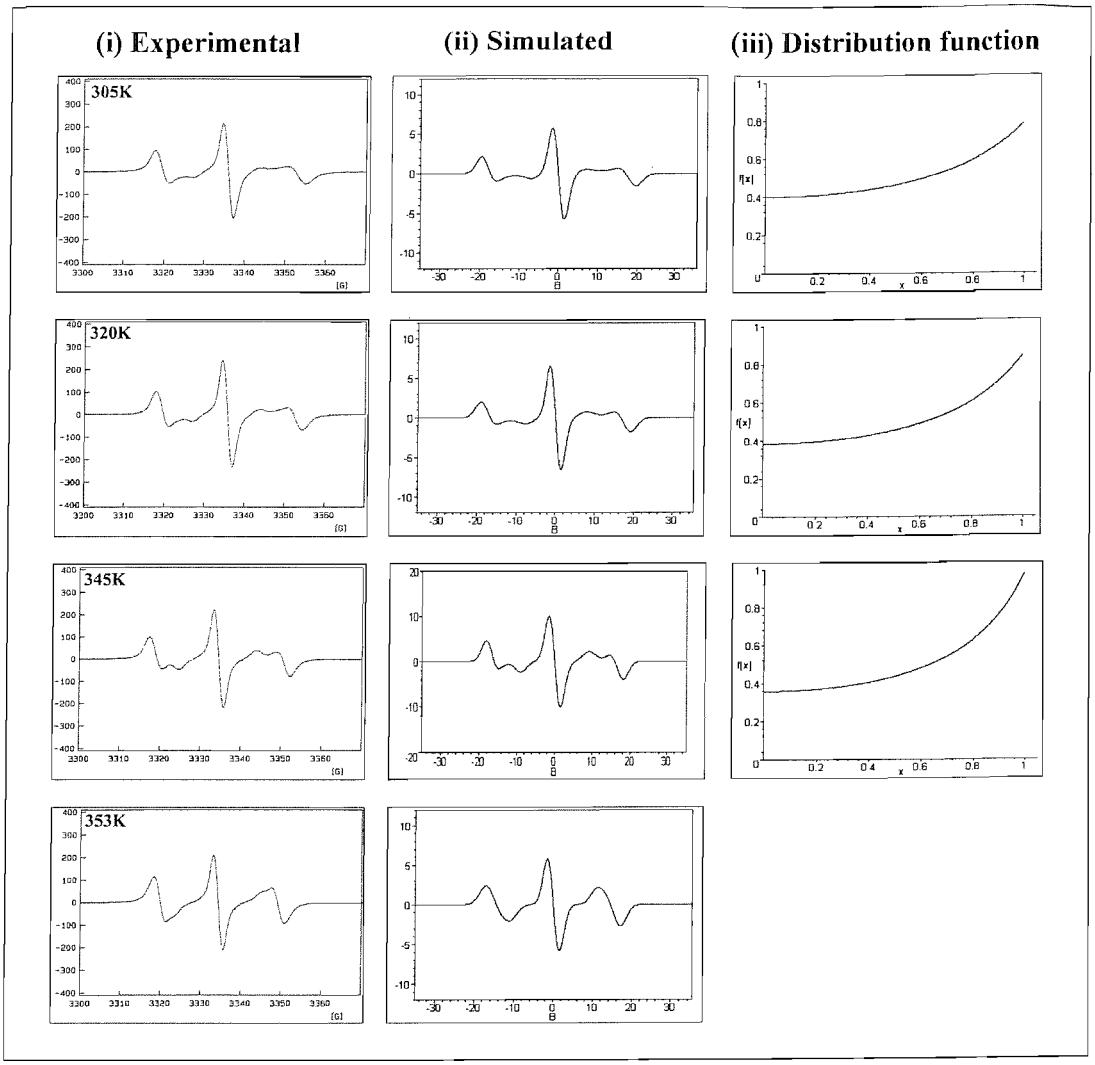

Figure 31: Experimental (i) and simulated (ii) spectra for ZLI-4792 + 10wt% TC8 along with the director orientational distribution function (iii).

5.7.3 ESR variable temperature results for ZLI-4792 + 10wt% TC9

The first spectrum is indicative of a random distribution of the director. As the temperature is increased the director is gradually aligned parallel to the magnetic field indicating that the network of the gelator is dissolving into the nematic liquid crystal and the director is no longer pinned at the surface. The fact that the nematic gel-nematic transition is lower than for the TC8 gel is interesting as it appears that there is an observed odd-even effect in the trimeric species too. The odd-spaced gelators are weaker gelling agents than the even-spaced trimeric gelators.

T / K	a	$\widetilde{A}_{\parallel}$ / G	$\widetilde{A}_{\perp}$ / G	ΔB_0 / G	ΔB_2 / G	ΔB_1 / G	$\overline{P}_2^n$
305	1.25	7.50	18.15	1.69	1.54	2.15	0.09
320	1.30	7.26	18.27	1.54	1.54	1.84	0.11
345	3.00	9.41	17.19	1.38	1.54	1.45	0.45
350	8.00	11.21	16.3	1.38	1.28	1.54	0.74

Table 15: The values for the distribution parameter a, the corresponding director orientational order parameters for ZLI-4792 + 10wt% of the TC9 gelator together with the hyperfine spacings and linewidths used to simulate the spectra.

The simulated spectra are consistent with their experimental counterparts.

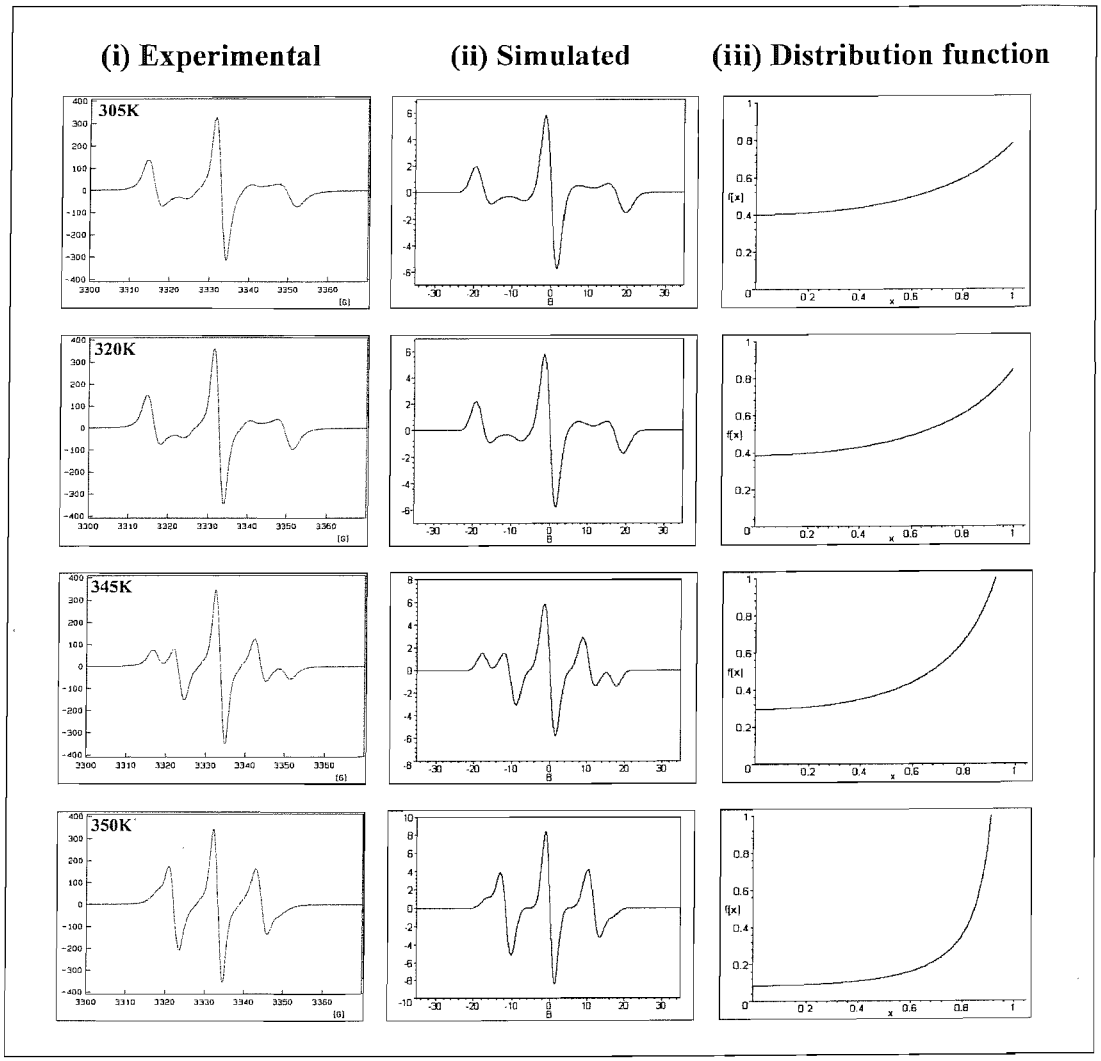

Figure 32: Experimental (i) and simulated (ii) spectra for ZLI-4792 + 10wt% TC9 along with the director orientational distribution function (iii).

5.7.4 ESR variable temperature results for ZLI-4792 + 10wt% TC10

The values of *a* used to simulate the spectra for cholestane dissolved in ZLI-4792 doped with 10wt% of the TC10 gelator are given in Table 16 together with the parallel and perpendicular hyperfine spacings and the linewidths for all three hyperfine lines. The corresponding director order parameters are also given in Table 16 and the experimental spectra along with the corresponding simulated spectra and the director distribution function plots are shown in Figure 33.

The first spectrum at 305K in Figure 33 shows a three dimensional distribution of the director. The network, made up of gelator, is preventing the magnetic field from aligning the director. As the temperature is increased there is little change in the spectrum indicating the director distribution is scarcely affected. The system remains gelled into the isotropic phase and as a consequence the isotropic transition temperature for the system is increased in comparison to the pure host mixture.

T / K	*a*	$\tilde{A}_{\parallel}$ / G	$\tilde{A}_{\perp}$ / G	ΔB_0 / G	ΔB_2 / G	ΔB_1 / G	$\overline{P}_2^n$
305	1.25	6.65	18.57	1.69	1.45	1.99	0.09
320	1.30	7.42	18.19	1.40	1.45	1.99	0.11
345	1.35	8.19	17.81	1.40	1.45	1.99	0.20

Table 16: The values for the distribution parameter *a*, the corresponding director orientational order parameters for ZLI-4792 + 10wt% of the TC10 gelator together with the hyperfine spacings and linewidths used to simulate the spectra.

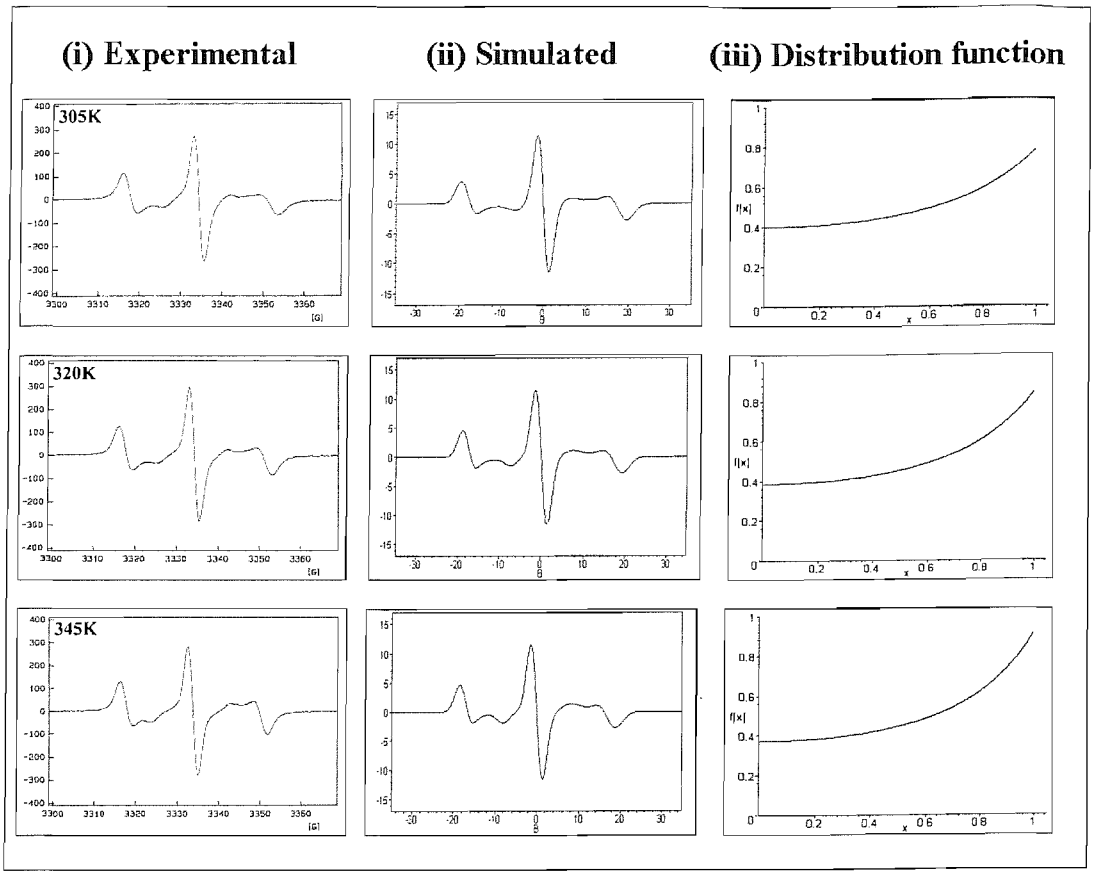

Figure 33: Experimental (i) and simulated (ii) spectra for ZLI-4792 + 10wt% TC10 along with the director orientational distribution function (iii).

5.8 Deuterium NMR

The ^{2}H NMR experiments in this section were kindly carried out by Azizah Mainal from the University of Southampton.

The deuteriated equivalents of the C8 (DC8-d_{10}) and C10 (DC10-d_{10}) dimers were synthesised to enable the study of the gel phase by deuterium NMR. It is of interest to examine what happens to the gelator when the gel is formed and the use of the deuteriated gelators allows such an observation.

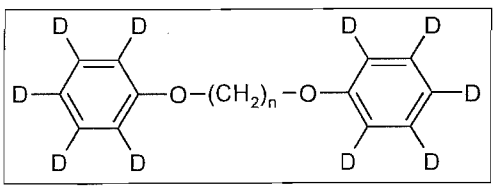

Figure 34: Molecular structure of 1,n-bis-(2,3,4,5,6-deuteriophenyl-1-yloxy)alkane with n=8 and 10.

ZLI-4792 containing 10wt% of the gelators was investigated using variable temperature deuterium NMR spectroscopy. These samples were prepared as described previously in Section 5.5 then they were transferred to a NMR tube. The spectrum of this deuteriated

gelator consists of two doublets; the first, which has the largest splitting, is due to the para-deuterons and the second doublet, which is split due to spin-spin coupling between adjacent deuterons, is from the ortho- and meta-deuterons which are not quite equivalent.

5.8.1 Variable temperature ^2H NMR for 10wt% 1,8-bis-(2,3,4,5,6-deuteriophenyl-1-yloxy)octane (DC8-d_{10}) in ZLI-4792

The spectra shown in Figure 35 are the variable temperature spectra for 10wt% 1,8-bis-(2,3,4,5,6-deuteriophenyl-1-yloxy)octane (DC8-d_{10}) in ZLI-4792 on cooling. The spectra have been autoscaled so the concentration of the gelator is related to the signal-to-noise level. The sample was left to equilibrate for 20 min in between changing the temperature. The first spectrum at 353K contains a single peak due to the gelator being dissolved in the isotropic phase. On lowering the temperature to 351K some nematic phase starts to appear indicated by the pair of doublets appearing, this shows that the gelator is distributed between the nematic phase and the isotropic phase. This is the biphasic region in which the nematic and isotropic phases coexist. On passing through the biphasic region the isotropic peak decreases in intensity and the nematic peaks increase in intensity until the entire sample is nematic and the isotropic peak is no longer present at 331K, which is consistent with the value (333K) for the nematic transition temperature obtained from polarising microscopy. On decreasing the temperature further the nematic doublets start to decrease in intensity which is indicative of the gelator gradually coming out of solution because the spectrum from the crystal is extremely weak due to it being spread over a very wide frequency range. At 308K the outer doublet has completely disappeared whilst the inner doublet has become very weak in intensity. The outer doublet vanishes first due to its low relative intensity in comparison to the other doublet, which is because there are only two para-deuterons whilst there are four ortho-deuterons and four meta-deuterons. This suggests that the formation of the gel phase is a gradual process starting with the gelator coming out of solution, followed by the formation of the sheet-like network.

The order parameter of the para-deuterons, S_{zz}, of the gelator has been calculated using

$$\Delta\tilde{\nu} = \frac{3}{2} q_{CD} S_{zz}, \tag{8}$$

where $\Delta\tilde{\nu}$ is the splitting of the outer doublet and q_{CD} is the quadrupolar coupling constant for aromatic deuterons and is equal to 186kHz. Figure 38 shows the variation of S_{zz} with temperature. As the temperature is decreased the order parameter decreases.

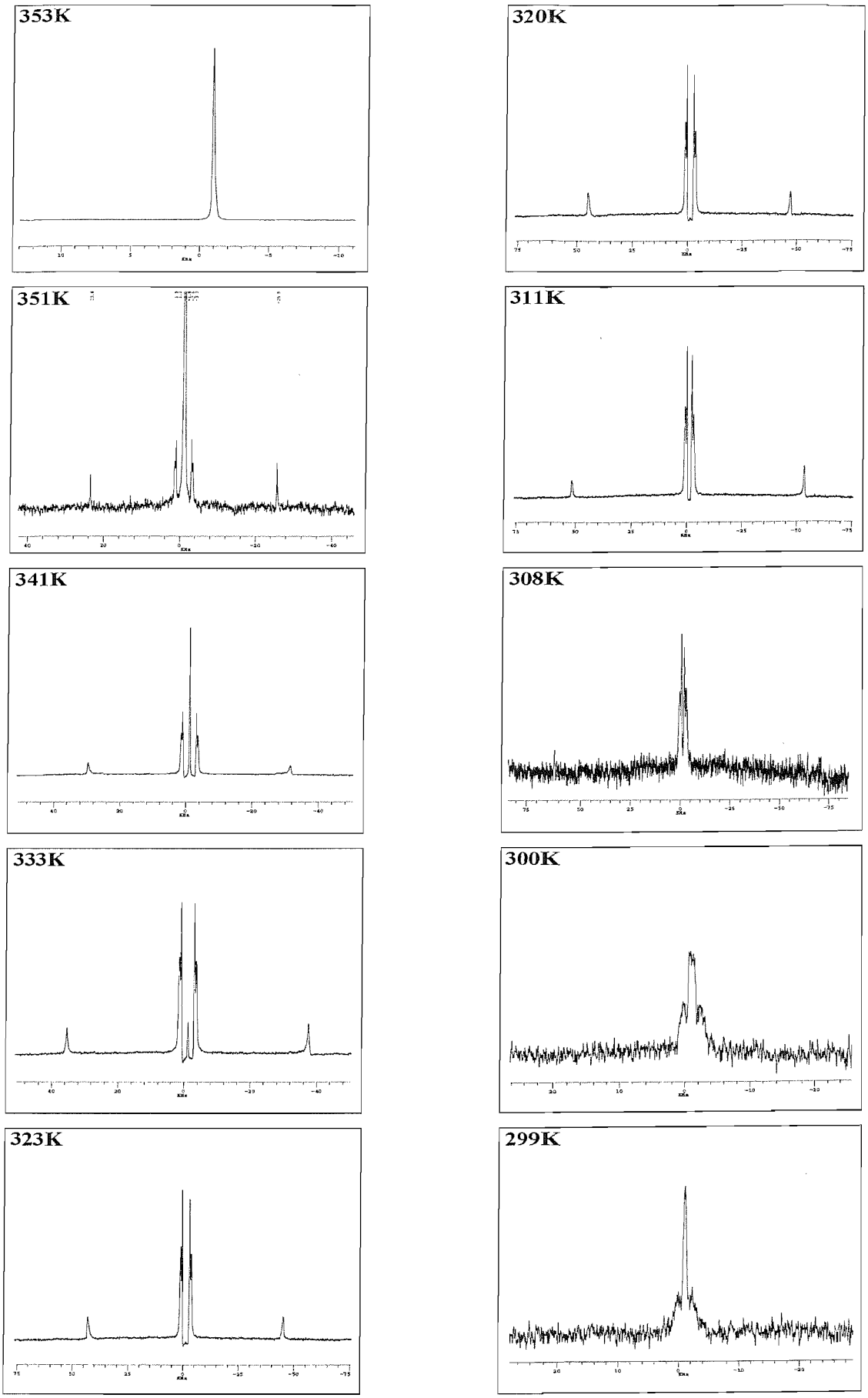

Figure 35: ^{2}H NMR variable temperature experiment for 10wt% 1,8-bis-(2,3,4,5,6-deuteriophenyl-1-yloxy)octane (DC8-d_{10}) in ZLI-4792.

5.8.2 Variable temperature ^2H NMR for 10wt% 1,10-bis-(2,3,4,5,6-deuteriophenyl-1-yloxy)dectane (DC10-d_{10}) in ZLI-4792

The spectra shown in Figure 36 are the variable temperature spectra for 10wt% 1,10-bis-(2,3,4,5,6-deuteriophenyl-1-yloxy)decane (DC10-d_{10}) in ZLI-4792 on cooling. The spectra have been autoscaled so the concentration of the gelator is related to the signal-to-noise level. The spectrum at 360K contains a single peak due to the isotropic phase. As the temperature is decreased two sets of doublets start to appear as the biphasic region is reached. This indicates that the DC10-d_{10} is dissolved in both the nematic and isotropic phases of the liquid crystal host. As the sample is cooled through the biphasic region something unusual is observed in the spectrum; the outer doublet starts to spread out and the quadrupolar splittings of both sets of doublets increase. This phenomenon has been observed previously and is due to the formation of a concentration gradient across the sample as it is cooled from the isotropic phase [12]. On cooling through the biphasic region droplets of nematic form, drop to the bottom of the sample and coalesce to form a layer of nematic phase and as the rate of molecular diffusion is slow in comparison to the experimental timescale the sample ends with several layers of nematic phase all with different concentrations. In the spectrum at 336K the outer doublet has been spread out so much that its intensity is very low. The isotropic peak has completely disappeared and the intensities of the nematic peaks are greatly reduced because the DC10-d_{10} is coming out of solution and by 291K very little remains in the liquid crystal phase of the host. This suggests that the formation of the gel phase is a gradual process starting with the gelator coming out of solution, followed by the formation of the sheet-like network.

The spectra shown in Figure 37 are the variable temperature spectra for 10wt% 1,10-bis-(2,3,4,5,6-deuteriophenyl-1-yloxy)decane (DC10-d_{10}) in ZLI-4792 on heating from the gel phase at room temperature. Again the spectra have been autoscaled so the concentration of the gelator is related to the signal-to-noise level. At 293K the system is in the gel phase and the intensity of the peaks in the spectrum are weak. On increasing the temperature, more of the gelator dissolves into, and is ordered by, the nematic phase. This is shown by the increase in the intensity of the peaks and the reduction of the noise level. The splitting of the outer doublet, due to the para-deuterons, decreases on increasing the temperature indicating a decrease in the order of the gelator, see Figure 38. At 333K the outer doublet begins to show a concentration gradient which persists until 343K. The biphasic region appears in between 333K and 338K, which is consistent with the values obtained from the cooling cycle and from polarising microscopy (334.9K). The system becomes isotropic at 353K, which is slightly lower than the value obtained on cooling.

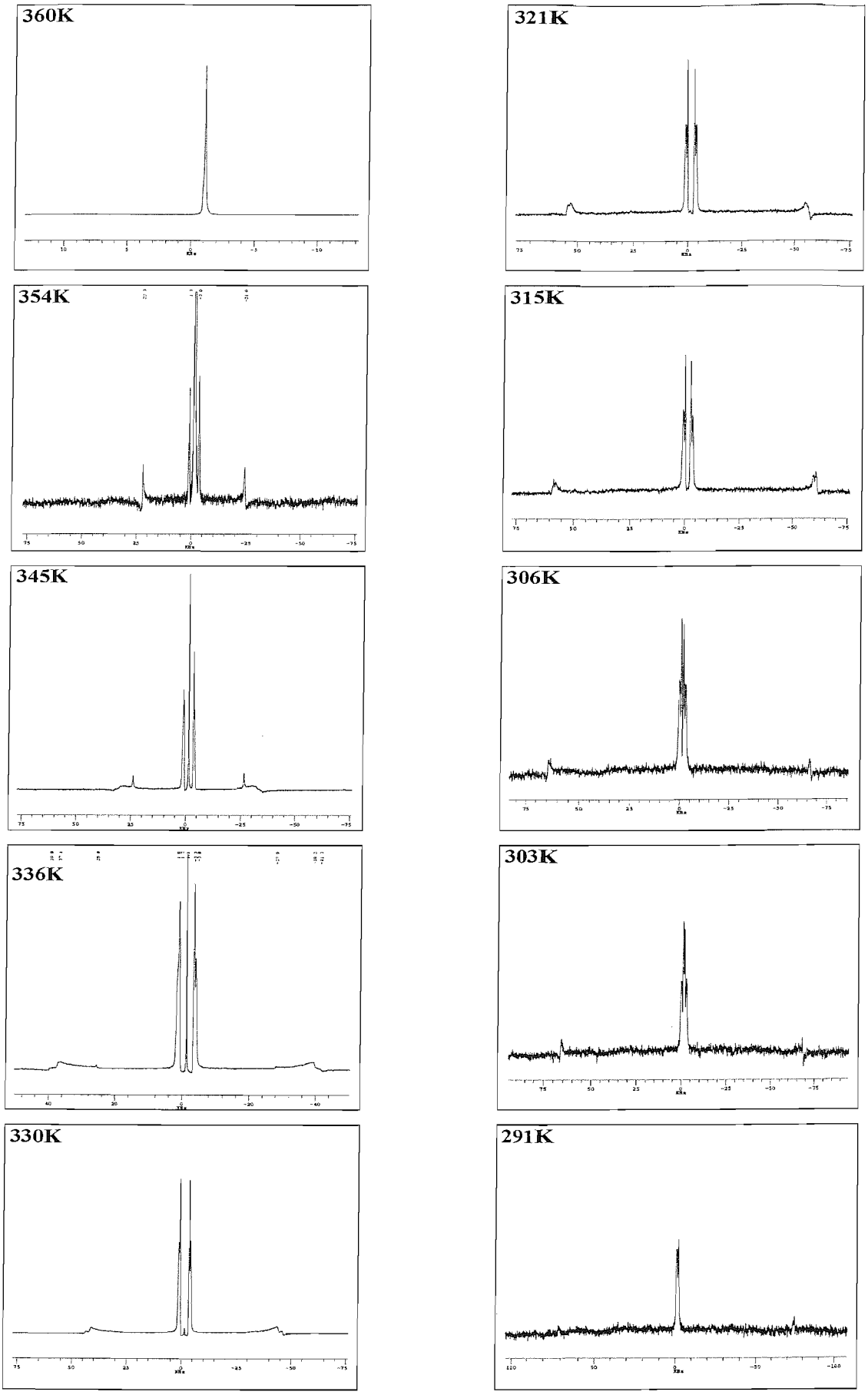

Figure 36: ^{2}H NMR variable temperature experiment for 10wt% 1,10-bis-(2,3,4,5,6-deuteriophenyl-1-yloxy)decane (DC10-d_{10}) in ZLI-4792 on cooling from the isotropic phase.

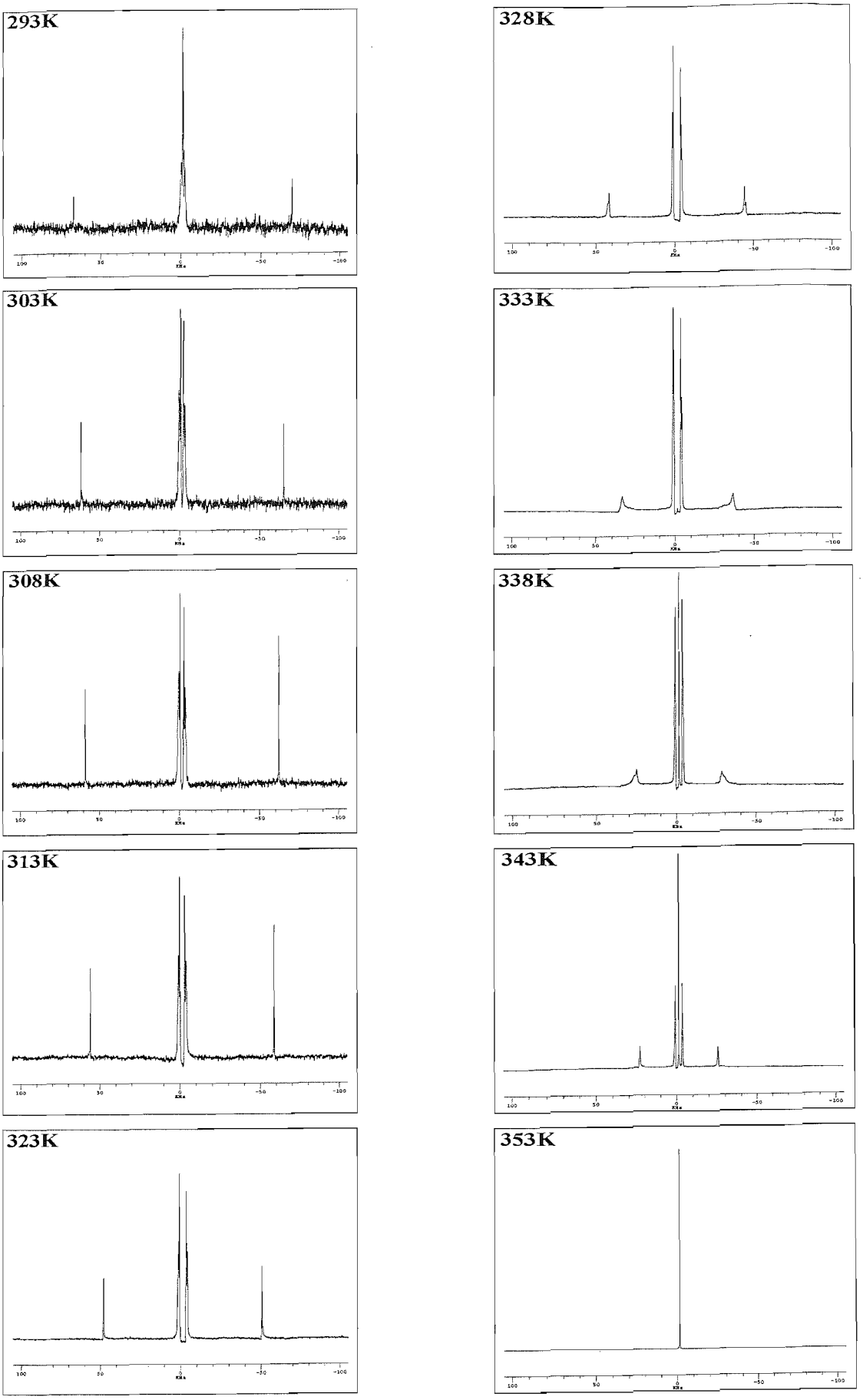

Figure 37: ^{2}H NMR variable temperature experiment for 10wt% 1,10-bis-(2,3,4,5,6-deuteriophenyl-1-yloxy)decane (DC10-d_{10}) in ZLI-4792 on heating from the gel phase.

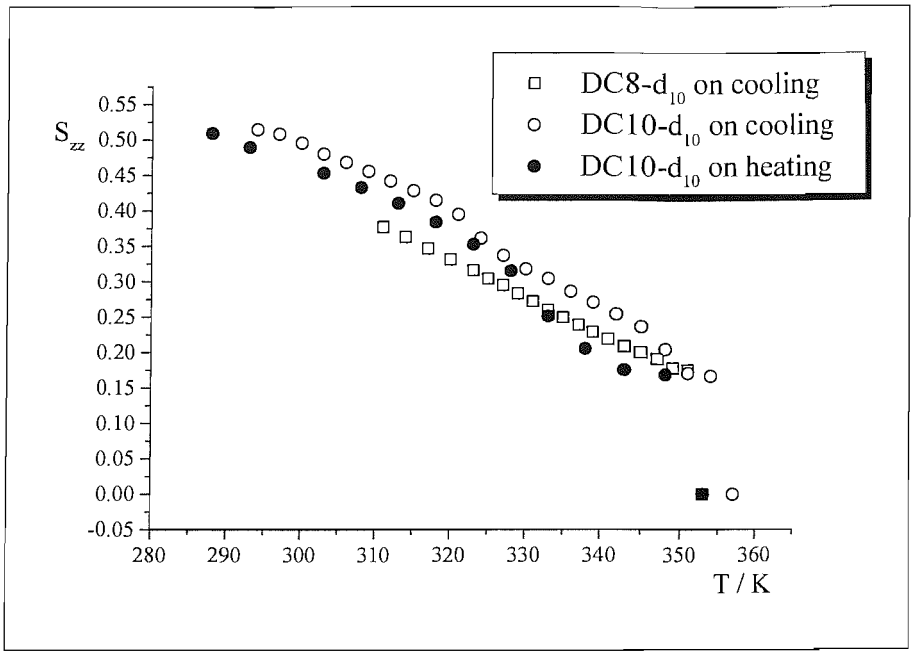

Figure 38: A plot showing the variation of the order parameter of the para-deuterons, S_{zz}, with temperature for 10wt% DC8-d_{10} in ZLI-4792 on cooling and 10wt% DC10-d_{10} in ZLI-4792 on heating and cooling.

The order parameter, S_{zz}, differs for the heating and cooling cycles for 10wt% DC10-d_{10} in ZLI-4792 because the concentration gradient makes it difficult to measure the splittings accurately. The order parameters for 10wt% DC10-d_{10} in ZLI-4792 is slightly higher than for 10wt% DC8-d_{10} in ZLI-4792 when comparing the cooling data. This shows that the DC10-d_{10} gelator is ordered by the nematic phase to a greater extent than the DC8-d_{10} gelator.

5.9 Conclusion

It has been shown that even-numbered spacer length dimers of the 1,n-bis-(phenyl-1-yloxy)alkane homologous series form gels in a series of liquid crystal hosts. These novel gelators have been compared with gels in which the fibrous network is held together by hydrogen bonds between the gelator molecules. Our new gelators are unable to form hydrogen bonds and the type of interaction between the gelator molecules, although unknown, is much weaker than hydrogen bonding. This is supported by the gradual destruction of the gel phase (i.e. the dissolution of the gelator) on heating observed in the ESR spectra for these new gelators. The hydrogen bonded gelators, however, do not dissolve on heating and the fibrous network remains present into the isotropic phase. The results from the NMR experiments indicate that the formation of the gel phase on cooling is also a gradual process and shows that the gelator comes out of solution when the gel is formed. This supports the theory that interactions between the gelator molecules leads to

the formation of the gel network which, considering the sheet-like packing of the crystals of the pure gelators, is probably made up of layers of sheets that trap the liquid crystal.

5.10 References

[1] T. Kato, T. Katsuna, K. Hanabusa and M. Ukon; Adv. Mater., **10**, (1998), 606.

[2] N. Mizoshita, Y. Suzuki, K. Kishimoto, K. Hanabusa and T. Kato; J. Mater. Chem., **12**, (2002), 2197.

[3] D. W. A. Sharp; *Dictionary of Chemistry*, **Vol. 2**, (1990), Penguin Books, London.

[4] P. W. Atkins; *Physical Chemistry*, **6th Edition**, (1998), Oxford University Press.

[5] A. Aggeli, I. A. Nyrkova, M. Bell, L. Carrick, T. C. B. McLeish, A. N. Semenov and N. Boden; P. N. A. S., **98**, (2001), 11857.

[6] K. Hanabusa, M. Yamada, M. Kimura and H. Shirai; Angew. Chem. Int. Ed. Engl., **35**, (1996), 1949.

[7] N. Mizoshita, K. Hanabusa and T. Kato; Adv. Mater., **11**, (1999), 392.

[8] N. Mizoshita, K. Hanabusa and T. Kato; Displays, **22**, (2001), 33.

[9] C. T. Imrie and G. R. Luckhurst in *Handbook of Liquid Crystals* Eds: D. Demus, J. W. Goodby, G. W.Gray, H. W. Spiess and V. Vill (Wiley-VCH, Weinheim, 1998) **2B**.

[10] S. M. Fan, G. R. Luckhurst and S. J. Picken; J. Chem. Phys., **101**, (1994), 3255.

[11] K. Araya and K. Iwasaki; Mol. Cryst. Liq. Cryst., **392**, (2002), 49.

[12] T. W. Cheung, S. Fan, G. R. Luckhurst and D. L. Turner; J. Chem.Soc., Faraday Trans., **93**, (1997), 3099.

Chapter 6

Experimental

6.1 Introduction

The general synthetic procedures are outline in Chapter 4 in Section 4.2.

The interpretation of the proton and carbon NMR spectra for the dimers containing fluorine and deuterium was aided using the following typical spin-spin coupling constants.

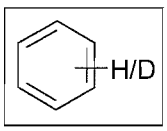

$^{1}J_{CH} = 159$ Hz

$^{1}J_{CD} = J_{CH} \times (\gamma_D/\gamma_H)$

$\gamma_D = 4.11 \times 10^{7}\ T^{-1}s^{-1}$

$\gamma_H = 26.75 \times 10^{7}\ T^{-1}s^{-1}$

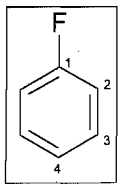

$^{1}J_{CF} = 245$ Hz

ortho / $^{2}J_{CF} = 21$ Hz

meta / $^{3}J_{CF} = 8$ Hz

para / $^{4}J_{CF} = 3$ Hz

These values are for mono-substituted benzene but the general trend in the coupling constants remains the same for poly-substituted benzene derivatives.

Each synthetic procedure has a prefixing code like *[sml/2954/23]*; this indicates the person who actually made the samples under supervision from Sophie Marchant-Lane and the lab book and page number in which the procedure can be found.

*[sml/2954/**]* = Sophie Marchant-Lane.

*[rjw/2920/**]* = Robert Wood (summer student).

[mnt] = Maria-Nefeli Tsaloglou (undergraduate student).

*[tod/3280/**]* = Tim Davis (summer student).

*[md/3978/**]* = Martin Davis (undergraduate student).

6.2 Synthesis and characterisation

6.2.1 Synthesis of 1,7-bis-(phenyl-1-yloxy)heptane, C7

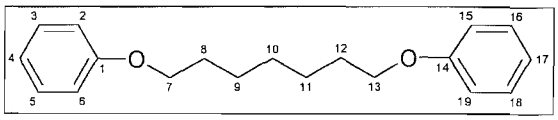

[sml/2954/23]

Phenol ($10.6x10^{-3}$mol, 1.00g) was dissolved in DMF (30ml) and potassium carbonate (5.13g) was added. The mixture was then stirred at ~100°C under N_2 for 2 h. This was then followed by the dropwise addition of 1,7-dibromoheptane ($5.31x10^{-3}$mol, 0.91ml). The mixture was again stirred under nitrogen for seven days at room temperature. TLC at this stage showed the reaction to be complete (50% DCM in 40/60 petroleum ether eluent). Water (2 x 50ml) was added to the reaction mixture, which was shaken vigorously, and a solid was recovered by filtration at the pump. The solid was recrystalised from the minimum quantity of hot ethanol (~5ml) to afford white crystals (1.05g, 70%) which had a mp = 54°C. (Lit. [1] mp. = 54.5°C).

^{1}H NMR($CDCl_3$) δ (ppm): 7.30 (m, 4H; C^3H, C^5H, $C^{16}H$, $C^{18}H$), 6.95 (m, 6H; C^2H, C^6H, $C^{15}H$, $C^{19}H$, C^4H, $C^{17}H$), 4.00 (t, J=6.62Hz, 4H; C^7H_2, $C^{13}H_2$), 1.75 (quintet, J=6.62Hz, 4H; C^8H_2, $C^{12}H_2$), 1.50 (m, 6H; C^9H_2, $C^{10}H_2$, $C^{11}H_2$).

^{13}C NMR ($CDCl_3$) δ (ppm): 159.3 (C^1, C^{14}), 129.6 (C^3, C^5, C^{16}, C^{18}), 120.7 (C^4, C^{17}), 114.6 (C^2, C^6, C^{15}, C^{19}), 67.9 (C^7, C^{13}), 29.4 (C^8, C^{12}), 29.3 (C^{10}), 26.2 (C^9, C^{11}).

EIMS (DCM) m/z: 284.3 ($[M]^+$, 19.7%), 107.2 ($[C_7H_7O]^+$, 16.7%), 95.2 ($[C_6H_7O]^+$, 12.3%), 94.2 ($[C_6H_6O]^+$, 100%), 69.2 ($[C_5H_9]^+$, 8.6%), 55.2 ($[C_4H_7]^+$, 48.4%), 41.2 ($[C_3H_5]^+$, 14.3%).

See Appendix C for full crystal structure analysis. The melting point is the same as the literature value which indicates purity and the proton NMR spectrum is clean which gives an indication of purity to ±5% accuracy. The parent ion in the mass spectrum has the same mass as the C7 dimer.

6.2.2 Synthesis of 1,8-bis-(phenyl-1-yloxy)octane, C8

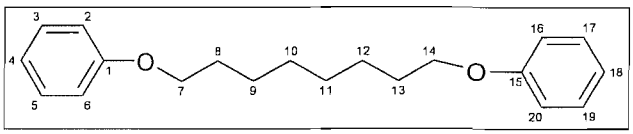

[sml/2954/21]

The synthetic procedure was identical to procedure 6.2.1. Phenol ($10.6x10^{-3}$mol, 1.00g), DMF (30ml), K_2CO_3 (5.13g) and 1,8-dibromooctane ($5.31x10^{-3}$mol, 0.98ml). The solid was recrystalised from the minimum quantity of hot ethanol (~5ml) to afford white crystals (1.11g, 70%) which had a mp= 84°C. (Lit. [1] mp = 84°C).

^{1}H NMR($CDCl_3$) δ (ppm): 7.30 (m, 4H; C^3H, C^5H, $C^{17}H$, $C^{19}H$), 6.95 (m, 6H; C^2H, C^6H, $C^{16}H$, $C^{20}H$, C^4H, $C^{18}H$), 4.00 (t, J=6.62Hz, 4H; C^7H_2, $C^{14}H_2$), 1.75 (quintet, J=6.62Hz, 4H; C^8H_2, $C^{13}H_2$), 1.50 (m, 8H; C^9H_2, $C^{10}H_2$, $C^{11}H_2$, $C^{12}H_2$).

^{13}C NMR ($CDCl_3$) δ (ppm): 159.3 (C^1, C^{15}), 129.6 (C^3, C^5, C^{17}, C^{19}), 120.6 (C^4, C^{18}), 114.6 (C^2, C^6, C^{16}, C^{20}), 68.0 (C^7, C^{14}), 29.5 (C^8, C^{13}), 29.4 (C^{10}, C^{11}), 26.2 (C^9, C^{12}).

EIMS (DCM) m/z: 298.4 ($[M]^+$, 19.9%), 107.2 ($[C_7H_7O]^+$, 13.2%), 95.2 ($[C_6H_7O]^+$, 14.6%), 94.2 ($[C_6H_6O]^+$, 100%), 79.2 ($[C_6H_7]^+$, 10.3%), 69.2 ($[C_5H_9]^+$, 48.8%), 55.2 ($[C_4H_7]^+$, 28.1%), 41.2 ($[C_3H_5]^+$, 16.8%).

See Appendix C for full crystal structure analysis. The melting point is the same as the literature value which indicates purity and the proton NMR spectrum is clean which gives an indication of purity to ±5% accuracy. The parent ion in the mass spectrum has the same mass as the C8 dimer.

6.2.3 Synthesis of 1,9-bis-(phenyl-l-yloxy)nonane, C9

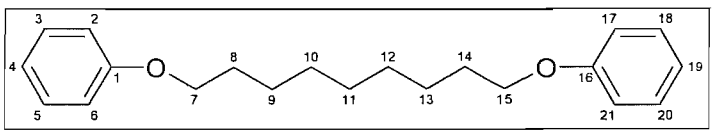

[rjw/2920/01]

The synthetic procedure was identical to that in 6.2.1 except that hot methanol was used for the recrystallisation because it gave larger crystals. Phenol ($6.0x10^{-3}$mol, 0.57g), DMF (25ml), K_2CO_3 (3.00g) and 1,9-dibromononane ($2.5x10^{-3}$mol, 0.51ml). White crystals were obtained (0.62g, 79%). which had a mp = 60°C. (Lit. [1] mp = 62°C).

^{1}H NMR($CDCl_3$) δ (ppm): 7.30 (m, 4H; C^3H, C^5H, $C^{18}H$, $C^{20}H$), 6.93 (m, 6H; C^2H, C^6H, $C^{17}H$, $C^{21}H$, C^4H, $C^{19}H$), 4.00 (t, J=6.62Hz, 4H; C^7H_2, $C^{15}H_2$), 1.75 (quintet, J=6.62Hz, 4H; C^8H_2, $C^{14}H_2$), 1.50 (m, 10H; C^9H_2, $C^{10}H_2$, $C^{11}H_2$, $C^{12}H_2$, $C^{13}H_2$).

^{13}C NMR ($CDCl_3$) δ (ppm): 159.1 (C^1, C^{16}), 129.4 (C^3, C^5, C^{18}, C^{20}), 120.5 (C^4, C^{19}), 114.5 (C^2, C^6, C^{17}, C^{21}), 67.8 (C^7, C^{15}), 29.5 (C^8, C^{14}), 29.3 (C^{10}, C^{11}, C^{12}), 26.1 (C^9, C^{13}).

EIMS (DCM) m/z: 312.4($[M]^+$, 17.5%), 107.2 ($[C_7H_7O]^+$, 12.6%), 95.2 ($[C_6H_7O]^+$, 19.4%), 94.2 ($[C_6H_6O]^+$, 100%), 79.2 ($[C_6H_7]^+$, 9.7%), 69.2 ($[C_5H_9]^+$, 35.6%), 57.2 ($[C_4H_9]^+$, 4.1%), 55.2 ($[C_4H_7]^+$, 29.1%), 41.2 ($[C_3H_5]^+$, 15.3%).

6.2.4 Synthesis of 1,10-bis-(phenyl-1-yloxy)decane, C10

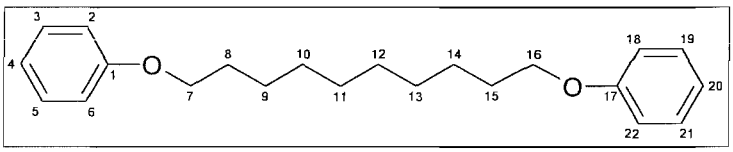

[rjw/2920/03]

The synthetic procedure was identical to that in 6.2.1 except that hot methanol was used for the recrystallisation. Phenol ($9.6x10^{-3}$mol, 0.90g), DMF (40ml), K_2CO_3 (4.80g) and 1,10-dibromodecane ($4.0x10^{-3}$mol, 1.20 g). White crystals were obtained (1.00g, 76%) which had a mp = 85°C. (Lit. [2] mp. = 85°C).

^{1}H NMR($CDCl_3$) δ (ppm): 7.30 (m, 4H; C^3H, C^5H, $C^{19}H$, $C^{21}H$), 6.94 (m, 6H; C^2H, C^6H, $C^{18}H$, $C^{22}H$, C^4H, $C^{20}H$), 4.00 (t, J=6.62Hz, 4H; C^7H_2, $C^{16}H_2$), 1.75 (quintet, J=6.62Hz, 4H; C^8H_2, $C^{15}H_2$), 1.50 (m, 12H; C^9H_2, $C^{10}H_2$, $C^{11}H_2$, $C^{12}H_2$, $C^{13}H_2$, $C^{14}H_2$).

^{13}C NMR ($CDCl_3$) δ (ppm): 159.2 (C^1, C^{17}), 129.4 (C^3, C^5, C^{19}, C^{21}), 120.5 (C^4, C^{20}), 114.5 (C^2, C^6, C^{18}, C^{22}), 67.9 (C^7, C^{16}), 29.5 (C^8, C^{15}), 29.3 (C^{10}, C^{11}, C^{12}, C^{13}), 26.1 (C^9, C^{14}).

EIMS (DCM) m/z: 326.3($[M]^+$, 28.8%), 107.2 ($[C_7H_7O]^+$, 13.4%), 94.1 ($[C_6H_6O]^+$, 100%), 79.2 ($[C_6H_7]^+$, 8.1%), 69.2 ($[C_5H_9]^+$, 17.1%), 55.2 ($[C_4H_7]^+$, 35.9%), 41.2 ($[C_3H_5]^+$, 25.3%).

6.2.5 Synthesis of 1,11-bis-(phenyl-1-yloxy)undecane, C11

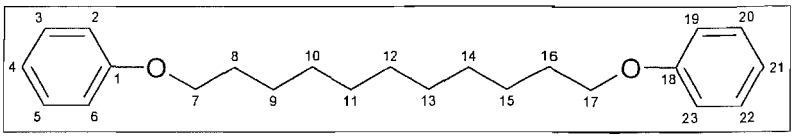

[mnt]

The synthetic procedure was identical to 6.2.1 except that column chromatography on silica (35% diethyl ether in petroleum ether 40-60) was used for purification. Phenol ($16.0x10^{-3}$mol, 1.50g), DMF (40ml), K_2CO_3 (6.50g) and 1,11-dibromoundecane ($8.0x10^{-3}$mol, 1.88ml). White crystals were obtained (1.35g, 50%) which had a mp = 64°C Lit. [3] mp = 66°C.

^{1}H NMR($CDCl_3$) δ (ppm): 7.28 (m, 4H; C^3H, C^5H, $C^{20}H$, $C^{22}H$), 6.93 (m, 6H; C^2H, C^6H, $C^{19}H$, $C^{23}H$, C^4H, $C^{21}H$), 3.97 (t, J=6.62Hz, 4H; C^7H_2, $C^{17}H_2$), 1.80 (quintet, J=6.62Hz, 4H; C^8H_2, $C^{16}H_2$), 1.40 (m, 14H; C^9H_2, $C^{10}H_2$, $C^{11}H_2$, $C^{12}H_2$, $C^{13}H_2$, $C^{14}H_2$, $C^{15}H_2$).

^{13}C NMR ($CDCl_3$) δ (ppm): 158.3 (C^1, C^{18}), 128.5 (C^3, C^5, C^{20}, C^{22}), 119.6 (C^4, C^{21}), 113.6 (C^2, C^6, C^{19}, C^{23}), 67.0 (C^7, C^{17}), 28.7 (C^8, C^{16}), 28.6 (C^{10}, C^{14}), 28.5 (C^{11}, C^{13}), 28.4 (C^{12}), 25.2 (C^9, C^{15}).

EIMS (DCM) m/z: 340.4 ($[M]^+$, 15.1%), 107.2 ($[C_7H_7O]^+$, 8.8%), 95.2 ($[C_6H_7O]^+$, 13.9%), 94.2 ($[C_6H_6O]^+$, 100%), 79.2 ($[C_6H_7]^+$, 7.5%), 69.2 ($[C_5H_9]^+$, 14.4%), 55.2 ($[C_4H_7]^+$, 24.4%), 41.2 ($[C_3H_5]^+$, 14.4%).

6.2.6 Synthesis of 1,12-bis-(phenyl-1-yloxy)dodecane, C12

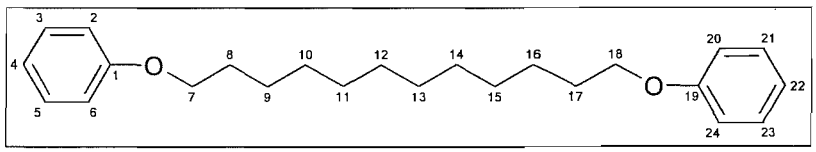

[mnt]

The synthetic procedure was identical to 6.2.1 except that column chromatography on silica (35% diethyl ether in petroleum ether 40-60) was used for purification. Phenol ($16.0x10^{-3}$mol, 1.5g), DMF (50ml), K_2CO_3 (6.5g), NaI (0.157g) and 1,12-dibromododecane ($8.0x10^{-3}$mol, 2.63g). White crystals were obtained (1.50g, 53%) which had a mp = 86°C. (Lit. [2] mp. = 86°C).

^{1}H NMR($CDCl_3$) δ (ppm): 7.20 (m, 4H; C^3H, C^5H, $C^{21}H$, $C^{23}H$), 6.84 (m, 6H; C^2H, C^6H, $C^{20}H$, $C^{24}H$, C^4H, $C^{22}H$), 3.90 (t, J=6.59Hz, 4H; C^7H_2, $C^{18}H_2$), 1.70 (quintet, J=6.59Hz, 4H; C^8H_2, $C^{17}H_2$), 1.30 (m, 16H; C^9H_2, $C^{10}H_2$, $C^{11}H_2$, $C^{12}H_2$, $C^{13}H_2$, $C^{14}H_2$, $C^{15}H_2$, $C^{16}H_2$).

^{13}C NMR ($CDCl_3$) δ (ppm): 159.2 (C^1, C^{19}), 129.4 (C^3, C^5, C^{21}, C^{23}), 120.4 (C^4, C^{22}), 114.5 (C^2, C^6, C^{20}, C^{24}), 67.9 (C^7, C^{18}), 29.4 (C^{10}, C^{11}, C^{12}, C^{13}, C^{14}, C^{15}), 26.1 (C^9, C^{16}).

EIMS (DCM) m/z: 354.3($[M]^+$, 25.2%), 107.2 ($[C_7H_7O]^+$, 10.7%), 95.2 ($[C_6H_7O]^+$, 14.2%), 94.2 ($[C_6H_6O]^+$, 100%), 79.2 ($[C_6H_7]^+$, 6.4%), 69.2 ($[C_5H_9]^+$, 17.6%), 55.2 ($[C_4H_7]^+$, 29.7%), 41.2 ($[C_3H_5]^+$, 21.8%).

6.2.7 Synthesis of 1,9-bis-(4-methylphenyl-1-yloxy)nonane, MeC9

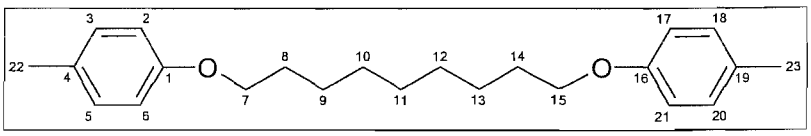

[rjw/2920/05]

The synthetic procedure was identical to 6.2.1 except that hot methanol was used for the recrystallisation. 4-methylphenol ($9.6x10^{-3}$mol, 1.04g), DMF (40ml), K_2CO_3 (4.8g) and 1,9-dibromononane ($4.0x10^{-3}$mol, 1.15g, 0.82ml). A white solid was obtained (0.48g, 35%) which had a mp= 63.5°C.

^{1}H NMR($CDCl_3$) δ (ppm): 7.09 (m, 4H; C^3H, C^5H, $C^{18}H$, $C^{20}H$), 6.81 (m, 4H; C^2H, C^6H, $C^{17}H$, $C^{21}H$), 3.90 (t, J=6.62Hz, 4H; C^7H_2, $C^{15}H_2$), 2.30 (singlet, 6H; $C^{22}H_3$, $C^{23}H_3$), 1.75 (quintet, J=6.62Hz, 4H; C^8H_2, $C^{14}H_2$), 1.49 (m, 10H; C^9H_2, $C^{10}H_2$, $C^{11}H_2$, $C^{12}H_2$, $C^{13}H_2$).

^{13}C NMR ($CDCl_3$) δ (ppm):157.1 (C^1, C^{16}), 130.0 (C^3, C^5, C^{18}, C^{20}), 129.8 (C^4, C^{19}), 114.5 (C^2, C^6, C^{17}, C^{21}), 68.2 (C^7, C^{15}), 29.7 (C^8, C^{14}), 29.5 (C^{10}, C^{11}, C^{12}), 26.2 (C^9, C^{13}), 20.6 (C^{22}, C^{23}).

A low yield was obtained due to problems with purification.

6.2.8 Synthesis of 1,10-bis-(4-methylphenyl-1-yloxy)decane, MeC10

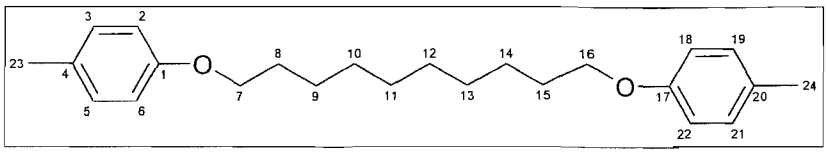

[rjw/2920/07]

The synthetic procedure was identical to 6.2.1 except that hot methanol was used for the recrystallisation. 4-methylphenol ($9.6x10^{-3}$mol, 1.04g), DMF (40ml), K_2CO_3 (4.8g) and 1,10-dibromodecane ($4.0x10^{-3}$mol, 1.20 g). A white solid was obtained (0.982g, 70%) which had a mp = 85°C.

^{1}H NMR($CDCl_3$) δ (ppm): 7.10 (m, 4H; C^3H, C^5H, $C^{19}H$, $C^{21}H$), 6.83 (m, 4H; C^2H, C^6H, $C^{18}H$, $C^{22}H$), 3.90 (t, J=6.62Hz, 4H; C^7H_2, $C^{16}H_2$), 2.30 (singlet, 6H; $C^{23}H_3$, $C^{24}H_3$), 1.80 (quintet, J=6.62Hz, 4H; C^8H_2, $C^{15}H_2$), 1.50 (m, 12H; C^9H_2, $C^{10}H_2$, $C^{11}H_2$, $C^{12}H_2$, $C^{13}H_2$, $C^{14}H_2$).

^{13}C NMR ($CDCl_3$) δ (ppm): 157.1 (C^1, C^{17}), 130.0 (C^3, C^5, C^{19}, C^{21}), 129.8 (C^4, C^{20}), 114.5 (C^2, C^6, C^{18}, C^{22}), 68.2 (C^7, C^{16}), 29.7 (C^8, C^{15}), 29.5 (C^{10}, C^{11}, C^{12}, C^{13}), 26.2 (C^9, C^{14}), 20.6 (C^{23}, C^{24}).

EIMS (DCM) m/z: 354.5 ($[M]^+$, 11.1%), 108.2 ($[C_7H_8O]^+$, 100%), 107.2 ($[C_7H_7O]^+$, 17.2%), 79.2 ($[C_6H_7]^+$, 4.2%), 69.2 ($[C_5H_9]^+$, 6.4%), 55.2 ($[C_4H_7]^+$, 15.5%), 41.2 ($[C_3H_5]^+$, 11.5%).

6.2.9 Synthesis of 1,7-bis-(4-fluorophenyl-1-yloxy)heptane, FC7

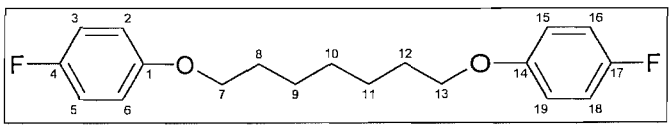

[sml/2954/35]

The synthetic procedure was identical to 6.2.1. 4-fluorophenol ($13.4x10^{-3}$mol, 1.50g), DMF (60ml), K_2CO_3 (7.4g), NaI ($6.69x^{-4}$mol, 0.10g) and 1,7-dibromoheptane ($6.69x10^{-3}$mol, 1.72 g, 1.14ml).White crystals were obtained (1.53g, 71%) which had a mp= 55.5°C.

^{1}H NMR($CDCl_3$) δ (ppm): 6.97 (m, 4H; C^3H, C^5H, $C^{16}H$, $C^{18}H$), 6.85 (m, 4H; C^2H, C^6H, $C^{15}H$, $C^{19}H$), 3.93 (t, J=6.52Hz, 4H; C^7H_2, $C^{13}H_2$), 1.77 (quintet, J=6.52Hz, 4H; C^8H_2, $C^{12}H_2$), 1.49 (m, 6H; C^9H_2, $C^{10}H_2$, $C^{11}H_2$).

^{13}C NMR ($CDCl_3$) δ (ppm): 158.7 (C^4, C^{17}, $^1J_{CF}$ = 238Hz), 155.7 (C^1, C^{14}, $^4J_{CF}$ = 2.9Hz), 116.2 (C^3, C^5, C^{16}, C^{18}, $^2J_{CF}$ = 23.3Hz), 115.8 (C^2, C^6, C^{15}, C^{19}, $^3J_{CF}$ = 8.7Hz), 68.9 (C^7, C^{13}), 29.6 (C^8, C^{12}), 29.5 (C^{10}), 26.2 (C^9, C^{11}).

EIMS (DCM) m/z: 320.3 ($[M]^+$, 20.8%), 112.0 ($[C_6H_5FO]^+$, 92.0%), 96.2 ($[C_6H_5F]^+$, 13.4%), 95.1 ($[C_6H_7O]^+$, 27.0%), 81.1 ($[C_5H_5O]^+$, 7.2%), 69.1 ($[C_5H_9]^+$, 7.6%), 55.0 ($[C_4H_7]^+$, 100%), 44.1 ($[C_3H_8]^+$, 13.1%), 41.1 ($[C_3H_5]^+$, 23.8%).

6.2.10 Synthesis of 1,9-bis-(4-fluorophenyl-1-yloxy)nonane, FC9

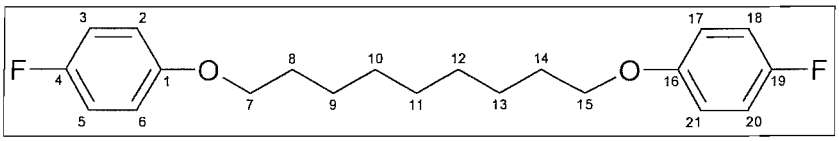

[rjw/2920/32]

The synthetic procedure was identical to 6.2.1 except that hot methanol was used for the recrystallisation. 4-fluorophenol ($9.6x10^{-3}$mol, 1.08g), DMF (40ml), K_2CO_3 (4.8g) and 1,9-dibromononane ($4.0x10^{-3}$mol, 1.15g, 0.82ml). White crystals were obtained (0.98g, 70%) which had a Melting point = 64.5°C.

^{1}H NMR($CDCl_3$) δ (ppm): 6.97(m, 4H; C^3H, C^5H, $C^{18}H$, $C^{20}H$), 6.83 (m, 4H; C^2H, C^6H, $C^{17}H$, $C^{21}H$), 3.92 (t, J=6.62Hz, 4H; C^7H_2, $C^{15}H_2$), 1.77 (quintet, J=6.62Hz, 4H; C^8H_2, $C^{14}H_2$), 1.41 (m, 10H; C^9H_2, $C^{10}H_2$, $C^{11}H_2$, $C^{12}H_2$, $C^{13}H_2$).

^{13}C NMR ($CDCl_3$) δ (ppm): 158.7 (C^4, C^{19}, $^1J_{CF}$ = 238Hz), 155.2 (C^1, C^{16}, $^4J_{CF}$ = 2.3Hz), 115.8 (C^3, C^5, C^{18}, C^{20}, $^2J_{CF}$ = 23.2Hz), 115.4 (C^2, C^6, C^{17}, C^{21}, $^3J_{CF}$ = 7.9Hz), 68.6 (C^7, C^{15}), 30.9 (C^8, C^{14}), 29.5 (C^{10}, C^{11}, C^{12}), 26.2 (C^9, C^{13}).

EIMS (DCM) m/z: 348.4 ($[M]^+$, 9.3%), 112.0 ($[C_6H_5FO]^+$, 100%), 96.2 ($[C_6H_5F]^+$, 6.4%), 95.2 ($[C_6H_7O]^+$, 22.0%), 81.2 ($[C_5H_5O]^+$, 7.6%), 69.3 ($[C_5H_9]^+$, 35.2%), 55.3 ($[C_4H_7]^+$, 37.2%), 44.2 ($[C_3H_8]^+$, 6.1%), 41.2 ($[C_3H_5]^+$, 25.9%).

HPLC: 99.7%.

6.2.11 Synthesis of 1,10-bis-(4-fluorophenyl-1-yloxy)decane, FC10

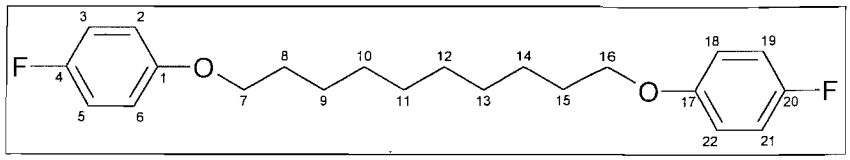

[sml/2954/04]

The synthetic procedure was identical to 6.2.1 except that hot methanol was used for the recrystallisation. 4-fluorophenol ($9.6x10^{-3}$mol, 1.08g), DMF (40ml), K_2CO_3 (4.8g) and 1,10-dibromodecane ($4.0x10^{-3}$mol, 1.20 g). White crystals were obtained (1.37g, 95%) which had a mp = 85°C.

^{1}H NMR($CDCl_3$) δ (ppm): 6.97 (m, 4H; C^3H, C^5H, $C^{19}H$, $C^{21}H$), 6.83 (m, 4H; C^2H, C^6H, $C^{18}H$, $C^{22}H$), 3.91 (t, J=6.62Hz, 4H; C^7H_2, $C^{16}H_2$), 1.77 (quintet, J=6.62Hz, 4H; C^8H_2, $C^{15}H_2$), 1.40 (m, 12H; C^9H_2, $C^{10}H_2$, $C^{11}H_2$, $C^{12}H_2$, $C^{13}H_2$, $C^{14}H_2$).

^{13}C NMR ($CDCl_3$δ (ppm): 158.8 (C^4, C^{20}, $^1J_{CF}$ = 237Hz), 155.2 (C^1, C^{17}, $^4J_{CF}$ = 2.3Hz), 115.9 (C^3, C^5, C^{19}, C^{21}, $^2J_{CF}$ = 22.6Hz), 115.6 (C^2, C^6, C^{18}, C^{22}, $^3J_{CF}$ = 7.9Hz), 68.7 (C^7, C^{16}), 31.1 (C^8, C^{15}), 29.5 (C^{10}, C^{11}, C^{12}, C^{13}), 26.2 (C^9, C^{14}).

EIMS (DCM) m/z: 362.5 ($[M]^+$, 8.4%), 112.2 ($[C_6H_5FO]^+$, 100%), 96.2 ($[C_6H_5F]^+$, 10.0%), 95.2 ($[C_6H_7O]^+$, 17.1%), 81.3 ($[C_5H_5O]^+$, 6.3%), 69.3 ($[C_5H_9]^+$, 17.6%), 55.3 ($[C_4H_7]^+$, 35.0%), 44.2 ($[C_3H_8]^+$, 16.4%), 41.2 ($[C_3H_5]^+$, 22.7%). HPLC: 100%.

6.2.12 Synthesis of 1,9-bis-(4-trifluoromethylphenyl-1-yloxy)nonane, CF3C9

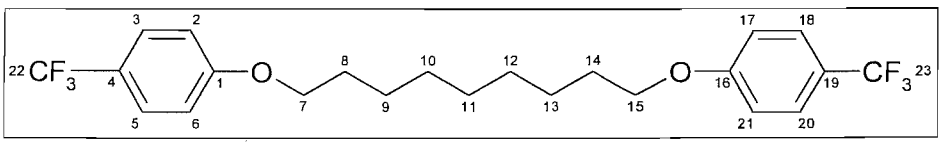

[rjw/2920/13]

The synthetic procedure was identical to 6.2.1 except that hot methanol was used for the recrystallisation. 4-trifluoromethylphenol ($9.6x10^{-3}$mol, 1.56g), DMF (40ml), K_2CO_3 (4.8g) and 1,9-dibromononane ($4.0x10^{-3}$mol, 1.15g, 0.82ml). A white solid was obtained (1.46g, 81%) which had a mp = 43.5°C.

^{1}H NMR($CDCl_3$) δ (ppm): 7.55(broad doublet, 4H; C^3H, C^5H, $C^{18}H$, $C^{20}H$, J=8.82Hz), 6.95 (broad doublet, J=8.09Hz, 4H; C^2H, C^6H, $C^{17}H$, $C^{21}H$), 4.00 (t, J=6.62Hz, 4H; C^7H_2, $C^{15}H_2$), 1.80 (quintet, J=6.62Hz, 4H; C^8H_2, $C^{14}H_2$), 1.43 (m, 10H; C^9H_2, $C^{10}H_2$, $C^{11}H_2$, $C^{12}H_2$, $C^{13}H_2$).

^{13}C NMR ($CDCl_3$) δ (ppm): 161.7 (C^1, C^{16}), 127.0 (C^3, C^5, C^{18}, C^{20}), 126.9 (C^4, C^{19}), 122.8 (C^{22}, C^{23}), 114.5 (C^2, C^6, C^{17}, C^{21}), 68.3 (C^7, C^{15}), 29.6 (S; C^8, C^{14}), 29.4 (C^{10}, C^{11}, C^{12}), 26.1 (C^9, C^{13}).

EIMS (DCM) m/z: 448.0 ($[M]^+$, 13.0%), 175.2 ($[C_8H_6F_3O]^+$, 15.9%), 162.2 ($[C_7H_5F_3O]^+$, 52.2%), 95.2 ($[C_6H_7O]^+$, 25.5%), 81.2 ($[C_5H_5O]^+$, 19.4%), 69.3 ($[CF_3]^+$, $[C_5H_9]^+$, 100%), 55.3 ($[C_4H_7]^+$, 91.4%), 44.2 ($[C_3H_8]^+$, 30.4%), 41.2 ($[C_3H_5]^+$, 57.1%). HPLC: 99.2%.

6.2.13 Synthesis of 1,10-bis-(4-trifluoromethylphenyl-1-yloxy)decane, CF3C10

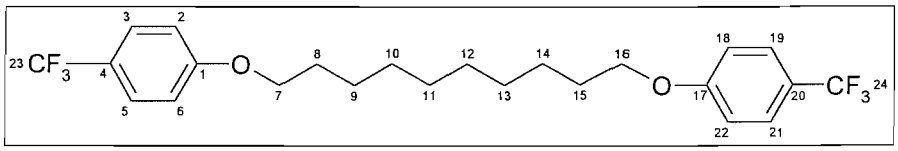

[rjw/2920/15]

The procedure was identical to 6.2.1 except that hot methanol was used for the recrystallisation. 4-trifluoromethylphenol ($9.6x10^{-3}$mol, 1.56g), DMF (40ml), K_2CO_3 (4.8g) and 1,10-dibromodecane ($4.0x10^{-3}$mol, 1.20 g). A white solid was obtained (1.20g, 65%) which had a mp = 62.5°C.

^{1}H NMR($CDCl_3$) δ (ppm): 7.55(broad doublet, J=8.82Hz, 4H; C^3H, C^5H, $C^{18}H$, $C^{20}H$), 6.95 (broad doublet, J=8.09Hz, 4H; C^2H, C^6H, $C^{17}H$, $C^{21}H$), 4.00 (t, J=6.62Hz, 4H; C^7H_2, $C^{16}H_2$), 1.82 (quintet, J=6.62Hz, 4H; C^8H_2, $C^{15}H_2$), 1.40 (m, 12H; C^9H_2, $C^{10}H_2$, $C^{11}H_2$, $C^{12}H_2$, $C^{13}H_2$, $C^{14}H_2$).

^{13}C NMR ($CDCl_3$) δ (ppm): 161.7 (C^1, C^{17}), 127.0 (C^3, C^5, C^{19}, C^{21}), 126.9 (C^4, C^{20}), 122.5 (C^{23}, C^{24}), 114.5 (C^2, C^6, C^{18}, C^{22}), 68.3 (C^7, C^{16}), 31.1 (C^8, C^{15}), 29.4 (C^{10}, C^{11}, C^{12}, C^{13}), 26.1 (C^9, C^{14}).

EIMS (DCM) m/z: 462.4 ($[M]^+$, 15.5%), 175.2 ($[C_8H_6F_3O]^+$, 17.0%), 162.2 ($[C_7H_5F_3O]^+$, 60.4%), 95.2 ($[C_6H_7O]^+$, 21.9%), 81.2 ($[C_5H_5O]^+$, 20.2%), 69.3 ($[CF_3]^+$, $[C_5H_9]^+$, 62.7%), 55.3 ($[C_4H_7]^+$, 100%), 41.2 ($[C_3H_5]^+$, 57.3%).

HPLC: 98.9%.

6.2.14 Synthesis of 1,9-bis-(2,3-difluorophenyl-1-yloxy)nonane, 23FC9

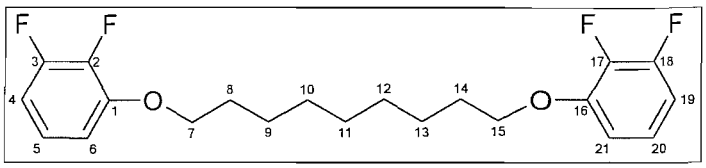

[sml/2954/31]

The synthetic procedure was identical to 6.2.1 except that column chromatography on silica (0.5% DCM in petroleum ether 40-60) was used for purification. 2,3-difluorophenol ($3.84x10^{-3}$mol, 0.50g), DMF (25ml), K_2CO_3 (3.70g), 1,9-dibromononane ($1.92x10^{-3}$mol, 0.55g, 0.39ml) and NaI ($1.92x10^{-4}$mol, 0.03g). White crystals were obtained (0.31g, 42%) which had a mp = 60.5°C.

^{1}H NMR($CDCl_3$) δ (ppm): 6.88 (m, 2H; C^5H, $C^{20}H$), 6.65 (m, 4H, C^6H, $C^{21}H$, C^4H, $C^{19}H$), 4.01 (t, J = 6.53Hz, 4H; C^7H_2, $C^{15}H_2$), 1.74 (quintet, J = 6.77Hz, 4H; C^8H_2, $C^{14}H_2$), 1.30 (m, 10H, C^9H_2, $C^{10}H_2$, $C^{11}H_2$, $C^{12}H_2$, $C^{13}H_2$).

^{13}C NMR ($CDCl_3$) δ (ppm): 153.1 (C^3, C^{18}), 150.7 (C^1, C^{16}), 140.7 (C^2, C^{17}), 123.2 (C^5, C^{20}), 110.0 (C^6, C^{21}), 109.0 (C^4, C^{19}), 70.0 (C^7, C^{15}), 29.8 (C^8, C^{14}), 29.4 (C^{10}, C^{11}, C^{12}), 26.0 (C^9, C^{13}).

EIMS (DCM) m/z: 384.0 ($[M]^+$, 10.0%), 130.1 ($[C_6H_4F_2O]^+$, 67.7%), 113.1 ($[C_6H_3F_2]^+$, 16.5%), 95.2 ($[C_6H_7O]^+$, 22.0%), 81.2 ($[C_5H_5O]^+$, 15.1%), 69.3 ($[C_5H_9]^+$, 100%), 55.3 ($[C_4H_7]^+$, 92.8%), 41.2 ($[C_3H_5]^+$, 66.0%).

6.2.15 Synthesis of 1,7-bis-(2,4-difluorophenyl-1-yloxy)heptane, 24FC7

[tod/3280/19]

The procedure was identical to 6.2.1 except that on addition of water an oil was formed which was extracted via an aqueous work up followed by column chromatography on silica (DCM) for purification. 2,4-difluorophenol ($19.2 x10^{-3}$mol, 1.84ml), DMF (50ml),

K_2CO_3 (4.80g) and 1,7-dibromoheptane (9.6 x10^{-3}mol, 1.64 ml). A colourless liquid was obtained. A colourless oil was obtained (1.68g, 49%) which had a mp = < 15°C.

^{1}H NMR($CDCl_3$) δ (ppm): 6.85 (m, 6H; C^3H, C^5H, C^6H, $C^{16}H$, $C^{18}H$ $C^{19}H$), 4.00 (t, J = 6.43Hz, 4H; C^7H_2, $C^{13}H_2$), 1.82 (quintet, J = 6.62Hz, 4H; C^8H_2, $C^{12}H_2$), 1.50 (m, 6H, C^9H_2, $C^{10}H_2$, $C^{11}H_2$).

^{13}C NMR ($CDCl_3$) δ (ppm): 158.0 (C^4, C^{17}), 154.4 (C^2, C^{15}), 143.8 (C^1, C^{14}), 115.7 (C^6, C^{19}), 110.3 (C^5, C^{18}), 104.9 (C^3, C^{16}), 70.3 (C^7, C^{13}), 29.3 (C^8, C^{12}), 29.2 (C^{10}), 26.0 (C^9, C^{11}).

EIMS (DCM) m/z: 356.0 ($[M]^+$, 10.0%), 130.1 ($[C_6H_4F_2O]^+$, 99.8%), 113.1 ($[C_6H_3F_2]^+$, 28.2%), 95.1 ($[C_6H_7O]^+$, 18.1%), 81.1 ($[C_5H_5O]^+$, 32.2%), 69.2 ($[C_5H_9]^+$, 41.0%), 55.1 ($[C_4H_7]^+$, 100%), 41.2 ($[C_3H_5]^+$, 61.2%).

6.2.16 Synthesis of 1,8-bis-(2,4-difluorophenyl-1-yloxy)octane, 24FC8

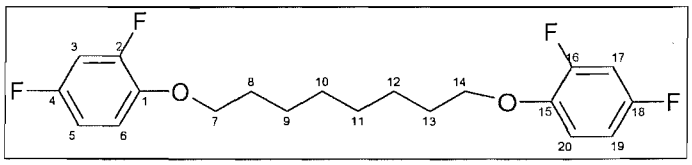

[sml/2954/25]

The procedure was identical to 6.2.1. 2,4-difluorophenol (11.53x10^{-3}mol, 1.10ml), DMF (60ml), K_2CO_3 (6.40g), 1,8-dibromooctane (5.77x10^{-3}mol, 1.06ml) and NaI (1.15 x10^{-3}mol, 0.17g). White crystals were obtained (1.57g, 73%) which had a mp = 52°C.

^{1}H NMR($CDCl_3$) δ (ppm): 6.85 (6H, m, C^3H, C^5H, C^6H, $C^{17}H$, $C^{19}H$, $C^{20}H$), 4.00 (t, J = 6.63Hz, 4H; C^7H_2, $C^{14}H_2$), 1.81 (quintet, J = 6.63Hz, 4H; C^8H_2, $C^{13}H_2$), 1.45 (m, 8H; C^9H_2, $C^{10}H_2$ $C^{11}H_2$, $C^{12}H_2$).

^{13}C NMR($CDCl_3$) δ (ppm): 158.0 (C^4, C^{18}), 154.8 (C^2, C^{16}), 151.0 (C^1, C^{15}), 115.6 (C^6, C^{20}), 110.3 (C^5, C^{19}), 104.9 (C^3, C^{17}), 70.3 (C^7, C^{14}), 29.3 (C^8, C^{13}), 25.9 (C^9, C^{10}, C^{11}, C^{12}).

EIMS (DCM) m/z: 370.4 ($[M]^+$, 7.0%), 143.0 ($[C_7H_5F_2O]^+$, 23.4%), 130.0 ($[C_6H_4F_2O]^+$, 80.0%), 113.1 ($[C_6H_3F_2]^+$, 8.9%), 81.2 ($[C_6H_9]^+$, 15.1%), 69.2 ($[C_5H_9]^+$, 100%), 55.0 ($[C_4H_7]^+$, 83.9%), 41.1 ($[C_3H_5]^+$, 70.8%).

6.2.17 Synthesis of 1,9-bis-(2,4-difluorophenyl-1-yloxy)nonane, 24FC9

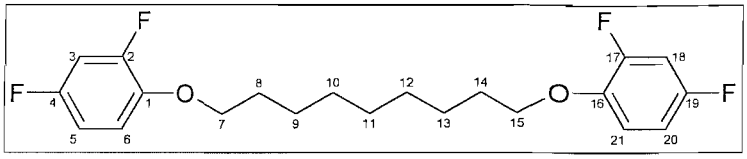

[tod/3280/21]

The procedure was identical to 6.2.1 except that on addition of water an oil was formed which was extracted via an aqueous work up followed by column chromatography (DCM) for purification. 2,4-difluorophenol (19.2 $x10^{-3}$mol, 1.84ml), DMF (50ml), K_2CO_3 (4.80g), 1,9-dibromononane (9.6 $x10^{-3}$mol, 1.95ml) and NaI (1.0 $x10^{-3}$mol, 0.15g). A colourless liquid was obtained. A colourless oil was obtained (1.10g, 32%) which had a mp= < 15°C.

^{1}H NMR($CDCl_3$) δ (ppm): 6.85 (m, 6H; C^3H, C^5H, C^6H, $C^{18}H$, $C^{20}H$ $C^{21}H$), 4.00 (t, J = 6.62Hz, 4H; C^7H_2, $C^{15}H_2$), 1.81 (quintet, J = 6.62Hz, 4H; C^8H_2, $C^{14}H_2$), 1.42 (m, 10H, C^9H_2, $C^{10}H_2$, $C^{11}H_2$, $C^{12}H_2$, $C^{13}H_2$).

^{13}C NMR ($CDCl_3$) δ (ppm): 158.0 (C^4, C^{19}), 154.7 (C^2, C^{17}), 151.0 (C^1, C^{16}), 115.7 (C^6, C^{21}), 110.3 (C^5, C^{20}), 104.9 (C^3, C^{18}), 70.4 (C^7, C^{15}), 29.6 (C^8, C^{14}), 29.4 (C^{10}, C^{11}, C^{12}), 26.0 (C^9, C^{13}).

EIMS (DCM) m/z: 384.2 ($[M]^+$, 48.1%), 143.1 ($[C_7H_5F_2O]^+$, 82.1%), 130.1 ($[C_6H_4F_2O]^+$, 100%), 113.1 ($[C_6H_3F_2]^+$, 32.3%), 95.2 ($[C_6H_7O]^+$, 41.6%), 81.2 ($[C_5H_5O]^+$, 34.2%), 69.1 ($[C_5H_9]^+$, 92.9%), 55.1 ($[C_4H_7]^+$, 92.2%), 41.2 ($[C_3H_5]^+$, 75.2%).

6.2.18 Synthesis of 1,10-bis-(2,4-difluorophenyl-1-yloxy)decane, 24FC10

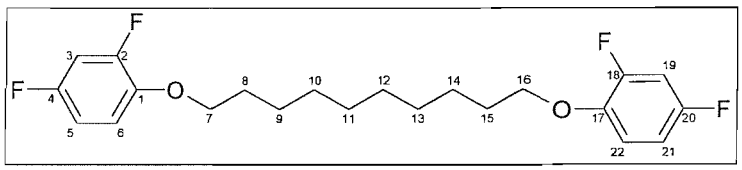

[sml/2954/27]

The procedure was identical to 6.2.1. 2,4-difluorophenol (11.53x10^{-3}mol, 1.10ml), DMF (60ml), K_2CO_3 (0.046mol, 6.40g), 1,10-dibromodecane (5.77x10^{-3}mol, 1.73g) and NaI (5.77 $x10^{-4}$mol, 0.09g). White crystals were obtained (1.79g, 78%) which had a mp= 60°C.

^{1}H NMR($CDCl_3$) δ (ppm): 6.85 (m, 6H; C^3H, C^5H, C^6H, $C^{19}H$, $C^{21}H$, $C^{22}H$), 4.00 (t, J = 6.63Hz, 4H; C^7H_2, $C^{16}H_2$), 1.80 (quintet, J = 6.60Hz , 4H; C^8H_2, $C^{15}H_2$), 1.40 (m, 12H; C^9H_2, $C^{10}H_2$ $C^{11}H_2$, $C^{12}H_2$, $C^{13}H_2$, $C^{14}H_2$).

^{13}C NMR($CDCl_3$) δ (ppm):158.0 (C^4, C^{20}), 154.8 (C^2, C^{18}), 143.9 (C^1, C^{17}), 115.6 (C^6, C^{22}), 110.2 (C^5, C^{21}), 104.9 (C^3, C^{19}), 70.4 (C^7, C^{16}), 29.5 (C^8, C^{15}), 26.0 (C^9, C^{10}, C^{11}, C^{12}, C^{13}, C^{14}).

EIMS (DCM) m/z: 398.2 ($[M]^+$, 11.0%), 143.0 ($[C_7H_5F_2O]^+$, 16.3%), 130.0 ($[C_6H_4F_2O]^+$, 84.3%), 95.1 ($[C_6H_7O]^+$, 14.1%), 81.2 ($[C_6H_9]^+$, 16.8%), 69.2 ($[C_5H_9]^+$, 46.6%), 55.1 ($[C_4H_7]^+$, 100%), 41.1 ($[C_3H_5]^+$, 75.9%).

6.2.19 Synthesis of 1,7-bis-(3,4-difluorophenyl-1-yloxy)heptane, 34FC7

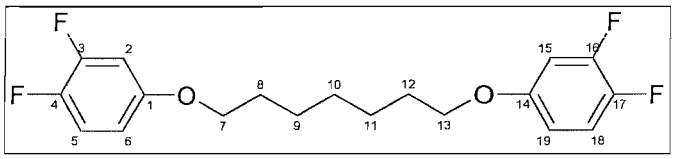

[sml/2954/48]

The procedure was identical to 6.2.1 except that on addition of water an oil was formed which was extracted via an aqueous work up followed by column chromatography (DCM) for purification. 3,4-difluorophenol (19.2 x10^{-3}mol, 2.5g), DMF (50ml), K_2CO_3 (4.80g), 1,7-dibromoheptane (9.6 x10^{-3}mol, 1.64ml). A low melting solid was obtained (1.10g, 32%) which had a mp = 28°C.

^{1}H NMR($CDCl_3$) δ (ppm): 7.06 (m, 2H; C^5H, $C^{18}H$), 6.72 (m, 2H; C^6H, $C^{19}H$), 6.59 (m, 2H; C^2H, $C^{15}H$), 3.92 (t, J = 6.41Hz, 4H; C^7H_2, $C^{13}H_2$), 1.80 (quintet, J = 6.60Hz, 4H; C^8H_2, $C^{12}H_2$), 1.50 (m, 6H; C^9H_2, $C^{10}H_2$ $C^{11}H_2$).

^{13}C NMR($CDCl_3$) δ (ppm): 155.4 (C^1, C^{14}), 152.0 (C^3, C^{16}, $^1J_{CF}$ = 233Hz, $^2J_{CF}$ = 13.9Hz), 146.4 (C^4, C^{17}, $^1J_{CF}$ = 285Hz, $^2J_{CF}$ = 12.9Hz), 117.2 (C^5, C^{18}, $^2J_{CF}$ = 18.0Hz), 109.7 (C^6, C^{19}, $^3J_{CF}$ = 12.5Hz, $^4J_{CF}$ = 6.0Hz), 104.1 (C^2, C^{15}, $^2J_{CF}$ = 20.3Hz), 68.7 (C^7, C^{13}), 29.0 (C^8, C^{12}, C^{10}), 25.9 (C^9, C^{11}).

EIMS (DCM) m/z: 356.0 ($[M]^+$, 6.0%), 130.0 ($[C_6H_4F_2O]^+$, 46.5%), 96.1 ($[C_6H_8O]^+$, 10.3%), 81.0 ($[C_6H_9]^+$, 9.8%), 55.0 ($[C_4H_7]^+$, 72.2%), 44.0 ($[C_3H_8]^+$, 100%), 41.1 ($[C_3H_5]^+$, 38.0%).

6.2.20 Synthesis of 1,10-bis-(3,4-difluorophenyl-1-yloxy)decane, 34FC10

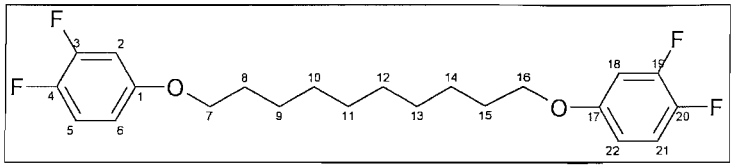

[tod/3280/07]

The procedure was identical to 6.2. 1 except that on addition of water an oil was formed which was extracted via an aqueous work up followed by column chromatography (DCM) for purification. 3,4-difluorophenol (19.2 $x10^{-3}$mol, 2.5g), DMF (50ml), K_2CO_3 (4.80g), 1,10-dibromodecane (9.6 $x10^{-3}$mol, 2.16ml). White crystals were obtained (1.79g, 47%) which had a mp = 41.5°C.

^{1}H NMR($CDCl_3$) δ (ppm): 7.05 (m, 2H; C^5H, $C^{21}H$), 6.69 (m, 2H; C^6H, $C^{22}H$), 6.58 (m, 2H; C^2H, $C^{18}H$), 3.90 (t, J = 6.62Hz, 4H; C^7H_2, $C^{16}H_2$), 1.77 (quintet, J = 6.60Hz, 4H; C^8H_2, $C^{15}H_2$), 1.40 (m, 12H; C^9H_2, $C^{10}H_2$ $C^{11}H_2$, $C^{12}H_2$, $C^{13}H_2$ $C^{14}H_2$).

^{13}C NMR($CDCl_3$) δ (ppm): 155.7 (C^1, C^{17}, $^3J_{CF}$ = 9.4Hz), 152.3 (C^3, C^{19}, $^1J_{CF}$ = 233Hz, $^2J_{CF}$ = 13.7Hz), 146.6 (C^4, C^{20}, $^1J_{CF}$ = 239Hz, $^2J_{CF}$ = 12.9Hz), 117.4 (C^5, C^{21}, $^2J_{CF}$ = 18.3Hz), 109.9 (C^6, C^{22}, $^3J_{CF}$ = 8.6Hz, $^4J_{CF}$ = 4.9Hz), 104.1 (C^2, C^{18}, $^2J_{CF}$ = 20.1Hz), 68.9 (C^7, C^{16}), 29.5 (C^8, C^{15}), 25.9 (C^9, C^{10}, C^{11}, C^{12}, C^{13}, C^{14}).

EIMS (DCM) m/z: 398.2 ($[M]^+$, 21.0%), 130.0 ($[C_6H_4F_2O]^+$, 72.3%), 81.2 ($[C_6H_9]^+$, 13.8%), 55.0 ($[C_4H_7]^+$, 100%), 44.0 ($[C_3H_8]^+$, 19.2%), 41.1 ($[C_3H_5]^+$, 76.8%).

6.2.21 Synthesis of 1,7-bis-(2,3,4-trifluorophenyl-1-yloxy)heptane, 234FC7

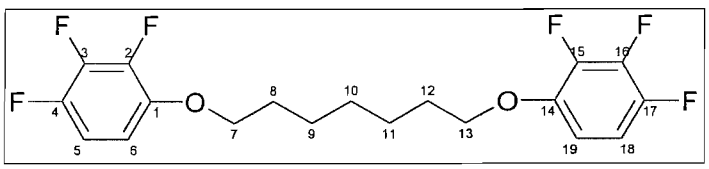

[sml/2954/24]

The procedure was identical to 6.2.1 except that column chromatography on silica (50% DCM in petroleum ether 40-60) was used to remove the remaining DMF. NMR showed the presence of monomer (~10%). The product was reacted with more 2,3,4-trifluorophenol ($1.23x10^{-4}$mol, 0.02g) and potassium carbonate. The 1,7-bis-(2,3,4-

trifluoro-phenyloxy)heptane was isolated by column chromatography (50% DCM in petroleum ether 40-60) as an off white solid. 2,3,4-trifluorophenol ($3.38x10^{-3}$mol, 0.50g), DMF (20ml), K_2CO_3 (1.68g) and 1,7-dibromoheptane ($1.69x10^{-3}$mol, 0.43g, 0.28ml). White crystals were obtained (0.11g, 17%) which had a mp = 45.5°C.

^{1}H NMR($CDCl_3$) δ (ppm): 6.87 (m, 2H; C^5H, $C^{18}H$), 6.65 (m, 2H, C^6H, $C^{19}H$), 4.01 (t, J = 6.43Hz, 4H; C^7H_2, $C^{13}H_2$), 1.83 (quintet, J = 6.43Hz, 4H; C^8H_2, $C^{12}H_2$), 1.50 (m, 6H, C^9H_2, $C^{10}H_2$, $C^{11}H_2$).

EIMS (DCM) m/z: 392.2 ($[M]^+$, 4.5%), 113.1 ($[C_6H_3F_2]^+$, 9.4%), 81.2 ($[C_6H_9]^+$, 12.3%), 69.1 ($[C_5H_9]^+$, 22.1%), 55.0 ($[C_4H_7]^+$, 100%), 41.1 ($[C_3H_5]^+$, 38.8%).

6.2.22 Synthesis of 1,9-bis-(2,3,4-trifluorophenyl-1-yloxy)nonane, 234FC9

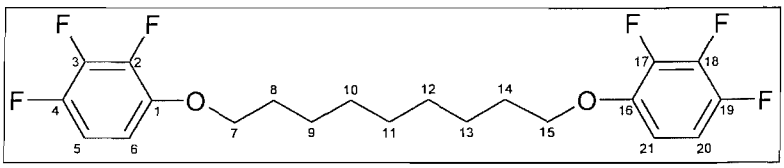

[sml/2954/30]

The procedure was identical to 6.2.1 except that column chromatography (15% DCM in petroleum ether 40-60) was used for purification. 2,3,4-trifluorophenol ($3.38x10^{-3}$mol, 0.50g), DMF (25ml), K_2CO_3 (1.66g) and 1,9-dibromononane ($1.65x10^{-3}$mol, 0.47g, 0.33ml). White crystals were obtained (0.17g, 25%) which had a mp= 36.5°C.

^{1}H NMR($CDCl_3$) δ (ppm): 6.87 (m, 2H; C^5H, $C^{20}H$), 6.65 (m, 2H, C^6H, $C^{21}H$), 4.01 (t, J = 6.62Hz, 4H; C^7H_2, $C^{15}H_2$), 1.82 (quintet, J = 6.62Hz, 4H; C^8H_2, $C^{14}H_2$), 1.43 (m, 10H, C^9H_2, $C^{10}H_2$, $C^{11}H_2$, $C^{12}H_2$, $C^{13}H_2$).

^{13}C NMR ($CDCl_3$) δ (ppm): 165.5 (C^1, C^{16}), 145.9 (C^4, C^{19}, ^1J = 265Hz), 145.7 (C^5, C^{18}, ^1J = 261Hz), 140.7 (C^6, C^{17}), 111.4 (C^5, C^{20}, ^2J = 18.4Hz, ^3J = 4.8Hz), 109.5 (C^6, C^{21}), 71.6 (C^7, C^{15}), 30.5 (C^8, C^{14}), 30.3 (C^{10}, C^{11}, C^{12}), 27.0 (C^9, C^{13}).

EIMS (DCM) m/z: 420.4 ($[M]^+$, 5%), 161.0 ($[C_7H_4F_3O]^+$, 16.6%), 131.1 ($[C_6H_2F_3]^+$, 12.3%), 81.2 ($[C_6H_9]^+$, 18.5%), 69.2 ($[C_5H_9]^+$, 100%), 55.1 ($[C_4H_7]^+$, 90.8%), 41.1 ($[C_3H_5]^+$, 76.6%).

6.2.23 Synthesis of 1,7-bis-(3,4,5-trifluorophenyl-1-yloxy)heptane, 345FC7

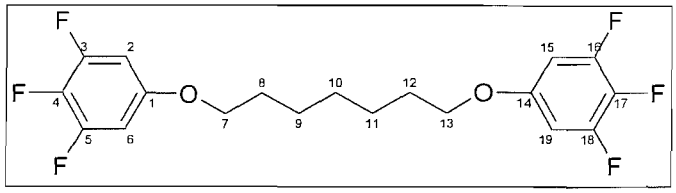

[sml/2954/47]

The procedure was identical to procedure 6.2.1 except column chromatography (15% DCM in petroleum ether 40-60) was used for purification twice. 3,4,5-trifluorophenol ($6.75x10^{-3}$mol, 1.00g), DMF (30ml), K_2CO_3 (3.70g), 1,7-dibromoheptane ($3.38x10^{-3}$mol, 0.58ml) and NaI ($3.38x10^{-4}$mol, 0.05g). A white solid was obtained (0.59g, 44%) which had a mp = 59.0°C.

^{1}H NMR($CDCl_3$) δ (ppm): 6.50 (m, 4H; C^2H, C^6H, $C^{15}H$, $C^{19}H$), 3.90 (t, J = 6.43Hz, 4H; C^7H_2, $C^{13}H_2$), 1.68 (quintet, J = 6.43Hz, 4H; C^8H_2, $C^{12}H_2$), 1.45 (m, 6H, C^9H_2, $C^{10}H_2$, $C^{11}H_2$).

^{13}C NMR ($CDCl_3$) δ (ppm): 153.0 (C^1, C^{14}, ^3J = 8.7Hz, ^4J = 2.9Hz), 151.3 (C^3, C^5, C^{16}, C^{18}, ^1J = 248Hz, ^2J = 16.5Hz, ^3J = 5.8Hz), 134.2 (C^4, C^{17}, ^1J = 243Hz), 97.7 (C^2, C^6, C^{15}, C^{19}, ^2J = 17.4Hz, ^3J = 6.8Hz), 67.4 (C^7, C^{13}), 28.0 (C^8, C^{10}, C^{12}), 24.5 (C^9, C^{11}).

EIMS (DCM) m/z: 392.1 ($[M]^+$, 21.0%), 161.0 ($[C_7H_4F_3O]^+$, 25.0%), 131.0 ($[C_6H_2F_3]^+$, 14.5%), 81.2 ($[C_6H_9]^+$, 12.4%), 69.2 ($[C_5H_9]^+$, 17.4%), 55.1 ($[C_4H_7]^+$, 100%), 41.1 ($[C_3H_5]^+$, 35.1%).

This yield is so low due to the purification method and the fact that monomer was present.

6.2.24 Synthesis of 1,9-bis-(3,4,5-trifluorophenyl-1-yloxy)nonane, 345FC9

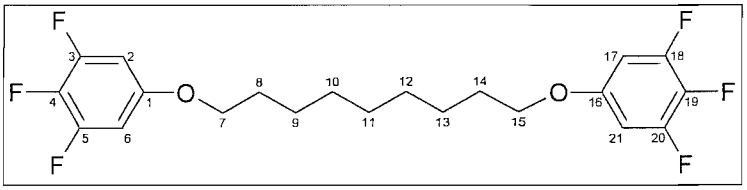

[sml/2954/33]

The procedure was identical to procedure 6.2.1 except column chromatography (15% DCM in petroleum ether 40-60) was used for purification twice. 3,4,5-trifluorophenol ($6.75x10^{-3}$mol, 1.00g), DMF (50ml), K_2CO_3 (3.70g), 1,9-dibromononane ($3.38x10^{-3}$mol, 0.69ml) and NaI ($3.38x10^{-4}$mol, 0.05g). A white solid was obtained (0.34g, 24%) which had a mp = 49.5°C.

^{1}H NMR($CDCl_3$) δ (ppm): 6.40 (m, 4H; C^2H, C^6H, $C^{17}H$, $C^{21}H$), 3.80 (t, J = 6.43Hz, 4H; C^7H_2, $C^{15}H_2$), 1.68 (quintet, J = 6.43Hz, 4H; C^8H_2, $C^{14}H_2$), 1.33 (m, 10H, C^9H_2, $C^{10}H_2$, $C^{11}H_2$, $C^{12}H_2$, $C^{13}H_2$).

^{13}C NMR ($CDCl_3$) δ (ppm): 153.1 (C^1, C^{16}, ^3J = 8.7Hz, ^4J = 2.9Hz), 151.3 (C^3, C^5, C^{18}, C^{20}, ^1J = 248Hz, ^2J = 16.5Hz, ^3J = 5.8Hz), 134.4 (C^4, C^{19}, ^1J = 243Hz), 97.7 (C^2, C^6, C^{17}, C^{21}, ^2J = 17.4Hz, ^3J = 6.8Hz), 67.5 (C^7, C^{15}), 28.0 (C^8, C^{14}), 27.8 (C^{10}, C^{11},C^{12}), 24.5 (C^9, C^{13}).

EIMS (DCM) m/z: 420.1 ($[M]^+$, 13.7%), 161.0 ($[C_7H_4F_3O]^+$, 22.8%), 131.0 ($[C_6H_2F_3]^+$, 12.0%), 81.2 ($[C_6H_9]^+$, 16.5%), 69.2 ($[C_5H_9]^+$, 100%), 55.1 ($[C_4H_7]^+$, 98.5%), 41.1 ($[C_3H_5]^+$, 86.4%).

This yield is so low due to the purification method and the fact that monomer was present.

6.2.25 Synthesis of 1,7-bis-(2,3,4,5,6-pentafluorophenyl-1-yloxy)heptane, PFC7

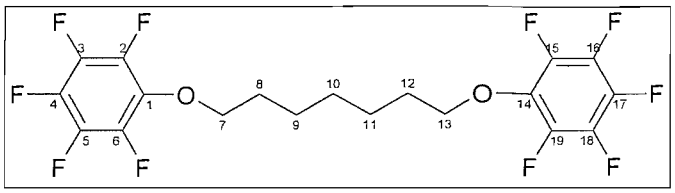

[sml/2954/45]

The procedure was identical to 6.2.1 except that column chromatography on silica (10% diethyl ether in petroleum ether 40-60) was used for purification. Pentafluorophenol ($10.87x10^{-3}$mol, 2.00g), DMF (60ml), K_2CO_3 (6.0g), 1,7-dibromoheptane ($5.44x10^{-3}$mol, 1.40g, 0.93ml) and NaI ($5.44x10^{-4}$mol, 0.08g). A colourless oil was obtained (0.82g, 33%) which had a mp < 15°C.

^{1}H NMR($CDCl_3$) δ (ppm): 4.08 (t, J = 6.41Hz, 4H; C^7H_2, $C^{13}H_2$), 1.72 (quintet, J = 6.59Hz, 4H; C^8H_2, $C^{12}H_2$), 1.40 (m, 6H, C^9H_2, $C^{10}H_2$, $C^{11}H_2$).

^{13}C NMR ($CDCl_3$) δ (ppm): 75.7 (C^7, C^{13}), 29.7 (C^8, C^{12}), 28.8 (C^{10}), 25.4 (C^9, C^{11}).

EIMS (DCM) m/z: 464.0 ($[M]^+$, 1.0%), 184.1 ($[C_6HF_5O]^+$, 6.2%), 97.1 ($[C_6H_9O]^+$, 26.6%), 69.1 ($[C_5H_9]^+$, 9.8%), 55.1 ($[C_4H_7]^+$, 100%), 44.1 ($[C_3H_8]^+$, 8.4%), 41.1 ($[C_3H_5]^+$, 23.6%).

6.2.26 Synthesis of 1,9-bis-(2,3,4,5,6-pentafluorophenyl-1-yloxy)nonane, PFC9

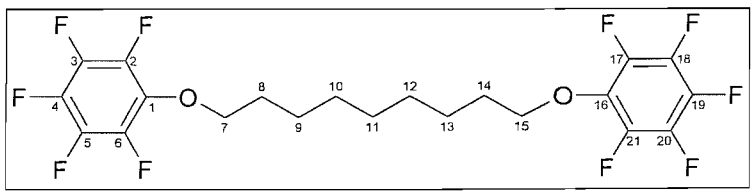

[sml/2954/37]

The procedure was identical to 6.2.1 except that column chromatography on silica (1% DCM in petroleum ether 40-60) was used for purification. 2,3,4,5,6-pentafluorophenol ($8.15x10^{-3}$mol, 1.50g), DMF (60ml), K_2CO_3 (4.50g), 1,9-dibromononane ($4.08x10^{-3}$mol, 1.16g, 0.83ml) and NaI ($4.08x10^{-4}$mol, 0.06g). A colourless oil was obtained (0.46g, 25%) which had a mp < 15°C.

^{1}H NMR($CDCl_3$) δ (ppm): 4.15 (t, J = 6.43Hz, 4H; C^7H_2, $C^{15}H_2$), δ1.78 (quintet, J = 6.43Hz, 4H; C^8H_2, $C^{14}H_2$), 1.40 (m, 10H, C^9H_2, $C^{10}H_2$, $C^{11}H_2$, $C^{12}H_2$, $C^{13}H_2$).

^{13}C NMR ($CDCl_3$) δ (ppm): 76.2 (C^7, C^{15}), 30.2 (C^8, C^{14}), 29.7 (C^{11}), 29.5 (C^{10}, C^{12}), 25.9 (C^9, C^{13}).

6.2.27 Synthesis of 1-(2,3,4,5,6-fluorophenyl-1-yloxy)-8'-(phenyl-1-yloxy)octane, NC8

(i) Synthesis of 1-bromo-(8-phenyl-1-yloxy)octane

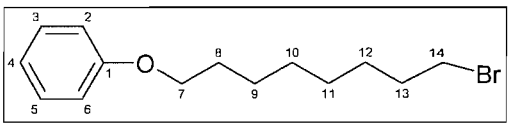

[md/3978/05]

Phenol ($21.3x10^{-3}$mol, 2.0g) and K_2CO_3 (5.3g) were refluxed in acetone (50ml) under N_2 for 45 min. A ten-fold excess of 1,8-dibromooctane (21.3mol, 39.1ml) was then added and the reaction was refluxed for a further five days. This excess ensures the production of the monomer and not the dimeric species. High vacuum distillation was then used to remove the excess 1,8-dibromooctane. Column chromatography (40-60 petroleum ether) was used for purification. A colourless oil was obtained (4.0g, 66%).

^{1}H NMR($CDCl_3$) δ (ppm): 7.29 (m, 2H; C^3H, C^5H), 6.93 (m, 3H; C^2H, C^4H, C^6H), 3.97 (t, J = 6.62Hz, 2H; C^7H_2), 3.43 (t, J = 6.80Hz, 2H; $C^{14}H_2$), 1.88 (quintet, 2H; C^8H_2), 1.79 (quintet, 2H; $C^{13}H_2$), 1.43 (m, 8H; C^9H_2, $C^{10}H_2$, $C^{11}H_2$, $C^{12}H_2$).

^{13}C NMR ($CDCl_3$) δ (ppm): 159.1 (C^1), 129.4 (C^3, C^5), 120.5 (C^4), 114.5 (C^2, C^6), 67.8 (C^7), 34.0 (C^{13}), 32.8 (C^{14}), 29.2 (C^8, C^{10}), 28.7 (C^{11}), 28.1 (C^{12}), 26.0 (C^9).

(ii) Synthesis of 1-(2,3,4,5,6-fluorophenyl-1-yloxy)-8'-(phenyl-1-yloxy)octane, NC8

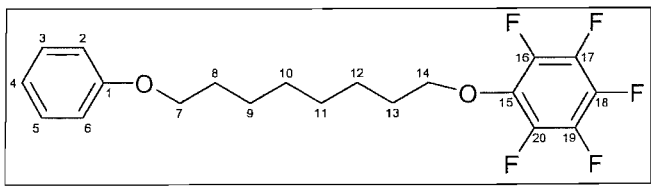

[sml/2954/43]

Pentafluorophenol ($3.51x10^{-3}$mol, 0.645g) and K_2CO_3 (5.30g) were refluxed in DMF (50ml) under N_2 for 4 h. The 1-bromo-(8-phenyl-1-yloxy)octane ($3.51x10^{-3}$mol, 1.00 g)

and NaI (0.053g) were added and the reaction mixture was then stirred at room temperature under nitrogen for seven days. On completion water (100ml) was added and the organic layer extracted into diethyl ether and an aqueous work-up was carried out. Column chromatography on silica (50% diethyl ether in petroleum ether 40-60) was used for purification. A low melting solid was obtained (1.11g, 82%) which has a mp = 31°C.
^{1}H NMR($CDCl_3$) δ (ppm): 7.19 (m, 2H; C^3H, C^5H), 6.83 (m, 3H; C^2H, C^4H, C^6H), 4.07 (t, J = 6.58Hz, 2H; $C^{14}H_2$), 3.88 (t, J = 6.58Hz, 2H; C^7H_2), 1.70 (quintet, 4H; C^8H_2, $C^{13}H_2$), 1.37 (m, 8H; C^9H_2, $C^{10}H_2$, $C^{11}H_2$, $C^{12}H_2$).

^{13}C NMR ($CDCl_3$) δ (ppm): 159.1 (C^1), 129.4 (C^3, C^5), 120.5 (C^4), 114.5 (C^2, C^6), 75.8 (C^{14}), 67.8 (C^7), 29.8 (C^8, C^{13}), 29.2 (C^{10}, C^{11}), 26.0 (C^{12}), 25.9 (C^9).

EIMS (DCM) m/z: 388.1 ($[M]^+$, 6.6%), 94.1 ($[C_6H_6O]^+$, 100%), 81.0 ($[C_6H_9]^+$, 2.3%), 69.1 ($[C_5H_9]^+$, 29.8%), 55.0 ($[C_4H_7]^+$, 27.7%), 41.1 ($[C_3H_5]^+$, 21.2%).

6.2.28 Synthesis of 1-(2,3,4,5,6-fluorophenyl-1-yloxy)-9'-(phenyl-1-yloxy)nonane, NC9

(i) Synthesis of 1-bromo-(9-phenyl-1-yloxy)nonane

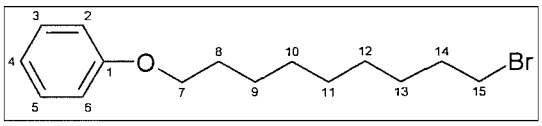

[md/3978/09]
Phenol ($21.3x10^{-3}$mol, 2.0g) and K_2CO_3 (5.30g) were refluxed in acetone (50ml) under N_2 for 45 minutes. A ten-fold excess of 1,9-dibromononane (21.3mol, 43.2ml) was then added and the reaction was refluxed for a further five days. This excess ensures the production of the monomer and not the dimeric species. High vacuum distillation was then used to remove the excess 1,9-dibromononane. Column chromatography on silica (40-60 petroleum ether) was used for purification. A colourless oil was obtained (3.65g, 57%).
^{1}H NMR($CDCl_3$) δ (ppm): 7.29 (m, 2H; C^3H, C^5H), 6.93 (m, 3H; C^2H, C^4H, C^6H), 3.96 (t, J = 6.61Hz, 2H; C^7H_2), 3.43 (t, J = 6.80Hz, 2H; $C^{15}H_2$), 1.87 (quintet, 2H; C^8H_2), 1.79 (quintet, 2H; $C^{14}H_2$), 1.40 (m, 10H; C^9H_2, $C^{10}H_2$, $C^{11}H_2$, $C^{12}H_2$, $C^{13}H_2$).

^{13}C NMR ($CDCl_3$) δ (ppm): 159.5 (C^1), 129.8 (C^3, C^5), 120.9 (C^4), 114.9 (C^2, C^6), 68.2 (C^7), 34.4 (C^{14}), 33.2 (C^{15}), 29.8 (C^8), 29.7 (C^{10}, C^{11}), 29.1 (C^{12}), 28.6 (C^{13}), 26.4 (C^9).

(ii) Synthesis of 1-(2,3,4,5,6-fluorophenyl-1-yloxy)-9'-(phenyl-1-yloxy)nonane, NC9

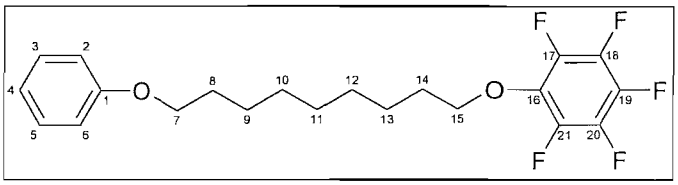

[sml/2954/41]

Pentafluorophenol ($1.67x10^{-3}$mol, 0.308g) and K_2CO_3 (0.47g) were refluxed in DMF (45ml) under N_2 for 4 hours. The 1-bromo-(9-phenyl-1-yloxy)nonane ($1.67x10^{-3}$mol, 0.50 g) and NaI (0.027g) were added and the reaction mixture was then stirred at room temperature under nitrogen for seven days. On completion water (100ml) was added and the organic layer extracted into diethyl ether and an aqueous work-up was carried out. Column chromatography (50% diethyl ether in petroleum ether 40-60) was used for purification. A colourless oil was obtained (0.52g, 77%) which has a mp < 15°C.

^{1}H NMR($CDCl_3$) δ (ppm): 7.19 (m, 2H; C^3H, C^5H), 6.83 (m, 3H; C^2H, C^4H, C^6H), 4.07 (t, J = 6.40Hz, 2H; $C^{15}H_2$), 3.88 (t, J = 6.40Hz, 2H; C^7H_2), 1.70 (quintet, J = 6.40Hz, 4H; C^8H_2, $C^{14}H_2$), 1.34 (m, 10H; C^9H_2, $C^{10}H_2$, $C^{11}H_2$, $C^{12}H_2$, $C^{13}H_2$).

^{13}C NMR ($CDCl_3$) δ (ppm): 159.1 (C^1), 129.4 (C^3, C^5), 120.5 (C^4), 114.5 (C^2, C^6), 75.8 (C^{15}), 67.8 (C^7), 30.3 (C^8, C^{14}), 29.3 (C^{10}, C^{11}, C^{12}), 26.0 (C^{13}), 25.5 (C^9).

EIMS (DCM) m/z: 402.2 ($[M]^+$, 40.1%), 94.0 ($[C_6H_6O]^+$, 100%), 81.2 ($[C_6H_9]^+$, 17.7%), 69.1 ($[C_5H_9]^+$, 68.0%), 55.1 ($[C_4H_7]^+$, 73.3%), 41.1 ($[C_3H_5]^+$, 61.4%).

6.2.29 Synthesis of 1-(2,3,4,5,6-fluorophenyl-1-yloxy)-10'-(phenyl-1-yloxy)decane, NC10

(i) Synthesis of 1-bromo-(10-phenyl-1-yloxy)decane

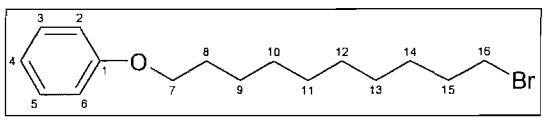

[md/3978/13]

Phenol ($21.3x10^{-3}$mol, 2.0g) and K_2CO_3 (5.3g) were refluxed in acetone (50ml) under N_2 for 45 minutes. A ten-fold excess of 1,10-dibromodecane (21.3mol, 63.8g, 47.8ml) was then added and the reaction was refluxed for a further five days. This excess ensures the production of the monomer and not the dimeric species. High vacuum distillation was then

used to remove the excess 1,10-dibromodecane. Column chromatography (40-60 petroleum ether) was used for purification. A colourless oil was obtained (2.98g, 45%).
^{1}H NMR($CDCl_3$) δ (ppm): 7.21 (m, 2H; C^3H, C^5H), 6.84 (m, 3H; C^2H, C^4H, C^6H), 3.88 (t, J = 6.40Hz, 2H; C^7H_2), 3.34 (t, J = 6.80Hz, 2H; $C^{16}H_2$), 1.78 (quintet, 2H; C^8H_2), 1.72 (quintet, 2H; $C^{15}H_2$), 1.32 (m, 12H; C^9H_2, $C^{10}H_2$, $C^{11}H_2$, $C^{12}H_2$, $C^{13}H_2$, $C^{14}H_2$).

^{13}C NMR ($CDCl_3$) δ (ppm): 159.5 (; C^1), 129.8 (C^3, C^5), 120.9 (C^4), 114.9 (C^2, C^6), 68.3 (C^7), 34.4 (C^{15}), 33.2 (C^{16}), 29.7 (C^8, C^{10}, C^{11}), 29.1 (C^{12}), 28.6 (C^{13}), 26.5 (C^9).

(ii) Synthesis of 1-(2,3,4,5,6-fluorophenyl-1-yloxy)-10'-(phenyl-1-yloxy)octane, NC10

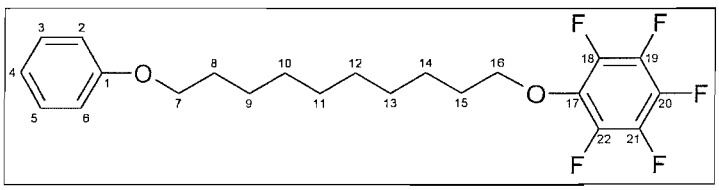

[sml/2954/40]
Pentafluorophenol ($3.19x10^{-3}$mol, 0.589g) and K_2CO_3 (0.88g) were refluxed in DMF (45ml) at 90°C under N_2 for 4 hours. The 1-bromo-(10-phenyl-1-yloxy)decane ($3.19x10^{-3}$mol, 1.0 g) and NaI (0.048g) were added and the reaction mixture was then stirred at room temperature under nitrogen for seven days. On completion water (100ml) was added and the organic layer extracted into diethyl ether and an aqueous work-up was carried out. Recrystallisation using hot ethanol was used for purification. White crystals were obtained (0.62g, 47%) which had a mp = 40°C.
^{1}H NMR($CDCl_3$) δ (ppm): 7.19 (m, 2H; C^3H, C^5H), 6.83 (m, 3H; C^2H, C^4H, C^6H), 4.07 (t, J = 6.40Hz, 2H; $C^{16}H_2$), 3.87 (t, J = 6.58Hz, 2H; C^7H_2), 1.70 (quintet, 4H; C^8H_2, $C^{15}H_2$), 1.32 (m, 12H; C^9H_2, $C^{10}H_2$, $C^{11}H_2$, $C^{12}H_2$, $C^{13}H_2$, $C^{14}H_2$).

^{13}C NMR ($CDCl_3$) δ (ppm): 159.1 (C^1), 129.4 (C^3, C^5), 120.5 (C^4), 114.5 (C^2, C^6), 75.8 (C^{16}), 67.7 (C^7), 30.1 (C^8, C^{15}), 29.4 (C^{10}, C^{13}), 29.3 (C^{11}, C^{12}), 26.0 (C^{14}) 25.5 (C^9).

EIMS (DCM) m/z: 416.2 ($[M]^+$, 13.1%), 94.0 ($[C_6H_6O]^+$, 100%), 81.1 ($[C_6H_9]^+$, 5.2%), 69.2 ($[C_5H_9]^+$, 31.6%), 55.2 ($[C_4H_7]^+$, 67.5%), 41.2 ($[C_3H_5]^+$, 39.8%).

6.2.30 Synthesis of 1,8-bis-(phenyl-1-yloxy)octane-d10, DC8

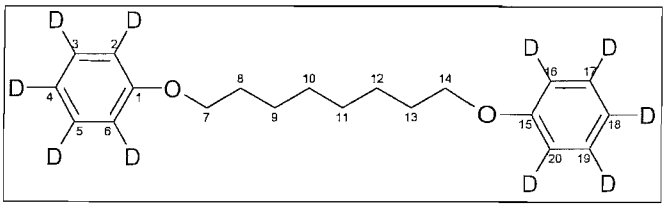

[md/3978/23]

The procedure was identical to 6.2.1 except that column chromatography (25% DCM in petroleum ether 40-60) followed by recrystallisation with methanol was used for purification. Phenol-d6 ($4.99x10^{-3}$mol, 0.50g), K_2CO_3 (1.38g), 1,8-dibromooctane ($2.50x10^{-3}$mol, 0.45ml) and NaI (0.037g). White crystals were obtained (0.28g, 36%) which had a mp = 84°C.

^{1}H NMR($CDCl_3$) δ (ppm): 3.88 (t, J=6.27Hz, 4H; C^7H_2, $C^{14}H_2$), 1.72 (quintet, J=6.53Hz, 4H; C^8H_2, $C^{13}H_2$), 1.37 (m, 8H; C^9H_2, $C^{10}H_2$, $C^{11}H_2$, $C^{12}H_2$).

^{13}C NMR ($CDCl_3$) δ (ppm): 159.5 (C^1, C^{15}), 129.3 (J_{CD}=24.3Hz, C^3, C^5, C^{17}, C^{19}), 125.2 (C^4, C^{18}), 114.6 (J_{CD}=24.3Hz, C^2, C^6, C^{16}, C^{20}), 68.3 (C^7, C^{14}), 29.7 (C^8, C^{13}, C^{10}, C^{11}), 26.4 (C^9, C^{12}).

EIMS (DCM) m/z: 308.4 ($[M]^+$, 10.3%), 99.1 ($[C_6D_6HO]^+$, 100%), 98.1 ($[C_6D_6O]^+$, 15.7%), 82.1 ($[C_6D_6]^+$, 39.1%), 69.2 ($[C_5H_9]^+$, 28.4%), 55.2 ($[C_4H_7]^+$, 19.5%), 41.2 ($[C_3H_5]^+$, 22.3%).

6.2.31 Synthesis of 1,10-bis-(phenyl-1-yloxy)decane-d10, DC10

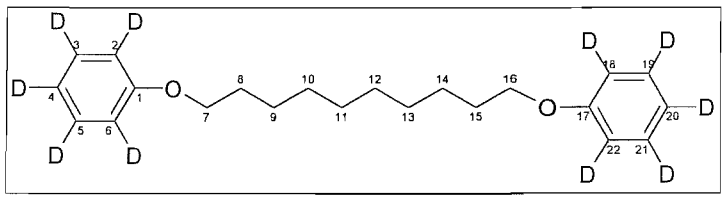

[md/3978/27]

The procedure was identical to procedure 6.2.1 except column chromatography (25% DCM in petroleum ether 40-60) followed by recrystallisation with methanol was used for purification. Phenol-d6 ($9.98x10^{-3}$mol, 1.0g), K_2CO_3 (2.76g), 1,10-dibromodecane

($4.99x10^{-3}$mol, 1.50g) and NaI (0.075g). White crystals were obtained (0.98g, 58%) which has a mp = 85°C.

^{1}H NMR($CDCl_3$) δ (ppm): 3.81 (t, J=6.53Hz, 4H; C^7H_2, $C^{16}H_2$), 1.63 (quintet, J=6.78Hz, 4H; C^8H_2, $C^{15}H_2$), 1.26 (m, 12H; C^9H_2, $C^{10}H_2$, $C^{11}H_2$, $C^{12}H_2$, $C^{13}H_2$, $C^{14}H_2$).

^{13}C NMR ($CDCl_3$) δ (ppm): 159.8 (C^1, C^{17}), 129.6 (J_{CD}=24.3Hz, C^3, C^5, C^{19}, C^{21}), 120.7 (J_{CD}=24.3Hz, C^4, C^{20}), 114.9 (J_{CD}=24.3Hz, C^2, C^6, C^{18}, C^{22}), 68.6 (C^7, C^{16}), 30.2 (C^8, C^{13}, C^{10}, C^{11}), 26.8 (C^9, C^{12}).

EIMS (DCM) m/z: 336.4 ($[M]^+$, 14.3%), 99.1 ($[C_6D_5H_3O]^+$, 100%), 98.2 ($[C_6D_5H_2O]^+$, 15.0%), 82.2 ($[C_6D_5H_2]^+$, 28.1%), 69.2 ($[C_5H_9]^+$, 14.5%), 55.2 ($[C_4H_7]^+$, 20.3%), 41.2 ($[C_3H_5]^+$, 16.2%).

6.2.32 Synthesis of 4,4`-bis-pentyloxy-biphenyl

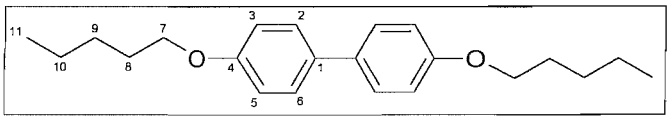

[sml/2954/14]

4,4`-dihydroxybiphenyl (0.5g, 2.69mmol), 1-bromopentane (0.81g, 5.38mmol, 0.67ml), sodium iodide (0.081g, 0.538mmol) and potassium carbonate (1.86g, 0.0135mol) were added to butanone (MEK) (15ml) and refluxed under nitrogen for 2 days. On completion water (2x50ml) was added and the resultant white precipitate was filtered and dried. Purification was achieved by recrystallisation using a 1:1 of petroleum ether and toluene at -20°C. White crystals were obtained (0.61g, 70%) which had a mp = 134.5°C. (Lit. [4] mp = 134°C).

^{1}H NMR($CDCl_3$) δ (ppm): 7.48 (doublet (split via W coupling), J = 8.82, 2.94Hz, 4H; C^2H, C^6H), 6.98 (doublet (split via W coupling), J = 8.82, 2.94Hz, 4H; C^2H, C^6H), 4.0 (t, J = 6.62Hz, 4H; C^7H_2), 1.81 (quintet, J = 6.62Hz, 4H; C^8H_2), 1.57 (m, 8H; C^9H_2, $C^{10}H_2$), 0.98 (t, J = 6.62Hz, 6H; $C^{11}H_3$).

^{13}C NMR($CDCl_3$) δ (ppm): 158.4 (C^4), 133.5 (C^1), 127.8 (C^2, C^6), 114.9 (C^3, C^5), 68.2 (C^7), 29.2 (C^8), 28.4 (C^9), 22.7 (C^{10}), 14.2 (C^{11}).

EIMS (DCM) m/z: 326.3 ($[M]^+$, 59.2%), 186.1 ($[C_{12}H_{10}O_2]^+$, 100%), 55.2 ($[C_4H_7]^+$, 4.5%), 41.2 ($[C_3H_5]^+$, 11.0%).

6.3 References

[1] S. Solonina, Zh. Russ. Fiz.-Khim. O-va; (1898), **30**, 618.

[2] V. Braun, Chem. Ber.; (1909), **42**, 4548.

[3] T. W.Cheung; PhD Thesis, Univ. of Southampton, (1990), 59.

[4] H. O. Wirth, F. U. Herrmann, G. Herrmann and W. Kern, Mol. Cryst., **4**, 321, (1968).

Appendix A

ESR Experimental Parameters

A.1 Parameters for ZLI-4792 + 10wt% C7

Temperature / K	Centre Field / G	Sweep width / G	Sweep Time / s	Pulse time / s
305	3331	40	0.66	0.025
307	3331	40	0.66	0.025
310	3331	40	0.66	0.020
312	3331	40	0.66	0.020
315	3333	40	0.66	0.010
317	3333	40	0.66	0.010
320	3333	50	0.66	0.010
325	3333	50	0.66	0.010

Table 1: Parameters for the variable temperature step-rotation experiment of ZLI-4792 + 10wt% C7.

A.2 Parameters for ZLI-4792 + 10wt% C8

The variable temperature step-rotation experiment was not carried out for this doped system due an unexpected formation of a gel phase, see Chapter 5.

A.3 Parameters for ZLI-4792 + 10wt% C9

Temperature / K	Centre Field / G	Sweep width / G	Sweep Time / s	Pulse time / s
305	3331	40	0.66	0.020
307	3333	40	1.31	0.090
310	3333	40	0.66	0.010
312	3333	40	1.31	0.030
315	3333	50	0.66	0.045
317	3333	40	0.66	0.025
320	3333	40	0.66	0.001
325	3333	40	0.66	0.010

Table 2: Parameters for the variable temperature step-rotation experiment of ZLI-4792 + 10wt% C9.

A.4 Parameters for ZLI-4792 + 10wt% C10

The variable temperature step-rotation experiment was not carried out for this doped system due an unexpected formation of a gel phase, see Chapter 5.

A.5 Parameters for ZLI-4792 + 10wt% C11

Temperature / K	Centre Field / G	Sweep width / G	Sweep Time / s	Pulse time / s
305	3331	40	0.66	0.025
307	3331	40	0.66	0.025
310	3331	40	0.66	0.025
312	3331	40	0.66	0.025
315	3331	40	0.66	0.025
317	3331	40	0.66	0.020
320	3331	40	0.66	0.020
325	3331	40	0.66	0.020

Table 3: Parameters for the variable temperature step-rotation experiment of ZLI-4792 + 10wt% C11.

A.6 Parameters for ZLI-4792 + 10wt% C12

The variable temperature step-rotation experiment was not carried out for this doped system due an unexpected formation of a gel phase, see Chapter 5.

A.7 Parameters for ZLI-4792 + 10wt% MeC9

Temperature / K	Centre Field / G	Sweep width / G	Sweep Time / s	Pulse time / s
305	3333	40	0.66	0.020
307	3333	40	0.66	0.020
310	3333	40	0.66	0.020
312	3333	40	0.66	0.010
315	3333	40	0.66	0.010
317	3333	40	0.66	0.020
320	3333	40	0.66	0.020
325	3333	40	0.66	0.020

Table 4: Parameters for the variable temperature step-rotation experiment of ZLI-4792 + 10wt% MeC9.

A.8 Parameters for ZLI-4792 + 10wt% MeC10

The variable temperature step-rotation experiment was not carried out for this doped system due an unexpected formation of a gel phase, see Chapter 5.

A.9 Parameters for ZLI-4792 + 10wt% FC7

Temperature / K	Centre Field / G	Sweep width / G	Sweep Time / s	Pulse time / s
305	3331	40	1.31	0.020
307	3331	40	0.66	0.080
310	3331	40	0.66	0.080
312	3331	40	0.66	0.050
315	3331	40	0.66	0.050
317	3332	40	0.66	0.040
320	3333	40	0.66	0.030
325	3333	40	0.66	0.030

Table 5: Parameters for the variable temperature step-rotation experiment of ZLI-4792 + 10wt% FC7.

A.10 Parameters for ZLI-4792 + 10wt% FC9

Temperature / K	Centre Field / G	Sweep width / G	Sweep Time / s	Pulse time / s
305	3333	40	1.31	0.020
307	3333	40	1.31	0.010
310	3333	40	1.31	0.010
312	3333	40	0.66	0.008
315	3333	40	0.66	0.005
317	3333	40	0.66	0.006
320	3331	40	0.66	0.006
325	3331	40	0.66	0.006

Table 6: Parameters for the variable temperature step-rotation experiment of ZLI-4792 + 10wt% FC9.

A.11 Parameters for ZLI-4792 + 10wt% CF3C9

Temperature / K	Centre Field / G	Sweep width / G	Sweep Time / s	Pulse time / s
305	3333	40	1.31	0.020
307	3333	40	1.31	0.009
310	3333	40	1.31	0.008
312	3333	40	1.31	0.008
315	3331	40	0.66	0.005
317	3331	40	0.66	0.005
320	3331	40	0.66	0.005
325	3331	40	0.66	0.005

Table 7: Parameters for the variable temperature step-rotation experiment of ZLI-4792 + 10wt% CF3C9.

A.12 Parameters for ZLI-4792 + 10wt% CF3C10

Temperature / K	Centre Field / G	Sweep width / G	Sweep Time / s	Pulse time / s
305	3333	40	0.66	0.015
307	3331	40	0.66	0.015
310	3333	40	0.66	0.015
312	3333	40	0.66	0.015
315	3333	40	0.66	0.015
317	3333	40	0.66	0.010
320	3333	40	0.66	0.008
325	3333	40	0.66	0.006

Table 8: Parameters for the variable temperature step-rotation experiment of ZLI-4792 + 10wt% CF3C10.

A.13 Parameters for ZLI-4792 + 10wt% 23FC9

Temperature / K	Centre Field / G	Sweep width / G	Sweep Time / s	Pulse time / s
305	3331	40	0.66	0.030
307	3331	40	0.66	0.020
310	3331	40	0.66	0.020
312	3331	40	0.66	0.015
315	3331	40	0.66	0.015
317	3331	40	0.66	0.015
320	3333	40	0.66	0.010
325	3333	40	0.66	0.010

Table 9: Parameters for the variable temperature step-rotation experiment of ZLI-4792 + 10wt% 23FC9.

A.14 Parameters for ZLI-4792 + 10wt% 24FC7

Temperature / K	Centre Field / G	Sweep width / G	Sweep Time / s	Pulse time / s
305	3335	40	1.31	0.030
307	3335	40	1.31	0.020
310	3335	40	1.31	0.040
312	3335	40	1.31	0.025
315	3334	40	0.66	0.009
317	3333	40	0.66	0.007
320	3334	40	0.66	0.007
325	3334	40	0.66	0.006

Table 10: Parameters for the variable temperature step-rotation experiment of ZLI-4792 + 10wt% 24FC7.

A.15 Parameters for ZLI-4792 + 10wt% 24FC8

Temperature / K	Centre Field / G	Sweep width / G	Sweep Time / s	Pulse time / s
305	3333	40	0.66	0.015
307	3331	40	0.66	0.015
310	3333	40	0.66	0.015
312	3333	40	0.66	0.015
315	3333	40	0.66	0.015
317	3333	40	0.66	0.010
320	3333	40	0.66	0.010
325	3333	40	0.66	0.008

Table 11: Parameters for the variable temperature step-rotation experiment of ZLI-4792 + 10wt% 24FC8.

A.16 Parameters for ZLI-4792 + 10wt% 24FC9

Temperature / K	Centre Field / G	Sweep width / G	Sweep Time / s	Pulse time / s
305	3333	40	1.31	0.020
307	3335	40	1.31	0.020
310	3335	40	1.31	0.015
312	3335	40	1.31	0.010
315	3334	40	1.31	0.010
317	3333	40	0.66	0.001
320	3334	40	0.66	0.001
325	3334	40	0.66	0.001

Table 12: Parameters for the variable temperature step-rotation experiment of ZLI-4792 + 10wt% 24FC9.

A.17 Parameters for ZLI-4792 + 10wt% 24FC10

Temperature / K	Centre Field / G	Sweep width / G	Sweep Time / s	Pulse time / s
305	3333	40	0.66	0.015
307	3331	40	0.66	0.015
310	3333	40	0.66	0.015
312	3333	40	0.66	0.008
315	3333	40	0.66	0.008
317	3333	40	0.66	0.008
320	3333	40	0.66	0.006
325	3333	40	0.66	0.006

Table 13: Parameters for the variable temperature step-rotation experiment of ZLI-4792 + 10wt% 24FC9.

A.18 Parameters for ZLI-4792 + 10wt% 34FC7

Temperature / K	Centre Field / G	Sweep width / G	Sweep Time / s	Pulse time / s
305	3331	40	1.31	0.150
307	3331	40	0.66	0.050
310	3332	40	0.66	0.050
312	3332	40	0.66	0.040
315	3332	40	0.66	0.040
317	3332	40	0.66	0.030
320	3332	40	0.66	0.030
325	3332	40	0.66	0.030

Table 14: Parameters for the variable temperature step-rotation experiment of ZLI-4792 + 10wt% 34FC7.

A.19 Parameters for ZLI-4792 + 10wt% 34FC10

Temperature / K	Centre Field / G	Sweep width / G	Sweep Time / s	Pulse time / s
305	3331	40	0.66	0.025
307	3331	40	0.66	0.025
310	3331	40	0.66	0.025
312	3331	40	0.66	0.020
315	3331	40	0.66	0.020
317	3331	40	0.66	0.020
320	3333	40	0.66	0.010
325	3333	40	0.66	0.010

Table 15: Parameters for the variable temperature step-rotation experiment of ZLI-4792 + 10wt% 34FC10.

A.20 Parameters for ZLI-4792 + 10wt% 234FC7

Temperature / K	Centre Field / G	Sweep width / G	Sweep Time / s	Pulse time / s
305	3333	40	0.66	0.015
307	3331	40	0.66	0.015
310	3333	40	0.66	0.009
312	3333	40	0.66	0.009
315	3333	40	0.66	0.008
317	3333	40	0.66	0.008
320	3333	40	0.66	0.006
325	3333	40	0.66	0.006

Table 16: Parameters for the variable temperature step-rotation experiment of ZLI-4792 + 10wt% 234FC7.

A.21 Parameters for ZLI-4792 + 10wt% 234FC9

Temperature / K	Centre Field / G	Sweep width / G	Sweep Time / s	Pulse time / s
305	3332	40	1.31	0.040
307	3332	40	0.66	0.020
310	3332	40	0.66	0.015
312	3332	40	0.66	0.015
315	3332	40	0.66	0.013
317	3332	40	0.66	0.013
320	3332	40	0.66	0.012
325	3332	40	0.66	0.010

Table 17: Parameters for the variable temperature step-rotation experiment of ZLI-4792 + 10wt% 234FC9.

A.22 Parameters for ZLI-4792 + 10wt% 345FC7

Temperature / K	Centre Field / G	Sweep width / G	Sweep Time / s	Pulse time / s
305	3332	40	1.31	0.040
307	3332	40	0.66	0.020
310	3332	40	0.66	0.015
312	3332	40	0.66	0.013
315	3332	40	0.66	0.010
317	3332	40	0.66	0.010
320	3332	40	0.66	0.009
325	3332	40	0.66	0.009

Table 18: Parameters for the variable temperature step-rotation experiment of ZLI-4792 + 10wt% 345FC7.

A.23 Parameters for ZLI-4792 + 10wt% 345FC9

Temperature / K	Centre Field / G	Sweep width / G	Sweep Time / s	Pulse time / s
305	3332	40	1.31	0.040
307	3332	40	0.66	0.020
310	3332	40	0.66	0.020
312	3332	40	0.66	0.012
315	3332	40	0.66	0.010
317	3332	40	0.66	0.010
320	3332	40	0.66	0.010
325	3332	40	0.66	0.008

Table 19: Parameters for the variable temperature step-rotation experiment of ZLI-4792 + 10wt% 345FC9.

A.24 Parameters for ZLI-4792 + 10wt% PFC7

Temperature / K	Centre Field / G	Sweep width / G	Sweep Time / s	Pulse time / s
305	3331	40	1.31	0.150
307	3331	40	1.31	0.180
310	3331	40	1.31	0.180
312	3331	40	0.66	0.040
315	3331	40	0.66	0.040
317	3331	40	0.66	0.030
320	3331	40	0.66	0.030
325	3331	40	0.66	0.030

Table 20: Parameters for the variable temperature step-rotation experiment of ZLI-4792 + 10wt% PFC7.

A.25 Parameters for ZLI-4792 + 10wt% PFC9

Temperature / K	Centre Field / G	Sweep width / G	Sweep Time / s	Pulse time / s
305	3332	40	1.31	0.040
307	3332	40	0.66	0.020
310	3332	40	0.66	0.015
312	3332	40	0.66	0.015
315	3332	40	0.66	0.013
317	3332	40	0.66	0.013
320	3332	40	0.66	0.012
325	3332	40	0.66	0.010

Table 21: Parameters for the variable temperature step-rotation experiment of ZLI-4792 + 10wt% PFC9.

A.26 Parameters for ZLI-4792 + 10wt% NC8

Temperature / K	Centre Field / G	Sweep width / G	Sweep Time / s	Pulse time / s
305	3333	40	0.66	0.025
307	3333	40	0.66	0.025
310	3333	40	0.66	0.025
312	3333	40	0.66	0.025
315	3333	40	0.66	0.025
317	3331	40	0.66	0.020
320	3331	40	0.66	0.020
325	3333	40	0.66	0.020

Table 22: Parameters for the variable temperature step-rotation experiment of ZLI-4792 + 10wt% NC8.

A.27 Parameters for ZLI-4792 + 10wt% NC9

Temperature / K	Centre Field / G	Sweep width / G	Sweep Time / s	Pulse time / s
305	3331	40	0.66	0.040
307	3331	40	0.66	0.030
310	3331	40	0.66	0.030
312	3331	40	0.66	0.030
315	3331	40	0.66	0.030
317	3331	40	0.66	0.030
320	3331	40	0.66	0.030
325	3333	40	0.66	0.020

Table 23: Parameters for the variable temperature step-rotation experiment of ZLI-4792 + 10wt% NC9.

A.28 Parameters for ZLI-4792 + 10wt% NC10

Temperature / K	Centre Field / G	Sweep width / G	Sweep Time / s	Pulse time / s
305	3331	40	0.66	0.040
307	3331	40	0.66	0.040
310	3331	40	0.66	0.030
312	3331	40	0.66	0.030
315	3331	40	0.66	0.030
317	3331	40	0.66	0.030
320	3333	40	0.66	0.018
325	3333	40	0.66	0.018

Table 24: Parameters for the variable temperature step-rotation experiment of ZLI-4792 + 10wt% NC10.

A.29 Parameters for ZLI-4792 + 10wt% DFS33

This compound was supplied by Hitachi for investigation into the relaxation time when doped in ZLI-4792.

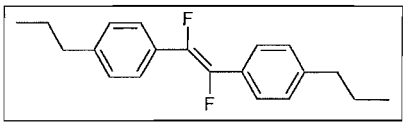

Temperature / K	Centre Field / G	Sweep width / G	Sweep Time / s	Pulse time / s
298	3335	50	2.62	0.45
305	3335	50	0.66	0.075
310	3335	50	0.66	0.075
315	3335	50	0.66	0.075
320	3335	50	0.66	0.075
325	3335	50	0.66	0.075
330	3336	50	0.66	0.075
335	3336	50	0.66	0.075

Table 25: Parameters for the variable temperature step-rotation experiment of ZLI-4792 + 10wt% DFS33.

Appendix B

ESR Results for the Doped Systems

B.1 Results for ZLI-4792 + 10wt% C7

T / K	τ / s	Error in τ / s	% Decrease compared to ZLI-4792	$\overline{P}_2$	$\beta_1 / °$	$\beta_2 / °$	$\beta_1 - \beta_2 / °$
305	0.96	± 0.07	10	0.66	36.0	25.9	10.1
307	0.92	± 0.07	13	0.64	35.8	25.3	10.5
310	0.73	± 0.04	22	0.62	34.8	22.4	12.4
312	0.69	± 0.04	24	0.61	36.5	22.9	13.6
315	0.63	± 0.04	21	0.59	37.5	22.6	14.9
317	0.56	± 0.03	28	0.58	35.4	19.9	15.5
320	0.50	± 0.03	26	0.55	34.8	18.1	16.7
325	0.42	± 0.03	32	0.49	34.2	15.3	18.9

Table 1: Results for ZLI-4792 + 10wt% C7.

B.2 Results for ZLI-4792 + 10wt% C9

T / K	τ / s	Error in τ / s	% Decrease compared to ZLI-4792	$\overline{P}_2$	$\beta_1 / °$	$\beta_2 / °$	$\beta_1 - \beta_2 / °$
305	0.97	± 0.07	9	0.67			
307	0.84	± 0.06	21	0.65	30.1	14.4	15.7
310	0.77	± 0.05	17	0.63	35.6	23.6	12.0
312	0.70	± 0.04	23	0.62	34.8	14.0	20.8
315	0.64	± 0.06	20	0.60	31.5	20.6	10.9
317	0.58	± 0.04	26	0.58	37.3	21.4	16.0
320	0.51	± 0.03	25	0.55	38.2	20.1	18.1
325	0.45	± 0.03	27	0.50	36.6	17.3	19.3

Table 2: Results for ZLI-4792 + 10wt% C9.

B.3 Results for ZLI-4792 + 10wt% C11

T / K	τ / *s*	Error in τ / *s*	% Decrease compared to ZLI-4792	$\overline{P}_2$	β_1 / °	β_2 / °	$\beta_1 - \beta_2$ / °
305	1.08	± 0.09	-1	0.68	35.5	26.6	8.9
307	1.00	± 0.07	6	0.67	35.0	25.6	9.4
310	0.81	± 0.06	13	0.65	34.5	23.5	11.0
312	0.77	± 0.05	15	0.64	36.3	24.0	12.3
315	0.72	± 0.04	10	0.62	34.3	22.0	12.3
317	0.70	± 0.04	10	0.61	35.8	22.7	13.1
320	0.60	± 0.04	12	0.59	35.0	20.4	14.6
325	0.50	± 0.04	19	0.54	33.3	17.4	15.9

Table 3: Results for ZLI-4792 + 10wt% C11.

B.4 Results for ZLI-4792 + 10wt% MeC9

T / K	τ / *s*	Error in τ / *s*	% Decrease compared to ZLI-4792	$\overline{P}_2$	β_1 / °	β_2 / °	$\beta_1 - \beta_2$ / °
305	1.13	± 0.08	-6	0.70	38.6	29.1	9.5
307	1.08	± 0.08	-2	0.69	38.5	28.9	9.4
310	0.98	± 0.06	-5	0.68	39.4	28.6	10.8
312	0.88	± 0.05	3	0.67	40.5	28.4	12.1
315	0.78	± 0.04	3	0.66	41.0	27.5	13.5
317	0.74	± 0.04	5	0.64	40.3	26.4	13.9
320	0.66	± 0.03	3	0.62	39.0	24.3	14.7
325	0.56	± 0.03	10	0.59	37.4	21.1	16.3

Table 4: Results for ZLI-4792 + 10wt% MeC9.

B.5 Results for ZLI-4792 + 10wt% FC7

T / K	τ / *s*	Error in τ / *s*	% Decrease compared to ZLI-4792	$\overline{P}_2$	β_1 / °	β_2 / °	$\beta_1 - \beta_2$ / °
305	0.99	± 0.06	7	0.68	30.4	16.3	14.1
307	0.94	± 0.07	11	0.68	35.1	25.1	10.0
310	0.83	± 0.07	11	0.66	31.5	21.6	9.9
312	0.80	± 0.06	12	0.66	32.6	22.0	10.6
315	0.77	± 0.05	4	0.65	39.2	26.0	13.2
317	0.68	± 0.04	13	0.63	34.4	21.5	12.9
320	0.60	± 0.04	12	0.61	34.0	19.8	14.2
325	0.53	± 0.03	15	0.58	33.5	18.2	15.3

Table 5: Results for ZLI-4792 + 10wt% FC7.

B.6 Results for ZLI-4792 + 10wt% FC9

T / K	τ / *s*	Error in τ / *s*	% Decrease compared to ZLI-4792	$\overline{P_2}$	β_1 / °	β_2 / °	$\beta_1 - \beta_2$ / °
305	1.03	± 0.05	4	0.69	35.8	19.6	16.2
307	0.89	± 0.05	16	0.67	31.2	15.8	15.4
310	0.79	± 0.05	15	0.66	30.3	13.6	16.7
312	0.76	± 0.05	16	0.65	32.4	21.4	11.0
315	0.68	± 0.05	15	0.63	33.3	20.8	12.5
317	0.59	± 0.04	24	0.61	32.9	19.1	13.8
320	0.54	± 0.04	21	0.59	32.6	17.7	14.9
325	0.48	± 0.03	23	0.55	31.6	15.9	15.7

Table 6: Results for ZLI-4792 + 10wt% FC9.

B.7 Results for ZLI-4792 + 10wt% CF3C9

T / K	τ / *s*	Error in τ / *s*	% Decrease compared to ZLI-4792	$\overline{P_2}$	β_1 / °	β_2 / °	$\beta_1 - \beta_2$ / °
305	1.04	± 0.05	3	0.69	33.1	18.1	15.0
307	0.99	± 0.05	7	0.67	32.9	17.6	15.3
310	0.90	± 0.05	3	0.66	32.6	16.2	16.4
312	0.84	± 0.05	8	0.65	32.4	15.4	17.0
315	0.74	± 0.05	8	0.63	34.4	22.2	12.2
317	0.72	± 0.05	8	0.61	34.8	22.2	12.6
320	0.62	± 0.04	9	0.59	33.7	20.1	13.6
325	0.54	± 0.04	13	0.55	32.9	17.2	15.7

Table 7: Results for ZLI-4792 + 10wt% CF3C9.

B.8 Results for ZLI-4792 + 10wt% CF3C10

T / K	τ / *s*	Error in τ / *s*	% Decrease compared to ZLI-4792	$\overline{P_2}$	β_1 / °	β_2 / °	$\beta_1 - \beta_2$ / °
305	1.19	± 0.10	-11	0.72	33.7	26.0	7.7
307	1.07	± 0.08	-1	0.71	33.4	25.0	8.4
310	1.03	± 0.08	-11	0.69	34.4	25.4	9.0
312	0.93	± 0.07	-2	0.69	33.7	24.2	9.5
315	0.82	± 0.05	-2	0.68	34.2	23.1	11.1
317	0.81	± 0.05	-4	0.67	35.2	23.9	11.3
320	0.77	± 0.05	-13	0.66	33.8	22.6	11.2
325	0.57	± 0.03	8	0.61	35.3	19.9	15.4

Table 8: Results for ZLI-4792 + 10wt% CF3C10.

B.9 Results for ZLI-4792 + 10wt% 23FC9

T / K	τ / *s*	Error in τ / *s*	% Decrease compared to ZLI-4792	$\overline{P}_2$	β_1 / °	β_2 / °	$\beta_1 - \beta_2$ / °
305	1.03	± 0.07	4	0.68	35.6	26.3	9.3
307	0.96	± 0.08	9	0.67	34.4	24.8	9.6
310	0.88	± 0.06	5	0.65	34.7	24.2	10.5
312	0.79	± 0.05	13	0.63	36.7	24.5	12.2
315	0.65	± 0.04	19	0.61	37.1	22.7	14.4
317	0.63	± 0.03	19	0.59	40.0	24.0	16.0
320	0.59	± 0.04	13	0.56	38.3	22.0	16.3
325	0.41	± 0.03	34	0.50	32.7	14.0	18.7

Table 9: Results for ZLI-4792 + 10wt% 23FC9.

B.10 Results for ZLI-4792 + 10wt% 24FC7

T / K	τ / *s*	Error in τ / *s*	% Decrease compared to ZLI-4792	$\overline{P}_2$	β_1 / °	β_2 / °	$\beta_1 - \beta_2$ / °
305	0.99	± 0.05	7	0.67	36.1	19.2	16.9
307	0.84	± 0.04	21	0.65	33.6	16.0	17.6
310	0.76	± 0.05	18	0.64	32.0	14.0	18.0
312	0.71	± 0.04	22	0.62	33.1	13.4	19.7
315	0.64	± 0.05	20	0.60	33.3	20.0	13.3
317	0.62	± 0.04	21	0.59	35.6	21.0	14.6
320	0.53	± 0.04	22	0.57	31.9	17.3	14.6
325	0.45	± 0.04	27	0.52	32.0	15.1	16.9

Table 10: Results for ZLI-4792 + 10wt% 24FC7.

B.11 Results for ZLI-4792 + 10wt% 24FC8

T / K	τ / *s*	Error in τ / *s*	% Decrease compared to ZLI-4792	$\overline{P}_2$	β_1 / °	β_2 / °	$\beta_1 - \beta_2$ / °
305	0.95	± 0.07	11	0.68	34.4	24.7	9.7
307	0.91	± 0.06	14	0.68	33.3	23.5	9.8
310	0.87	± 0.05	6	0.68	40.6	28.3	12.3
312	0.81	± 0.05	11	0.67	36.6	24.7	11.9
315	0.71	± 0.04	11	0.64	33.5	21.4	12.1
317	0.66	± 0.04	15	0.63	34.4	21.2	13.2
320	0.61	± 0.04	10	0.61	35.8	21.3	14.5
325	0.46	± 0.03	26	0.55	34.1	16.5	17.6

Table 11: Results for ZLI-4792 + 10wt% 24FC8.

B.12 Results for ZLI-4792 + 10wt% 24FC9

T / K	τ / *s*	**Error in** τ / *s*	% Decrease compared to ZLI-4792	$\overline{P}_2$	β_1 / °	β_2 / °	$\beta_1 - \beta_2$ / °
305	1.00	± 0.07	7	0.68	36.7	19.6	17.1
307	0.89	± 0.06	16	0.66	34.6	17.2	17.4
310	0.81	± 0.05	13	0.65	33.6	15.4	18.2
312	0.75	± 0.05	18	0.63	33.3	14.5	18.8
315	0.68	± 0.04	15	0.62	33.1	13.0	20.0
317	0.66	± 0.04	15	0.61	40.4	25.0	15.4
320	0.54	± 0.04	21	0.58	36.0	19.7	16.3
325	0.45	± 0.03	27	0.53	35.1	16.7	18.4

Table 12: Results for ZLI-4792 + 10wt% 24FC9.

B.13 Results for ZLI-4792 + 10wt% 24FC10

T / K	τ / *s*	**Error in** τ / *s*	% Decrease compared to ZLI-4792	$\overline{P}_2$	β_1 / °	β_2 / °	$\beta_1 - \beta_2$ / °
305	0.96	± 0.07	9	0.68	36.2	26.1	10.1
307	0.94	± 0.07	11	0.67	35.1	25.1	10.0
310	0.81	± 0.05	13	0.66	36.2	24.5	11.7
312	0.76	± 0.05	16	0.66	33.2	22.0	11.2
315	0.73	± 0.04	9	0.65	36.3	23.6	12.7
317	0.69	± 0.05	12	0.63	34.5	21.7	12.8
320	0.66	± 0.04	3	0.62	35.4	21.8	13.6
325	0.48	± 0.03	23	0.56	35.6	17.7	17.9

Table 13: Results for ZLI-4792 + 10wt% 24FC10.

B.14 Results for ZLI-4792 + 10wt% 34FC7

T / K	τ / *s*	**Error in** τ / *s*	% Decrease compared to ZLI-4792	$\overline{P}_2$	β_1 / °	β_2 / °	$\beta_1 - \beta_2$ / °
305	1.01	± 0.04	6	0.68	37.2	19.9	17.3
307	0.97	± 0.07	8	0.67	36.3	26.3	10.0
310	0.91	± 0.06	2	0.65	37.6	26.5	11.1
312	0.85	± 0.06	7	0.64	35.8	24.6	11.2
315	0.76	± 0.05	5	0.63	32.6	21.5	11.1
317	0.70	± 0.04	10	0.61	38.9	24.7	14.2
320	0.65	± 0.03	4	0.59	41.2	25.4	15.8
325	0.58	± 0.03	6	0.56	37.1	21.2	15.9

Table 14: Results for ZLI-4792 + 10wt% 34FC7.

B.15 Results for ZLI-4792 + 10wt% 34FC10

T / K	τ / *s*	Error in τ / *s*	% Decrease compared to ZLI-4792	$\overline{P}_2$	β_1 / °	β_2 / °	$\beta_1 - \beta_2$ / °
305	1.05	± 0.07	2	0.68	37.8	28.1	9.7
307	0.99	± 0.08	7	0.67	34.9	25.4	9.5
310	0.89	± 0.06	4	0.66	38.2	26.9	11.3
312	0.77	± 0.05	15	0.64	33.5	22.1	11.4
315	0.73	± 0.04	9	0.63	34.4	22.2	12.2
317	0.69	± 0.05	12	0.61	34.0	21.3	12.7
320	0.57	± 0.03	16	0.58	34.9	19.8	15.1
325	0.47	± 0.03	24	0.54	35.3	17.4	17.9

Table 15: Results for ZLI-4792 + 10wt% 34FC10.

B.16 Results for ZLI-4792 + 10wt% 234FC7

T / K	τ / *s*	Error in τ / *s*	% Decrease compared to ZLI-4792	$\overline{P}_2$	β_1 / °	β_2 / °	$\beta_1 - \beta_2$ / °
305	1.00	± 0.07	7	0.68	36.2	26.5	9.7
307	0.94	± 0.07	11	0.67	34.9	24.8	10.1
310	0.82	± 0.05	12	0.65	36.9	25.5	11.4
312	0.76	± 0.05	16	0.64	34.6	22.8	11.8
315	0.67	± 0.04	16	0.63	33.5	20.8	12.7
317	0.63	± 0.04	19	0.62	34.8	21.0	13.8
320	0.59	± 0.04	13	0.61	33.4	19.3	14.1
325	0.48	± 0.03	23	0.55	36.2	18.1	18.1

Table 16: Results for ZLI-4792 + 10wt% 234FC7.

B.17 Results for ZLI-4792 + 10wt% 234FC9

T / K	τ / *s*	Error in τ / *s*	% Decrease compared to ZLI-4792	$\overline{P}_2$	β_1 / °	β_2 / °	$\beta_1 - \beta_2$ / °
305	0.97	± 0.04	9	0.67	38.3	19.9	18.4
307	0.88	± 0.06	17	0.66	38.2	26.9	11.3
310	0.79	± 0.06	15	0.64	33.5	22.6	10.9
312	0.76	± 0.05	16	0.64	37.3	24.6	12.7
315	0.70	± 0.04	13	0.62	35.4	22.4	13.0
317	0.64	± 0.04	18	0.61	35.3	21.3	14.0
320	0.59	± 0.04	13	0.59	36.2	21.0	15.2
325	0.50	± 0.03	19	0.55	34.8	18.1	16.7

Table 17: Results for ZLI-4792 + 10wt% 234FC9.

B.18 Results for ZLI-4792 + 10wt% 345FC7

T / K	τ / *s*	Error in τ / *s*	% Decrease compared to ZLI-4792	$\overline{P}_2$	β_1 / °	β_2 / °	$\beta_1 - \beta_2$ / °
305	1.06	± 0.05	1	0.70	33.9	19.0	14.9
307	0.99	± 0.07	7	0.69	35.3	25.8	9.5
310	0.88	± 0.06	5	0.68	33.5	23.5	10.0
312	0.86	± 0.06	5	0.67	34.4	23.9	10.5
315	0.83	± 0.06	-4	0.64	35.2	24.0	11.2
317	0.78	± 0.05	0	0.63	36.8	24.3	12.5
320	0.71	± 0.04	-4	0.61	35.9	22.9	13.0
325	0.56	± 0.03	10	0.57	35.8	20.0	15.8

Table 18: Results for ZLI-4792 + 10wt% 345FC7.

B.19 Results for ZLI-4792 + 10wt% 345FC9

T / K	τ / *s*	Error in τ / *s*	% Decrease compared to ZLI-4792	$\overline{P}_2$	β_1 / °	β_2 / °	$\beta_1 - \beta_2$ / °
305	0.95	± 0.05	11	0.66	32.4	16.9	15.5
307	0.82	± 0.06	23	0.65	34.7	23.6	11.1
310	0.78	± 0.06	16	0.63	34.4	22.8	11.6
312	0.76	± 0.05	16	0.62	35.5	23.3	12.2
315	0.70	± 0.04	13	0.60	36.0	22.9	13.1
317	0.68	± 0.04	13	0.59	35.6	22.2	13.4
320	0.59	± 0.04	13	0.56	35.7	20.4	15.3
325	0.52	± 0.04	16	0.52	34.6	17.9	16.7

Table 19: Results for ZLI-4792 + 10wt% 345FC9.

B.20 Results for ZLI-4792 + 10wt% PFC7

T / K	τ / *s*	Error in τ / *s*	% Decrease compared to ZLI-4792	$\overline{P}_2$	β_1 / °	β_2 / °	$\beta_1 - \beta_2$ / °
305	0.98	± 0.04	8	0.68	37.8	20.0	17.8
307	0.95	± 0.05	10	0.67	35.0	18.1	16.9
310	0.92	± 0.05	1	0.66	37.0	18.7	18.3
312	0.89	± 0.05	2	0.64	38.6	27.1	11.5
315	0.83	± 0.05	-4	0.63	40.9	27.9	13.0
317	0.73	± 0.04	6	0.61	40.1	26.0	14.1
320	0.67	± 0.04	1	0.60	41.2	25.7	15.5
325	0.53	± 0.03	15	0.57	37.2	20.0	17.2

Table 20: Results for ZLI-4792 + 10wt% PFC7.

B.21 Results for ZLI-4792 + 10wt% PFC9

T / K	τ / *s*	Error in τ / *s*	% Decrease compared to ZLI-4792	$\overline{P}_2$	β_1 / °	β_2 / °	$\beta_1 - \beta_2$ / °
305	0.90	± 0.05	16	0.67	35.3	17.4	17.9
307	0.85	± 0.06	20	0.66	34.0	23.5	10.5
310	0.79	± 0.05	15	0.65	35.7	24.0	11.7
312	0.76	± 0.05	16	0.64	35.2	23.4	11.8
315	0.73	± 0.04	9	0.62	36.3	23.4	12.9
317	0.66	± 0.04	15	0.61	35.8	22.0	13.8
320	0.62	± 0.03	9	0.59	38.1	22.6	15.5
325	0.55	± 0.03	11	0.55	37.5	20.6	16.9

Table 21: Results for ZLI-4792 + 10wt% PFC9.

B.22 Results for ZLI-4792 + 10wt% NC8

T / K	τ / *s*	Error in τ / *s*	% Decrease compared to ZLI-4792	$\overline{P}_2$	β_1 / °	β_2 / °	$\beta_1 - \beta_2$ / °
305	0.98	± 0.07	8	0.68	37.3	27.1	10.2
307	0.85	± 0.05	20	0.68	32.9	22.8	10.1
310	0.81	± 0.05	13	0.66	38.7	26.3	12.4
312	0.75	± 0.04	18	0.64	40.3	26.4	13.9
315	0.67	± 0.04	16	0.62	34.3	21.3	13.0
317	0.64	± 0.04	18	0.61	35.3	21.3	14.0
320	0.58	± 0.03	15	0.59	35.6	20.4	15.2
325	0.44	± 0.02	29	0.55	38.2	18.1	20.1

Table 22: Results for ZLI-4792 + 10wt% NC8.

B.23 Results for ZLI-4792 + 10wt% NC9

T / K	τ / *s*	Error in τ / *s*	% Decrease compared to ZLI-4792	$\overline{P}_2$	β_1 / °	β_2 / °	$\beta_1 - \beta_2$ / °
305	1.02	± 0.07	5	0.68	41.1	30.3	10.8
307	0.95	± 0.06	10	0.67	39.4	28.3	11.1
310	0.92	± 0.06	1	0.66	38.2	27.1	11.1
312	0.88	± 0.05	3	0.65	39.8	27.8	12.0
315	0.73	± 0.04	9	0.63	34.4	22.2	12.2
317	0.67	± 0.04	14	0.62	37.8	23.4	14.4
320	0.60	± 0.04	12	0.60	33.9	19.7	14.2
325	0.47	± 0.03	24	0.56	35.7	17.9	17.8

Table 23: Results for ZLI-4792 + 10wt% NC9.

B.24 Results for ZLI-4792 + 10wt% NC10

T / K	τ / *s*	Error in τ / *s*	% Decrease compared to ZLI-4792	$\overline{P}_2$	β_1 / °	β_2 / °	$\beta_1 - \beta_2$ / °
305	0.94	± 0.07	12	0.68	33.1	23.7	9.4
307	0.90	± 0.07	15	0.68	29.1	20.6	8.5
310	0.83	± 0.05	11	0.66	38.3	26.4	11.9
312	0.78	± 0.05	14	0.65	38.1	25.5	12.6
315	0.69	± 0.04	14	0.63	40.3	25.4	14.9
317	0.65	± 0.04	17	0.62	35.5	21.9	13.6
320	0.61	± 0.04	10	0.60	34.6	20.4	14.2
325	0.52	± 0.03	16	0.57	34.6	18.4	16.2

Table 24: Results for ZLI-4792 + 10wt% NC10.

B.25 Results for ZLI-4792 + 10wt% DFS33

Temperature / K	τ / *s*	Error in τ / *s*	$\overline{P}_2$	β_1 / °	β_2 / °	$\beta_1 - \beta_2$ / °
293	1.39	± 0.04	0.79	31.9	13.6	18.3
298	1.13	± 0.05	0.77	37.2	15.7	21.5
305	0.88	± 0.06	0.75	34.7	25.8	8.9
310	0.75	± 0.05	0.74	34.8	25.1	9.7
315	0.63	± 0.04	0.72	35.1	23.9	11.2
320	0.53	± 0.03	0.71	35.4	22.2	13.2
325	0.48	± 0.03	0.69	34.0	20.0	14.0
330	0.46	± 0.03	0.68	31.5	18.1	13.4
335	0.38	± 0.02	0.65	35.3	18.0	17.3

Table 25: Results for ZLI-4792 + 10wt% DFS33.

Appendix C

Crystallographic data

Single Crystal X-ray structural analyses were made James Orton using a Nonius Kappa CCD diffractometer and Nonius FR591 rotating anode X-ray generator. The data was processed using the Collect [1], HKL [2] and maXus [3] software and structures were solved using SHELX-97 [4] in the WinGX [5] suite of programs. All H atom fixed at idealized positions, with a riding model and fixed thermal parameters [U_{ij} = 1.2Uij (eq) for the atom to which they are bonded] used for subsequent refinements.

C.1 Crystallographic data for 1,7-bis-(phenyloxy)heptane

The crystallisation of 1,7-bis-(phenyloxy)heptane in hot methanol yielded plate-like crystals.

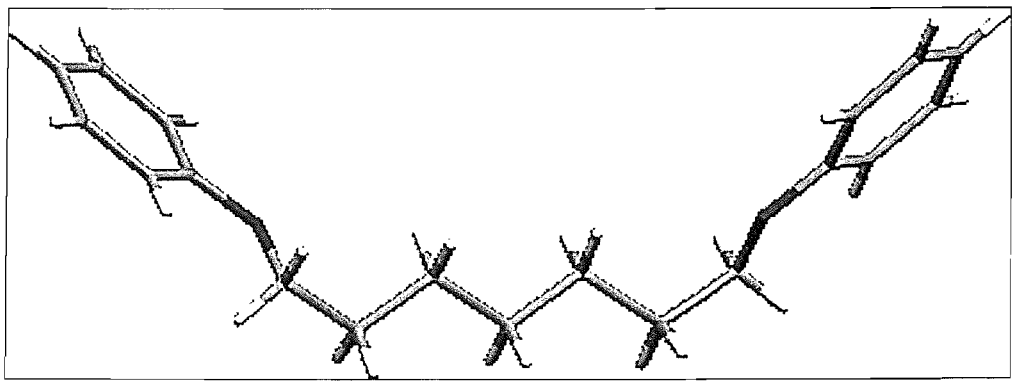

Table 1. Crystal data and structure refinement.

Identification code	**O4jbo015**	
Empirical formula	$C_{19}H_{24}O_2$	
Formula weight	284.38	
Temperature	120(2) K	
Wavelength	0.71073 Å	
Crystal system	Monoclinic	
Space group	*C*2/*c*	
Unit cell dimensions	a = 30.498(6) Å	α = 90°
	b = 5.0673(10) Å	β = 110.68(3)°
	c = 11.141(2) Å	γ = 90°
Volume	1610.7(6) Å^3	
Z	4	
Density (calculated)	1.173 Mg / m^3	
Absorption coefficient	0.074 mm^{-1}	
F(000)	616	
Crystal	Plate; Colourless	
Crystal size	0.25 x 0.20 x 0.04 mm^3	

θ range for data collection	3.66 – 27.49°
Index ranges	$-38 \le h \le 38, -6 \le k \le 6, -14 \le l \le 14$
Reflections collected	10802
Independent reflections	1840 [$R_{int} = 0.1016$]
Completeness to $\theta = 27.49°$	99.4 %
Absorption correction	Semi-empirical from equivalents
Max. and min. transmission	0.9970 and 0.9817
Refinement method	Full-matrix least-squares on F^2
Data / restraints / parameters	1840 / 0 / 96
Goodness-of-fit on F^2	1.170
Final R indices [$F^2 > 2\sigma(F^2)$]	$R1 = 0.0558$, $wR2 = 0.1511$
R indices (all data)	$R1 = 0.0696$, $wR2 = 0.1590$
Largest diff. peak and hole	0.190 and –0.242 e Å^{-3}

Diffractometer: *Nonius KappaCCD* area detector (ϕ scans and ω scans to fill *asymmetric unit* sphere). **Cell determination:** DirAx (Duisenberg, A.J.M.(1992). J. Appl. Cryst. 25, 92-96.) **Data collection:** Collect (Collect: Data collection software, R. Hooft, Nonius B.V., 1998). **Data reduction and cell refinement**: *Denzo* (Z. Otwinowski & W. Minor, *Methods in Enzymology* (1997) Vol. **276**: *Macromolecular Crystallography*, part A, pp. 307–326; C. W. Carter, Jr. & R. M. Sweet, Eds., Academic Press). **Absorption correction**: *SORTAV* (R. H. Blessing, Acta Cryst. A**51** (1995) 33–37; R. H. Blessing, J. Appl. Cryst. **30** (1997) 421–426). **Structure solution**: *SHELXS97* (G. M. Sheldrick, Acta Cryst. (1990) A**46** 467–473). **Structure refinement**: *SHELXL97* (G. M. Sheldrick (1997), University of Göttingen, Germany). **Graphics:** *ORTEP3 for Windows* (L. J. Farrugia, J. Appl. Crystallogr. 1997, 30, 565).

Special details:

All H atom fixed at idealized positions, with a riding model and fixed thermal parameters [U_{ij} = 1.2Uij (eq) for the atom to which they are bonded] used for subsequent refinements.

Table 2. Atomic coordinates [× 10^4], equivalent isotropic displacement parameters [Å^2 × 10^3] and site occupancy factors. U_{eq} is defined as one third of the trace of the orthogonalized U^{ij} tensor.

Atom	x	y	z	U_{eq}	$S.o.f.$
O1	1183(1)	776(2)	611(1)	25(1)	1
C8	616(1)	4163(4)	–245(2)	26(1)	1
C10	0	4141(5)	–2500	27(1)	1
C4	1466(1)	–844(3)	1559(2)	22(1)	1
C5	1470(1)	–913(4)	2817(2)	24(1)	1
C2	2056(1)	–4258(4)	2067(2)	26(1)	1
C3	1760(1)	–2511(3)	1190(2)	24(1)	1
C1	2063(1)	–4340(4)	3330(2)	27(1)	1
C7	881(1)	2577(3)	947(2)	24(1)	1
C9	293(1)	2488(4)	–1348(2)	26(1)	1
C6	1772(1)	–2670(4)	3694(2)	27(1)	1

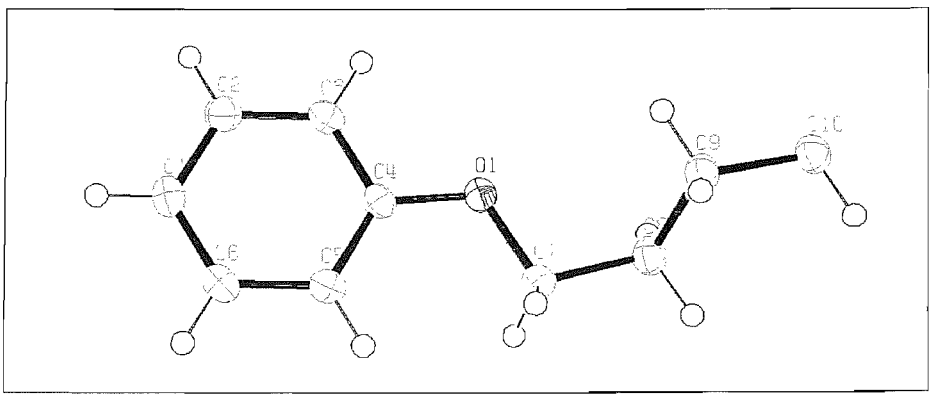

Table 3. Bond lengths [Å] and angles [°].

O1–C4	1.374(2)
O1–C7	1.438(2)
C8–C7	1.518(2)
C8–C9	1.531(2)
C8–H8A	0.9900
C8–H8B	0.9900
C10–C9^{i}	1.529(2)
C10–C9	1.529(2)
C10–H10A	0.9900
C10–H10B	0.9900
C4–C3	1.396(2)
C4–C5	1.397(2)
C5–C6	1.400(2)
C5–H5	0.9500
C2–C3	1.389(2)
C2–C1	1.400(2)
C2–H2	0.9500
C3–H3	0.9500
C1–C6	1.387(3)
C1–H1	0.9500
C7–H7A	0.9900
C7–H7B	0.9900
C9–H9A	0.9900
C9–H9B	0.9900
C6–H6	0.9500
C4–O1–C7	117.71(13)
C7–C8–C9	113.66(15)
C7–C8–H8A	108.8
C9–C8–H8A	108.8
C7–C8–H8B	108.8
C9–C8–H8B	108.8
H8A–C8–H8B	107.7
C9^{i}–C10–C9	113.6(2)
C9^{i}–C10–H10A	108.9
C9–C10–H10A	108.9
C9^{i}–C10–H10B	108.9
C9–C10–H10B	108.9
H10A–C10–H10B	107.7
O1–C4–C3	115.42(14)
O1–C4–C5	124.54(15)
C3–C4–C5	120.04(16)
C4–C5–C6	119.12(16)
C4–C5–H5	120.4
C6–C5–H5	120.4
C3–C2–C1	120.09(16)
C3–C2–H2	120.0
C1–C2–H2	120.0
C2–C3–C4	120.30(15)
C2–C3–H3	119.8
C4–C3–H3	119.8
C6–C1–C2	119.43(16)
C6–C1–H1	120.3
C2–C1–H1	120.3
O1–C7–C8	107.53(13)
O1–C7–H7A	110.2
C8–C7–H7A	110.2
O1–C7–H7B	110.2
C8–C7–H7B	110.2
H7A–C7–H7B	108.5
C10–C9–C8	112.93(15)
C10–C9–H9A	109.0

C8–C9–H9A	109.0
C10–C9–H9B	109.0
C8–C9–H9B	109.0
H9A–C9–H9B	107.8
C1–C6–C5	121.02(16)
C1–C6–H6	119.5
C5–C6–H6	119.5

Symmetry transformations used to generate equivalent atoms:
(i) –x,y,–z–1/2

Table 4. Anisotropic displacement parameters [Å^2× 10^3]. The anisotropic displacement factor exponent takes the form: $-2\pi^2[h^2a^{*2}U^{11} + \cdots + 2\,h\,k\,a^*\,b^*\,U^{12}]$.

Atom	U^{11}	U^{22}	U^{33}	U^{23}	U^{13}	U^{12}
O1	24(1)	30(1)	20(1)	2(1)	6(1)	6(1)
C8	22(1)	26(1)	25(1)	1(1)	4(1)	1(1)
C10	23(1)	29(1)	25(1)	0	4(1)	0
C4	20(1)	24(1)	19(1)	–1(1)	4(1)	–3(1)
C5	26(1)	26(1)	22(1)	–1(1)	8(1)	0(1)
C2	22(1)	29(1)	27(1)	–2(1)	8(1)	0(1)
C3	23(1)	28(1)	19(1)	–2(1)	6(1)	–3(1)
C1	25(1)	29(1)	25(1)	4(1)	4(1)	1(1)
C7	23(1)	26(1)	24(1)	–2(1)	7(1)	1(1)
C9	23(1)	27(1)	24(1)	1(1)	3(1)	2(1)
C6	29(1)	30(1)	20(1)	1(1)	7(1)	–2(1)

Table 5. Hydrogen coordinates [× 10^4] and isotropic displacement parameters [Å^2 × 10^3].

Atom	x	y	z	U_{eq}	*S.o.f.*
H8A	844	5089	–543	31	1
H8B	425	5521	–16	31	1
H10A	–212	5293	–2236	32	0.50
H10B	212	5293	–2764	32	0.50
H5	1271	217	3073	29	1
H2	2254	–5398	1809	31	1
H3	1758	–2451	336	28	1
H1	2266	–5530	3932	33	1
H7A	1068	3768	1644	29	1
H7B	659	1591	1246	29	1
H9A	486	1227	–1627	32	1
H9B	80	1453	–1033	32	1
H6	1778	–2719	4552	32	1

C.2 Crystallographic data for 1,8-bis-(phenyloxy)octane

The crystallisation of 1,8-bis-(phenyloxy)octane in hot methanol yielded plate-like crystals.

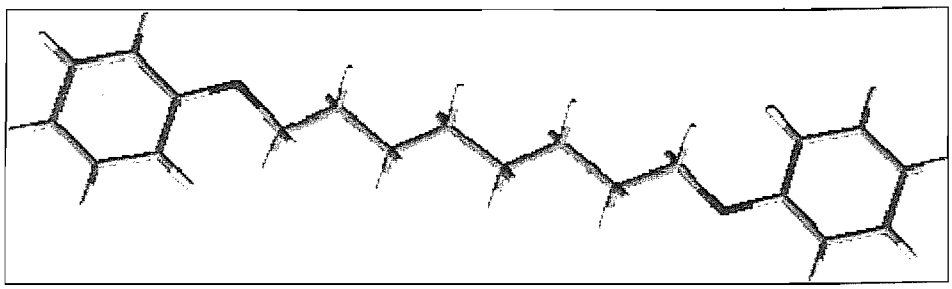

Table 1. Crystal data and structure refinement.

Identification code	**04jbo011**	
Empirical formula	$C_{20}H_{26}O_2$	
Formula weight	298.41	
Temperature	120(2) K	
Wavelength	0.71073 Å	
Crystal system	Monoclinic	
Space group	$P2_1/c$	
Unit cell dimensions	a = 17.848(7) Å	α = 90°
	b = 7.1298(16) Å	β = 93.15(3)°
	c = 6.602(2) Å	γ = 90°
Volume	838.9(5) Å^3	
Z	2	
Density (calculated)	1.181 Mg / m^3	
Absorption coefficient	0.074 mm^{-1}	
F(000)	324	
Crystal	Block; Colourless	
Crystal size	0.03 × 0.03 × 0.01 mm^3	
θ range for data collection	3.08 – 27.47°	
Index ranges	$-22 \le h \le 23$, $-9 \le k \le 9$, $-8 \le l \le 8$	
Reflections collected	11945	
Independent reflections	1916 [R_{int} = 0.1062]	
Completeness to θ = 27.47°	99.3 %	
Absorption correction	Semi–empirical from equivalents	
Max. and min. transmission	0.9993 and 0.9978	
Refinement method	Full-matrix least-squares on F^2	
Data / restraints / parameters	1916 / 0 / 101	
Goodness-of-fit on F^2	1.136	
Final R indices [$F^2 > 2\sigma(F^2)$]	$R1$ = 0.0776, $wR2$ = 0.1611	
R indices (all data)	$R1$ = 0.1129, $wR2$ = 0.1796	
Extinction coefficient	0.30(3)	
Largest diff. peak and hole	0.517 and –0.706 e Å^{-3}	

Diffractometer: *Nonius KappaCCD* area detector (ϕ scans and ω scans to fill *asymmetric unit* sphere). **Cell determination:** DirAx (Duisenberg, A.J.M.(1992). J. Appl. Cryst. 25, 92-96.) **Data collection:** Collect (Collect: Data collection software, R. Hooft, Nonius B.V., 1998). **Data reduction and cell refinement**: *Denzo* (Z. Otwinowski & W. Minor, *Methods in Enzymology* (1997) Vol. **276**: *Macromolecular Crystallography*, part A, pp. 307–326; C. W. Carter, Jr. & R. M. Sweet, Eds., Academic Press). **Absorption correction**: *SORTAV* (R. H. Blessing, Acta Cryst. A**51** (1995) 33–37; R. H. Blessing, J. Appl. Cryst. **30** (1997) 421–426). **Structure solution**: *SHELXS97* (G. M. Sheldrick, Acta Cryst. (1990) A**46** 467–473). **Structure refinement**: *SHELXL97* (G. M. Sheldrick (1997), University of Göttingen, Germany). **Graphics:** *ORTEP3 for Windows* (L. J. Farrugia, J. Appl. Crystallogr. 1997, 30, 565).

Special details:

All H atom fixed at idealized positions, with a riding model and fixed thermal parameters [U_{ij} = 1.2*U*ij (eq) for the atom to which they are bonded] used for subsequent refinements.

Table 2. Atomic coordinates [$\times 10^4$], equivalent isotropic displacement parameters [$Å^2 \times 10^3$] and site occupancy factors. U_{eq} is defined as one third of the trace of the orthogonalized U^{ij} tensor.

Atom	*x*	*y*	*z*	U_{eq}	*S.o.f.*
C1	682(1)	4986(3)	2789(3)	30(1)	1
C2	1254(1)	5931(3)	3905(3)	31(1)	1
C3	1977(1)	5950(3)	3234(3)	29(1)	1
C4	2137(1)	5036(3)	1443(3)	26(1)	1
C5	1575(1)	4045(3)	353(3)	28(1)	1
C6	849(1)	4038(3)	1043(3)	29(1)	1
C7	3027(1)	4564(3)	−1136(3)	28(1)	1
C8	3796(1)	5313(3)	−1581(3)	29(1)	1
C9	4068(1)	4619(3)	−3603(3)	27(1)	1
C10	4855(1)	5342(3)	−4001(3)	28(1)	1
O1	2865(1)	5221(2)	855(2)	30(1)	1

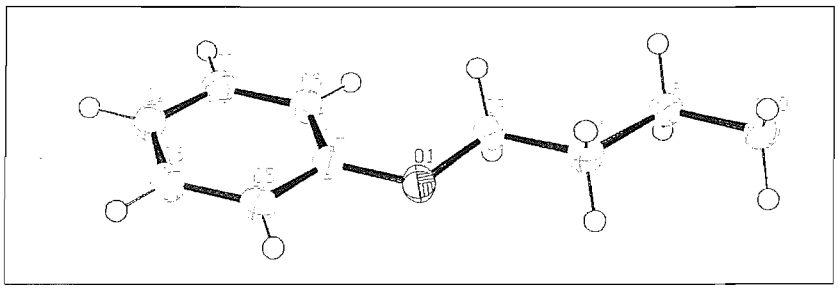

Table 3. Bond lengths [Å] and angles [°].

C1–C6	1.383(3)
C1–C2	1.398(3)
C1–H1	0.9500
C2–C3	1.388(3)
C2–H2	0.9500
C3–C4	1.393(3)
C3–H3	0.9500
C4–O1	1.381(2)
C4–C5	1.395(3)
C5–C6	1.396(3)
C5–H5	0.9500
C6–H6	0.9500
C7–O1	1.440(2)
C7–C8	1.516(3)
C7–H7A	0.9900
C7–H7B	0.9900
C8–C9	1.527(3)
C8–H8A	0.9900
C8–H8B	0.9900
C9–C10	1.533(2)
C9–H9A	0.9900
C9–H9B	0.9900
C10–C10^{i}	1.524(3)
C10–H10A	0.9900
C10–H10B	0.9900
C6–C1–C2	119.33(17)
C6–C1–H1	120.3
C2–C1–H1	120.3
C3–C2–C1	120.06(17)
C3–C2–H2	120.0
C1–C2–H2	120.0

C2–C3–C4	120.32(18)
C2–C3–H3	119.8
C4–C3–H3	119.8
O1–C4–C3	115.74(16)
O1–C4–C5	124.34(16)
C3–C4–C5	119.91(17)
C4–C5–C6	119.18(17)
C4–C5–H5	120.4
C6–C5–H5	120.4
C1–C6–C5	121.14(17)
C1–C6–H6	119.4
C5–C6–H6	119.4
O1–C7–C8	107.00(15)
O1–C7–H7A	110.3
C8–C7–H7A	110.3
O1–C7–H7B	110.3
C8–C7–H7B	110.3
H7A–C7–H7B	108.6
C7–C8–C9	112.94(16)
C7–C8–H8A	109.0
C9–C8–H8A	109.0
C7–C8–H8B	109.0
C9–C8–H8B	109.0
H8A–C8–H8B	107.8
C8–C9–C10	112.28(16)
C8–C9–H9A	109.1
C10–C9–H9A	109.1
C8–C9–H9B	109.1
C10–C9–H9B	109.1
H9A–C9–H9B	107.9
$C10^{i}$–C10–C9	113.48(19)
$C10^{i}$–C10–H10A	108.9
C9–C10–H10A	108.9
$C10^{i}$–C10–H10B	108.9
C9–C10–H10B	108.9
H10A–C10–H10B	107.7
C4–O1–C7	117.73(14)

Symmetry transformations used to generate equivalent atoms:
(i) –x+1,–y+1,–z–1

Table 4. Anisotropic displacement parameters [$Å^2 \times 10^3$]. The anisotropic displacement factor exponent takes the form: $-2\pi^2[h^2a^{*2}U^{11} + \cdots + 2\,h\,k\,a^*\,b^*\,U^{12}]$.

Atom	U^{11}	U^{22}	U^{33}	U^{23}	U^{13}	U^{12}
C1	26(1)	32(1)	32(1)	4(1)	5(1)	2(1)
C2	38(1)	28(1)	28(1)	0(1)	8(1)	2(1)
C3	33(1)	26(1)	27(1)	2(1)	0(1)	0(1)
C4	26(1)	25(1)	27(1)	5(1)	4(1)	2(1)
C5	32(1)	26(1)	27(1)	−1(1)	2(1)	2(1)
C6	27(1)	30(1)	30(1)	2(1)	0(1)	−1(1)
C7	29(1)	28(1)	26(1)	−3(1)	3(1)	1(1)
C8	28(1)	31(1)	30(1)	−1(1)	3(1)	−1(1)
C9	26(1)	29(1)	28(1)	1(1)	0(1)	1(1)
C10	26(1)	29(1)	29(1)	−2(1)	0(1)	−1(1)
O1	27(1)	38(1)	27(1)	−2(1)	4(1)	−2(1)

Table 5. Hydrogen coordinates [$\times 10^4$] and isotropic displacement parameters [$Å^2 \times 10^3$].

Atom	*x*	*y*	*z*	U_{eq}	*S.o.f.*
H1	183	4996	3225	36	1
H2	1147	6561	5124	37	1
H3	2364	6590	3998	34	1
H5	1684	3383	−845	34	1
H6	464	3370	301	35	1
H7A	2645	5029	−2158	33	1
H7B	3026	3176	−1173	33	1
H8A	4161	4927	−477	35	1
H8B	3778	6701	−1598	35	1
H9A	3712	5039	−4714	33	1
H9B	4072	3231	−3605	33	1
H10A	4847	6731	−4005	33	1
H10B	5207	4935	−2876	33	1

C.3 References

[1] "Collect" data collection software, B.V. Nonius, (1999).

[2] Z. Otwinowski, W, Minor, Processing of X-ray Diffraction Data Collected in Oscillation Mode. Methods in Enzymology, Volume **276**: Macromolecular Crystallography, part A, p.307-326, 1997, C. W. Carter, Jr, R. M. Sweet, Eds., Academic Press.

[3] S. Mackay. C. J. Gilmore, C. Edwards, M. Tremayne, N. Stuart, K. Shankland. MaXus: *a computer program for the solution and refinement of crystal structures from diffraction data* University of Glasgow, Scotland, UK, B. V. Nonius, Delft, The Netherlands and MacScience Co. Ltd., Yokohama, Japan, 1998.

[4] SHELX-97 - Programs for Crystal Structure Analysis (Release 97-2); G. M. Sheldrick, *Institut für Anorganische Chemie der Universikit, Tammanstrasse* 4, D3400 Guttingen, Germany, 1998.

[5] WinGX - L.J. Farrugia; *J. Appl. Cryst.*, ***32***, (1999), 837.